5-1-2013 12:00 AM

Application of Mixed Iron Oxides in Subsurface Remediation Technologies

Saidur Rahman Chowdhury
The University of Western Ontario

Supervisor
Dr Ernest K. Yanful
The University of Western Ontario

Graduate Program in Civil and Environmental Engineering
A thesis submitted in partial fulfillment of the requirements for the degree in Doctor of Philosophy

APPLICATION OF MIXED IRON OXIDES IN SUBSURFACE REMEDIATION TECHNOLOGIES

(Thesis format: Integrated Articles)

By

SAIDUR RAHMAN CHOWDHURY

Graduate Program in Engineering

Department of Civil and Environmental Engineering

A thesis submitted in partial fulfillment

of the requirements for the degree of

Doctor of Philosophy

The School of Graduate and Postdoctoral Studies

Western University

London, Ontario, Canada

ABSTRACT

Heavy metal contamination of soil and groundwater has been a concern in water supply and public health in many countries where the water supply system draws primarily from groundwater. In the present study, mixed maghemite-magnetite nanoparticles have been used as adsorbents for Cr(VI), As and Cd(II) removal. From the study, it is apparent that the removal of Cr(VI), Cd(II) and As(V) by mixed iron oxide nanoparticles depends on pH, temperature, contact time, solid/liquid ratio and initial concentration of heavy metals. The results showed that Cr(VI) adsorption on mixed maghemite-magnetite was dependent on solution pH between 3 and 6. Theoretical multiplet analyses in X-ray photoelectron spectroscopy (XPS) study showed that during Cr adsorption, the amount of maghemite increased from 70 to 89%. Fe(II) was transformed into Fe(III) by the redox reaction and Cr(VI) species were reduced to Cr(III) species. In arsenic removal study, it was found that the percent of maghemite also increased for As(V) and As(III) adsorption. At the same time, the percentage of magnetite was reduced for both cases. Thus, a redox reaction occurred on the mixed magnetite-magheamite surface when arsenic was introduced. In cadmium removal study, adsorption capacity of mixed maghemite-magnetite for Cd(II) ions increased with an increase in the pH of the adsorbate solution. The results showed that 0.8 g/L of 20-60 nm maghemite-magnetite particles removed up to 1.5 mg/L Cd. The XPS surveys confirmed that As, Cr(VI) and Cd(II) ions may undergo oxidation-reduction reactions upon exposure to mixed maghemite-magnetite, or may be fixed by complexation to the oxygen atoms in the oxyhydroxy groups. The investigation of transport and chemical states analysis during arsenic removal by

monolith slag from nickel smelting revealed that slag was efficient in arsenic removal, attaining equilibrium sorption capacities in the range of 1000-1054 µg/g for an initial arsenic concentration of C_0 = 10 mg/L. Column studies showed the sorption of arsenic by smelter slag (a waste material) was complex and involved both chemisorption and physical sorption. Sorption capacities for As(V) were significantly higher for Ni smelter slag. Raman spectroscopy and XPS results demonstrate that the As reacted with a large proportion of the slag in the experiment. Thus, further investigation would be necessary to evaluate the applicability of mixed iron oxide loaded particles for subsurface remediation at field scale.

Key Words: Arsenic, chromium, cadmium, adsorption, mixed magnetite-maghemite, nanoparticles, Thermodynamics.

CO- AUTHORSHIP

This thesis was written in accordance with the guidelines and regulations for a manuscript format stipulated by the School of Graduate Studies at Western University. The candidate conducted all the laboratory experiments; analyzed and interpreted the laboratory data under the close guidance and supervision of Dr. E.K. Yanful. The candidate wrote the draft manuscript of the following chapters:

Chapter 3

Chowdhury, S.R., Yanful, E.K**.** and Pratt, A.R., 2011." Arsenic removal from aqueous solutions by mixed magnetite-maghemite nanoparticles". Environmental Earth Sciences, 64: 411-423.

Chapter 4

Chowdhury, S.R., Yanful, E.K**.,** and Pratt, A.R., 2012. "Chemical states in XPS and Raman analysis during removal of Cr(VI) from contaminated water by mixed maghemite–magnetite nanoparticles". Journal of Hazardous Materials, 235–236, 246–256.

Chapter 5

Chowdhury, S.R., and Yanful, E.K., 2012. "Kinetics of cadmium(II) uptake by mixed maghemite- magnetite nanoparticles", Journal of Environmental Management. In Final Review.

Chapter 6

Chowdhury, S.R**.,** Yanful, E.K**.** and Pratt, A.R., 2013 "Transport and chemical states analysis during arsenic removal by monolith slag from nickel smelter", Submitted to Water Research. WR-S-13-01424 (Under Review).

ACKNOWLEDGEMENTS

This thesis was written with the assistance of many people. First of all, I would like to express my sincere appreciation and gratitude to my supervisor, Dr. Ernest K. Yanful, for his continuous encouragement and invaluable guidance and support throughout the progress of this study. I have learned the fundamental knowledge of research work under his supervision that will help me to build my future career. I would like to thank Dr. Allen R. Pratt, Adjunct Professor, Department of Earth Science, UWO, for his assistance, insightful discussion as well as guidance to interpret the surface modeling.

Special thank to Mr. Tim Stephens, laboratory technician, for his assistance with ICP-OES analysis. I would like to thank my fellow graduate students and friends who helped me learn through their constructive and beneficial discussions. I am sincerely grateful to the professors, technicians, and administrative assistants of the Department of Civil and Environmental Engineering and the Geotechnical Research Center at Western University for their support and help. The support of Administrative staffs such as C. Quintus, W. Barrett, C. Walter and S. Laurence is highly appreciated.

Finally, I would like to thank my parents, my wife and my son for their endless support and constant encouragement throughout my academic career.

To the ultimate source of love, care and support

My mother Raihana Chowdhury

My wife and my son

My dear family

TABLE OF CONTENTS

LIST OF TABLES

LIST OF FIGURES

NOMENCLATURES

As	Arsenic
N_0	Adsorptive capacity
BE	Electron Binding Energy
q_e	Equilibrium adsorbed concentration (mg/g)
Cr	Chromium
Cd	Cadmium
Ce	Equlibrium Concentration
C_0	Initial Solute Concentration
C_B	Solute concentration at breakthrough
ρ_b	Dry density of adsorbent
EXAFS	X-ray Absorption Fine Structure Spectroscopy
EPA	Environmental Protection Agency
D	Hydrodynamic dispersion coefficient
ICP-OES	Inductively Coupled Plasma-optical Emission Spectroscopy
K_d	Distribution Coefficient
α_L	Dispersivities
D_H	Mechanical dispersion coefficient
nZV	Nano Zero-valent Iron
DO	Dissolved Oxygen

PRB	Permeable Reactive Barrier
n	Porosity of the medium
RC	Removal Capacity
E_h	Redox potential
SEM	Scanning Electron Microscopy
S/L	Solid-liquid ratio
XPS	X-ray Photoelectron Spectroscopy
XRD	X-ray Diffraction
XRF	X-ray Fluorescence
ΔG^0	Standard Gibbs free energy
ΔH^0	Standard enthalpy
ΔS^0	Standard entropy changes
k_{ad}	Adsorption rate constant
De	Effective molecular diffusion (m^2/s)
R	Retardation factor
E_k	Electron Kinetic Energy
LAB	Lewis acid base
FWHM	Full Width half maximum
Y_{id}	The percent chemical species adsorbed
t	The contact time (min)
a	The gradient of linear plot
k_{id}	Intra-particle diffusion rate constant (min^{-1})

CHAPTER 1

INTRODUCTION

1.1Background

Groundwater contamination by heavy metals is a major concern in soil and water environments. Among heavy metals, arsenic (As), chromium (Cr) as well as cadmium (Cd) cause widespread surface and groundwater contamination. Evidence of chronic arsenicosis has been found in populations ingesting arsenic-contaminated drinking water in southwestern Taiwan (Chen et al. 1985), Bangladesh (Smith et al. 2000), Chile (Borgono and Greiber, 1971), India (Mandal et al. 1998), the United States (U.S. EPA, 2001), Mexico (Cebrian et al. 1983), Argentina and Canada (Hindmarsh et al. 1977). Chromium (VI) is found widely in groundwater in North America and elsewhere. It is considered a very toxic ion. Bartlett et al. (1976) reported that Cr(VI) species is known to be more toxic than its trivalent oxidation state. According to Fendorf et al. (1997), Cr(VI) is very toxic to living organisms, is corrosive and a strong oxidant and more mobile in soils than arsenate. These authors further reported that chromium(VI) causes multiple effects after large single doses, including cytotoxicity and direct tissue damage, immune effects such as contact dermatitis in humans and also causes cancer in animals and humans after prolonged exposures. Again, another contaminant is cadmium (Cd^{2+}) which is a toxic heavy metal. Sharma (2008) found its harmful effects on fauna, flora and human beings. Geologic formations, such as soil and bedrocks, are primary sources of

arsenic and chromium contamination in soil-water environment in many parts of the world.

Sanchez et al. (1999) noted that high concentrations of these heavy metals in subsurface or groundwater can constitute long-term health risks to ecosystems and humans. They reported that metals exist in soils and sediments in various fractions, chemical species or forms, namely: adsorptive, exchangeable, carbonate-bound, oxide-bound, organic matter-bound and detrital forms or crystal lattice metals. These geochemical forms of heavy metals in the subsurface affect their solubility, which directly control their mobility, the risk of ground water pollution and bioavailability. Kanel et. al. (2006) and Sanchez et al. (1999) explained that heavy metal ions are toxic to living organisms and non-degradable as well as persistent in the subsurface. Therefore, the elimination of heavy metal ions from aqueous environment is very essential to protect public health. Exposure to heavy metals, even at trace level, is considered to be a risk for human beings (Mohan et al. 2007). Huge amounts of metals-contaminated water have been released to the environment as a result of industrial activities. According to the EPA and the WHO, human exposure to toxic heavy metals can cause many infections and diseases (e.g. cancer). Negative health impacts from these toxic metals have become major issues, making it necessary for scientists and engineers to develop innovative, economical approaches to treat surface water as well as groundwater. According to Blowes et al. (2000), the distribution of heavy metals in subsurface and surface water has been extensively investigated in recent years because of the need for information about the levels and controls of As, Cr(V) and Cd(II) concentrations and the association

of heavy metals with sediments. Kocar et al. (2012) have noted that the motivation for these heavy metal contamination studies has been for various purposes such as investigations of trace metal insufficiencies in diets; heavy metal pollution, accumulation in surface water and groundwater as well as in marine organisms.

To remedy arsenic, chromium and cadmium contamination, several methods are used including precipitation, electrochemical reduction, adsorption, ion exchange, solvent extraction, nano-filtration and reverse osmosis (Mayo et al. 2006; and Hu et al. 2004). Fendorf et al. (1997) demonstrated that a monodentate complex, a bidentate-binuclear complex, and a bidentate-mononuclear complex could be formed when As and Cr were reacted with iron oxides. These authors found that extended X-ray absorption fine structure spectroscopy (EXAFS) provided direct evidence for inner sphere adsorption of arsenate and chromate on goethite. Adsorption of arsenic and chromium on different adsorbents such as iron, iron oxide, iron coated sand, and iron coated activated carbon (Petrusevski et al. 2002), and granular ferric hydroxides (Driehaus et al. 1998) have also been investigated. Natural ores and minerals, namely kaolinite (Guha et al. 1990), feldspar (Prasad, 1994), magnetite (Shipley et al. 2009), hematite and maghemite (Tuutijarvi et al. 2009) have also been used for the adsorption of arsenic though not as extensively as other materials. Arsenic, chromium and cadmium in groundwater can be removed using nanoparticles and currently, a lot of research is being conducted in the field scale. However, their use is limited due to high operation costs and technical difficulties. Increasingly, stringent environmental regulations pertaining to discharges containing heavy metals necessitate the development of technically and economically

feasible processes for the removal of arsenic, chromium and cadmium from waste stream, groundwater as well as from subsurface water.

Many published papers have demonstrated that iron compounds have a high affinity for the adsorption of arsenic, chromium and cadmium compound. Mayo et al. (2006) and Hu et al. (2004) reported that magnetite nanoparticles are potential adsorbent for arsenic and chromium removal in drinking water and are therefore suitable for treating arsenic and chromium contaminated water. Among these processes, the application of mixed magnetite-maghemite-goethite iron oxides, iron compound loaded slag and nano scale mixed magnetite-maghemite in the remediation of contaminated water is a promising area of research. Adsorption by these reactive media is also an emerging process in site remediation. The surface properties of iron oxides are key factors in the adsorption of heavy metals. Electrostatic attraction and redox reactions among iron oxides, arsenic, chromium or cadmium species accelerate the removal of these metals from aqueous solution. The application of these reactive oxides in permeable reactive barriers (PRB) can lead to the removal of heavy metals (As and Cr) from groundwater. To improve understanding of As, Cr and Cd removal mechanisms and to extend the use of different iron oxides in subsurface remediation, extensive research was needed. Thus, the investigation of these mixed iron oxides for the removal of heavy metals from the subsurface was necessary to define their scope for the development of site remediation technologies. In this study, mixed magnetite-maghemite, or mixed magnetite-maghemite-goethite with other iron minerals were considered for the use in the design of permeable reactive barrier for groundwater remediation.

1.2 Objectives of the study

The broad objective of this research was to select the best reactive medium for subsurface remediation. The specific objectives of the study are : (i) to determine the mechanism of Cr(VI), As and Cd(II) adsorption on mixed magnetite-maghemite iron oxides particles; (ii) to analyze the kinetics of cadmium(II) uptake by mixed maghemite- magnetite nanoparticles; (iii) to investigate the performance of mixed maghemite-magnetite nanoparticles in Cr(VI) removal by examining adsorption kinetics, reaction mechanisms and associated thermodynamic parameters and finally, (iv) to investigate the application of fayalite-mixed iron oxide loaded Ni smelter slag for As(V) removal.

Sorption kinetics was studied to improve our understanding of controlling kinetics and the governing mechanisms (e.g., surface versus intraparticle diffusion) of sorption. This study investigated the effect of contact time, pH, solid/liquid ratio and temperature on the adsorption and distribution coefficient of heavy metal on mixed γ-Fe_2O_3-Fe_3O_4 surfaces. The study also included the investigation of the application of fayalite-mixed iron oxide loaded Ni smelter slag for subsurface remediation technology as well as the calculation of the rate constants, removal capacity and contaminant transport over time for As(V) removal in the fayalite-mixed iron oxides (magnetite-maghemite-goethite) loaded Ni smelter slag columns simulating PRB.

Surface analytical techniques were performed to assess bonding in iron oxides as well as in contaminant adsorbed iron oxide to evaluate sorption mechanisms. XRD, SEM and Raman spectroscopy were conducted to evaluate oxide species and secondary minerals on mixed iron oxides surfaces. The identification of the chemical states of the adsorbed Cr using XPS and Raman analyses during the removal of As and Cr(VI) from aqueous solution by mixed maghemite–magnetite nanoparticles was another objective of this study. Fe and Cr are both transition elements. Thus, multiple analysis of Cr or As loaded iron oxides in XPS data produced additional information in the field of geochemistry. Moreover, theoretical multiplet analysis or multiplet splitting of Fe 2P XPS spectra of fresh mixed iron oxide and contaminant adsorbed mixed iron oxides as well as bonding in contaminant adsorbed iron oxides were also investigated to evaluate sorption mechanisms. Mineralogy of pure and adsorbed Ni smelter slag as well as reactive slag effectiveness for arsenic removal was also determined in this study.

1.3 Contribution of the thesis

The work described in this study involved batch and column laboratory experiments as well as theoretical analysis using different models. Mixed magnetite-maghemite (Fe_3O_4-γ-Fe_2O_3) nanoparticles are potential adsorbents for arsenic, chromium and cadmium removal in water and are therefore suitable for treating heavy metal contaminated water. The study investigated the adsorption mechanism of arsenic, chromium and cadmium ions on mixed magnetite-maghemite nano or different scale particles. This is one of the very few studies that have, to date, examined arsenic, chromium or cadmium removal

from aqueous solution by mixed magnetite-maghemite nanoparticles. Although magnetite and maghemite can separately remove greater amounts of these metals from aqueous solution than the mixture (Shipley et al. 2009; and Lim et al. 2009), it is probably more realistic and practical to investigate the removal efficiency of the mixture because of the common association of the two minerals in nature. In addition, most commercial grade 'magnetite or maghemite' nanoparticles used in field scale remediation of heavy metal contamination would likely be a mixture of magnetite and maghemite or hematite because of slight oxidation during storage or shipping. Electrostatic attraction and oxidation-reduction between heavy metal and mixed magnetite-maghemite-goethite are the postulated mechanisms for removal from aqueous solutions. Specific adsorption (chemisorption) and nonspecific adsorption (electrostatic attraction) were investigated to determine the application of crystalline iron oxides for As, Cr and Cd anion ligand from aqueous phase. The key contributions of this research are as follows:

a) This thesis suggests that arsenic adsorption involved the formation of weak arsenic-iron oxide complexes at the magnetite-maghemite surface. The relative content of the Fe(II) decreased for As(V) and As(III) loaded magnetite-maghemite sorbent indicating oxidation on mixed surface as well as increase in maghemite from 30.1% to 47.2%. Again, smaller amounts (41.5% to 32.2%) of Fe(III) decreases on As(V) loaded magnetite-maghemite sorbent in magnetite spectra indicating a decrease in magnetite content on mixed magnetite-maghemite sorbent.

b) Although many previous researchers have looked at Cr(VI) removal by adsorption, very few studies have focused on the removal by mixed maghemite-magnetite. This thesis, however, did not delineate the mechanisms occurring in the surface and bulk adsorbent. In the present study, the nature and stability of the adsorbate-adsorbent interaction at the surface scale were determined. The outcomes of this study would benefit the water and wastewater industry in three aspects: (i) control and mitigation of Cr(VI) by adsorption processes; (ii) treatment of Cr(VI) contaminated wastewater; and (iii) remediation of Cr(VI) contaminated groundwater. The identification of the chemical states of the adsorbed Cr using XPS and Raman spectroscopy analyses during Cr(VI) removal by mixed maghemite–magnetite nanoparticles was also a major contribution of the study. The Raman and XPS data confirm that electrostatic attraction and oxidation–reduction reactions are the main mechanisms for the removal of Cr(VI) from aqueous solutions. Fe and Cr are both transition elements. Thus, it is clear that multiplet analysis of Cr(VI) loaded mixed iron oxides in XPS data has produced additional geochemical information and identified the sorption mechanisms. From the Raman study, it may be inferred that, in addition to adsorption reactions, diffusion reactions were also important during the removal of Cr(VI) by mixed iron oxides.

c) This thesis identified the adsorption kinetics and distribution or diffusion models of Cd(II) removal by mixed iron oxide nanoparticles (γ-Fe_2O_3-Fe_3O_4). Results from this study can be used to evaluate the utility of mixed maghemite-magnetite nanoparticles for heavy Cd removal at the field scale. In this study, theoretical multiplet analysis of the Cd adsorbed γ-Fe_2O_3-Fe_3O_4 was also a novel contribution to the literature on XPS studies.

However, no published study has, to date, investigated the effect of contact time, pH, solid/liquid ratio and temperature on the removal and distribution coefficient of Cd on mixed γ-Fe_2O_3-Fe_3O_4 surfaces.

d) Investigation was also be carried out to evaluate the applicability of mixed iron oxide particles for the construction of permeable reactive barriers. To date, not a single reactive barrier containing mixed FeO has been installed to remediate Cr/As from sub-surface. The principal aims of the work were to experimentally investigate the adsorption capacity and rate of heavy metals onto the mixed iron oxides loaded Ni-smelter slag sorbent in column systems. The study also reveals the extent to which existing mathematical models for contaminant transport can determine the experimental data and thereby serve as an aid in understanding experimental phenomena and to assess the potential utilization of fayalite-mixed iron oxide loaded Ni smelter slags as permeable reactive subsurface barrier media in remediation of heavy metal contamination in groundwater. This study can also help to develop a new reactive medium for barriers that is used to reduce the severe contamination of soil and groundwater.

1.4 Organization of the thesis

This thesis consists of seven chapters and one appendix. Chapter 1 contains background, objectives and contribution of the thesis.

Chapter 2 discusses the literature review including the surface chemistry of iron oxides, the adsorption process of different iron oxides, heavy metals (e.g. As, Cr and Cd) in subsurface and iron oxides containing permeable reactive barriers (PRBs) etc. The characteristics of iron oxide particles in aqueous solution and background study of heavy metal adsorption on different iron-oxides are also discussed in this chapter.

Chapter 3 deals with As(III) and As(V) ions removal from aqueous solutions by adsorption on magnetite-maghemite nanoparticles. This chapter discusses different isotherms' models and determines As(III) and As(V) ions maximum adsorption capacity (mg/g) and Gibbs free energy (ΔG^0, kJ/mol) by using Langmuir's model. The results of the X-ray photoelectron spectroscopy (XPS) studies for the determination of surface composition after adsorption are also included in this chapter. Finally, it concludes that arsenic species is removed by magnetite-maghemite nanoparticles through the formation of weak complexes on the surface of the magnetite.

Chapter 4 discusses chemical states in XPS and Raman analysis during removal of Cr(VI) from contaminated water by mixed maghemite–magnetite nanoparticles. This chapter deals with instrumentation for XPS and Raman spectroscopy, temperature, the retention time, adsorption isotherms as well as thermodynamic parameters and the adsorption rate constant (k_{ad}) of mixed maghemite-magnetite nanoparticles. This chapter also interprets theoretical multiplet analysis of the fresh and Cr adsorbed γ-Fe_2O_3-Fe_3O_4 mixture particles.

Chapter 5 deals with the effect of contact time, pH, solid/liquid ratio and temperature on the adsorption and distribution coefficient of Cd on mixed γ-Fe_2O_3-Fe_3O_4 surfaces. Adsorption kinetics study and the intraparticle diffusion model are also discussed in this chapter. Moreover, multiple linear regression modelling for the Cd adsorption data, an investigation of the elemental composition and chemical oxidation states of surface as well as near-surface species using X-ray Photoelectron Spectroscopy (XPS) are interpreted in this chapter.

Chapter 6 contains a feasibility study regarding the application of fayalite-mixed iron oxide loaded Ni smelter slag as reactive medium in PRB. This chapter discusses kinetics, transport and implications of slag for subsurface remediation. The mineralogical investigation of fresh and As reacted slag as well as arsenic migration through columns is also included in this chapter.

Chapter 7 provides conclusions and recommendation for future studies and engineering application of the magnetite-maghemite-goethite particles in arsenic, chromium and cadmium ions removal.

The appendix contains different thermodynamic parameter calculations; column parameters at different pH as well as controlled thermodynamic condition; and the table of results obtained from surface analysis.

1.5 References

Bartlett, R.J., and Kimble, J.M., 1976. Behavior of Chromium in Soils: II. Hexavalent Forms. J Environ Qual. 5,383-386.

Borgono, J.M., and Greiber, R., 1971. Epidemiological study of arsenicism in the city of Antofagasta. In: Trace substances in environmental health. V. D.D. Hemphill (ed.). University of Missouri, Columbia, MO. 13.

Blowes, D.W., Ptacek, C.J., Benner, S.G., McRae, C.W.T., Bennett, T.A., Puls, R.W., 2000. Treatment of inorganic contaminants using permeable reactive barriers. Journal of Contaminant Hydrology 45, 123–137.

Cebrian, M.E., Albores, A., Aguilar, M., and Blakely, E., 1983. Chronic arsenic poisoning in the north of Mexico. Hum. Toxicol. 2, 121.

Chen, C.J., Chuang, Y.C., Lin, T.M., and Wu, H.Y., 1985. Malignant neoplasms among residents of a blackfoot disease-endemic area in Taiwan: high-arsenic artesian well water and cancers. Cancer Res. 45, 5895.

Driehaus, W., and Jekel, M., 1998. Granular ferric hydroxide — a new adsorbent for the removal of arsenic from natural water. J. Water SRT Aqua. 47, 1-6.

Fendorf, S., Eick, M.J., and Grossl, P., 1997. Arsenate and chromate retention mechanisms on goethite. 1. Surface structure. Environ. Sci. Technol. 31, 315.

Guha, S., and Chaudhuri, M., 1990. Removal of As(III) from groundwater by low cost materials. Asian Environ. 12, 42.

Hindmarsh et al., 1977. Electromyographic abnormalities in chronic environmental arsenicalism. Journal of Analytical Toxicology, 1:270–276.

Hu et al., 2004. Removal of Cr(VI) by magnetite nanoparticle. Water science and Technology 50 (12), 139-146.

Lim, S.F., Zheng Y.M., and Chen, J.P., 2009. Organic Arsenic Adsorption onto a Magnetite Sorbent. Langmuir 25(9), 4973-4978.

Kanel, S.R., Choi, H., Kim, J.Y., Vigneswaran, S., Shim, W.G., 2006. Removal of Arsenic(III) from Groundwater using low-Cost Industrial By-products—Blast Furnace Slag. Water Qual. Res. J. Canada 41, (2), 130–139.

Kocar, B.D., and Fendorf, S., 2012. Arsenic Release and Transport in Sediments of the Mekong Delta. Interdisciplinary Studies on Environmental Chemistry—Environmental Pollution and Ecotoxicology, TERRAPUB. pp. 117–124.

Mandal, B.K., Chowdhury, T.R., Samanta, G., Mukherjee, D.P., Chanda, C.R., Saha, K.C., and Chakraborti, D., 1998. Impact of safe water for drinking and cooking on five arsenic-affected families for 2 years in West Bengal, India. Sci. Total Environ. 218, 185–201.

Mayo et al., 2007. The effect of nanocrystalline magnetite size on arsenic removal. Science and Technology of Advanced Materials 8, 71–75.

Mohan, D., and Pittman, C.U., 2007. Arsenic removal from water/wastewater using adsorbents—A critical review. Journal of hazardous materials, doi:10.1016.

Palmer, C.D., and Wittbrodt, P.R., 1991. Processes Affecting the Remediation of Chromium-Contaminated Sites. Environmental Health Perspectives 92, 25-40.

Petrusevski, B., Boere, J., Shahidullah, S.M., Sharma, S.K., and Schippers, J.C., 2002. Adsorbent-based point-of-use system for arsenic removal in rural areas. J Wat. SRT-Aqua. 51, 135-144.

Prasad G., 1994. Removal of As (V) from aqueous systems by adsorption onto some geological materials. InNriague JO (ed.), Arsenic in the environment, Part I. John Wiley and Sons, Inc.

Sanchez, A.G., Alastuey, A., Querol, X., 1999. Heavy metal adsorption by different minerals: application to the remediation of polluted soils. The Science of the Total Environment 242, 179-188.

Sharma, Y.C., 2008. Thermodynamics of removal of cadmium by adsorption on an indigenous clay, Chem. Eng. J. 145, 64–68.

Shipley, H.J., Yean, S., Kan, A.T., and Tomson, M.B., 2009. Adsorption of arsenic to magnetite nanoparticles: effect of Particle concentration, pH, ionic strength, and temperature. Environmental Toxicology and Chemistry 28(3), 509–515.

Smith, A.H., Lingas, E.O., and Rahman, M., 2000. Contamination of drinking-water by arsenic in Bangladesh: a public health emergency. Bull. WHO 78, 1093–1103.

Tuutijärvi,T., Sillanpääa, J.L.M., Chenb, G., 2009. As(V) adsorption on maghemite nanoparticles. Journal of Hazardous Materials 166 , 1415–1420.

U.S.EPA., 2001. National Primary Drinking Water Regulations: Arsenic and clarifications to compliance and new source contaminants monitoring — Final Rule. 40 CFR Parts 9, 141, and 142. U.S. Environmental Protection Agency, Washington, DC, January 22.

CHAPTER 2

LITERATURE REVIEW

2.1 Iron oxides

Aerobic weathering of surface magmatic rocks in both water and soil environment generates the formation of Fe(III) and Fe(II) oxides. Iron is in the trivalent state in the most common compounds. Most iron oxides have low solubility in aqueous solution and a high energy of crystallization (Cornell et al. 2003). They make only minute crystals in the environment. Thus, iron oxides have high specific surface areas.

Hematite (α-Fe_2O_3) is found more in aerobic soils of subtropical, mediterranean and humid to sub-humid tropical. It's color is red if finely divided and black or grey if coarsely crystalline. The magnetic behaviour of hematite depends on crystallinity/ particle size and the extent of cation substitution. Hematite is less soluble than magnetite or maghemite. Acidity constants (pKa_1 and pKa_2) of hematite are 8.86 and 10.1 (Cornell et al. 2003).

Magnetite (Fe_3O_4) is a black color. It is a ferromagnetic mineral containing both Fe(II) and Fe(III). It is responsible for the magnetic properties of rocks. This mineral contains two different cation sites in the structure such as (a) tetrahedral occupied by Fe(III) and (b) octahedral occupied by Fe(III) and Fe(II) that form the basis for two interpenetrating magnetic sub-lattices. According to Cornell et al. (2003), the surface hydroxyl groups, arising from adsorption of water or from structural OH, are the functional groups of iron

oxides. Charge on the iron oxide surface is established by the dissociation (ionization) of the surface hydroxyl groups. According to Cornell et al. (2003), the acidity constant of magnetite, pK_{a1} is 5.6. Thus, at pH values smaller than 5.6, dominant functional groups of iron oxide surface would be Fe^{2+} or $FeOH^{+}$. Thus, iron oxide would attract negatively charged heavy metal species at low pH.

Maghemite (γ-Fe_2O_3) is a red-brown and ferromagnetic mineral. It is iso-structural with magnetite, but with cation deficient sites. It exists in soil as a weathering product of magnetite and as the product of heating other Fe oxides in the presence of organic matter. It is widespread in soils of tropical and subtropical regions. It contains a structure similar to that of magnetite but differs from magnetite in that all or most Fe is in the trivalent state. According to Tuutijarvi et al. (2009), maghemite has a point of zero charge at pH_{pzc} 7.5 and the more acidic the condition the more positive was the surface charge of the maghemite surface. Thus, maghemite can adsorb negative species at acidic pH. Hydrothermal magnetite deposits are found at many locations around the Pacific basin, Chile, Peru, Central America, Australia, Sweden and Japan (Guilbert and Park, 1986) and Brazil (Faria et al. 1997 and Dana, 1997). Under anoxic conditions, magnetite (Fe_3O_4) is topotactically oxidized by protons in water to create maghemite (γ-Fe_2O_3):

$$Fe_3O_4 + 2\,H^{+} \longrightarrow \gamma\text{-}Fe_2O_3 + Fe^{2+} + H_2O \quad \ldots\ldots\ldots\ldots\ldots\ldots\ldots\ldots \quad (2.1)$$

According to Faria et al. (1997), this reaction is strongly affected by solution pH and although rapid at low pH, is likely to be negligible for pH greater than 7. In nature, most iron oxides are found in mixed forms.

Cornell et al. (2003) reported that Goethite (α-FeOOH), one of the most thermodynamically stable iron oxides, is a common mineral form under oxidizing conditions as a weathering product of iron bearing minerals. It can adsorb heavy metal species from aqueous solutions (Sanchez et al. 1999). It exists in the soil as the most common Fe-O mineral because of its high thermodynamic stability.

2.2 Surface Chemistry of Iron Oxides

The surface charge of different iron oxides is dependent on the medium's pH. Moreover, natural particles hold surface charge from structural substitutions and disorder (referred to as intrinsic surface charge) and reactions with ionic species in aqueous solutions (referred to as adsorption reactions). Cornell et al. (2003) described that these adsorption reactions follow two procedures such as adsorption reactions with proton or hydroxyls (e.g. from water molecules dissociation) and adsorption with other ions or ligands in solution. The central ions of different iron oxides perform as Lewis acids and share their structural OH against other ligands. Under dry condition, surface Fe atoms can be unsaturated and surface Fe atoms act as Lewis acids because they carry unoccupied atomic orbitals. Moreover, they undergo reaction with Lewis bases (electron pair donor) in aqueous system. During adsorption, the water molecules dissociate and result in a

surface covered with OH^- groups coordinated to the underlying Fe-atoms. These hydroxyl functional groups are chemically reactive entities at the surface of the iron oxide solid particles in aqueous environment. They contain a double pair of electrons together with a dissociable hydrogen atom which allow them to react with acid and base. According to Cornell et al. (2003), the Fe-O surface charge depends on the dissociation of the surface hydroxyl groups. They further reported that adsorption or desorption depends on solution pH represented by the following dissociation reactions:

$$\equiv FeOH_2^+ \leftrightarrow \equiv FeOH + H^+ \quad \text{..... (2.2)}$$

$$\equiv FeOH \leftrightarrow \equiv FeO^- + H^+ \quad \text{..... (2.2a)}$$

The charge on the solid particles that exists as a result of the ionization of the surface hydroxyl group is balanced by a layer of counter ions of opposite charge located in the aqueous solution. The surface charge together with the layer of counter ions in the solution phase is defined as the electrical double layer (EDL). The separation of charges in the EDL generates the development of a difference in potential between the surface and the solution. This depends on solution pH and temperature. Positively or negatively charged surface can be generated because of adsorption or desorption reactions happening on the iron oxide surface. Most iron oxides have a point of zero charge (pzc) in the pH range 6-10 (Sposito, 1984). Thus, positive, negative and neutral functional groups can coexist on the surface of Fe-O.

2.3 The adsorption process of different iron oxides

The adsorption process of different iron oxides involves interaction of the contaminant with the adsorbent i.e. Fe-O with surface OH^- groups. Cornell et al. (2003) explained that the metal ion (Fe) acts as a Lewis acid and reacts with OH^- groups for other ligands (anions) to form a surface complex. Anion metal species usually adsorb on FeO either specifically or non-specifically. Specific adsorption is also called chemisorption, inner sphere adsorption or ligand exchange by replacing the surface hydroxyl groups by the adsorbing ligand. Adsorption of anions on the minerals generally takes place by three mechanisms (Stumm, 1992 and Sposito, 1984) such as inners sphere complex formation, outer sphere surface complex and adsorption in the diffuse-ion swarm.

During inner sphere complex formation, the anion is bound directly to the particle surface resulting in a decrease or increase in surface charge. There is no water molecule interposed between the functional group and the binding ions or molecules. Specific adsorbing or inner sphere complex ions modify the surface charge on iron oxides and are usually tightly bound (Cornell et al. 2003).

If at least one water molecule is interposed between the functional group and the ion, non-specific or outer sphere complex formation occurs. This is due to electrostatic forces and depends on the ionic strength of the system. Cornell et al. (2003) reported that the adsorbing species retains its primary hydration shell. When the adsorption system is governed by electrostatic attraction, the surface must contain an overall positive charge in

order for anion adsorption on the surface. In contrast, an overall positive charge is not required in the case of iron oxide particles in the specific adsorption system. Thus, it explains that adsorption may occur at any pH in specific or inner sphere adsorption system and may take place on a neutral surface or even with same surface charge species (Cornell et al. 2003). Moreover, the diffuse-ion swarm involves almost exclusively electrostatic bonding and is affected only by surface charge and valence. The corresponding adsorption products are less stable than specific adsorption (Cornell et al. 2003). Strength of adsorption could be as follows: Inner-sphere > Outer-sphere > Diffuse ion swarm.

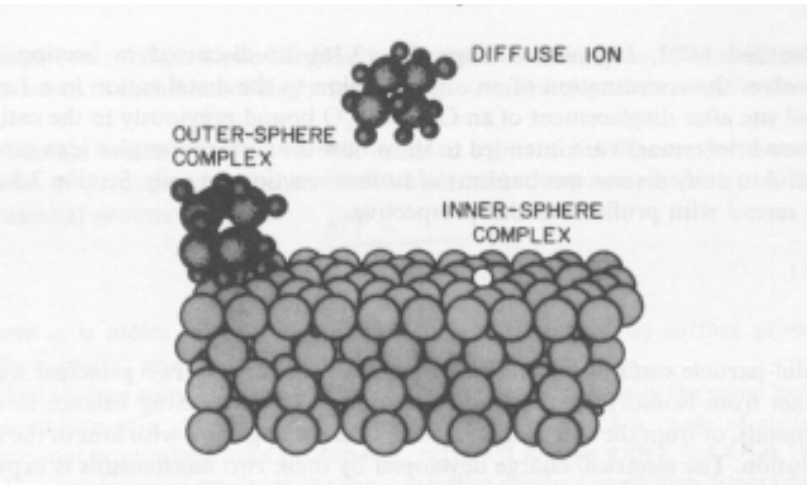

Figure 2.1: Surface complex formation on adsorbent (Sposito, 1984).

The Langmuir and Freundlich isotherms were used to interpret the nature of adsorption of arsenic or chromium on magnetite, hematite or mixed magnetite and maghemite nanoparticles (Hu et al. 2004; Yean et al. 2005; Hu et al. 2005 and Mayo et al. 2007). The

experimental data obtained at fixed pH were applied to the linearized forms of Langmuir and Freundlich isotherms which showed the suitability for measuring adsorption. Adsorption of simple inorganic anion on iron oxides was investigated (Cornell et al. 2003). The electrostatic attraction as well as redox reactions between different iron oxide and contaminant species would be the principle mechanism in the adsorption system. Yean et al. (2005) reported from potentiometric titrations that in the pH range 4 to 6.8, the surface of magnetite particles contained a positive surface charge, and a point of zero charge was found at pH 6.8. Tuutijarvi et al. (2009) found a point of zero charge of maghemite at pH_{pzc} 7.5. They further reported that the more acidic the condition the more positive was the surface charge of the adsorbent and, accordingly, the more attractive to As(V) species, namely $H_2AsO_4^-$ or $HAsO_4^{2-}$. According to Singh et al. (1996), the adsorption of arsenate would be favoured electrostatically up to the pH_{zpc} (7) of the hematite but the solute from the solid phase to the bulk phase beyond this point, specific adsorption (chemisorption) plays an important role.

Reaction at the iron oxide/solution interface influences crystallization and dissolution of these compounds, their stability as well as their interactions with adsorbing species. Crystallographic considerations specify that the surface hydroxyl groups (-OH) might be coordinated to one, two or three underlying iron atoms and the overall density of these groups depends on both the crystal structure and the extent of development of the different crystal faces (Cornell et al. 2003). They further reported that anions are ligands i.e. they possess one or more atoms with a lone pair of electrons. Ligands are specifically or non-specifically adsorbing. The number of functional groups on crystallized iron

oxides (determined by the maximum uptake of adsorbed species) depend on the size of the adsorbed molecule or ion, the density and arrangement of the functional groups, the pH of the system, and the time of the reaction. Cornell et al. (2003) demonstrated that anions that adsorb on iron oxides include phosphate, silicate, selenite, arsenate, chloride, fluoride, chromate and oxalate. The effect of rising pH on anion adsorption is the result of two opposing effects. Those are as follows: 1) the increase in the relative concentration of the anionic forms of the conjugate acid as the pK_a is approached, which promotes adsorption on the oppositely charged surface and 2) the decrease with rising pH in the number of surface $FeOH_2^+$ groups.

2.4 Heavy metals in subsurface

Sanchez et al. (1999) reported that high concentrations of heavy metals in the environment may create long-term health risks to ecosystems and humans. Heavy metal solubility is strongly dependent on soil pH. In calcareous and clay soils, heavy metal solubility is low, whereas in acidic soils a significant amount of the metal may dissolve and become available for uptake by plants. In addition, the acidification of soils as a consequence of the oxidation of pyrite slurry can cause the remobilization of heavy metals. This represents a major threat to surface and ground waters. The geochemical forms of heavy metals in soils affect their solubility, which directly influence their mobility, the risk of ground water pollution, and bioavailability. Soluble forms strongly depend on the relative contribution of solid soil components such as silicates, carbonates, oxides and organic matter etc. The type and degree of adsorption capacity of these soil

fractions are very different and complex in the case of metal retention (Sanchez et al. 1999). Kanel et al. (2006) and Sanchez et al. (1999) reported that most of heavy metal ions are non-degradable and persistent in the subsurface. They are toxic to living organisms. Therefore, the removal of heavy metal ions from water environment is very essential to protect public health. Mohan et al. (2007) reported that exposure to heavy metals, even at trace level, is considered to be a risk for human beings. As a result of industrial activities, a large amount of metals-contaminated water has been released to the environment and causes severe contamination. The symptoms and infections from these toxic metals have started to be a very important issue, making it crucial for researchers to create innovative as well as economical approaches to treat water from surface and groundwater environment.

2.4.1 Arsenic Release and Transport in subsurface

The two most important factors controlling the speciation and solubility of Arsenic are pH and redox potential. Under oxidizing conditions at pH less than 6.9, $H_2AsO_4^-$ is the dominant species, whereas $HAsO_4^{-2}$ predominates at higher pH. Under reducing conditions at a pH value less than 9.2, the uncharged arsenite species H_3AsO_3 is dominant. In contrast to the pH dependency of As(V), As(III) was found virtually independent of pH in the absence of other specifically adsorbed anions (Vu et al. 2003). Most often, more trivalent arsenic than pentavalent arsenic is found in reducing groundwater conditions, whereas the converse is true in oxidizing groundwater

conditions. The stabilities of arsenic species under different pH and redox conditions are shown in Table 2.1.

Table 2.1: The stabilities of arsenic species under different pH and redox conditions (Vu et al. 2003)

Oxidizing condition		Reducing condition	
pH	As(V)	pH	As(III)
0-2	H_3AsO_4	0-9	H_3AsO_3
3-6	$H_2AsO_4^-$	10-12	$H_2AsO_3^-$
7-11	$HAsO_4^{2-}$	13	$HAsO_3^{2-}$
12-14	AsO_4^{3-}	14	AsO_3^{3-}

Kanel et al. (2006) noted that arsenic, a common toxic element, exists in both inorganic and organic forms in water and subsurface. Iron arsenate ($FeAsO_4$) is one of the most common minerals found in subsurface. It can be defined as the direct and immediate source of arsenic because of its availabilities in the compound such as scorolite ($FeAs_4$. $2H_2O$) and hydrated mixture of arsenate and sulphate also called pitticite (BGS and DPHE, 2001). These are common alteration products of arsenopyrite (Singh, 2004). According to Chowdhury et al. (1999), arsenopyrite (FeAsS) is another widespread arsenic bearing mineral from natural sources. Moreover, many sulfide minerals, especially pyrite (FeS_2), also hold high quantities of arsenic and subsequently leach into aquifer as a result of arsenopyrite oxidation and acidification of the resulting leachate (Nickson et al. 1998; Nickson et al. 2000). They further reported that beside arsenic

bearing minerals, arsenic is often found in sediment in association with manganese and iron oxyhydroxides. The release of arsenic from those minerals is due to the reductive dissolution of these oxyhydroxides, which could eventually change the aquifers conditions.

Arsenic in the subsurface can also be generated from the leaching of geological materials, input from geothermal sources, mining wastes and landfills either anthropogenically or naturally (Harvey et al. 2006). The anthropogenic sources include agro-chemicals, electric poles painted with arsenic preservatives, mining activities, industrial wastes and fossil fuel burning (Karim, 2000). Bhattacharyya et al. (1997) reported that uncontrolled anthropogenic activities such as smelting of metal ores, use of arsenical pesticides and plant/wood preservative agents can release arsenic to groundwater. They further reported that natural sources of arsenic can be found in 250 naturally occurring minerals. These include minerals (particularly sulfides), oxides (particularly metal oxides), and volcanic-derived sediments. They can affect large areas, such as extensive aquifers. Mineral extraction and processing, glass manufacturing, wood preserving pesticide production and application, waste pile leaching and coal/oil production and processing are the most common anthropogenic sources (Bhattacharyya et al. 1997).

Arsenic mobility can be controlled in subsurface as well as aquifers by two ways: (1) adsorption and desorption reactions and (2) solid-phase precipitation and dissolution reactions (U.S. Geological Survey, 1999 and Harvey et al. 2006)). The original source of arsenic was most likely oxidation of sulfide minerals, principally pyrite. Harvey et al.

(2006) further reported that in the Ganges delta, pyrite oxidation occurred during weathering at the source in the Himalayas and that arsenic was transported and deposited in association with the resulting iron oxides. They further reported that As is found predominantly in the inorganic form in oxidation states of +5 or +3. In oxidizing conditions, the oxyanion arsenate [As(V)] is the predominate species (Vu et al. 2003). The reactive interaction of As(V) with the subsurface media significantly affects the movement of As in soil and ground water (Harvey et al. 2006). The equilibrium adsorption of As(V) to pure solid phases and soils has been studied extensively as documented in recent reviews. These studies have illustrated that Fe oxy-hydroxides strongly interact with dissolved As(V). The degree of As(V) adsorption on Fe oxy-hydroxides is extremely pH-dependent.

Arsenic found on iron oxide surfacse is an example of an adsorption reaction. Desorption is defined as separation of arsenic from any adsorbent surface in the reverse reaction. The formation of a solid phase from components present in aqueous solution is referred to as solid-phase precipitation. Dissolution of volcanic glass within an aquifer is an example of solid-phase dissolution. Arsenic adsorption and desorption reactions depend on the changes in pH, occurrence of redox (reduction/oxidation) reactions, presence of competing anions, and solid-phase structural changes at the atomic level. Moreover, solid-phase precipitation and dissolution reactions are subject to the influence of solution chemistry, including pH, redox state and chemical composition of organic and inorganic compounds.

Arsenopyrite (FeAsS) and arsenic-rich iron oxyhydroxides are the two possible sources responsible for arsenic contamination in the subsurface (Chowhdury et al 1999). Since arsenopyrite can hold As(III) ions in small proportion with ions of As(V) which is the dominant constituent, it is quite likely that arsenic in the alluvium occurs as ferric arsenate ($FeAsO_4$), with ferric arsenite ($FeAsO_3$) in minor proportion (Nickson et al. 2000; BGS and DPHE, 2001). They further reported that the presence of an oxidizing agent, most commonly atmospheric oxygen (as O_2), controls the oxidation rates of sulfide minerals. The availabilities of oxygen in deep aquifers are dependent on the amount of oxygen present in recharge water because deep aquifers are separated from the atmosphere. Increased pumping of groundwater can significantly control the oxidation of sulfide mineral and arsenic release into aquifers. Thus, increased pumping and reduced recharge can accelerate the oxidation rates of arsenic bearing sulfide mineral by lowering the water table and exposing mineral to atmosphere (BGS and DPHE, 2001).

Nickson et al. (2000) demonstrated that the dissolution of ironoxyhydroxides in subsurface can take place due to the presence of reducing environment. Microbial activity in sediments as well as burial of organic matter in subsurface plays an important role in the generation of reducing conditions (BGS and DPHE, 2001). A number of factors can control the rates of arsenic release reactions under such conditions. Those include rates of sedimentation, diffusion of gases and microbial reactions, but they are likely to be relatively rapid on a geological timescale. The reducing conditions and release from iron oxyhydroxides in the subsurface are the main reasons for the presence of high arsenic concentrations in sedimentary aquifers (BGS and DPHE, 2001). According to Nickson et

al. (2000), lowering of pH can also accelerate the dissolution of iron oxyhydroxides and subsequent release of associated arsenic, as illustrated in Eq-2.3.

$$Fe(OH)_3.AsO_4 \longrightarrow Fe(OH)_2^{+} + H_2O + AsO_4^{3-} \quad \ldots\ldots\ldots (2.3)$$

The release of arsenic from arseniferous Fe-oxyhydroxides in reducing groundwater is the most common process in sediments where rapid consumption of O_2 by microbial metabolism of organic matter generates a strongly reducing environment (Badruzzaman et al 1998; Nickson et al. 1998; Nickson et al. 2000).

2.4.2 Chromium in subsurface

According to Pratt et al. (1997) described that Chromium is an essential industrial metal used in diverse products and processes. They further noted that much of the groundwater withdrawn in North America and elsewhere is supplied by shallow aquifers, which are susceptible to contamination from industrial, agricultural and domestic activities. Chromium has been releasing in to the environment via leakage, poor storage, or improper disposal practices at many locations (Palmer and Wittbrodt, 1991; Calder, 1988). Cr(VI) and Cr(III) are the two common oxidation states exposed to the environment. Cr(VI) is relatively mobile in the subsurface as well as extremely toxic, mutagenic, teratogenic (Abbasi and Soni, 1984), and carcinogenic (Yassi and Nieboer, 1988). Cr(III) is immobile under moderately alkaline to slightly acidic conditions, and has relatively low toxicity. Blowes (2002) reported that the hexavalent state of Cr forms chromate (CrO_4^{2-}) or bichromate ($HCrO_4^{-}$).

There are several mineral phases containing Cr(VI) that exist at chromium contaminated sites. Palmer and Wittbrodt (1991) showed the common compound such as $PbCr0_4$ (crocoite), $PbCr0_4.H_20$ (iranite), and K_2CrO_4 (tarapacaite) in chromium sludge from a hardchrome plating facility. $CaCrO_4$ was formed at a seepage face in a drainage ditch where there was high evaporation. Most of the Cr contaminated groundwater was at equilibrium with $BaCrO_4$, (hashemite) and makes a complete solid solution with $BaSO_4$ (Rai et al. 1988). Palmer et al. (1994) reported that this solid solution can be a major impediment to the remediation of chromium contaminated sites by pump and treat methods. Chromium contamination creates severe impacts on human health as well as the environment. The potential risk of chromium entering the groundwater flow system and being transported beyond compliance boundaries should be evaluated to protect the groundwater contamination by heavy metal. Chromium is found in the subsurface either in solution or in association with the solid phase or rock. Natural reductants have been identified by researchers that can transform the more toxic hexavalent form of chromium to the less toxic trivalent form. Palmer et al. (1994) noted that this Cr(III) precipitates as a fairly insoluble hydroxide under alkaline to slightly acidic conditions, thereby immobilizing it within the soil. They further reported that Cr (Vl) is a strong oxidant and is reduced in the presence of electron donors. Toxic Cr (Vl) can be reduced to the less toxic Cr(III) in soils and precipitated as an insoluble hydroxide phase.

Electron donors commonly found in soils such as aqueous Fe(II), ferrous iron minerals, reduced sulfur and soil organic matter. The reduction of Cr(Vl) by ferrous iron can be illustrated as

$$HCrO_4^- + 31\% + 7H^+ \longrightarrow Cr^{3+} + 3Fe^{3+} + 4H_2O \ldots\ldots\ldots\ldots\ldots \quad (2.4)$$

Palmer et al. (1994) described that this reaction is very fast on the time scales of interest for most environmental problems with the reaction going to completion in less than 5 minutes, even in the presence of dissolved oxygen. In the subsurface, Cr(Vl) can also be reduced by microbes (Palmer et al. 1994)). Both aerobic and anaerobic reduction by microbes can occur, however, the latter is more common. Blowes (2002) reported chromate-containing minerals are very soluble. Because the chromate ion has a negative charge, chromate adsorption on aquifer minerals is limited. They explained that as a result, chromate can exist at concentrations well above water quality guidelines and may migrate with the flowing groundwater in aquifers. In contrast, the reduced state, Cr(III) produces insoluble precipitates under slightly acidic and neutral conditions, limiting Cr(III) to very low concentrations in most aquifers. Thus, the reduction of Cr(VI) to Cr(III) limits both the concentration and mobility of dissolved chromium. This difference is very important because Cr(VI) is very lethal and carcinogenic whereas Cr(III) is a nutrient at trace levels. Moreover, Cr(VI) species are attenuated naturally because minerals containing reduced forms of iron and sulfur are abundant in many aquifers (Blowes, 2002). These minerals decrease hexavalent chromium to trivalent chromium and accelerate the precipitation of insoluble solids such as chromium hydroxide. Organic carbon-rich materials in the subsurface can also reduce hexavalent chromium. Palmer et al. (1994) reported that in aquifers where these reduced sediments are abundant and the concentrations of hexavalent chromium are low, the attenuation capacity of the aquifer can be sufficient to prevent chromium migration. According to Tzou et al. (2003), phosphate (P), organic ligands, and light sources, can control Cr(VI) retention by the soil components. The existence of phosphate (P) or organic ligands not only competes with

solution Cr(VI) for surface sites, but also results in releasing sorbed Cr(VI). Again, the presence of orthophosphate prevents the adsorption of Cr(VI), most likely by competition for adsorption sites.

2.4.3. Cadmium (Cd) in Environment

Cadmium is a toxic heavy metal of vital environmental as well as occupational concern. According to Moore et al. (1984), the stable state of Cadmium (Cd) in the natural environment is Cd^{+2}. It is silvery white and ductile with a faint blue tinge. Singh et al. (1998) demonstrated that Cd is most commonly found associated with zinc in carbonate and sulfide ores. Thus, humans were unknowingly contaminating the environment with Cd through their production of metals. It has been released to the subsurface through the combustion of fossil fuels, metal production, application of phosphate fertilizers, electroplating, and the manufacturing of batteries, pigments, and screens. This heavy metal has resulted in severe contamination of soil as well as water (Naidu et al. 1994 and Sharma, 2008 and Boparai et al. 2009). Sharma (2008) noted that discharge of untreated effluents from various industries into water resources has been one of the major sources of Cd pollution. Wang et al. (2010) showed that Cd has been included in the red list of priority pollutants by the Department of Environment, UK and in the black list of Dangerous Substance Directive in European Economic Community. The US Environment Protection Agency has also classified Cd as carcinogenic compound.

According to Waalkes (2000), cadmium is a toxic transition ('heavy') metal of continuing occupational and environmental concern with a wide variety of adverse effects. He further reported that cadmium has an extremely long biological half-life that essentially makes it a cumulative toxin and to date there are no proven effective treatments for chronic cadmium intoxication. According to Naidu et al. (1994), cadmium accumulates primarily in the liver and kidney where it is bound to metallothionein (MT), a low molecular weight metal binding protein thought to detoxify the metal through high affinity sequestration. They further reported that Cadmium (Cd) has been classified as a human carcinogen and tertogen affecting lungs, kidneys, liver and reproductive organs. Occupational exposure to cadmium is associated with lung cancers in humans, while other sites, potentially including the prostate, are not definitively established. The World Health Organization (WHO) guideline for Cd has set a maximum concentration of 0.003mg L^{-1} in drinking water. In the field of environmental pollution there are few subjects that, during recent years, have developed as rapidly as the study of toxic metals. According to Boparai et al. (2009), given pervasive cadmium contamination and the low drinking water guideline, there is considerable interest in the development of techniques to remove cadmium from contaminated water.

Naidu et al (1994) described that high concentrations of heavy metals in soils can constitute long-term health risks to ecosystems and humans. They further reported that heavy metal solubility is strongly dependent on soil acidity. In calcareous and clay soils, Cd(II) solubility is low, whereas in acidic soils a significant amount of the Cd(II) can dissolve and become available for uptake by plants. In addition, the acidification of soils

as a consequence of the oxidation of pyrite slurry can cause the mobilization of Cd(II) minerals. This represents a major threat to surface and groundwater. According to Naidu et al (1994), the persistence and mobility of Cd in soils are determined largely by the extent of adsorption by soil particles.

Sharma (2008) described that chemical precipitation is the most common conventional method for cadmium treatment but large amounts of sludge produced during the treatment poses disposal problems. They further noted that ion exchange, vacuum evaporation, solvent extraction, membrane technologies, etc. are well known methods employed for treatment of cadmium containing wastewaters. Adsorption shows comparatively a simpler treatment of large volumes of Cd containing effluents and wastewaters. But, the high cost of most adsorbent and their losses in regeneration limit their application at large scale in developing nations like India.

2.4.4 Contaminant migration theory

The movement or migration of contaminant through the column or soil bed is of interest in the prediction of contaminant impact from sources such as point or nonpoint sources. There are three main mechanisms for contaminant migration through subsurface. These are advection, diffusion, and dispersion. According to Rowe and Booker (1985), in many applications the movement of contaminants are primarily in one direction and can be predicted using one-dimensional dispersion-advection equation for a layered deposit or different layers of soil. The type of mass transfer by which dissolved substance is removed from the aqueous phase due to the interaction between the solid matrix material

of the porous medium and the substance is generally referred to as adsorption. Adsorption plays an important role in mass transport through subsurface. According to Freeze and Cherry (1979) and Rowe and Booker (1985), the 1-D mass conservation equation for the transport of a reactive solute through saturated, homogeneous, isotropic media with steady state flow is as follows:

$$\frac{\partial C}{\partial t} = \frac{D_e}{R}\frac{\partial^2 C}{\partial z^2} - \frac{v_s}{R}\frac{\partial C}{\partial z} \quad \ldots\ldots\ldots\ldots\ldots\ldots \quad (2.5)$$

Where C, De, R, Vs, and k_d represent concentration of contaminant, coefficient of hydrodynamic dispersion, retardation factor, Darcy velocity and distribution coefficient, respectively. The retardation factor, R (= $1+\rho_d/n*k_d$), measures the capacity of a particular adsorbent to adsorb solutes that yield in solute attenuation during contaminant movement. Dispersion is dependent on varations in the fluid velocity or Darcy velocity. Moreover, variations of hydraulic conductivity and porosity also play a important role. Hydrodynamic dispersion represents the combination of mechanical dispersion which is a physical mechanism and effective diffusion as a chemical mechanism (e.g. De= D+ Dm). The mechanical dispersion can be expressed as a function of seepage velocity. It can be determined by the following equation:

$$Dm = \alpha * \nu \quad \ldots\ldots\ldots\ldots\ldots\ldots\ldots\ldots\ldots\ldots \quad (2.5a)$$

Where, α= Dispersivity (m) and ν= Seepage or groundwater velocity (m/s). According to Fetter (1999), the greater the flow path length, the larger of the value of longitudinal dispersivities needed to fit the data to the advection-dispersion equation. When hydraulic conductivity of the media and velocity of feed solution are very low, mechanical dispersion can be ignored and the hydrodynamic dispersion (De) would be equal to the

effective molecular diffusion (D). Dispersion consists of longitudinal and tranverse dispersion. In three dimension, dispersion involves spreading in transverse and vertical directions. Dispersion occurs by differences in the fluid velocities within a pore.

A Peclet number ($Pe = v_x*L/D_L$) represents a dimensionless number that can relate the effectiveness of mass transport by advection to the effectiveness of mass transport by either dispersion or diffusion. L represents the flow length and D_L is the longitudinal dispersion. Fetter (1999) reported that Peclet number increases with flow path length as advective transport becomes more dominant over dispersive transport. He further reported that for mass transport near the inlet boundary, it is important to use the correct transport equation to measure the dispersion coefficient and other parameters. A quantitative measurement of the dispersion coefficient is a pre-requisite for the solution of hydrological problems dealing with the transport of contaminant.

Several software packages, such as POLLUTEv7, CXTFIT, EnviroScape, Migrate and Multimed for Windows, have been developed which simulate contaminant migration in a porous medium. The software used in the current study was Pollutev7 which has been utilized in As(V) migration through column simulating PRB. This program uses a one and a half dimensional solution to the advection-dispersion equation. Unlike finite element and finite difference formulations, POLLUTEv7 does not need a time-marching procedure, and thus involves relatively little computational effort while also avoiding the numerical problems of alternate approaches. POLLUTEv7 can model linear- non-linear sorption, radioactive and biological decay, transport through fractures, passive sinks, phase changes and time-varying properties.

2.5 Background study of heavy metal adsorption on different iron-oxides

Many published papers (Hu et al. 2004, Mohan et al. 2007, Shipley et al. 2009, and Tuutijarvi et al. 2009) have demonstrated that iron oxides have high affinity for the adsorption of arsenic and chromium compounds. Magnetite nanoparticles are potential sorbents for arsenic and chromium removal in drinking water and are therefore suitable for treating arsenic and chromium contaminated water (Hu et al. 2004, and Mayo et al. 2006,). Mohan et al. (2007) reported As(V) and As(III) removal by goethite, hematite, granular ferric hydroxide (GFH), iron oxide coated sand, Ferrihydrite, $FeCl_3$ treated tea fungal biomass and iron oxide coated cement (IOCC). Naturally occurring ores and minerals, namely kaolinite (Guha et al. 1990), feldspar (Prasad, 1994), magnetite (Shipley et al. 2009), hematite and maghemite (Tuutijarvi et al. 2009) have also been used for the adsorption of arsenic though not as extensively as other materials.

Singh et al. (1998) described that hematite (α-Fe_2O_3), one of the crystalline iron oxides can remove cadmium (Cd) and the maximum removal of saturation was found to be 98% at a temperature of 20^0C and pH 9.2 for an initial concentration of 44.88 µmol/L and hematite 40 g/L. Naidu et al. (1994) reported that fresh Goethite (α-FeOOH) can also remove Cd from aqueous solution and removal depends on solution pH. Cornell et al. (2003) and Petrova et al. (2011) showed that, magnetite (Fe_3O_4), commonly found in the environment, can form via several pathways, including biotic and abiotic reduction of ferric iron Fe^{3+} oxides and the oxidation of ferrous iron Fe^{2+} and iron metal (Fe^O), can also adsorb cadmium (Cd), cobalt, chromium and arsenic from aqueous solution. The

controlling mechanism is a function of the standard redox potential of the contaminant metal and solution pH condition. Singh et al. (1998) also observed that a monolayer coverage of adsorbate was involved in the adsorption process. Electrostatic attractions as well as surface complexation were the major removal mechanisms.

A number of researchers have observed that several adsorption processes follow the Langmuir isotherm. Examples include As(III) adsorption by hematite (Singh et al., 1988), As(III) and As(V) adsorption by activated carbon, activated bauxite, activated alumina (Gupta et al., 1978) and amorphous iron hydroxide (Harper et al., 1992), and As(V) adsorption by amorphous aluminum hydroxide (Anderson et al. 1976). Previous studies have presented maximum As(III) adsorption capacity for hematite, activated bauxite, activated alumina and iron(III) hydroxide loaded coral lime stone (Fe-coral) are 2.63, 16, 14 and 0.17 µmol /g, respectively (Gupta et al., 1978; Singh et al., 1988; Harper et al. 1992; and Maeda et al. 1992). For As(V) adsorption by activated bauxite, activated alumina, activated carbon and Fe-coral, the calculated maximum adsorption capacities are 52, 67, 10 and 0.2 µmol/g (Gupta et al. 1978 and Maeda et al. 1992).

Previous researches (Powell et al., 1995; Pratt et al., 1997; Blowes et al., 2000; and Astrup et al., 2000) have shown that the removal of Cr(VI) by Fe^0 is achieved by a coupled reduction–oxidation reaction followed by precipitation as $Cr(OH)_3$, Fe(III)–Cr(III) hydroxide and Fe(III)–Cr(III) oxyhydroxide. Recently, due to iron's reducing capacity and ability to alter its valence state into more favourable forms for sorption and reductive precipitation, commercially available iron has been also successfully used for

the remediation of acid mine drainage (AMD) contaminated by a large numbers of metals and trace elements such as As, Cd, Cr, Hg, Ni and Zn (Lindsay et al. 2008). According to Boparai et al. (2009), nano Zerovalent iron(nZVI) particles were used to investigate the removal of Cd^{2+} in the concentration range of 25–450 mgL^{-1} and the maximum adsorption capacity of nZVI for Cd^{2+} was found to be 769.2 mgg^{-1} at 297K. They further reported that the overall adsorption process was endothermic and spontaneous in nature.

Fendorf et al. (1997) found a monodentate complex, a bidentate-binuclear complex, and a bidentate-mononuclear complex among iron oxides and arsenic or chromium compound. According to Tuutijarvi et al. (2009) and Hu et al. (2005), maghemite (γ-Fe_2O_3) can also reduce arsenic and chromium concentration. According to Singh et at. (1993), hematite can remove Cr(VI) and the maximum removal (97%) was observed at 40^0C and pH 2.7 with initial concentrations of 19.23 μ-mol/L Cr(VI) and 40 g/L hematite. They reported that the uptake of Cr(VI) increases as pH decreases. The Langmuir and Freundlich isotherms were used to interpret the nature of adsorption of arsenic or chromium on magnetite, hematite or mixed magnetite, maghemite and hematite nanoparticles (Hu et al. 2004; Yean et al. 2005; Hu et al. 2005, Mayo et al. 2007, and Mohan et al. 2007). The experimental data obtained at fixed pH were applied to the linearized forms of Langmuir and Freundlich isotherms which showed the suitability for measuring adsorption. The Langmuir and Freundlich isotherms were used to interpret the nature of adsorption of arsenic, chromium or organic contaminants on magnetite, goethite and hematite particles (Mohan et al. 2007). According to Cornell et al. (2003), anions that adsorb on iron oxides include phosphate, silicate, selenite, arsenate, chloride, fluoride, chromate, citrate and

oxalate. Anion adsorption at any pH shows an increasing trend with rising concentration of the adsorbing species. Anion adsorption by iron oxides at high pH can be controlled by two opposing effects. Those are the increase in the relative concentration of the anionic forms of the conjugate acid and the decrease with rising pH in the number of surface $FeOH_2^+$ groups.

Arsenate sorption on both goethite and gibbsite decreased with increasing initial phosphate to arsenate molar ratios. Again, the presence of orthophosphate prevented the adsorption of Cr(VI), most likely by competition for adsorption sites. Moreover, blast furnace slag (BFS), a steel industrial by-product containing iron compound, was tested for the removal of As(III). As(III) is a highly toxic, mobile and predominant species in anoxic groundwater (Kanel et al. 2006). They further reported that batch adsorption experiments were performed to determine the feasibility of Blast furnace slag (BFS) as an adsorbent for removing As(III) from groundwater as As(III) concentration and the pH of water were varied. From their study, it was found that the maximum As(III) adsorption capacity by BFS having FeO and CaO as the main component was 1.40 mg As(III)/g of BFS at 1 mg/L As(III) initial concentration, at 25^0C.

2.6 Iron Oxide Surface Analysis by X-ray Photoelectron Spectroscopy (XPS), Raman, XRD and SEM

The nature of the mineral precipitation and factors affecting the extent of mineral precipitation can be examined by surface analytical techniques. In this study, several analytical techniques were used, including aqueous inorganic ion concentration profiles

and analyses of groundwater-treated mixed iron oxides by Scanning Electron Microscopy (SEM), X-ray photoelectron spectroscopy (XPS) and Raman Spectroscopy to identify and quantify precipitates that form at the adsorbent surface.

XPS spectral lines are identified after the ejection of electron from the shell (1s, 2s, 2p, etc.). The ejected photoelectron has electron Binding Energy (BE):

$$BE = E_K - h\nu - \Phi \qquad (2.5)$$

Where: BE= Electron Binding Energy; E_k= Electron Kinetic Energy; Φ_{spec}= Spectrometer Work Function. Each electron holds its binding energy. By knowing this binding energy one can tell what element it is coming from. An important advantage of XPS is its capability to obtain information on chemical states from the variations in binding energies, or chemical shifts, of the photoelectron lines.

Mutiplet splitting occur for more core level photopeaks when the atom holds unpaired valence electrons. The multiplet-splitting of p and higher sublevels is more complicated due to orbital-angular momentum coupling (Grosvenor et al. 2004). Hochella (1988) reporte that 2p sublevels of transition metals in high-spin or paramagnetic states exhibit considerable line broadening due to complex multiplet splitting phenomena and despite the complexity of these line shapes, spectra of this sort can still be utilized to assess the oxidation state of the iron in the near-surface of minerals. Significant changes were investigated after Cr(VI), As(III) and As(V) adsorption. Ferrous (Fe^{2+}), ferric (Fe^{3+}) compounds or As or Cr(VI) adsorbed Ferrous (Fe^{2+}), ferric (Fe^{3+}) compounds were investigated by XPS multiplet peaks to find out oxidation state and the composition. XPS spectra analysis is useful for fitting of the complex Fe $2p_{3/2}$ spectra for γ-Fe_2O_3, α-Fe_2O_3 as well as Fe_3O_4 where both Fe^{2+} and Fe^{3+} species are present. The multiplets analysis of

XPS data helped to determine the degree of ionic character of the Fe-ligand bond or contaminant absorbed the Fe-ligand bond.

Raman spectroscopy is dependant on a change in the polarization of a molecule to produce Raman scattering. When a beam of photons strikes a molecule, the photons are scattered elastically (Rayleigh scattering) and inelastically (Raman scattering) generating Stoke's and anti-Stokes lines. Raman spectra expressed in wave numbers which have units of inverse length. In order to convert between spectral wave-length and wave numbers of shift in the Raman spectrum, the following formula can be used:

Raman shift expressed in wave number, $\Delta\omega = (1/\lambda_o - 1/ \lambda_1)$ ……. (2.6)

Where, λ_o = excitation wavelength and λ_1= Raman spectrum wave number. Vibrational information is specific to the chemical bonds and symmetry of molecules. In the Raman analysis, samples are much larger in volume than XPS, on the order of 40 times. Units for Raman spectra can be expressed in wave numbers which have units of inverse length. Raman spectra are helpful to identify oxide species and secondary minerals on iron surfaces. In this study, hematite (α-Fe_2O_3), magnetite or maghemite were identified by a group of bands. In addition, Raman spectroscopic measurements were conducted to examine the changes in oxide films on the iron surface. Raman identifications in this study were based on available literature data.

Hitachi S4500 or Hitachi SU6600 Field Emission Scanning Electron Microscope (FESEM) were used to scan the surface of the particles. Surface porosity can also be checked by FESEM. The samples were mounted on carbon adhesive tape. Samples will gold-coated to minimize electron beam charging effects. The backscattered and secondary electrons for the surface analyses were used to identify the differences in

surface patterns between original particles and contaminant reacted particles. X-ray diffractometer (XRD) using Bruker D8 operated with Ni-filtered CuK_α radiation generated at 40 kV and 40 mA, and 0.5° beam slit, was used in the bulk samples. Diffraction patterns for selected samples were recorded by continuous scans from 10 to 81° 2θ, over 28 minutes. The As or Cr-loaded magnetite-maghemite-goethite particles after adsorption were characterized using XRD (X-ray diffraction). The results from XRD analysis investigated the identical peaks of the As or Cr adsorbed particles with standard Fe_3O_4- γ-Fe_2O_3 - α-FeOOH crystalline phases. Powder X-ray diffraction techniques were used to identify mineral precipitates by their crystal structures. Qualitative measurements for phase identification were measured using the ICDD (international Centre for Diffraction Data) database.

2.7 Iron oxides containing permeable reactive barriers (PRBs)

According to Vance (1997), permeable reactive barriers (PRBs) provide in situ treatment of groundwater released from source zones and can be installed as permanent, semi-permanent, or replaceable units across the flow path of a contaminant plume and act as a treatment wall. When the contaminated water passes through the reactive zone of the barrier, the contaminants are either immobilized or chemically transformed to a more desirable (e.g., less toxic, more readily biodegradable, etc.) state (U.S. EPA, 1997a).

PRBs are not currently used to directly remediate contaminant source areas, only to intercept and treat contaminant plumes. In order to successfully install a PRB, a thorough site characterization must be conducted. The entire plume must flow through and react

with the reactive media. It must not be able to pass over, under, or around the barrier and the reactive zone must be capable of reducing the contaminant to concentration goals without rapidly plugging with precipitates or losing its reactivity. To achieve this success, knowledge is required of: 1) plume locations 2) plume direction 3) contaminant concentrations 4) hydrologic changes with time 5) concentration attenuation over time and distance 6) Stratigraphic variations in permeability 7) Confining layers 8) Fracturing and 9) aqueous geochemistry. Barrier design, location, emplacement methodologies, and estimated life expectancy are based on the site characterization information. PRBs are installed down-gradient of a source zone, vertically intersecting the contaminated groundwater flow. They can be installed with trenching, if the targeted portion of the aquifer is shallow and surface improvements do not interfere with access. PRBs can also be installed by well injection. Injection through standard vertical wells is the least expensive option but horizontal borings can be installed beneath existing structures and are able to create a uniform reactive zone.

According to Gavaskar et al. (1998), Blowes et al (2000) and Guo et al. (2007), granular zero-valent iron, colloidal iron, ferrous iron-containing compounds, pyrite, granular ferric hydroxide, hematite and siderite can be used as a reactive media for the remediation of contaminated groundwater with inorganic compounds. They further reported that estimating residence time and hydraulic capture zone in the reactive permeable barriers are the most important design specifications for PRB construction. Groundwater flow system, organic-inorganic compositions and hydrologic parameters (e.g. hydraulic conductivity, porosity and hydraulic gradient) are also important design specifications (Gavaskar et al. 1998).

Mackenzie et al. (1999) reported that permeable reactive barriers containing zero-valent iron were more widely used to remediate contaminated groundwaters and there remained much uncertainty in predicting their long-term performance. They focused on two factors affecting performance and lifetime of the granular iron media: plugging at the treatment zone entrance and precipitation in the bulk iron media. Plugging at the system entrance was due to mineral precipitation promoted by dissolved oxygen in the influent groundwater and has an issue in aerobic aquifers. Designs to minimize plugging in field applications where the groundwater is oxygenated include the use of larger iron particles and admixing sand of comparable size with the iron particles. Over longer treatment times, precipitation of $Fe(OH)_2$ and $FeCO_3$ in low carbonate waters and of $Fe(OH)_2$, $FeCO_3$ and $CaCO_3$ in higher carbonate waters begin to dominate porosity losses in PRB (Mackenzie et al. 1999). Iron is reduced by water under the anaerobic conditions that exist in the bulk of the media.

$$Fe^0 + 2H_2O \longleftrightarrow Fe^{2+} + H_2(g) + 2OH^- \quad \text{.....(2.7)}$$

The resultant rise in pH can lead to the precipitation of ferrous hydroxide:

$$Fe^{2+} + 2OH^- \longleftrightarrow Fe(OH)_2 \quad \text{..... (2.8)}$$

In carbonate-containing waters, the rise in pH from the anaerobic corrosion of iron shifts the carbonate–bicarbonate equilibrium and lead to the precipitation of ferrous carbonate (siderite) and calcium carbonate. Thus, three main precipitates form in PRB due to the chemistry in the iron zone. Each of these precipitates reduces the pore volume in a granular iron system. Mackenzie et al. (1999) reported that the control of pH within the

iron media by addition of ferrous sulfide was revealed not to reduce significantly calcium and carbonate precipitates, indicating that mineral precipitation was controlled by more than simple carbonate equilibrium considerations.

Kanel et al. (2006) reported that steel slag was also studied as a permeable reactive barrier material for the removal of As at high concentrations (final treated groundwater was 500 µg/L) for mine tailing leachate. Park et al. (2008) investigated the feasibility of utilizing the slag to remove toxic Cr(VI) from the aqueous phase. Main mechanism of Cr (VI) removal by the slag was its reduction into Cr(III) by the Fe(II) released from the slag under acidic conditions. Guo et al. (2007) also reported that a continuous column experiment was carried out under dynamic flow conditions in order to study the efficiency of low-cost permeable reactive barriers (PRBs) to remove several inorganic contaminants from acidic solutions and a 50:50 w/w waste iron/sand mixture was used as candidate reactive media in order to activate precipitation and promote sorption and reduction–oxidation mechanisms. Thus, permeable reactive barriers containing mixed iron oxide compounds could be employed at a fixed pH for in situ remediation of groundwater contaminated with redox active metals. Proper design and investigation are necessary to find out the applicability of iron oxide particles for the construction of permeable reactive barriers.

2.7 References

Astrup, T., S. Stipp, L.S., and Christensen., T.H., 2000. Immobilization of Chromate from Coal Fly Ash Leachate Using an Attenuating Barrier Containing Zero-valent Iron. Environmental Science and Technology, 34 (19), 4163-4168.

Badruzzaman, A. B. M., Ahmed, M. F., Hossain, M. D., Jalil, M. A., and Ali, M. A., 1998 Arsenic contamination in groundwater in northeastern Bangladesh. J. Civil Eng., IEB 26 (2), 129–140.

Bhattacharya, P., Chatterjee, D., and Jacks, G., 1997. Occurrence of arsenic-contaminated groundwater in alluvial aquifers from delta plains, Eastern India: Options for safe drinking water supply.Wate Res. Develop.13,79 –92.

Benjamin et al., 1996. Sorption and filtration of metals using iron-oxide-coated sand.Water Science Technology, 30, 2609-2620.

Biesinger, M.C., Brown, C., Mycroft, J.R., Davidson, R.D., McIntyre, N.S., 2004. X-ray photoelectron spectroscopy studies of chromium compounds. Surface And Interface Analysis. 36: 1550–1563

BGS & DPHE (British Geological Survey and Department of Public Health Engineering) .2001. Arsenic contamination of groundwater in Bangladesh (eds. D. G. Kinniburgh and P. L. Smedley). BGS Technical Report WC/00/19. British Geological Survey, Keyworth, UK.

Blowes, D., 2002.Tracking Hexavalent Cr in Groundwater . Scienc 295, 5562.

Blowes, D.W., Ptacek, C.J., Benner, S.G., McRae, C.W.T., Bennett, T.A., Puls, R.W., 2000. Treatment of inorganic contaminants using permeable reactive barriers. Journal of Contaminant Hydrology 45, 123–137.

Boparai, H.K., Joseph, M., Caroll, D,M., 2009. Kinetics and thermodynamics of cadmium ion removal by adsorption onto nano zerovalent iron particles. Journal of Hazardous Materials, 186, 458-465.

Chowdhury, T. R., Basu, G. K., Mandal, B. K., Biswas, B. K., Samanta G., Chowdhury U. K., Chanda, C. R., Lodh, D., Roy, S. L., Saha, K. C., Roy, S., Kabir, S., Quamruzzaman, Q., and Chakraborti, D., 1999. Arsenic poisoning in the Ganges delta. *Nature* 401, 545–546.

Cornell, R., and Schwetmann, U., 2003. The Iron Oxides: Structure, Properties, Reactions, Occurrence and Uses. Weinheim: Willey-VCH, 2003.

Dana, J., and Salisbury, E., 1997. Dana's new mineralogy: The system of mineralo 8th ed., by Richard V. Gaines, H. Catherine Skinner, Eugene E. Foord, Brian Ma Abraham Rosenzweig, Vandall T. king, John Wiley & Sins , Inc, New York.

Faria, D.L.A., Silva**,** S. V., and Oliveira, M.T., 1997. Raman Microspectroscopy of Some Iron Oxides and Oxyhydroxides. Journal Of Raman Spectroscopy, 28, 873.

Fetter, C.W., 1993. Contaminant Hydrogeology (Second Edition).Waveland Press, Inc.Illinois.

Fendorf, S., Eick, M.J., and Grossl, P., 1997. Arsenate and chromate retention mechanisms on goethite. 1. Surface structure. Environ. Sci. Technol. 31, 315.

Gavaskar, A.R., Gupta, N., Sass, B.M., Janosy, R.J., and Sullivan, D., 1998. Permeable barriers for groundwater remediation- Design, construction and monitoring. ISBN 1-57477-036-5.

Guo, H., Stuben, D., Berner, Z., 2007. Removal of As from aqueous solution by natural siderite and hematite. Applied Geo-chem. 22, 1039-1051.

Guha, S., and Chaudhuri, M., 1990. Removal of As(III) from groundwater by low cost materials. Asian Environ. 12, 42.

Gui, J., and Devine, T.M., 1991. In situ vibrational spectra of the passive film on iron in buffered borate solution. Corrosion Science. 32 (10), 1105-1124.

Gui, L., Yang, Y., Jeen, S.W., Gillham, W. R., Blowes, D.W., 2009. Reduction of chromate by granular iron in the presence of dissolved $CaCO_3$. Applied Geochemistry 24, 677–686.

Guilbert, J.M., and Park, C.F., 1986, The Geology of Ore Deposits, W.H. Freeman and Company 985p.

Gupta, K.S., Chen, K.Y., 1978. Arsenic removal by adsorption. J WPCF (Wineries, fresh pack food processors) 50, 493.

Harper, T.R., Kingham, N.W., 1992. Removal of arsenic from wastewater using chemical precipitation methods. Wat Environ Res. 64, 200.

Harvey, C. F., Ashfaque, K.N., Yu, W., Badruzzaman, A.B.M., Ali, M.A., Oates, P.M., Michael, H.A., Neumann, R.B., Beckie, R., Islam, S., and Ahmed, M.F., 2006. Groundwater dynamics and arsenic contamination in Bangladesh. Chem. Geol., 228, 112–136

Hu, J., Lo, I.M.C., Chen, G., 2004. Removal of Cr(VI) by magnetite nanoparticle.Water Sci. Technol. 50 (12), 139e146.

Hu et al., 2005. Removal and recovery of Cr(VI) from wastewater by maghemite nanoparticles. Water Research 39, 4528–4536.

Joshi, A., and Chaudhri, M., 1996. Removal of Arsenic from ground water by iron oxide coated sand. Jounal of Environmental Engineering. 122(8).

Vu, K.B., Kaminski, M.D., and Nuñez, L., 2003. Review of Arsenic Removal Technologies for Contaminated Groundwaters. ANL-CMT-03/2. Argonne National Laboratory 9700 South Cass Avenue Argonne, IL 60439

Kamolpornwijit, W., Liang, L., West, O.R., Moline, G.R., Sullivan, A.B., 2003. Preferential flow path development and its influence on long-term PRB performance: column study. Journal of Contaminant Hydrology 66 , 161–178.

Kanel, S.R., Choi, H., Kim, J.Y., Vigneswaran, S., Shim, W.G., 2006. Removal of Arsenic(III) from Groundwater using low-Cost Industrial By-products—Blast Furnace Slag. Water Qual. Res. J. Canada 41, (2), 130–139.

Karim, M., 2000. Arsenic in Groundwater and Health Problems in Bangladesh. Journal of Water Research 34(1), 304-310.

Kocar, B.D., and Fendorf, S., 2012. Arsenic Release and Transport in Sediments of the Mekong Delta. Interdisciplinary Studies on Environmental Chemistry—Environmental Pollution and Ecotoxicology, TERRAPUB. pp. 117–124.

Lindsay, M.J., Ptacek, C.J., Blowes, W. D., Gould, D.W., 2008. Zero-valent iron and organic carbon mixtures for remediation of acid mine drainage. Appl. Geochem. 23(8), 2214-2225.

Lo, I.M.C., Lam, C.S.C., and Lai, K.C.K., 2006. Hardness and carbonate effects on the reactivity of zero-valent iron for Cr(VI) removal .Water Research 40, 595 – 605.

Mackenzie, P.D., Horney, D. P., and Sivavec, T.M., 1999. Mineral precipitation and porosity losses in granular iron columns. Journal of Hazardous Materials 68, 1–17.

Maeda, S., Ohki, A., Saikoji, S., and Naka, K., 1992. Iron (III) hydroxide-loaded coral lime stone as an adsorbent for arsenic (III) and Arsenic(V). Sep Sci Technol. 27, 681.

Mayo, J.T., Yavuz, C., Yean, S., Cong, L., Shipley, H., Yu, W., Falkner, J., Kan, A., Tomson, M., and Colvin, V.L., 2007. The effect of nanocrystalline magnetite size on arsenic removal. Science and Technology of Advanced Materials, 8, 71–75.

Mckay, G., Otterburn, M.S., and Sweeney, A.G., 1981. Surface mass transfer processes during color removal from effluent using silica. Water Res., 15, 327-331.

Mohan, D., and Pittman, C.U., 2007. Arsenic removal from water/wastewater using adsorbents—A critical review. Journal of hazardous materials, doi:10.1016.

Moore, J.W., and Ramamoorthy, S., 1984. Heavy Metals in Natural Waters. Springer-Verlag New York Inc. ISBN 3-540-90885-4.

Mycroft, J.R, Nesbitt, H.W, and Pratt A.R., 1995. Oxidation of arsenopyrite by air and air saturated distilled water and implications of mechanism of oxidation. Geochim.Comochim.Acta; 59: 721.

Naidu, R., Bolan, N.S., Kookana, R.S., Tiller, K.G., 1994. Ionic-strength and pH effects on the sorption of cadmium and the surface charge of soils. European Journal of Soil Science, 45, 419-429.

Nickson, R., McArthur J., Burgess, W., Ahmed, K. M., Ravenscroft, P.,and Rahman, M., 1998. Arsenic poisoning of Bangladesh groundwater. Nature 395, 338.

Nickson, R. T., McArthur, J. M., Ravenscroft, P., Burgess, W. G., and Ahmed, K. M., 2000. Mechanism of arsenic release to groundwater, Bangladesh and West Bengal. Appl. Geochem. **15,** 403–413.

Oblonsky, L. J., and Devine, T.M, 1995. A surface enhanced Raman spectroscopic study of the passive films formed in borate buffer in iron, nickel, chromium and stanless stell. Corrosion Science. 37(1), 17-41.

Odziemkowski, M.S., Schuhmacher, T.T., Gillham, R.W., and Reardon, E.J., 1998. Mechanism of oxide film formation on iron in simulating groundwater solutions: Raman spectroscopic studies. Corrosion Science. 40 (2/3), 371-389.

Ogata and Banks., 1961. A solution of the Differential Equation of Longitudinal Dispersion in Porous Media. Professional paper no. 411-A-USGS, Geological Survey, Washington D.C.

Park et al., 2008. Mechanism and kinetics of Cr(VI) reduction by waste slag generated from iron making industry. Hydrometallurgy 93 (2008) 72–75.

Palmer, C.D., and Puls, R.W., 1994. Natural Attenuation of Hexavalent Chromium in Ground Water and Soils, U.S. EPA Ground Water Issue Paper, EPA/540/S-94/505 (U.S. EPA, Office of Research and Development, Washington, October 1994).

Palmer, C.D., and Wittbrodt, P.R., 1991. Processes affecting the remediation of chromium-contaminated sites. Environmental Health Perspectives, 92: 25-40.

Philip, B., Rifai, H.S., and Newell, C.J., 1999. Ground Water Contamination: Transport and Remediation (2nd Edition).

Petrova, T.M., Fachikov, L., and Hristov, J., 2011. The Magnetite as Adsorbent for some Hazardous Species from Aqueous Solutions: a Review. International Review of Chemical Engineering (I.RE.C.H.E.), 3,2, 134.

Powell, R.M., Puls, R.W., Hightower, S.K., Sabatini, D.A., 1995. Coupled iron corrosion and chromate reduction: mechanisms for subsurface remediation. Environ. Sci. Technol. 29, 1913–1922.

Prasad, G., 1994. Arsenic in the Environment. Part 1. New York 33.

Pratt, A.R., Blowes, D.W., Ptacek, C.J., 1997. Products of chromate reduction on proposed subsurface remediation material. Environ. Sci. Technol. 31, 2492–2498.

Pratt, A.R., Muir, I.J., and Nesbitt, H.W., 1994. X-ray photoelectron and Auger electron spectroscopic studies of pyrrhotite and mechanism of air oxidation. Geochimica et Cosmochimica Acta 58, 827-841.

Rai, D., Zachara, J.M., Eary, L.E., Ainsworth, C.C., Amonette, J.E., Cowan, C.E., Szeimeczka, R.W., Resch, C.T., Schmidt, R.L., Smith, S.C., and Girvin, D.C., 1988. Chromium Reactions in Geologic Materials. Electric Power Institute Res. Inst. Rept. EA-5741,Palo Alto, CA, 287 pp

Rowe, R.K., and Booker, J.R., 1985. Rowe, R.K., and Booker, J.R., 1985. 1 D pollutant migration in soils of finite depth. Journal of Geotechnical Engineering, ASCE, Vol. 111, GT4, pp. 479-499.

Sanchez, A.G., Alastuey, A., Querol, X., 1999. Heavy metal adsorption by different minerals: application to the remediation of polluted soils. The Science of the Total Environment 242, 179-188.

Sawyer, C. N., Mccarty, P.L., and Parkin, G. F., 1994. Chemistry for Environbmental Engineering- Four Edition. McGraw-Hill, Inc. New York, NY 10020.

Sharma, Y.C., 2008. Thermodynamics of removal of cadmium by adsorption on an indigenous clay, Chem. Eng. J. 145, 64–68.

Schnoor, J.L., 1996. Environmental Modeling-Fate and Transport of pollutants in water, air and soil. John Wiley and Sons, Inc.

Shen, H., and Wilson, J.T., 2007. TCE removal from groundwater in flow-through columns simulating a PRB constructed with plant mulch. Environ. Sci. Technol. 41, 4077-4083.

Singh, T.S., and Pant, K.K., 2004. Equilibrium, kinetics and thermodynamic studies for adsorption of As(III) on activated alumina. Separation and Purification Technology 36, 139–147.

Singh, D.B., Rupainwar, D.C., Prasad, G., Jayaprakas, K.C., 1998. Studies on the Cd (II) removal from water by adsorption. Journal of Hazardous Materials 60, 29–40.

Singh, D.B., Gupta,G.S., Prassad,G., and Rupainwar, D.C., 1993. The use of hematite for Cr(VI) removal. J.Environ.Sci.Health, A28(8),1813-1826.

Singh, D.B., Prassad, G., and Rupainwar, D.C., 1996. Adsorption technique for the treatment of As(V)-rich effluents. Colloids and Surfaces: A .Physicochemical and Engineering Aspects 111, 49-56.

Singh, D.B., Prasad, G., Rupainwar, D.C., Singh, V.N., 1988. As(III) removal from aqueous solution by adsorption. Wat, Air, Soil Pollut. 42, 373.

Shipley, H.J., Yean, S., Kan, A.T., and Tomson, M.B., 2009. Adsorption of arsenic to magnetite nanoparticles: effect of Particle concentration, pH, ionic strength, and temperature. Environmental Toxicology and Chemistry 28(3), 509–515.

Sposito, G., 1984. The surface chemistry of soils. Oxford University Press New york Clarendon Pres Oxford, 1984.

Stumm, W., 1992. Chemistry of the solid- water interface. J. Willey & Sons INC.

Tuutijärvi, T., Sillanpääa, J.L.M., Chenb, G., 2009. As(V) adsorption on maghemite nanoparticles. Journal of Hazardous Materials 166, 1415–1420

Tzou, Y.M., Wang, M.K., and Loeppert, R.H., 2003. Effects of Phosphate, HEDTA, and Light Sources on Cr(VI) Retention by Goethite". Soil and Sediment Contamination: An International Journal, 12 (1), 69 – 84.

U.S. Environmental Protection Agency. 1997a. Permeable Reactive Subsurface Barriers for the Interception and Remediation of Chlorinated Hydrocarbon and Chromium (VI) Plumes in Ground Water. U.S. EPA Remedial Technology Fact Sheet. EPA/600/F-97/008. July 1997.

Vance, D., 1997. Reactive Barriers to Treat Areas Adjacent to Source Zone." Environmental Technology-Journal of Advanced Science and Technology. Vol 7, Issue 4. July/August.

Vu, K.B., Kaminski, M.D., and Nuñez, L., 2003. Review of Arsenic Removal Technologies for Contaminated Groundwaters. ANL-CMT-03/2. Argonne National Laboratory 9700 South Cass Avenue Argonne, IL 60439.

Waalkes, M.P., 2000. Cadmium carcinogenesis in review. Journal of Inorganic Biochemistry 79 (2000) 241–244

Wang, F.Y., Wang, H., Ma, J.W., 2010. Adsorption of cadmium (II) ions from aqueous solution by a new low-costadsorbent—Bamboo charcoal. Journal of Hazardous Materials177 (2010) 300–306.

Wang, Y., Morin, G., Ona-Nguema, G , Menguy, N., Juillot, F., Aubry, E., Guyot, F.O., Calas, G., and Brown G.E., 2008. Arsenite sorption at the magnetite–water interface

during aqueous precipitation of magnetite: EXAFS evidence for a new arsenite surface complex. Geochimica et Cosmochimica Acta 72, 2573–2586.

White, A. F., Peterson, M. L., Hochella, M. F., 1994. Electrochemistry and dissolution kinetics of magnetite and ilmenite. Geochim. Cosmochim. Acta, *58*, 1859-1875.

Yean, S., Cong, L., Yavuz, C.T., Mayo, J.T., and Yu, W.W., 2005. Effect of magnetite particle size on adsorption and desorption of arsenite and arsenate. Materials Research Society. J. Mater. Res. 20 (12).

CHAPTER 3

ARSENIC REMOVAL BY MIXED MAGNETITE-MAGHEMITE NANOPARTICLES

3.1 Introduction

According to Shih (2005), arsenic ranks twentieth in abundance in the earth's crust, fourteenth in seawater and twelfth in the human body. Both organic and inorganic arsenic exist in natural waters but organic arsenic is of less environmental concern as it undergoes biotransformation and detoxification through methylation. Ferguson et al., (1976) reported that inorganic arsenic in aquatic environment has different oxidation states such as −3, 0 +3 and +5. They further explained that As(III) exists primarily as $H_3AsO_3^0$, H_2AsO^{3-}, $HAsO_3^{2-}$, and AsO_3^{3-} under reducing environment whereas different hydrolyzed species of As(V), namely $H_3AsO_4^0$, $H_2AsO_4^-$, $HAsO_4^{2-}$, and AsO_4^{3-}, are found in water under oxidizing environment. Although environmental restrictions and regulations have controlled the production and use of arsenic and its compounds, they are still extensively used in metallurgy, agriculture, forestry, electronics, pharmaceuticals, glass, and the ceramic industry. Arsenic causes wide-spread groundwater contamination. Evidence of chronic arsenicosis has been observed in populations ingesting arsenic-contaminated drinking water in many parts of the world. Karim, (2000) and Neff, (1997) described that major sources of arsenic are geologic formations such as soil and bedrocks, weathering of rocks, mine tailings, industrial wastes discharge, fertilizers, agricultural use of pesticides, smelting of metals, and burning of fossil fuels.

A version of this paper was accepted for publication in Environmental Earth Science Journal.

Several methods are used to remedy arsenic contamination. Those treatment methods are precipitation, electrochemical reduction, adsorption, ion exchange, solvent extraction,

nano filtration and reverse osmosis (Mayo et al., 2006 and Hu et al., 2004). Hossain et al. (2005) noted that these technologies do not perform well in actual field trials and improved systems are needed. As(III) adsorption on different sorbents such as coconut husk carbon, carbon from fly ash, iron oxide coated polymeric material, and hybrid polymeric sorbent has been investigated (Demarco et al., 2003; Ioannis et al., 2002, and Manju et al., 2000). Iron and iron coated sand, iron coated activated carbon (Petrusevski et al., 2002), and granular ferric hydroxides (Driehaus et al., 1998) have also been applied as adsorbents for arsenic removal from water and waste water. However, their use is limited due to high operation cost, sludge formation, and technical difficulties in the preparation of materials. Naturally occurring ores and minerals, namely kaolinite (Guha et al., 1990), magnetite (Yean et al. 2005 and Shipley et al. 2009), maghemite (Lim et al., 2009), hematite and feldspar (Prasad, 1994), have also been used for the adsorption of arsenic though not as extensively as other materials.

Magnetite-maghemite (Fe_3O_4- γ-Fe_2O_3) nanoparticles are potential sorbents for arsenic removal in drinking water and are therefore suitable for treating arsenic contaminated water. As maghemite and magnetite are generally found to be an oxidation product of iron, the association of the two minerals would be a common occurrence in nature (Grosvenor et al. 2004). In this study, commercially prepared 20-40 nm 'magnetite' particles, identified in subsequent laboratory characterization to be mixed magnetite-maghemite, were used for the removal of arsenic from aqueous solutions. Magnetite-maghemite mixture has affinity for heavy metals by adsorbing them from a liquid phase. To capitalize on this advantage of mixed magnetite-maghemite particles, the present

study aimed to investigate the effectiveness of nano-size magnetite-maghemite particles in contaminated groundwater remediation. X-ray photoelectron spectroscopy (XPS) was employed to probe the interactions of the sorbent with arsenic. The overall purpose of the study was to investigate the performance of magnetite-maghemite nanoparticles in arsenic removal by examining the mechanism(s) of inorganic arsenic uptake. This is one of the few studies that have, to date, examined arsenic removal from aqueous solution by mixed magnetite-maghemite nanoparticles. Although magnetite and maghemite may separately remove greater amounts of arsenic from solution than the mixture (Shipley et al. 2009; Lim et al., 2009), it is probably more realistic and practical to examine the removal efficiency of the mixture because of the common association of the two minerals in nature. In addition, most commercial grade 'magnetite' nanoparticles used in field scale remediation of arsenic contamination would likely be a mixture of magnetite and maghemite because of slight oxidation during storage or shipping.

3.2 Materials and Methods

3.2.1 Sample Preparation and Adsorbent

All solutions used in the experiments were prepared from certified reagent grade chemicals, which were used without further purification. Solutions were prepared with de-ionized water. Glass volumetric flasks and reaction vessels were treated with 10% HNO_3 and rinsed several times with de-ionized water before they were used. Both As(V) and As(III) stock solutions were prepared by dissolving arsenic oxides (As_2O_5 and As_2O_3) powder in de-ionized water, by using 4 g/L NaOH since both oxides have

enhanced solubility in NaOH solution. For each stock solution, redox potential was measured using a WTW Multi 340i ORP electrode (Wellheim, Germany) to confirm the targeted As(V) and As(III).

Commercially available 20-40 nm 'magnetite' particles were obtained from Reade Advanced Materials (Rhode Island, U.S.A.). The particles contains 99.99% magnetite nanoparticles. Subsequent laboratory characterization prior to the adsorption studies, presented later in this paper, indicated that the particles were actually a mixture of magnetite and maghemite (30.8% maghemite and 69.2 % magnetite nanoparticles). The BET surface area of the mixed particles provided by the manufacturer was 60 m^2/g. The mixture arrived in powder form in an airtight plastic bag. Further examination of the as-received sample showed that the particles were dispersed and of a purity of more than 98%. Impurities were identified through subsequent laboratory characterization. The particles had black and spherical morphology, and the bulk density was measured to be 0.84 g/cm^3. Figure 3.1 demonstrates 200,000X magnification image of magnetite-maghemite nanoparticles (20-40 nm) using Hitachi S4500 scanning electron microscopy (SEM). A 200,000X magnification was also used to check surface porosity but the image did not show the presence of pores at 200,000X magnification and the mixture of magnetite-maghemite appeared to be highly uniform.

3.2.2 Batch Experiments

Batch experiments were run for complete adsorption on the magnetite-maghemite mixture. In a sonication bath, the mixture was dispersed in solution for 20 min. Known amount of arsenic stock solution was mixed with magnetite-maghemite mixture solution and held in a slowly rotating rack of a shaker that provided a gentle end-over-end tumbling (28 rpm) for 24 hr. Standard acid (0.1 M HNO_3) and base (0.1 M NaOH) solutions were used for pH adjustment. After shaking, the mixtures were centrifuged at 5000 rpm for 30 min to separate the As-adsorbed magnetite-maghemite particles. After separation from supernatant solutions, solid samples were dried in a vacuum desiccator. Then dried arsenic adsorbed magnetite-maghemite nanoparticles were kept in an airtight ceramic dish to prevent any reaction with air. 0.2 µm Nalgene Surfactant-Free Cellulose Acetate (SFCA) syringe filters (VWR International, Mississauga, Ontario, Canada) were used to filter the supernatant solutions. The filtrate was acidified with 0.1 M HNO_3 for As measurements. ICP-OES (inductively coupled plasma-optical emission spectroscopy) was used to determine arsenic concentrations in the filtrate. The minimum detection limit of ICP-OES for arsenic is 0.01 mg/L. The experiments were carried out in duplicate and the mean values were considered. Blank samples used in the experiments showed no detectable arsenic adsorption on the surface of the mixed magnetite-maghemite nanoparticles.

3.2.3 Equilibrium Modeling

The experimental data obtained at pH 5 were applied to the linearized forms of Langmuir and Freundlich [Eqs. (3.1) and (3.2), respectively], which were suitable for measuring adsorption as well as to interpret the nature of adsorption of arsenic on magnetite-maghemite nanoparticles.

$$C_e/q_e = 1/bq_m + C_e/q_m \quad (3.1)$$

$$Lnq_e = Ln\ K + (1/n * Ln\ C_e) \quad (3.2)$$

where C_e and q_e are equilibrium solute concentration (mg/L) and equilibrium adsorption capacity (mg/g), respectively. The other parameters, q_m, b and n are isotherm constants. The value of q_m is adsorption maxima or adsorption capacity (mg/g) in Eq (3.1).

3.2.4 Instrumentation for X-ray Photoelectron Spectroscopy (XPS)

A Kratos Axis Ultra XPS instrument was used to determine elemental composition and chemical oxidation states of surface and near-surface species. A monochromatic Al Kα x-ray source was used to analyze for all samples. In XPS, chamber pressures was kept in the range of 10^{-7}-10^{-6} Pa and the resolution function of the instrument was found to be 0.35 eV (Grosvenor et al. 2004). In this study, the charge neutralizer filament was used during all experiments to maintain charging of the samples. The conditions used for the survey scans were as follows: energy range =1100–0 eV, pass energy =160 eV, step size = 0.7 eV, sweep time = 180 s and x-ray spot size = 700 * 400 μm. For the high-resolution spectra, an energy range of 40–20 eV was applied, depending on the peak being examined, with a pass energy of 10 eV and a step size of 0.05 eV.

3.3. Results and Discussion

3.3.1 Effect of pH on arsenic removal by mixed magnetite-maghemite

The effect of pH on As(III) and As(V) adsorption by magnetite-maghemite nanoparticles was studied in the pH range of 1-14 at a contact time of 24 hrs and As(III) and As(V) concentrations of 1.5 mg/L each. Figure 3.2 illustrates the effect of pH on removal capacity (%) by mixed magnetite-maghemite nanoparticles. The data show that adsorption decreases as pH increases. Variations in As(V) adsorption on magnetite-maghemite in the pH range 2 – 6.5 were found to be small. As(V) adsorption decreased sharply above pH 7. Again, variations in As(III) adsorption on magnetite-maghemite in the pH range 2 – 9 were negligible. The removal capacity (%) of arsenic species on mixed magnetite-magheite was 98 % or 3.69 mg/g for As(III) and 99% or 3.71 mg/g for As(V) at pH 2 under room temperature. These results clearly show that magnetite-maghemite nanoparticles can adsorb As(III) and As(V) more readily in an acidic pH range.

The surface hydroxyl groups, arising from adsorption of water or from structural OH, are the functional groups of iron oxides. They contain a double pair of electrons together with a dissociable hydrogen atom which can help them to react with both acids and bases. Charge on the iron oxide surface is established by the dissociation (ionization) of the surface hydroxyl groups. This surface properties control adsorption or desorption of protons depending on the pH of the solution. According to Cornell et al. (1996) magnetite

produces Fe^{2+} and its hydrolysis products ($FeOH^{+}$, $Fe(OH)_2^0$, and $Fe(OH)_3^-$) depending on the solution pH. They further stated that acidity constant of magnetite (69.2% of used adsorbent), pK_{a1} is 5.6. Thus, at pH <5.6, dominant functional groups of iron oxide surface would be Fe^{2+} or $FeOH^{+}$. Thus iron oxide would attract negative arsenic species at low pH. At higher pH, the surface hydroxyl groups on the iron oxide surface are $Fe(OH)_2^0$, and $Fe(OH)_3^-$. Thus in this study, negative charge iron oxide surface repelled negative charge arsenic species at the higher pH value. Maghemite is formed through the oxidation of magnetite, therefore Fe(III) in solution would form hydrated ferric oxides (HFO) nanoparticles. Even if As(V) is reduced to As(III), adsorption will keep arsenic on the magnetite-maghemite surface through a Lewis acid base (LAB) interactions.

The variation in removal efficiency at different pH values may be attributed to the affinities of the mixed magnetite-maghemite for the different species of As(V) and As(III) present at different pH values, namely AsO_4^{3-}, $HAsO_4^{2-}$, $H_2AsO_4^-$, H_3AsO_4, AsO_3^{3-}, $HAsO_3^{2-}$, $H_2AsO_3^-$, and $H_3AsO_3^0$. At pH 2.3 to 6.9, the predominant species of As(V) is $H_2AsO_4^-$ (Nordstrom and Archer, 2003). The adsorption free energy of $H_2AsO_4^-$ ion may be lower than that of $HAsO_4^{2-}$ and AsO_4^{3-}, and this would explain why $H_2AsO_4^-$ is more favorably adsorbed than $HAsO_4^{2-}$ and AsO_4^{3-}. From literature, the first pKa value for As(III) in aqueous solution is 9.17 (Nordstrom and Archer, 2003) and the predominant species of As(III) at pH below 9.17 is neutral or chargeless, namely $H_3AsO_3^0$. Thus the adsorption of the nonionic form of As(III) on magnetite-maghemite surface would not change significantly at pH below 9.17. However, at increasing pH

values (beyond 9.17), As(III) uptake decreases because of the higher concentration of OH^- ion present in the reaction mixtures.

Yean et al. (2005) showed from potentiometric titrations that the surface of magnetite particles contained a positive surface charge up to pH 6.7, a point of zero charge of 6.8 and a negative surface charge in the pH range 6.9-9.5. Tuutijarvi et al. (2009) reported that maghemite has a point of zero charge at pH_{pzc} 7.5. They further reported that the more acidic the condition the more positive was the surface charge of the adsorbent and, accordingly, the more attractive to negative As species. Thus, depending on pH, magnetite-maghemite particles can adsorb either negatively or positively charged species by electrostatic attraction.

3.3.2 Mixed magnetite-maghemite and equilibrium time

The kinetics of As(V) and As(III) adsorption were studied by varying the contact time between magnetite-maghemite and the respective solution from 10 to 240 min using 0.4 g/L adsorbent at a metal (As) concentration of 2 mg/L and pH 6.5. The effect of contact time on the adsorption of As(V) and As(III) on magnetite-maghemite nanoparticles at fixed metal concentration is shown in Figure 3.3. The adsorption on mixed magnetite-maghemite seems to take place in two phases. The first phase involved rapid metal adsorption within 10 min of contact time because of the availability of the adsorption sites in the solution and was followed by subsequent slower uptake. In addition, the rapid metal uptake by magnetite-maghemite nanoparticles is perhaps attributed to external

surface adsorption, which is different from the microporous adsorption process. Since nearly all the sorption sites of mixed magnetite-maghemite nanoparticles exist in the exterior of the adsorbent compared to the porous adsorbent, it is easy for arsenic species to access these active sites, thus resulting in a rapid approach to equilibrium. When experiments were run at pH 6.5 and 2 mg/L of initial concentrations, equilibrium was achieved in 3 hrs. At equilibrium, the adsorbed amount of arsenic As(V) and As(III) was almost 4.85 and 4.75 mg/g, respectively, representing 92% of As(V) and 91% of As(III) removal efficiencies by magnetite-maghemite nanoparticles. In addition, the adsorption of As(III) and As(V) on the mixed magnetite and maghemite mixture may involve two steps. First, As(III) and As(V) species migrate from the bulk fluid phase to the outer particle surface of the adsorbent for contact (film diffusion). Second, there might be electro-static attraction or reaction occurring between adsorbate (As(III) or As(V) species) and adsorbent.

3.3.3 Adsorption Isotherms and reactions

The adsorption data were fitted with the isotherm equations to identify the most appropriate adsorption parameters for future modeling and scale up. Calculated correlation coefficients for the isotherms using linear regression analysis for As(III) and As(V) adsorption at pH 5 are shown in Table 3.1. As indicated, the results show that adsorption by magnetite-maghemite nanoparticles is well described by the Freundlich and Langmuir isotherm equations. The Langmuir isotherm model can be used to determine adsorption maxima, q_m (mg/g). Figure 3.4 shows Langmiur plots for As(III) and As(V)

adsorption by magnetite-maghemite nanoparticles. Gupta et al. (1978) noted that Langmuir adsorption is a reversible phenomenon and that the coverage is monolayer.

A number of researchers have observed that several adsorption processes follow the Langmuir isotherm. Examples include As(III) adsorption by hematite (Singh et al. 1988), As(III) and As(V) adsorption by magnetite (Shipley et al. 2009), activated carbon, activated bauxite and activated alumina (Gupta et al. 1978) and amorphous iron hydroxide (Harper et al. 1992), and As(V) adsorption by amorphous aluminum hydroxide (Anderson et al. 1976). Previous studies have presented maximum As(III) adsorption capacity for hematite, activated bauxite, activated alumina, iron(III) hydroxide loaded coral limestone (Fe-coral) and magnetite are 2.63, 16, 14, 0.17 μmol/g and 0.2 mmol/g, respectively (Gupta et al. 1978; Singh et al., 1988; Harper et al. 1992; and Maeda et al., 1992 and Ohe et al. 2005). For As(V) adsorption by activated bauxite, activated alumina, activated carbon, Fe-coral and magnetite, the calculated maximum adsorption capacities are 52, 67, 10, 0.2 μmol/g and 0.2 mmol/g (Gupta et al., 1978 ; Maeda et al. 1992 and Ohe et al. 2005), respectively. In the present study, As(III) and As(V) adsorption capacities of magnetite-maghemite nanoparticles at room temperature and pH 5, calculated from Langmuir isotherm, are 109 and 120 μmol/g. It is evident that magnetite-maghemite nanoparticles are more effective adsorbents than hematite and Fe-coral but less than magnetite. According to Raven et al. (1998), the maximum adsorption of As(V) on hydrated ferrous oxide (HFO) was approximately 0.25 mol As/mol Fe at pH 4.6 and 8.0. Dixit and Hering (2003) stated that similar maximum sorption capacities for As(III) and As(V) on goethite was found to be 16 mmol As/mol Fe. In the present study, As(V)

and As(III) sorption maxima on 20-40 nm magnetite-maghemite particles was found to be 10 mmol As/mol Fe at pH 5. Despite the reported higher arsenic species removal from water by HFO and goethite, the findings on arsenic removal by magnetite-maghemite nanoparticles are still significant because magnetite-maghemite particles are found more in natural soil than HFO and goethite (Wang et al. 2008).

The adsorption efficiency of the process can be calculated by using the following equation:

$$r = 1/(1+ bC_0) \qquad (2)$$

where r is a dimensionless separation factor and C_0 is the initial As(III) or As(V) concentration (mg/L) and b represents the Langmuir isotherm constant (L/mg). A value of $r < 1$ indicates favorable adsorption and a value greater than one represents unfavorable adsorption (Mckay et al. 1985). Calculated values of r for all initial concentrations of As(III) and As(V) were found to be less than 0.2 at room temperature (22^0 C) in this study. Thus, it can be concluded that the adsorption of As(III) and As(V) on magnetite-maghemite nanoparticles was highly favorable at the concentrations and temperature studied.

Standard Gibbs free energy (ΔG^0, kJ/mol) for the adsorption process was measured using the following equation:

$$Ln(1/b) = \Delta G^0/ RT \qquad (3)$$

where b represents the Langmuir constant related to the energy of adsorption, R is the ideal gas constant (8.314 J/K mol) and T is temperature (K). A negative ΔG^0 value

means the reaction or process is spontaneous and thermodynamically stable, while a positive value suggests that the reaction or process is in the reverse direction. In this study, the negative ΔG^0 values (32.6-32.5 kJ mol^{-1}) obtained for As(III) and As(V) adsorption on magnetite-maghemite nanoparticles at room temperature confirm the feasibility of the adsorption process and the spontaneous nature of adsorption.

3.3.4 X-ray Photoelectron Spectroscopy (XPS) Analysis

The As-loaded magnetite-maghemite particles after As adsorption at fixed pH were characterized using XRD (X-ray diffraction) and XPS (X-ray photoelectron spectroscopy) techniques. The results from XRD analysis (Fig. 3.5) show that the identical peaks of the As-adsorbed particles match well with standard Fe_3O_4- γ-Fe_2O_3 without other crystalline phases appearing after adsorption.

In this study, the elemental composition and chemical oxidation states of surface and near-surface species were analyzed using XPS and all spectra were drawn and analyzed using the Casa-XPS software (Fairley, 1999-2003). XPS wide scan spectra of fresh magnetite-maghemite and arsenic adsorbed magnetite-maghemite sorbents are illustrated in Figure 3.6. Three major peaks at binding energies of 282.25, 348.05, 527.25 and 301.85 eV, designated for the C 1s, Ca 2p, O1s, and Mg KLL respectively, are observed for the virgin sorbent (Figure 3.6a). Significant changes can be found in Figure 3.6b and 3.6c after As(III) and As(V) adsorption; the peak at binding energy of 348.05 eV for Ca

2p disappears in As(III) loaded sorbent while a new weak peak at binding energy of about 45-46.7 eV for As 3d appears in arsenic sorbed magnetite-maghemite sorbents.

The As 3d spectrum of the arsenic adsorbed sorbent can be deconvoluted into two individual component peaks, which originate from the different valent arsenic atom and overlap on each other. According to Nesbitt et al., 1995 and Lim et al., 2009, the As $3d_{5/2}$ peak for As(III) and As(V) were set to binding energy ranges of 44.0 eV to 45.5 eV and 45.2 eV to 46.8 eV, respectively. As shown in Figure 3.7, the peaks at binding energies of 44.5 and 45.2 eV can be assigned to the arsenite (As(III)) and arsenate (As(V)) atom, respectively. These two assignments reflect the different chemical valence of inorganic arsenic on the sorbent. The quantitative analysis of As(V) adsorbed sorbent obtained from Fig 3.7a that 56.5% of As(V) and 43.5% of As(III) are present as demonstrated in Table 2. This result suggest the reduction of As(V) to As(III) on the sorbent surface. In Fig 3.7b, the quantitative analysis of As(III) adsorbed sorbent shows 68.9% of As(III) and 31% of As(V) species on the sorbent surface. This result indicates solid state oxidation-reduction between arsenate and arsenite on the surface of the sorbent.

The Fe 2p high resolution spectra were fitted following the example of Pratt et al. (1994) using theoretical multiplet peak (Gupta et al., 1974 and 1975). The peak full width at half maximum (FWHM) was generally held to be between 1.0 and 1.5 eV. The XPS results, shown in Fig 3.8, present the theoretical multiplet peaks for iron and arsenic adsorbed iron at the surface of the Fe_3O_4 and γ-Fe_2O_3 mixture. Theoretical multiplet analysis of the Fe_3O_4-γ-Fe_2O_3 mixture gave 30.8% of maghemite and 69.2% of magnetite

(Fig. 3.8a). After arsenic adsorption on the magnetite-maghemite mixture, it was found that the percent of maghemite increased to 47.2% (Fig 3.8b) for As(V) adsorption and 70.5% (Fig 3.8c) for As(III) adsorption. At the same time, the percentage of magnetite was reduced for both cases. Thus, the results show that a redox reaction occurred on the magnetite-maghemite mixture surface when arsenic was introduced. Changes in the relative abundance of Fe(II) and Fe(III) in magnetite and maghemite spectra (Fig. 3.8b and 3.8c) upon arsenite and arsenate sorption process are quantitatively elucidated as indicated in Table 3.3. It shows that the relative content of the Fe(II) decreases from 25.9 to 20.1 % for As(V) loaded magnetite-maghemite sorbent indicating oxidation on mixed surface as well as increase in maghemite from 30.1% to 47.2%. The relative content of the Fe(II) decreased from 25.9% to 11.2% for As(III) loaded magnetite-maghemite sorbent resulting in the percent of maghemite increasing to 70.5% for As(III) adsorption. Again, smaller amount (41.5% to 32.2%) of Fe(III) decreases on As(V) loaded magnetite-maghemite sorbent in magnetite spectra (Fig.3.8b) indicating decrease in magnetite content (69.1% to 52%) on mixed magnetite-maghemite sorbent.

In XPS data, adventitious elements (carbon and oxygen) spectra are very important because these elements can change the reactivity of surfaces even if the sample is prepared in vacuum. The usual source of this contamination is the air or residual gases in the vacuum. As shown in Figure 3.9, the C 1s spectra can be deconvoluted into three peaks representing three functional groups of C-H, C-O, and C=O at binding energies of 284.80, 286.3, and 288.87 eV, respectively. Table 2 shows that the C-O content (C-OH and C-O-C) decreases from 13.9 to 10% while that of C=O increases from 6.0 to 12.7%

due to the arsenic uptake, indicating the oxidation of C-O to C=O on As loaded magnetite-maghemite sorbent surface. The C 1s labelled peak is related to the differential charging of a small proportion of the adsorbed As species. This is seen by the small contribution near 42 eV in the As 3d (As(V)) data. There is no indication of charging in the Fe 2p or O 1s data.

Figure 3.10 shows O 1s spectra of the fresh magnetite-maghemite sorbent, arsenite loaded sorbent and arsenate loaded sorbent at pH 5. The peaks at binding energy of 529.4, 531.7 and 531.6 eV can be assigned to Fe-O (lattice oxygen in magnetite-maghemite mixture), As_2O_3 and As_2O_5 (Wagner et al., 1980).

Compared with the virgin sorbent (Figure 3.10a), metal oxide spectrum of the arsenate and arsenite loaded sorbents (Figure 3.10b and c) were increased in component peak areas (74.5% and 75.2% respectively). The spectrum FWHM at 531.08 eV were changed after the adsorption (Figure 3.10b and c) indicating As-O on the sorbent surface. Table 2 shows that the metal oxide content increases from 70.7 to 75.2 % and O 1s Hydroxide decreases from 23.9% to 16% indicating the formation of As-O, which is due to the binding of arsenic onto the oxygen atom in the adsorbent. Thus, the adsorption mechanism of As(III) and As(V) onto Fe_3O_4 -γ-Fe_2O_3 surface is suggested to be a physico-chemical reaction as well as electrostatic attraction at pH of 5. The amount of arsenic used in the XPS spectrum analysis, was very low (0.1-0.5 atomic percent) compared to the amount of iron detected (24-27 at. %), any iron-arsenic complex

contribution to the Fe 2p spectrum would be obscured by the large magnetite-maghemite signal.

3.4 Conclusions

Application of magnetite-maghemite nanoparticles for arsenic removal has great potential in water and wastewater engineering. From this study, it is apparent that the removal of arsenic by magnetite-maghemite nanoparticles depends on pH, contact time and initial concentration of arsenic. The results show that magnetite-maghemite nanoparticles can adsorb As(III) and As(V) better in an acidic pH range. For 2 mg/L of As(V) and As(III) concentrations, equilibrium was achieved in 3 hrs at pH 6.5. The maximum arsenic removal was found to be almost 99% at pH 2 when initial concentration was kept at 1.5 mg/L for both arsenic species. The negative Gibb free energy, ΔG^0, values (32.6-32.5 kJ mol^{-1}) calculated for As(III) and As(V) uptake on magnetite-maghemite nanoparticles at room temperature confirm the feasibility of the adsorption process and the spontaneous nature of adsorption. X-ray photoelectron spectroscopy (XPS) studies confirmed the presence of arsenic on the surface of magnetite-maghemite nanoparticles. Changes in the relative abundance of Fe(II) and Fe(III) in magnetite and maghemite spectra upon arsenite and arsenate sorption process indicates the redox reaction occurring on mixed surface. Electrostatic attraction and oxidation-reduction between arsenic and mixed magnetite-maghemite are the postulated mechanism for removal of arsenic from aqueous solutions. Thus, magnetite-maghemite particles can also be used site remediation. Mixed magnetite-maghmite particles can be applied in the design of permeable reactive barriers

for groundwater remediation. Permeable reactive barriers containing magnetite-maghemite particles could be employed at a fixed pH for in situ remediation of groundwater contaminated with redox active metals. Proper design and investigation are necessary to find out the applicability of magnetite-maghemite particles for the construction of permeable reactive barriers.

3.5 References

Abbasi, S.A. and Soni, R., 1984. Teratogenic Effects of Chromium(VI) in the Environment as Evidenced by the Impact of Larvae of Amphibian Rand tigrina: Implications in the Environmental Management of Chromium. Int. J. Environmental Studies, 23: 131-137.

Acharyya, S.K., 1999. Arsenic poisoning of Bangladesh groundwater. Nature 401, 545.

Anderson, M.A., Ferguson, J.F., Gavis, J., 1976. Arsenate adsorption on amorphous aluminium hydroxide. J Colloid Interface Sci. 54, 391.

British Geological Survey (BGS) and Government of the People's Republic of Bangladesh., 2001. Arsenic contamination of groundwater in Bangladesh. Technical Report. WC/00/19.Vol.1.

Cornell, R.M., and Schwertmann, U., 1996. The iron oxides- structure, properties, reactions, occurrence and uses. VCH Publishers, New York, NY (USA). ISBN 3-527-28576-8.

Daou, T.J., Begin-Colin, S., Greneche, J.M., Thomas, F., Derory, A., Bernhardt, P., Legare, P., and Pourroy, G., 2007. Phosphate Adsorption Properties of Magnetite-Based Nanoparticles. Chem. Mater. 19, 4494-4505.

Demarco, M.J., Sengupta, A.K., and Greenleaf, J.E., 2003. Arsenic removal using a polymeric/inorganic hybrid sorbent. Water Res. 37(1), 164-176.

Dixit, S., and Hering, J.G., 2003. Comparison of arsenic(V) and arsenic(III) sorption onto iron oxide minerals: Implications for arsenic mobility. Environ. Sci. Technol. 37**,** 4182.

Driehaus, W., and Jekel, M., 1998. Granular ferric hydroxide — a new adsorbent for the removal of arsenic from natural water. J. Water SRT Aqua 47, 1-6.

Fendorf, S., Eick, M.J., and Grossl, P., 1997. Arsenate and chromate retention mechanisms on goethite. Surface structure. Environ. Sci. Technol. 31, 315.

Ferguson, J.F., and Gavis, J., 1972. A review of the arsenic cycle in natural waters. Water Res. 6, 1259-1274.

Fairley, N., 1999-2003. CasaXPS Version 2.2.19.

Grosvenor, A.P., Kobe, B.A., Biesinger, M.C., and McIntyre, N.S., 2004. Investigation of multiplet splitting of Fe 2p XPS spectra and bonding in iron compounds. Surf. Interface Anal. 36: 1564–1574.

Grosvenor, A.P., Kobe, B.A., and McIntyre, N.S., 2004. Examination of the oxidation of iron by oxygen using X-ray photoelectron spectroscopy and QUASES. Surafce Science 565, 151-162.

Guha, S., and Chaudhuri, M., 1990. Removal of As(III) from groundwater by low cost materials. Asian Environ. 12, 42.

Gupta, K.S., Chen, K.Y., 1978. Arsenic removal by adsorption. J WPCF (Wineries, fresh pack food processors) 50, 493.

Gupta. R.P., S.K. Sen, S.K., 1974. Phys. Rev. 10, 71.

Gupta. R.P., S.K. Sen, S.K., 1975. Phys. Rev. 12, 15.

Harper, T.R., and Kingham, N.W., 1992. Removal of arsenic from wastewater using chemical precipitation methods. Wat Environ Res. 64, 200.

Hossain et al., 2005. Environ. Sci. Technol. 39, 4300.

Hu et al., 2004. Removal of Cr(VI) by magnetite nanoparticle. Water science and Technology 50 (12), 139-146.

Ioannis, A. K., and Anastasios, I. Z., 2002. Removal of arsenic from contaminated water sources by sorption onto iron-oxide-coated polymeric materials. Water Research 36, 5141–5155.

Jain, A., and Loeppert, R.H., 2000. Effect of competing anions on the adsorption of arsenate and arsenite ferrihydrite. J. Environ. Qual. 29, 1422–1430.

Karim, M., 2000. Arsenic in Groundwater and Health Problems in Bangladesh. Journal of Water Research 34(1), 304-310.

Lim, S.F., Zheng, Y.M., and Chen, J.P., 2009. Organic Arsenic Adsorption onto a Magnetic Sorbent. Langmuir**,** 25(9), 4973–4978

Maeda, S., Ohki, A., Saikoji, S., and Naka, K., 1992. Iron (III) hydroxide-loaded coral lime stone as an adsorbent for arsenic (III) and Arsenic(V). Sep Sci Technol. 27, 681.

McKay, G., Bino, M.J., and Altamemi, A.R., 1985. The adsorption of various pollutants from aqueous solutions on to activated carbon. Wat Res. 14, 277.

Manju, G.N., Raji, C., and Anirudhan, T.S., 2000. Treatment of arsenic(III) containing wastewater by adsorption on hydrotalcite. Ind. J. Environ. Health 42 (1).

Manning B. A., and Goldberg, S., 1996. Modeling competitive adsorption of arsenate with phosphate and molybdate on oxide minerals. Soil Sci. Soc. Am. J. 60, 121–131.

Mayo et al., 2007. The effect of nanocrystalline magnetite size on arsenic removal. Science and Technology of Advanced Materials 8, 71–75.

Neff, J.M., 1997. Ecotoxicology of arsenic in the marine environment—Review. Environmental Toxicology and Chemistry. 16 (5), 917-927.

Nesbitt, I.J and Pratt, A.R., 1995. Oxidation of arsenopyrite by air and air-saturated, distilled water and implications for mechanism of oxidation. Geochimica et Cosmochimica Acta, 59 (9), 1773-1786.

Nordstrom, D.K., and D.G. Archer, D.G., 2003. Arsenic thermodynamic data and environmental geochemistry. In: Biogeochemistry of Environmentally Important Trace Elements (eds Y.Cai & O. C. Braids), Oxford University Press 1-25 (Chapter 1).

Ohe, K., Tagai, Y., and Nakamura, S., 2005. Adsorption behavior of As(III) and As(V) using magnetite. Journal of Chemical Engineering of Japan. 38(8), 671.

Patanayak, J., Mondal, K., Mathew, S., and Lalvani, S.B., 2000. Parametric evaluation of the removal of As(V) and As(III) by carbon-based adsorbents. Carbon 38, 589.

Pierce, M.L., and Moore, C.B., 1982. Adsorption of arsenite on amorphous iron hydroxide from dilute aqueous solution. Environ. Sci. Technol. 14, 214–216.

Prasad, G., 1994. Arsenic in the Environment. Part 1. New York 33.

Pourbaix, M., 1974. Atlas of electrochemical equilibria in aqueous solutions. National Association of Corrosion Engineers, Houston, TX, USA.

Petrusevski, B., Boere, J., Shahidullah, S.M., Sharma, S.K., and Schippers, J.C., 2002. Adsorbent-based point-of-use system for arsenic removal in rural areas. J Wat. SRT-Aqua. 51, 135-144.

Pratt A.R., Muir I.J., and Nesbitt H.W. 1994. X-ray photoelectron and Auger electron spectroscopic studies of pyrrhotite and mechanism of air oxidation. Geochimica et Cosmochimica Acta 58, 827-841.

Qiu, S.R., Lai, H.F., Roberson, M.J., Hunt, M.L., Amrhein, C., Giancarlo, L.C., Flynn, G.W., Yarmoff, J.A., 2000. Removal of contaminants from aqueous solution by reaction with iron surfaces. Langmuir 16, 2230–2236.

Raven, K.P., Jain, A., and Loeppert, R.H., 1998. Arsenite and arsenate adsorption on ferrihydrite: Kinetics, equilibrium, and adsorption envelopes. Environ. Sci. Technol. 32, 344.

Roberts, E.D., Johnson, C.E., 1975. Photoelectron and $L_{2.3}$ MM auger electron energies for arsenic. J. Phys. C: Solid State Phys. 8, 1301-1309.

Ryu, J.H., Gao, S., Dahlgren, R.A., and Zierenberg, R.A., 2002. Arsenic distribution, speciation and solubility in shallow groundwater of Owens Dry Lake, California. Geochimica et Cosmochimica Acta 66 (17), 2981–2994.

Singh, D.B., Prasad, G., Rupainwar, D.C., Singh, V.N., 1988. As(III) removal from aqueous solution by adsorption. Wat, Air, Soil Pollut. 42, 373.

Shih, M., 2005. An overview of arsenic removal by pressure-driven membrane processes. Desalination 172(1), 85-97.

Shipley H.J., Yean, S., Kan, A.T., and Tomson, M.B., 2009. Adsorption of arsenic to magnetite nanoparticles: effect of particle concentration, ph, ionic strength, and temperature. Environmental Toxicology and Chemistry, 28, (3), 509–515.

Tejedor-Tejedor, M.I., and Anderson, M.A., 1990. Protonation of phosphate on the surface of goethite as studied by CTR-FTIR and electrophoretic mobility. Lanngmuir 6, 602–611.

Wang, Y., Morin, G., Ona-Nguema, G , Menguy, N., Juillot, F., Emmanuel Aubry, E., Guyot, F.O., Calas, G., Brown G.E., 2008. Arsenite sorption at the magnetite–water interface during aqueous precipitation of magnetite: EXAFS evidence for a new arsenite surface complex. Geochimica et Cosmochimica Acta 72, 2573–2586.

Wagner, C.D., Riggs, W.M., Davis, L.E., Muilenberg, G.E., 1979. Handbook of x-ray photoelectron spectroscopy. Perkin-Elmer Corporation, Physical Electronics Division, Eden Prairie, MN.

Wagner, C.D., Zatko, D.A., and Raymond. R.H., 1980. Use of the oxygen KLL Auger lines in identification of surface chemical states by electron spectroscopy for chemical analysis. Anal. Chem. 52: 1445–1451.

Yassi, A. and Nieboer, E., 1988. Carcinogenicity of Chromium compounds. IN: Chromium in the Natural and Human Environments (J.O. Nriaguand E. Nieboer,editors): 443-496.

Yean, S., Cong, L., Yavuz, C.T., Mayo, J.T., and Yu, W.W., 2005. Effect of magnetite particle size on adsorption and desorption of arsenite and arsenate. J. Mater. Res. 20 (12).

List of Tables

Table 3.1: Comparison of adsorption isotherms for As(III) and As(V) adsorption by magnetite-maghemite nanoparticles at room temperature.

Arsenic species	**pH**	Correlation coefficient for different isotherms, R^2	
		Langmuir	Freundlich
As(III)	5	0.96	0.97
As(V)	5	0.98	0.98

Table 3.2: Binding Energies and relative content of As, C and O in adsorbents.

Valence state	Sample	Elemental Oxidation State	Binding energy (eV)	Peak Area (%)	FWHM
As 3d	As(III) Loaded sorbent	As(III) (As_2O_3)	44.69	0	1.5
		As(III) (As_2O_3)	44.0	68.9	1.5
		As(V) (As_2O_5)	45.89	0	1.5
		As(V) (As_2O_5)	45.2	31.1	1.5
As 3d	As(V) Loaded sorbent	As(III) species (As_2O_3)	44.69	0	1.5
		As(III) (As_2O_3)	44.0	43.5	1.5
		As(V) (As_2O_5)	45.89	0	1.5
		As(V) (As_2O_5)	45.2	56.5	1.5
C Is	Fresh Magnetite-Maghemite Sorbent	O-C=O	288.87	6.1	0.98
		C-OH, C-O-C	286.30	13.9	1.31
		C=C, C-H	284.8	80.1	1.31
C Is	As (III) Loaded sorbent	O-C=O	288.62	12.7	1.38
		C-OH, C-O-C	286.30	12.6	1.39
		C=C, C-H	284.8	74.7	1.39
C Is	As (V) Loaded sorbent	O-C=O	288.35	12.6	1.9
		C-OH, C-O-C	286.30	10	1.5
		C=C, C-H	284.8	57.4	1.5

O 1s	Fresh Magnetite-Maghemite Sorbent	Metal Oxide (Fe-O)	529.86	70.7	1.13
O 1s	As (III) Loaded sorbent	Metal Oxide	530.03	75.2	1.32
O 1s	As (V) Loaded sorbent	Metal Oxide	529.83	74.5	1.74

Table 3.3: Multiplet peak positions, FWHM and areas used to fit the XPS data. Peak parameters were obtained from Grosvenor et al. 2004.

Sample Name	**Metal Oxide**	**Binding Energy (eV)**	**FWHM**	**Area (%)**
Magnetite-Maghemite Mixture	Maghemite (sat)	718.37	1.59	0.3%
	Maghemite	713.30	1.45	3.1
	Maghemite	711.80	1.45	7.4
	Maghemite	710.80	1.35	10.2
	Maghemite	709.80	1.25	10.2
	Fe(III) Magnetite	713.75	1.36	4.5
	Fe(III) Magnetite	712.55	1.36	9.4
	Fe(III) Magnetite	711.45	1.36	13.1
	Fe(III) Magnetite	710.35	1.36	14.5
	Fe(II) Magnetite	710.55	1.41	3.7
	Fe(II) Magnetite	709.45	1.21	11.1
	Fe(II) Magnetite	708.45	1.21	11.1

As(V) Loaded Sorbent	Maghemite (sat)	718.37	1.59	0.3
	Maghemite	713.11	1.45	5.3
	Maghemite	711.61	1.45	7.9
	Maghemite	710.61	1.35	17.0
	Maghemite	709.61	1.25	17.1
	Fe(III) Magnetite	713.74	1.44	3.5
	Fe(III) Magnetite	712.54	1.44	7.3
	Fe(III) Magnetite	711.44	1.44	10.2
	Fe(III) Magnetite	710.34	1.44	11.2
	Fe(II) Magnetite	710.54	1.79	2.9
	Fe(II) Magnetite	709.44	1.59	8.6
	Fe(II) Magnetite	708.44	1.59	8.6
As(III) Loaded Sorbent	Maghemite (sat)	718.69	2.32	0.8
	Maghemite	713.39	1.45	7.2
	Maghemite	711.89	1.45	16.9
	Maghemite	710.89	1.35	23.2
	Maghemite	709.89	1.25	23.2
	Fe(III) Magnetite	713.39	1.45	7.2
	Fe(III) Magnetite	712.56	1.44	4.0
	Fe(III) Magnetite	711.46	1.44	5.5
	Fe(III) Magnetite	710.36	1.44	6.1
	Fe(II) Magnetite	710.56	1.38	1.6
	Fe(II) Magnetite	709.46	1.18	4.9
	Fe(II) Magnetite	708.46	1.18	4.7

List of Figures

Figures

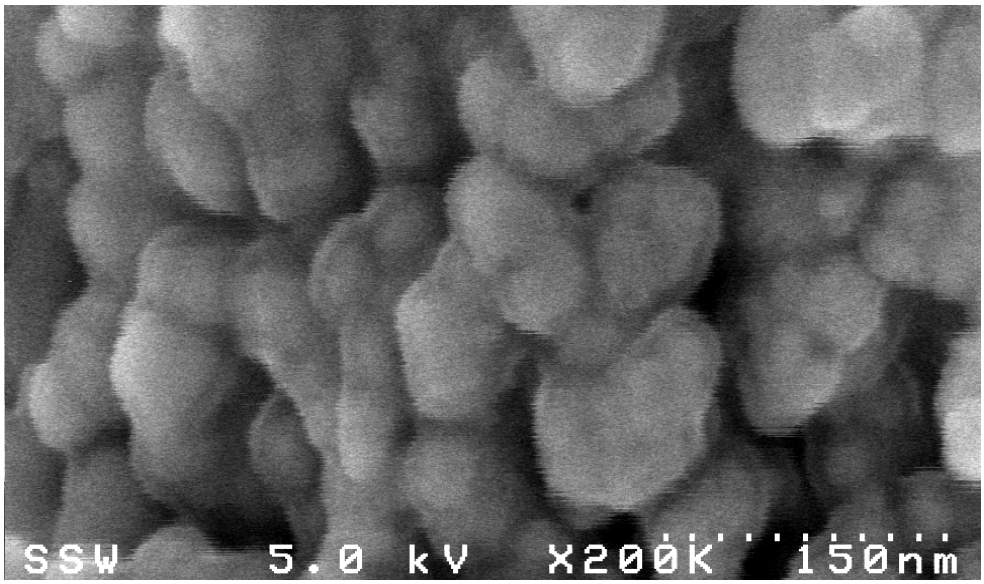

Figure 3.1: 200,000X magnification image of magnetite-maghemite nanoparticles (20-40 nm) using Hitachi S4500 scanning electron microscopy (SEM).

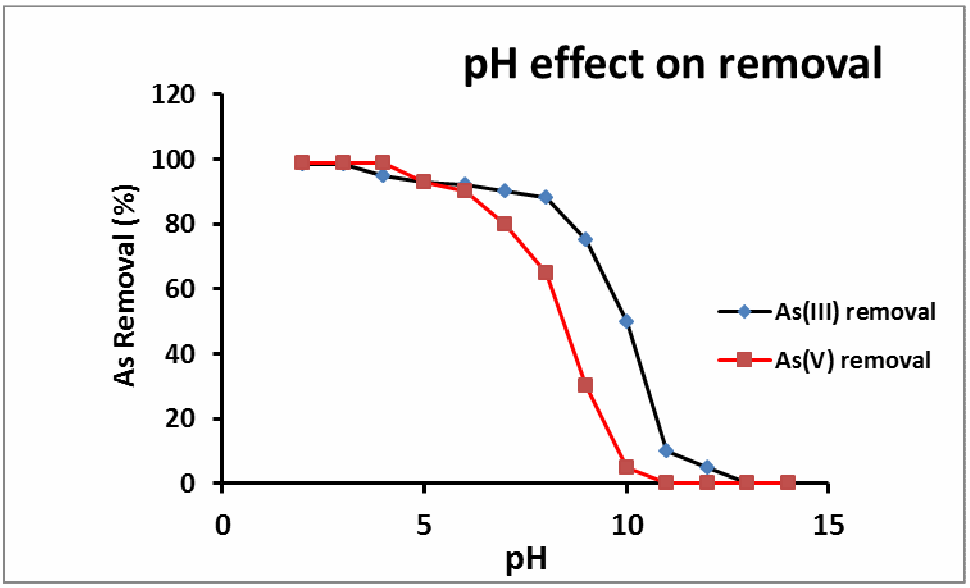

Figure 3.2: Effect of pH on the As(III) and As(V) removal by magnetite-maghemite nanoparticles. (Initial concentration for both arsenic: 1.5 mg/L, magnetite-maghemite nanoparticles dosage: 0.4 g/L and room temperature).

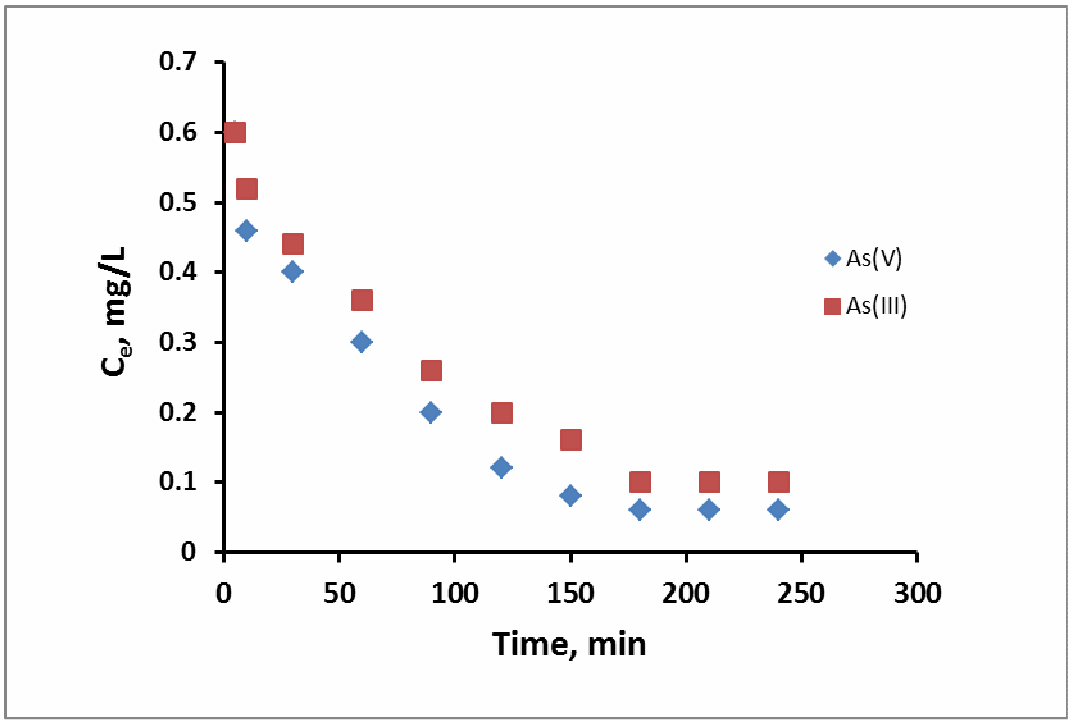

Figure 3.3: Effect of contact time on the adsorption of As(III) and As(V) removal by magnetite-maghemite nanoparticles at pH 6.5 and room temperature. (Initial concentration : 2 mg/L, Adsorbent concentration: 0.4 g/L)

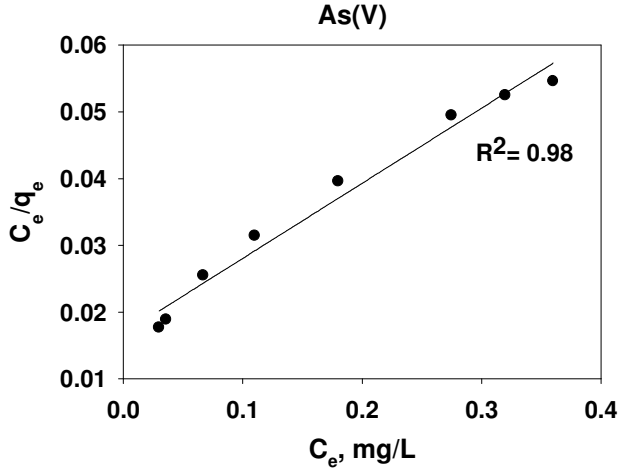

(a)

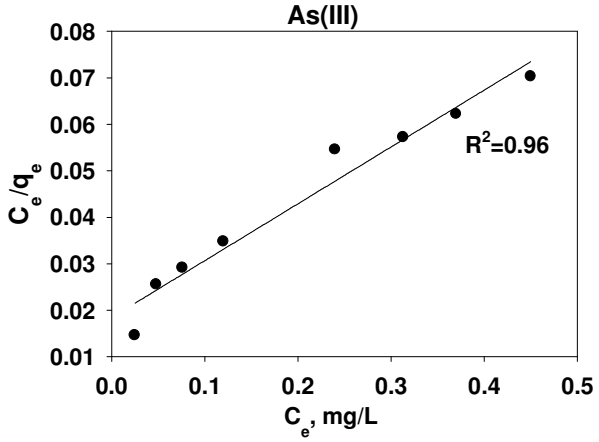

(b)

Figure 3.4: Langmiur isotherm plots for As(III) and As(V) adsorption by magnetite-maghemite nanoparticles (initial concentration: 0.5 – 3.5 mg/L; contact time: 24 hrs; pH = 5; magnetite-maghemite nanoparticles dosage: 0.4 g/L).

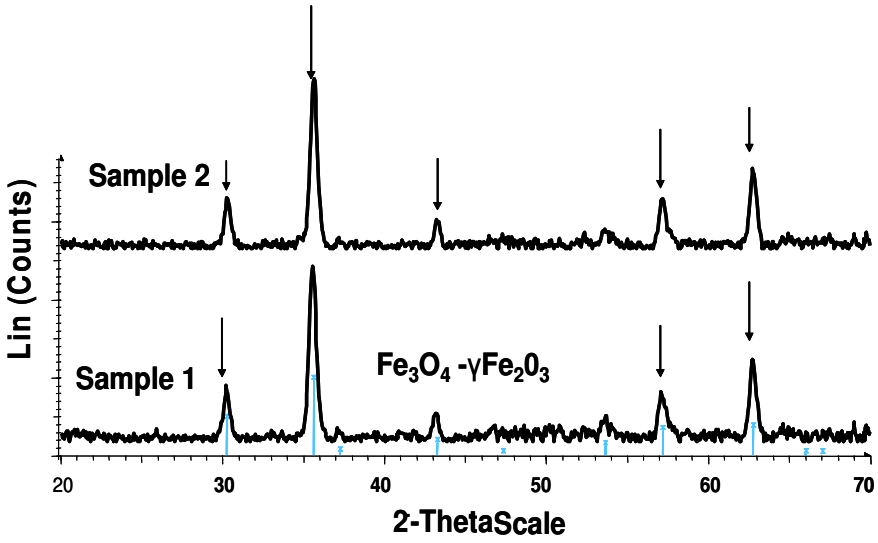

Sample 1 XRD patterns of magnetite-maghemite particles before adsorption

Sample 2 XRD patterns of magnetite-maghemite particles after adsorption

Figure 3.5: X-ray diffractograms showing magnetite-magheamite particles: sample 1 before arsenic(V) adsorption; sample 2 after arsenic(V) adsorption.

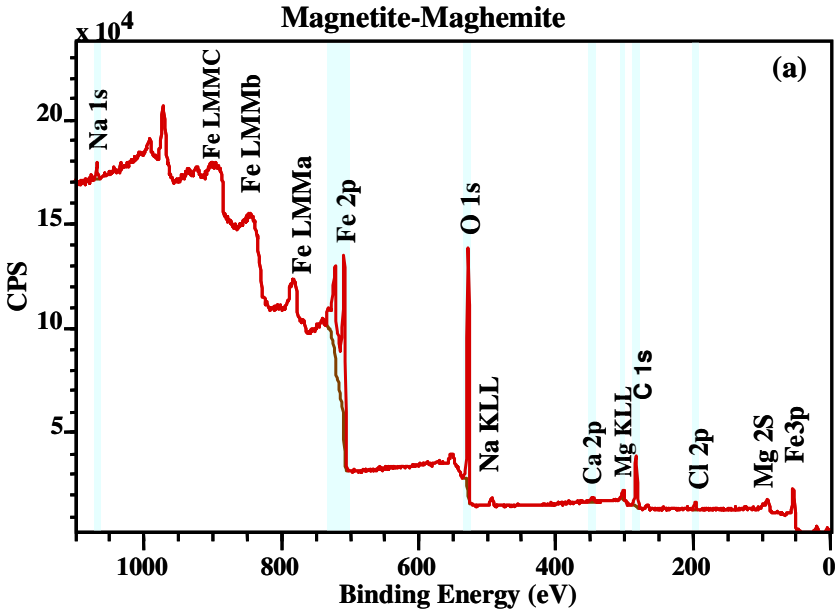
Magnetite-Maghemite
x 10^4
(a)
CPS
Binding Energy (eV)
Na 1s
Fe LMMC
Fe LMMb
Fe LMMa
Fe 2p
O 1s
Na KLL
Ca 2p
Mg KLL
C 1s
Cl 2p
Mg 2S
Fe3p

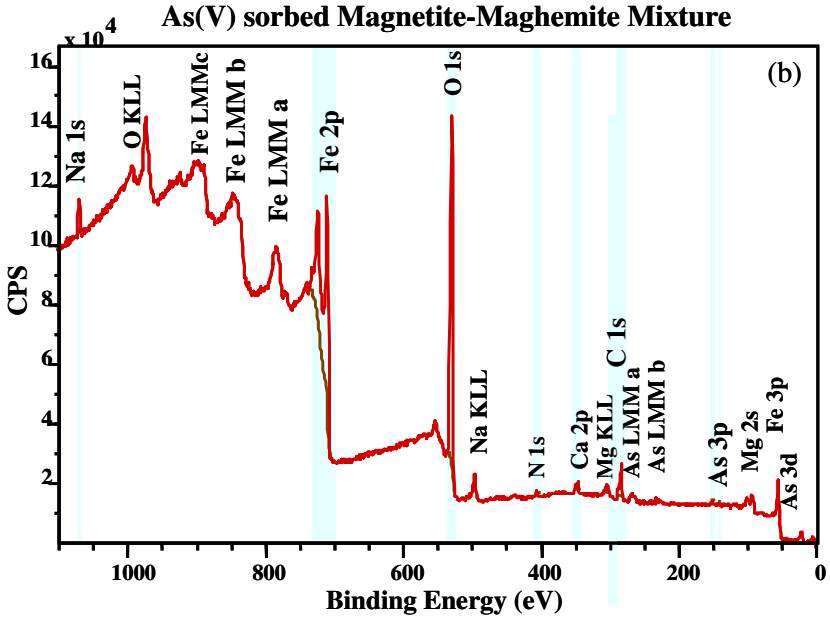
As(V) sorbed Magnetite-Maghemite Mixture
x 10^4
(b)
CPS
Binding Energy (eV)
Na 1s
O KLL
Fe LMMc
Fe LMM b
Fe LMM a
Fe 2p
O 1s
Na KLL
N 1s
Ca 2p
Mg KLL
As LMM a
C 1s
As LMM b
As 3p
Mg 2s
Fe 3p
As 3d

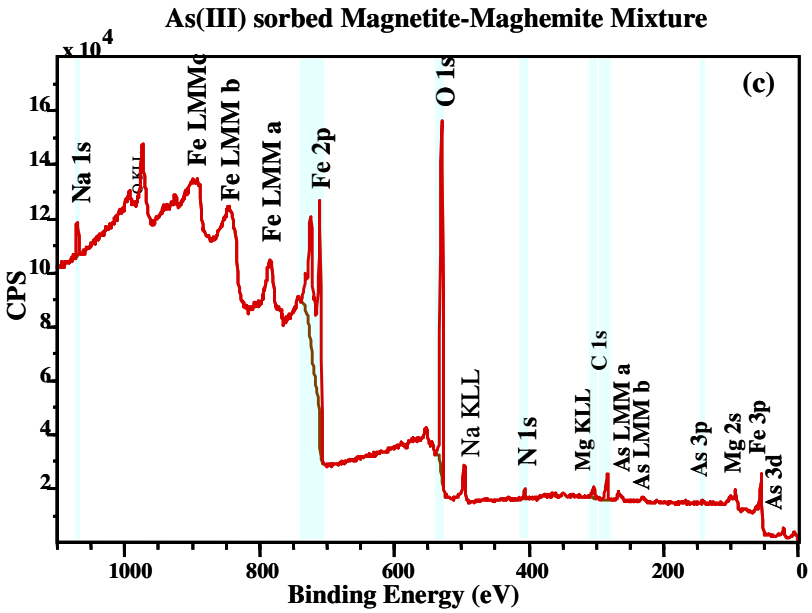

Figure 3.6: XPS wide scan spectra of the (a) fresh magnetite-maghemite mixture (b) As(V) loaded magnetite-maghemite mixture (c) As(III) loaded magnetite-maghemite mixture.

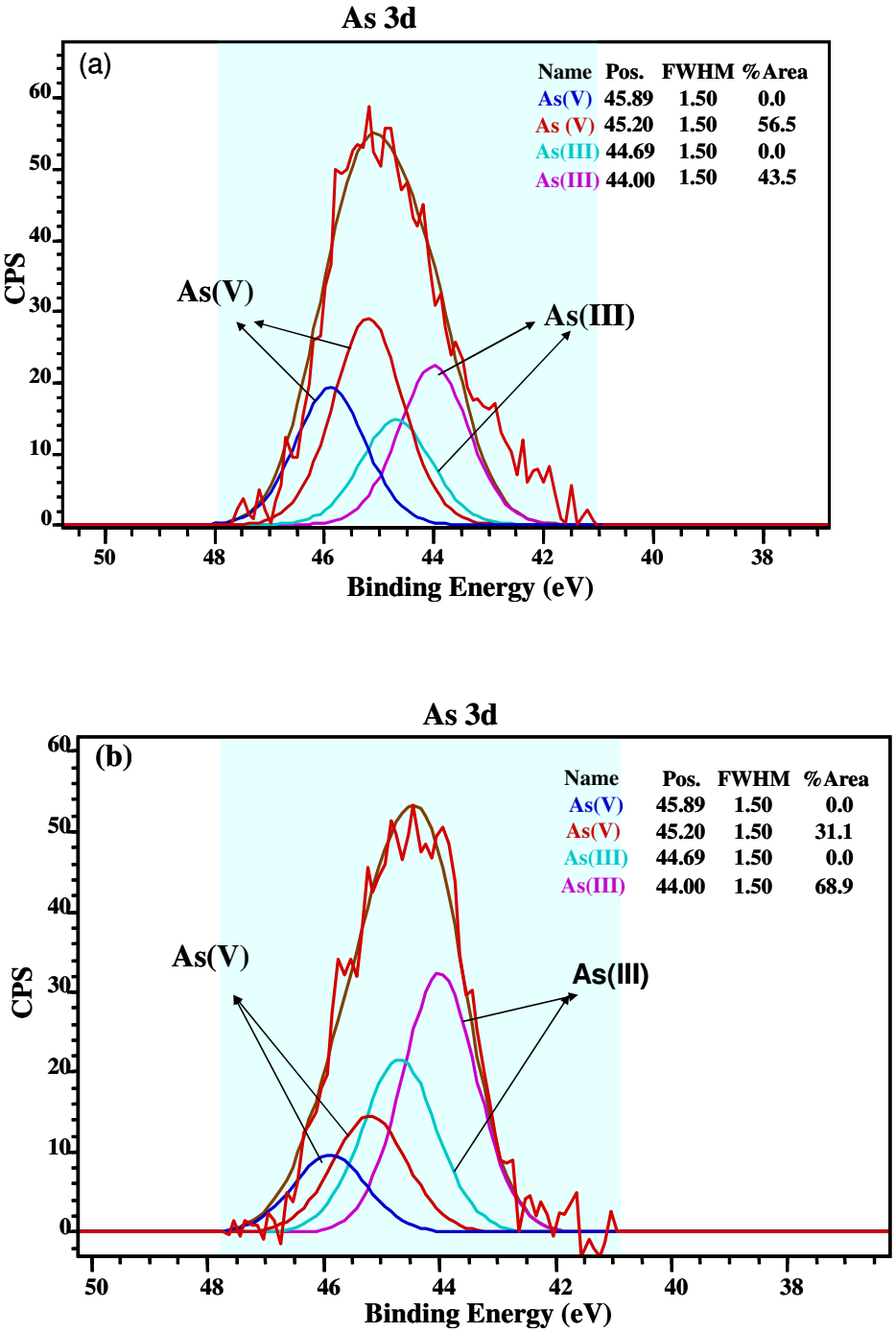

Figure 3.7: As 3d XPS spectra of (a) As(V) loaded (b) As(III) loaded magnetite-mghemite mixture. (state background subtracted in data).

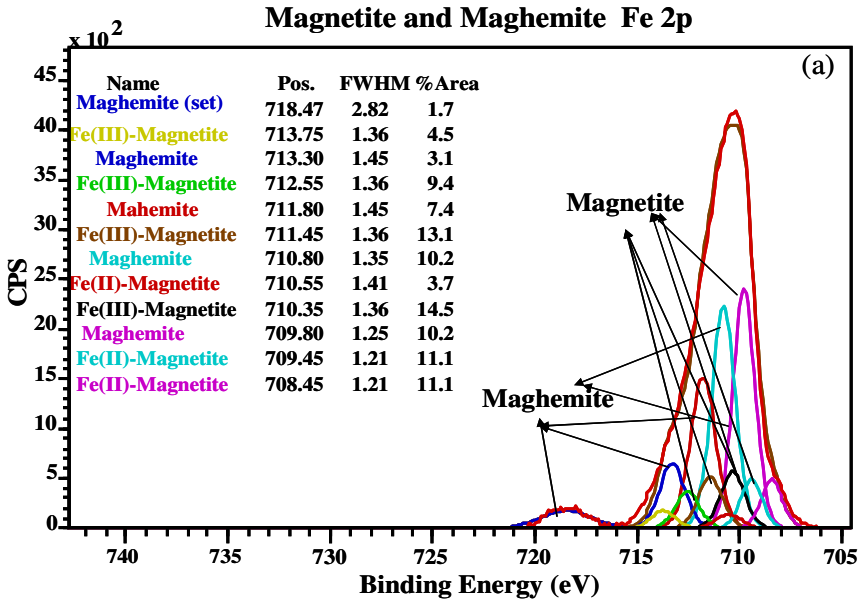
Magnetite and Maghemite Fe 2p
x 10^2
(a)
Name Pos. FWHM %Area
Maghemite (set) 718.47 2.82 1.7
Fe(III)-Magnetite 713.75 1.36 4.5
Maghemite 713.30 1.45 3.1
Fe(III)-Magnetite 712.55 1.36 9.4
Mahemite 711.80 1.45 7.4
Fe(III)-Magnetite 711.45 1.36 13.1
Maghemite 710.80 1.35 10.2
Fe(II)-Magnetite 710.55 1.41 3.7
Fe(III)-Magnetite 710.35 1.36 14.5
Maghemite 709.80 1.25 10.2
Fe(II)-Magnetite 709.45 1.21 11.1
Fe(II)-Magnetite 708.45 1.21 11.1
Magnetite
Maghemite
CPS
Binding Energy (eV)

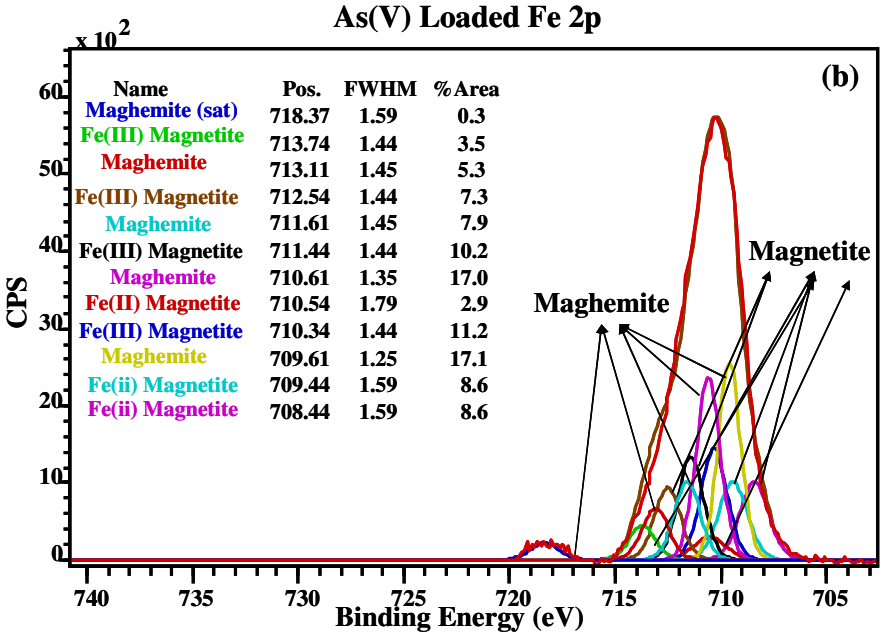
As(V) Loaded Fe 2p
x 10^2
(b)
Name Pos. FWHM %Area
Maghemite (sat) 718.37 1.59 0.3
Fe(III) Magnetite 713.74 1.44 3.5
Maghemite 713.11 1.45 5.3
Fe(III) Magnetite 712.54 1.44 7.3
Maghemite 711.61 1.45 7.9
Fe(III) Magnetite 711.44 1.44 10.2
Maghemite 710.61 1.35 17.0
Fe(II) Magnetite 710.54 1.79 2.9
Fe(III) Magnetite 710.34 1.44 11.2
Maghemite 709.61 1.25 17.1
Fe(ii) Magnetite 709.44 1.59 8.6
Fe(ii) Magnetite 708.44 1.59 8.6
Magnetite
Maghemite
CPS
Binding Energy (eV)

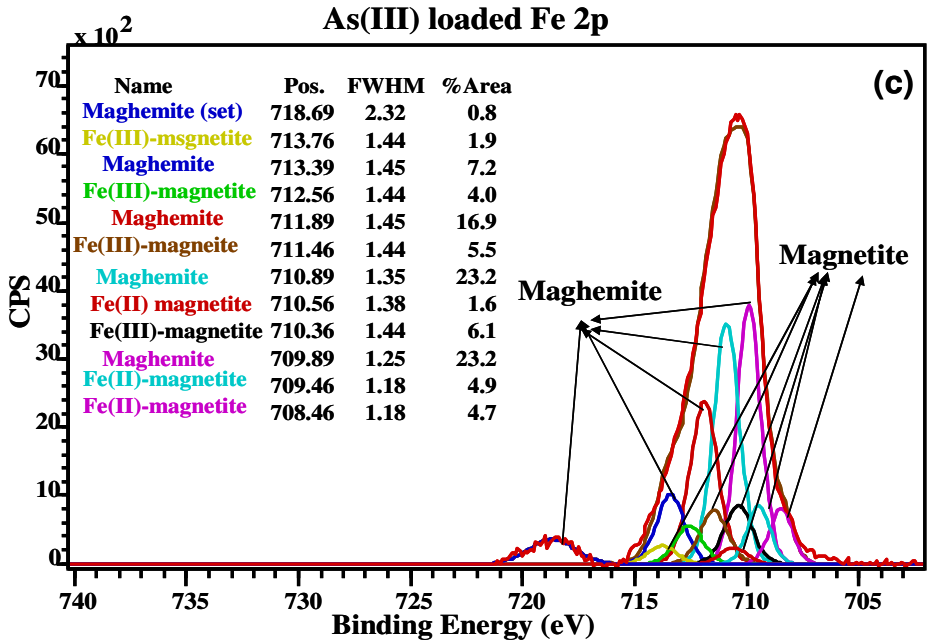

[a] Component information for each of the theoretically derived GS multiplets came from a digitized reproduction of the graphs found in the original paper (Fairley, 1999-2003).

Figure 3.8: XPS spectra (a) nanoscale magnetite-magheamite particles (b) As(V)-adsorbed magnetite-magheamite mixture particles at pH 5 and (c) As(III)- adsorbed magnetite-magheamite mixture particles at pH 5.

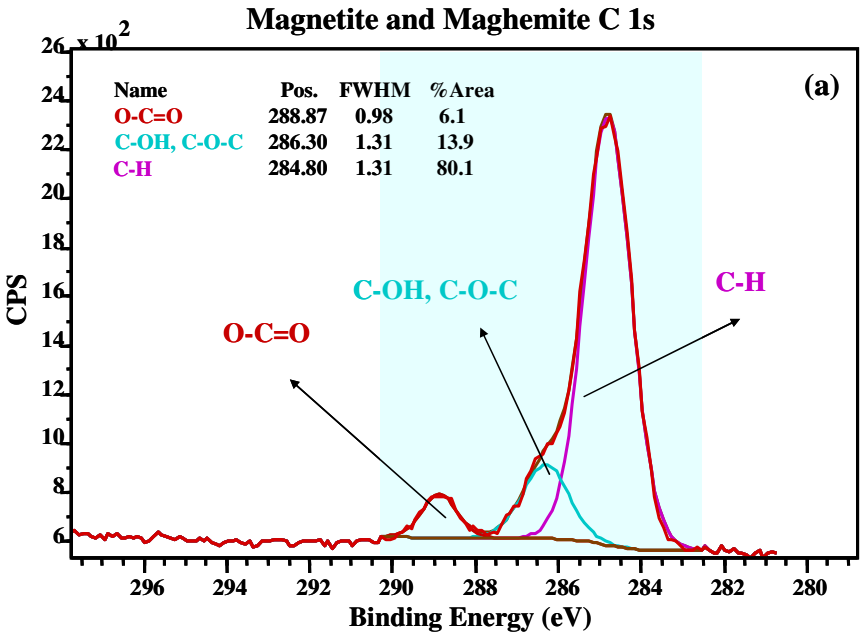
Magnetite and Maghemite C 1s
x 10^2
(a)
Name Pos. FWHM %Area
O-C=O 288.87 0.98 6.1
C-OH, C-O-C 286.30 1.31 13.9
C-H 284.80 1.31 80.1
O-C=O
C-OH, C-O-C
C-H
CPS
Binding Energy (eV)

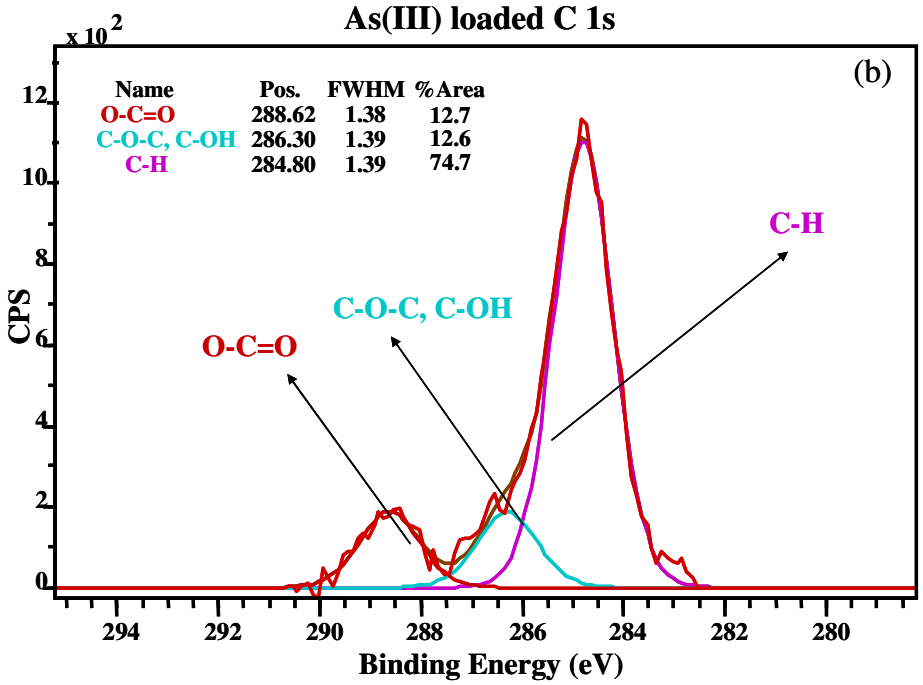
As(III) loaded C 1s
x 10^2
(b)
Name Pos. FWHM %Area
O-C=O 288.62 1.38 12.7
C-O-C, C-OH 286.30 1.39 12.6
C-H 284.80 1.39 74.7
C-H
C-O-C, C-OH
O-C=O
CPS
Binding Energy (eV)

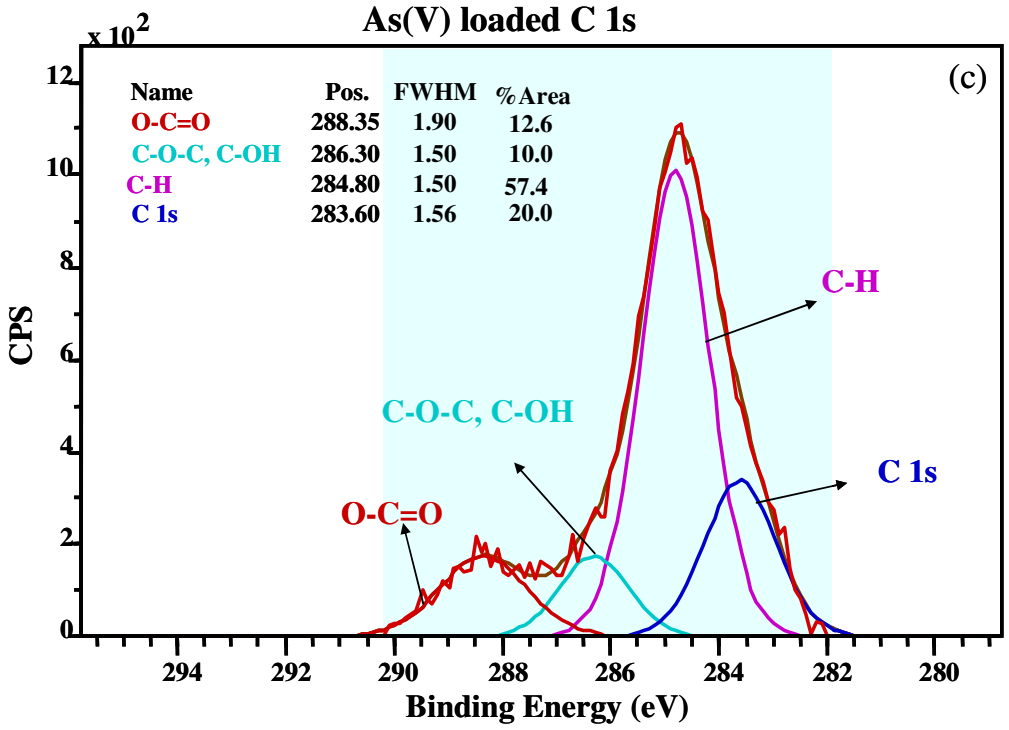

Figure 3.9: C 1s XPS spectra of (a) the pure sorbent (b) As(III) loaded (c) As(V) loaded magnetite and maghemite mixture.

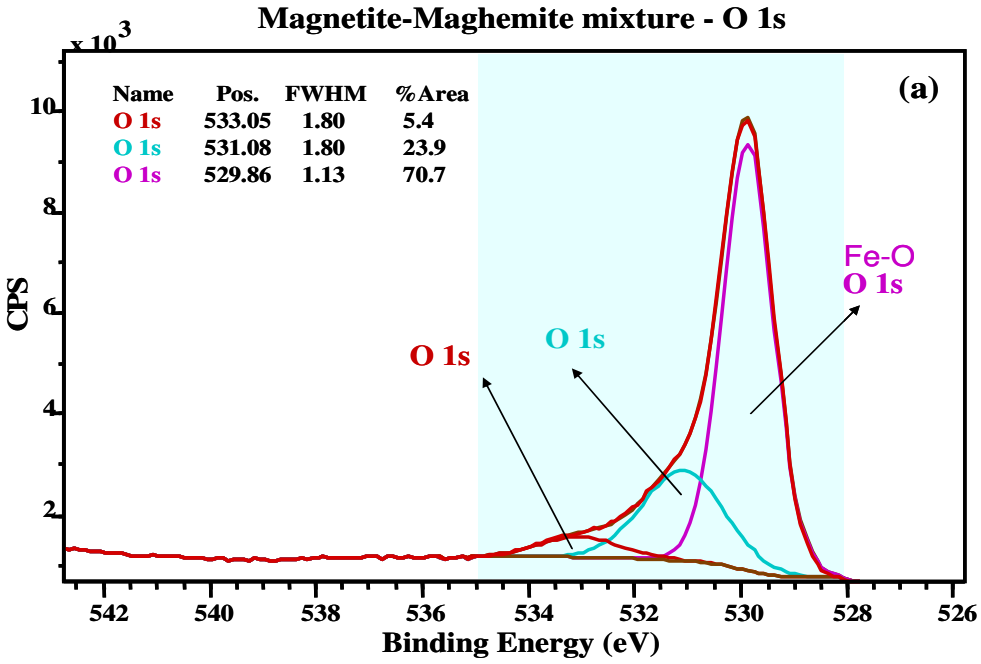
Magnetite-Maghemite mixture - O 1s
x 10^3
Name Pos. FWHM %Area
O 1s 533.05 1.80 5.4
O 1s 531.08 1.80 23.9
O 1s 529.86 1.13 70.7
(a)
Fe-O
O 1s
O 1s
O 1s
CPS
Binding Energy (eV)

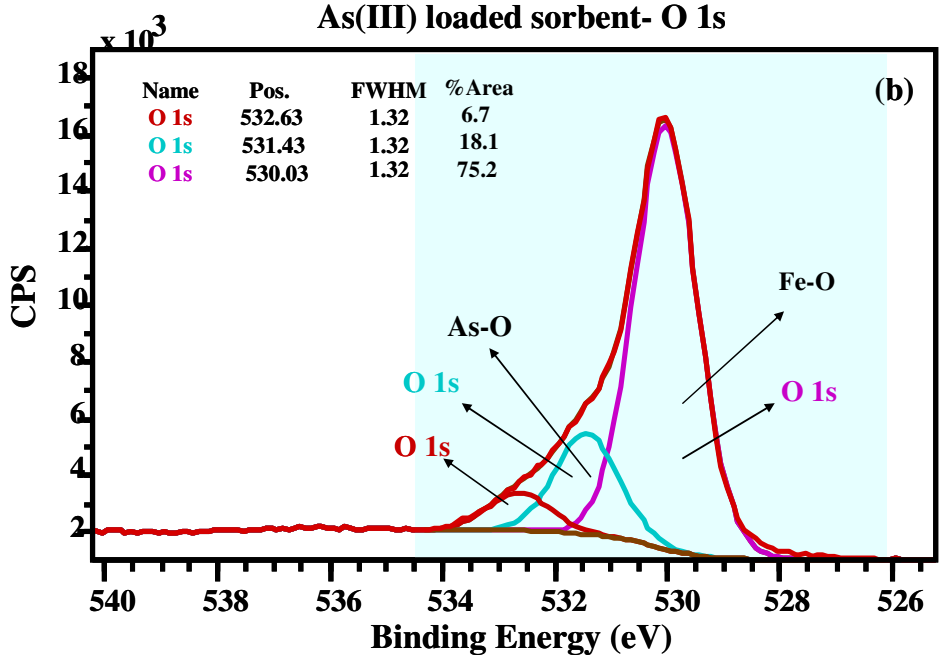
As(III) loaded sorbent- O 1s
x 10^3
Name Pos. FWHM %Area
O 1s 532.63 1.32 6.7
O 1s 531.43 1.32 18.1
O 1s 530.03 1.32 75.2
(b)
Fe-O
As-O
O 1s
O 1s
O 1s
CPS
Binding Energy (eV)

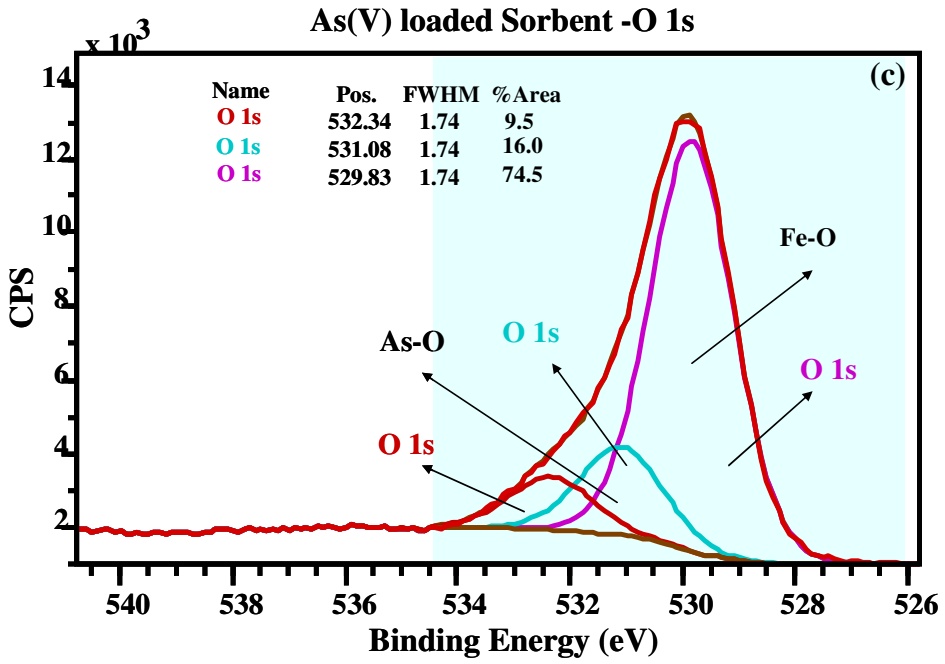

Figure 3.10: O 1s spectra of (a) the fresh magnetic-maghemite sorbent and (b) arsenite loaded sorbent (c) arsenate loaded sorbent at pH 5.

CHAPTER 4

CHEMICAL STATES IN XPS AND RAMAN ANALYSIS DURING REMOVAL OF CR(VI) FROM CONTAMINATED WATER BY MIXED MAGHEMITE–MAGNETITE NANOPARTICLES

4.1 Introduction

Chromium is extensively used for electroplating, leather tanning and corrosion protection and is found widely in groundwater in North America and elsewhere (Blowes, 2002). Naturally occurring chromium results primarily from the weathering of chromite and other chromium bearing minerals present in bedrock and soil (Blowes, 2002 and Nriagu et al. 1988). Uncontrolled dumping of chromium containing waste stream leached into the subsurface and finally reached aquifers. Studies have shown that most chromium contamination is due to human activities. Cr(III) is the most common type of naturally occurring chromium, but it is basically immobile in the aqueous environment, with natural waters having only traces of chromium unless the pH is very low. Chromium is present in the Cr(VI) state under strong oxidizing conditions and is found as chromate. Chromium occurs in oxidation states ranging from + 6 to -2. However, only the +6 and +3 oxidation states are commonly encountered in the natural environment. Cr(VI), a hazardous material, is found in solution as monomeric ions $H_2CrO_4^0$, $HCrO_4^-$ (bichromate), and CrO_4^{2-} (chromate), or as the dimeric ion $Cr_20_7^{2-}$ (dichromate) (Palmer et al. 1991 and Richard et al. 1991). According to Dupont and Guillon (2003), Cr(VI) species are highly toxic agents that are corrosive to the flesh and act as carcinogens,

mutagens, and teratogens in biological systems. Singh et al. (1993) noted that the toxicity of Cr(VI), a hazardous material, is higher than that of Cr(III), probably due to the increased solubility of Cr(VI) species compared to Cr(III).

A variety of techniques have been developed for the removal of chromium compounds from industrial wastewater. Among all removal technologies, adsorption processes are the most promising for the removal of this hazardous element from water and wastewater. Different iron oxides and hydroxides (for example, goethite, hematite, maghemite and magnetite) have been used as the metal adsorbent (Singh et al. 1993 and Cornell et al. 2003). Previous research (Pratt et al. 1997; Blowes et al. 2003 and Astrup et al. 2000) has shown that the removal of Cr(VI) by Zero-Valent Iron (ZVI) (Fe^0) is achieved by a coupled reduction–oxidation reaction followed by precipitation as $Cr(OH)_3$, Fe(III)–Cr(III) hydroxide and Fe(III)–Cr(III) oxyhydroxide. However, highly reactive properties, improper handling during application and toxicity of nano Zero-Valent Iron (nZVI) limit the potential uses of nZVI for site remediation (Zhou et al. 2009). These authors further reported that nZVI produces free radicals through the transformation process and free radicals are highly reactive, unstable molecules that are in need of an additional electron for stabilization. Because of this, they can affect antioxidant enzymatic activities, peroxidation of membrane lipids, modification of nucleic acids, and eventually cause cell death and tissue injury. If nZVI particles are directly introduced to lakes or streams for surface water remediation; there would be a higher risk of exposure to wildlife through consumption and respiration. According to Gavaskar et al.(2005), when assessing the pros and cons of using nZVI for remediation, the toxicity of the potential by-products

needs to be considered. If the contaminant cannot be completely degraded and the by-products are a greater environmental concern than the original target contaminant, then using nZVI might not be the best solution for remediation. There is published evidence that nZVI particles may be more toxic than nanoscale iron oxide (Phenrat et al. 2009). For example, Phenrat et al (2009) showed that oxidative stress increases in rodent (BV2) microglia of the following order: fresh nZVI > aged nZVI (11 days)> magnetite = surface-modified nZVI. These researchers reported that fresh nZVI produced morphological evidence of mitochondrial swelling and apoptosis. Thus, iron oxide is less toxic than nZVI.

According to Cornell et al. (2003), magnetite is one of the most abundant and widespread iron oxides found in diverse geological environments. These authors reported that maghemite occurs in soils as a weathering product of magnetite. Thus the association of the two minerals in nature is very common. Magnetite is known to undergo the following phase transitions with temperature increase to finally generate hematite (Faria et al. 1997).

$$Fe_3O_4 \xrightarrow{200\,^{\circ}C} \gamma - Fe_2O_3 \xrightarrow{400\,^{\circ}C} \alpha Fe_2O_3$$

This equation indicates the transition of magnetite to hematite when temperature increases. Hu et al. (2006) reported that most adsorbents are highly porous materials, providing adequate surface area for adsorption. However, the occurrence of intra-particle diffusion can reduce the adsorption rate and available capacity, especially for macromolecules. Hu et al. (2006) further noted that the development of an adsorbent with a large surface area and appreciable diffusion resistance is very important in practical

engineering applications. Singh et al. (1993) reported that hematite removed Cr(VI) with a maximum removal of 97% at 40^0C, pH 2.7 and initial concentrations of 19.23 µmol/L Cr(VI) and 40 g/L hematite. They reported that the uptake of Cr(VI) increases as pH decreases. Petrova et al. (2011) observed that magnetite (Fe_3O_4), removed several aqueous contaminants, such as arsenic, chromium, uranium and carbon tetrachloride, in laboratory studies. According to Amin et al.(2010), magnetite surface in highly acidic media can be highly protonated and thus able to take up Cr(VI) in the anionic form, $HCrO_4^-$. Yuan et al. (2009) observed that, with a decrease in pH, magnetite surface becomes more positively charged and facilitates the attraction of negatively charged Cr(VI) anions.

Hu et al. (2004) showed that magnetite iron oxide adsorbed Cr(VI) species at acidic pH but the chromium was desorbed at high pH. Again, according to Hu et al. (2005) maghemite iron oxide can adsorb Cr(VI) from wastewater at low pH and maximum adsorption occurred at pH 2.5. Undoubtedly, the surface properties of iron oxides are key factors in the adsorption of chromium by magnetite-maghemite nanoparticles. According to Grosvenor et al. (2004), iron oxide films produced after short oxygen exposure times contained a mixture of magnetite (Fe_3O_4) and maghemite (γ-Fe_2O_3). The use of magnetite nanoparticles for chromium decontamination of water has been proposed based on its magnetic properties (Hu et al. 2004). In the acidic pH range, most chromium species in aqueous solution are negatively charged. Thus electrostatic attraction between magnetite-maghemite nanoparticles and metal species leads to the removal of chromium compounds from aqueous solution. Hu et al. (2004) reported that Cr(VI) adsorption by magnetite was a combination of electrostatic attraction and ligand exchange under various pH

conditions. Hu et al. (2005) noted that maghemite (γ-Fe_2O_3) can also reduce chromium concentration. These authors reported that electrostatic attraction is the key mechanism of chromium removal by maghemite from aqueous solutions and the process is highly dependent on initial concentration, pH, temperature and coexisting common ions. Hu et al. (2004)) noted that with the latest developments in nanotechnology, magnetite and maghemite nanoparticles have been successfully synthesized and have received significant attention in the solution of environmental problems, such as the remediation of contaminated soils. Hu et al. (2006) showed that the magnetite nanoparticles possess the advantages of large surface area, high number of surface active sites, and strong magnetic properties, which lead to high adsorption efficiency, high contaminant removal rates, and easy and rapid separation of adsorbent from solution via a magnetic field. Many researchers (Cornell et al. 2003 and Hu et al. 2005) showed 20-30% recovery of magnetite or maghemite from the portion that underwent electrostatic binding. According to Cornell et al. (2003), the desorption from magnetite and hematite in base solution was 20%.

The objective of the present study was to investigate Cr(VI) removal mechanisms from different water samples using a mixture of maghemite and magnetite, in batch experiments. The overall purpose was to investigate the performance of mixed maghemite-magnetite nanoparticles in Cr(VI) removal by examining adsorption kinetics, reaction mechanisms and associated thermodynamic parameters. This is one of the few recent studies that have investigated Cr(VI) removal from aqueous solution by mixed maghemite-magnetite nanoparticles. Most commercial grade ‘magnetite’ nanoparticles

employed in remediation work would likely be a mixture of magnetite and maghemite because of slight oxidation during handling and sampling. Although magnetite and maghemite may separately remove greater amounts of Cr(VI) from solution than the mixture [Hu et al 2006 and Petrova et al. 2011), it is probably more realistic and practical to investigate the removal efficiency of the mixture because of the common occurrence or association of the two minerals in nature. The identification of the chemical states of the adsorbed Cr using XPS and Raman analyses during the removal of Cr(VI) from aqueous solution by mixed maghemite–magnetite nanoparticles was another objective of this study.

4.2 Materials and Methods

4.2.1 Particle characterization

Commercially available 20-60 nm 'magnetite' particles were obtained from Reade Advanced Materials (Rhode Island, U.S.A.). Subsequent laboratory characterization prior to the adsorption studies, presented later in this paper, showed that the particles were actually a mixture of maghemite and magnetite nanoparticles. The surface area of the 20-60 nm mixed magnetite-maghemite particles was determined using the N_2 adsorption method and applying the Brunauer, Emmett, Teller (BET) equation and was found to have an average value of 49 m^2/g. The mixed maghemite-magnetite nanoparticles arrived in powder form in an airtight plastic bag. Further examination and characterization of the as-received sample showed that the maghemite and magnetite nanoparticles mixture were dispersed. They contained 99.9% pure 20-60 nm magnetite-maghemite particles that had

a black and spherical morphology and a bulk density of 0.8 g/cm^3. X-ray photoelectron spectroscopy analysis (Table 4.1) showed that the 'magnetite' was actually a mixed oxide, γ-Fe_2O_3-Fe_3O_4, consisting of 73.9% maghemite and 26.1% magnetite. In chapter 3, mixed magnetite-maghemite was used to determine the arsenic removal. Results showed that when magnetite was dominant in the mixtures, arsenic was successfully adsorbed. In this chapter, we used adsorbent to remove Cr(VI) from aqueous solutions when maghemite was dominant in the mixture particles. Figure 4.1 shows a 100,000X magnification image of the maghemite-magnetite nanoparticles (20-60 nm) obtained using a Hitachi S4500 scanning electron microscopy (SEM). A 100,000X magnification was also used to check surface porosity but the image did not show the presence of pores at 100,000X magnification and the mixture of magnetite and maghemite appeared to be highly uniform.

4.2.2 Sample Preparation

Certified reagent grade chemicals were used to prepare all solutions for the experiments without further purification. Solutions were prepared with de-ionized water. Glass volumetric flasks and reaction vessels were treated with 10% HNO_3 and rinsed several times with de-ionized water before use. Chromium(VI) stock solutions were prepared by dissolving a chromium oxide (CrO_3) salt in de-ionized water. For each stock solution, redox potential was measured using a WTW Multi 340i ORP electrode (Wellheim, Germany) to confirm the presence of the targeted Cr(VI) species.

0.4 g/L of maghemite-magnetite particles were added to a desired concentration of stock (Cr) solution in 2000 mL plastic bottles. Solutions were prepared with de-ionized water. Standard acid (0.1 M HNO_3) and base (0.1 M NaOH) solutions were used for pH adjustment. The pH of each solution was measured using an Orion combination electrode. In the batch test, Cr concentrations were kept in the range of 0.5- 4 mg/L.

4.2.3 Adsorption Experiments

Batch experiments were performed for complete adsorption on the maghemite-magnetite mixture. The mixture was dispersed in solution in a sonication bath for 20 min. A known amount of Cr(VI) stock solution (in the range of 0.5 - 3.5 mg/L) was mixed with maghemite-magnetite mixture and held in a slowly rotating rack shaker that provided a gentle end-over-end tumbling (28 rpm) for 24 hr. After shaking, the mixtures were centrifuged at 5000 rpm for 30 min. The supernatant solutions were separated and solid samples were dried in a vacuum desiccator. Then dried Cr adsorbed maghemite-magnetite nanoparticles were kept in an airtight ceramic dish to prevent any reaction with air. The supernatant solutions were filtered through 0.2 µm Nalgene Surfactant-Free Cellulose Acetate (SFCA) syringe filters (VWR International, Mississauga, Ontario, Canada). The pH of each solution was measured immediately after sampling for Cr measurements. The filtrate was acidified with 1% nitric acid. ICP-OES (inductively coupled plasma-optical emission spectroscopy) was used to measure chromium concentrations in the filtrate. The experiments were carried out in duplicate and the mean

values were considered. Blank samples used in the experiments showed no detectable Cr(VI) adsorption on the surface of the adsorbents.

4.2.4 Instrumentation for XPS and Raman Spectroscopy

A Kratos Axis Ultra XPS instrument was used to measure all spectra. All samples were analyzed with a monochromatic A Kα X-ray source (15 mA, 14 KV) using analysis chamber pressures of 10^{-7}-10^{-6} Pa. The resolution function of the instrument was found to be 0.35 eV using silver Fermi edge (Grosvenor et al., 2004). The charge neutralizer filament was used during all experiments to control charging of the samples. The conditions applied for the survey scans were as follows: energy range =1100–0 eV, pass energy =160 eV, step size = 0.7 eV, sweep time = 180 s and x-ray spot size = 700 * 400 μm. An energy range of 40–20 eV was used for the high-resolution spectra, depending on the peak being examined, with a pass energy of 10 eV and a step size of 0.05 eV. The sampling volume of the XPS for the sample (a 10 nm depth of penetration and a slot of 700 microns by 160 microns) was approximately 100 cubic microns. All dried samples were introduced into the spectrometer via a glove box. The glove box was filled with N_2 (g) or Ar (g) so as to minimize the chance of the samples reacting with air or airborne impurities. Dried mineral samples were fractured in a vacuum so that fresh and clean faces were present during analysis.

Raman spectrum was obtained with a Renishaw Model 2000 Raman Spectrometer system equipped with a 633 nm He-Ne laser. Laser Raman spectroscopy is dependent on a

change in the polarization of a molecule to produce Raman scattering. The sampling volume for the Raman is approximately 40,000 cubic microns. In this study, the Cr-sorbed iron oxides were immediately transferred to a Teflon®-faced butyl rubber septum; and a cap was added and tightened. The sample was analyzed in macro mode with a laser spot size on the order of tens of microns with an approximate laser power of 1 mW at the sample. When a beam of photons strikes a molecule, the photons are scattered elastically (Rayleigh scattering) and inelastically (Raman scattering) generating Stokes and anti-Stokes lines. Raman spectra are expressed in wave numbers which have units of inverse length. In macro mode, samples used in the Raman are much larger volume than the XPS, on the order of 40 times.

4.3. Results and Discussion

4.3.1 Effect of pH on adsorption

The dependence of metal adsorption on pH can be clarified from the perspective of surface chemistry in an aqueous phase. The surfaces of metal oxides are generally covered with hydroxyl groups that vary in form at different pH levels. The surface hydroxyl groups from the adsorption of water or from structural OH are the functional groups of iron oxides. These groups have a double pair of electrons together with a dissociable hydrogen atom which can help them to react with both acids and bases. Charge on the iron oxide surface is generated by the dissociation (ionization) of the surface hydroxyl groups. This situation corresponds to adsorption or desorption of

protons depending on the pH of the solution. According to Cornell et al. (2003) magnetite generates Fe^{2+} and its hydrolysis products ($FeOH^+$, $Fe(OH)_2^0$, and $Fe(OH)_3^-$) depending on the solution pH. Cornell et al. (2003) further reported that acidity constant of magnetite (26.1% of used adsorbent), $pK_{a1,}$ is 5.6. Thus, at pH lower than 5.6, the dominant functional groups of iron oxide surface would be Fe^{2+} or $FeOH^+$. According to Cornell et al. (2003) for the most iron oxide the acidity constants, pKas, usually fall between 5 and 10 and generate Fe^{2+} , Fe^{3+} and its hydrolysis products ($FeOH^+$, $Fe(OH)_2^0$, and $Fe(OH)_3^-$) depending on the solution pH. Although the mixed maghemite- magnetite is made up of two types of iron oxides, the acidity constants of a specific surface group depend on the abundance of Fe^{2+} or Fe^{3+} and its hydrolysis products. Thus, the dominant functional groups of most iron oxide surfaces would be Fe^{2+} or $FeOH^+$ when solution pH is acidic; and $Fe(OH)_2^0$ and $Fe(OH)_3^-$) when solution pH is basic.

Thus iron oxide would attract negative Cr(VI) species at low pH. At higher pH, the surface hydroxyl groups on the iron oxide surface are $Fe(OH)_2^0$, and $Fe(OH)_3^-$. Thus negatively charged iron oxide surface would repel negatively charged Cr(VI) species at the higher pH value. Maghemite is formed through the oxidation of magnetite, therefore Fe(III) in solution would form hydrated ferric oxides (HFO) nanoparticles. Adsorption will keep Cr(VI) on the maghemite-magnetite surface through a Lewis acid base (LAB) interactions. According to Cornell et al.(2003), iron oxide surfaces coordinate with hydroxyl ions or water molecules which share their lone electron pair with Fe. Thus, surface Fe atoms are Lewis acids that react with Lewis bases (e.g. water). They further noted that the surface hydroxyl groups of the iron oxides are the chemically reactive entities at the surface of the solid in an aqueous environment possessing a double pair of

electrons that enables them to react with acid and bases. Figure 4.2 shows the equilibrium solute concentration of Cr(VI) in the solution after adsorption at different pH values indicating high pH dependency during Cr(VI) removal by mixed maghemite-magnetite particles. A maximum adsorption efficiency of 95 % was found at pH 2.5 and the adsorbed amount was 3.6 mg/g for an initial Cr(VI) concentration of 1.5 mg/L. The surface coverage on maghemite-magnetite by Cr(VI) was found to be 1.5 μmol/m^2 at 1.5 mg/L of initial Cr(VI) concentration. The amount of Cr(VI) removed from solution decreased with increasing pH and the removal efficiency was less than 60% at pH greater than 6 indicating more ready adsorption in the lower acidic pH range. The affinities of the maghemite-magnetite for the different species of Cr(VI) existing at acidic pH values, namely $H_2CrO_4^0$, $HCrO_4^-$, CrO_4^{2-}, and $Cr_20_7^{2-}$ (Candela et al. 1995) may be different, and attributed to the variation in removal efficiency at different pH values. Weng et al. (1997) reported that the adsorption free energy of $HCrO_4^-$ and CrO_4^{2-} is - 2.5 to - 0.6 and -2.1 to-0.3 kcal/mol, respectively. Optimum adsorption takes place at pH below 4 (Figure 4.2). Thus, $HCrO_4^-$ is more favourably adsorbed than CrO_4^{2-} at the same concentration because of lower adsorption free energy of $HCrO_4^-$. At lower pH, the removal of Cr(VI) is mainly due to the adsorption of $HCrO_4^-$, which is expected to be adsorbed in larger quantities than CrO_4^{2-} under the same adsorption affinity. Cr(VI) uptake decreased slowly because of the higher concentration of OH^- ions present in the adsorption process which competed with Cr(VI) species for the adsorption sites. When CrO_4^{2-} concentration is much higher than $HCrO_4$ at higher pH, the adsorption free energy of CrO_4^{2-} is lower, and only under such a circumstance can CrO_4^{2-} adsorption be more favourable than $HCrO_4^-$. Yean et al. (2005) showed from potentiometric titrations that the

surface of magnetite particles had a positive surface charge up to pH 6.8, a point of zero charge of 6.8 and a negative surface charge in the pH range 6.8-9.5. Santiago et al. (2012) reported that the point of zero charge for magnetite particles is dependent on the solution temperature and pH_{pzc} is decreasing from 7.1 to 6.53 when solution temperature is increased from 0 to 50^0C. Since the point of zero charge of iron oxides does not change significantly in the temperature range of 10-50^0C, the change in protonation/deprotonation (acidity) constants of the surface groups would be negligible.

According to Tuutijarvi et al. (2009) maghemite has a point of zero charge at pH_{pzc} 7.5 and the more acidic the condition the more positive was the surface charge of the adsorbent and, accordingly, the more attractive to negative Cr(VI) species. Thus, mixed maghemite-magnetite particles can adsorb either negatively or positively charged species by electrostatic attraction depending on pH.

4.3.2 Temperature and the retention time

The removal rates of Cr(VI) at different temperatures are shown in Figure 4.3. For an initial Cr(VI) concentration of 1.5 mg/L, equilibrium was achieved after 2 hr when experiments were run at pH 4. In the study by Hu et al. (2005) involving magnetite, adsorption equilibrium was achieved in 1 hr. At equilibrium, the removal efficiencies of Cr(VI) by maghemite-magnetite nanoparticles at the initial Cr(VI) concentrations of 1.5 mg/L were 69 % to 91% in the temperature range of 10-50^0C.

The rapid metal uptake by maghemite-magnetite nanoparticles may be attributed to external surface adsorption, which is different from microporous adsorption. Since nearly all the sorption sites of mixed maghemite-magnetite nanoparticles exist in the exterior of the adsorbent compared to the porous adsorbent, it is easy for Cr(VI) species to access these active sites, thus resulting in a rapid approach to equilibrium (Singh et al. 1993). In addition, the adsorption of Cr(VI) on the maghemite-magnetite mixture may involve two steps. First, Cr(VI) species migrate from the bulk fluid phase to the outer particle surface of the adsorbent for contact (film diffusion) (Singh et al. 1993). Second, there might be electrostatic attraction or reaction occurring between adsorbate (Cr(VI) species) and adsorbent (Singh et al. 1993).

4.3.3 Adsorption isotherms and thermodynamic parameters

The experimental data found at pH 4 were used in the linearized forms of the Langmuir isotherm [Eq. (4.1)] to estimate adsorption parameters and to describe the nature of adsorption of Cr(VI) on maghemite-magnetite nanoparticles .

$$C_e/q_e = 1/bq_m + C_e/q_m \qquad (4.1)$$

where C_e and q_e are equilibrium solute concentration (mg/L) and equilibrium adsorbed concentration (mg/g), respectively. The terms q_m and b represent the adsorption maxima or adsorption capacity (mg/g) and energy of adsorption, respectively. These adsorption parameters may be used in future modelling and scale up studies. Figure 4.4 presents Langmuir plots for Cr(VI) adsorption by maghemite-magnetite nanoparticles. As

indicated, the data (R^2 values of 0.95 to 0.99) show that adsorption by maghemite-magnetite nano-particles is well described by the Langmuir isotherm. Figure 4.4 also shows that Cr(VI) adsorption increases with an increase in temperature. The maximum Cr(VI) removal was found to be 95%, 87% and 78% at the temperature of 50, 22 and 10^0C respectively (Fig. 4.4) when initial concentration was 0.5 mg/L Again, when the initial Cr(VI) concentration was 3 mg/L in Figure 4.4, the maximum removal achieved was 78%, 66% and 45% at the temperature of 50, 22 and 10^0C respectively. Thus, initial concentration also shows influence on removal efficiency. Gupta et al. (1978) noted that Langmuir adsorption is a reversible phenomenon and that the coverage is monolayer with a finite number of adsorption sites. These authors further reported that once a site is filled, no further sorption can occur at that site as long as the surface reaches a saturation point.

In order to calculate the adsorption efficiency, the dimensionless equilibrium parameter was determined from the following equation:

$$r = 1/(1+ bC_0) \qquad (4.2)$$

where r is a dimensionless separation factor, C_0 is the initial Cr(VI) concentration (mg/L) and b is the Langmuir isotherm constant (L/mg). A value of $r < 1$ represents favourable adsorption and a value greater than one represents unfavourable adsorption (Mckay et al.1985). In the present study, calculated values of r for all initial concentrations of Cr(VI) were found to be less than 0.5 at the investigated temperatures.

According to Altundogan et al. (2000), standard Gibbs free energy (ΔG^0), standard enthalpy (ΔH^0) and standard entropy changes (ΔS^0) for the adsorption process may be calculated from Eqs. (4.3)-(4.5):

$$\text{Ln}(1/b) = \Delta G^0 / RT \qquad (4.3)$$

$$\text{Ln } b = \text{Ln } b_0 - \Delta H^0 / RT \qquad (4.4)$$

$$\Delta G^0 = \Delta H^0 - T\,\Delta S^0 \qquad (4.5)$$

where b is Langmuir constant which is related to the energy of adsorption, b_o is a constant, R is the ideal gas constant (8.314 J mol^{-1} K^{-1}) and T is temperature (K). A negative value for ΔG^0 indicates spontaneous adsorption and a positive entropy change (ΔS^0) suggests structural changes in adsorbate and adsorbent (Altundogan et al. 2000 and Sawyer et al. 1994). In the present study, the negative ΔG^0 values obtained for Cr(VI) adsorption on maghemite-magnetite nanoparticles (Table 4.2) confirm the feasibility and spontaneous nature of adsorption. The effect of temperature on the removal rate of targeted contaminants is an important design-consideration for field applications because the temperature of groundwater or wastewater in field applications is generally lower or higher than the room temperature of laboratory experiments. In this study, the calculated value, ΔH^o, are about 9.0 Kj mol^{-1} using equation (4.3)-(4.4). The positive value of ΔH^o reflects the chemical changes that accompany heat absorption during adsorption i.e. endothermic adsorption (Dash et al. 2007), which explains why elevated temperature led to enhanced Cr adsorption onto the surfaces of mixed iron oxides. Elevated temperature might also have increased the kinetic energy of anion species so that they could be

transported easily to adsorption sites (Dash et al. 2007). Thus, as shown in Table 4.2, it can be concluded that the adsorption of Cr(VI) on maghemite-magnetite nanoparticles was highly favorable at the concentrations and temperatures studied. In this study, the decrease in free energy change with the rise in temperature shows increased feasibility of adsorption at increasing temperatures (Altundogan et al. 2000).

The adsorption rate constant (k_{ad}) was estimated from the following first order rate equation:

$$\text{Log } (q_e - q_t) = \text{Log } q_e - (k_{ad}/2.303)*t \qquad (4.6)$$

Where q_e and q_t (both in mg g^{-1}) are the amount of Cr(VI) adsorbed per unit mass of mixed maghemite-magnetite at equilibrium and time, t, respectively, and k_{ad} is the rate constant (min^{-1}). A linear plot of log ($q_e - q_t$) versus time at different temperatures implies that the process is of the first order (Fig. 4.5). The values of k_{ad} at 10^0, 22^0 and 50 ^{0}C are found to be 0.014, 0.02 and 0.03 min^{-1} indicating better removal at higher temperature.

4.3.4 X-ray Photoelectron Spectroscopy (XPS) and Raman Analysis

The Cr-loaded maghemite-magnetite particles after Cr adsorption at a fixed pH were characterized using XRD (X-ray diffraction) and XPS (X-ray photoelectron spectroscopy) techniques. The results of XRD analysis (Fig. 4.6) demonstrate that identical peaks of the Cr-loaded particles match well with those of standard γ-Fe_2O_3-Fe_3O_4 and that no other crystalline post-adsorption phases were present. However, it is clear that the intensity of all peaks in Figure 6 decreased after Cr adsorption. The peak

shift from 73^0 to 74^0 2θ (in Fig. 4.6) indicates the oxidation of magnetite to maghemite following Cr adsorption at the mixed maghemite-magnetite surface (Sadiq et al. 1988). The elemental composition and chemical oxidation states of surface and near-surface species were investigated using XPS. All spectra were drawn and analyzed using the Casa-XPS software (Fairley, 2003). XPS wide scan spectra of fresh maghemite-magnetite and Cr adsorbed maghemite-magnetite sorbents are illustrated in Figure 4.7. Three major peaks at binding energies of 282.25, 348.05, 527.25 and representing C 1s, Ca 2p, and O 1s, respectively, are observed for the virgin sorbent (Figure 4.7a). Significant changes can be seen in Figure 4.7b after Cr(VI) adsorption; the peak at binding energy of 583.05 eV for Cr 2p appears in the Cr(VI) loaded sorbent.

The Fe 2p high resolution spectra were fitted following the example of Pratt et al. (1994) using theoretical multiplet peak (Gupta and Sen, 1975). The peak full width at half maximum (FWHM) was generally held to be between 1.0 and 3.3 eV. The XPS results, shown in Fig 4.8, present the theoretical multiplet peaks for iron and chromium adsorbed iron at the surface of the Fe_3O_4 and γ-Fe_2O_3 mixture. Theoretical multiplet analysis of the γ-Fe_2O_3- Fe_3O_4 mixture gave 73.9% of maghemite and 26.1% of magnetite (Fig. 4.8a). No sharp hematite peak was observed in the XPS spectra. After Cr(VI) adsorption on the maghemite-magnetite mixture, it was found that the percent of maghemite increased to 88.7% (Fig 4.8b). At the same time, the percentage of magnetite was reduced (Fig. 4.8b). Thus, the results suggest that a redox reaction occurred on the mixed maghemite-magnetite surface when Cr(VI) was introduced. Changes in the relative abundance of Fe(II) and Fe(III) in magnetite and maghemite spectra (Fig. 4.8a and 4.8b) upon Cr(VI)

adsorption are quantitatively elucidated in Table 4.1. The data show that in magnetite spectra, the relative content of the Fe(III) and Fe(II) decreases from 17.9 to 20.1 % for Fe(III) and 8.2 to 3.6 for Fe(II) indicating the reduction of magnetite in the mixture particles. This indicated oxidation on the mixed oxides surface as well as an increase in the amount of maghemite from 73.9% to 88.7%. Figure 4.9 shows the difference in Fe $2p_{3/2}$ spectra between maghemite-magnetite particles and Cr(VI)-adsorbed maghemite-magnetite particles at pH 4.0. The spectra have been background subtracted, normalized and then subtracted from fresh adsorbent to Cr(VI)-adsorbed absorbent. Figure 4.9 clearly shows that the intensity of the peak decreased after Cr adsorption and that the peaks before and after reaction of Fe $2p_{3/2}$ were not the same. The results also illustrate the decreased intensity and increased binding energy tendency when spectra have been subtracted from spectra before and after Cr(VI) adsorbed spectra. This also supports the explanation of reaction mechanism provided in this study.

The Cr 2p spectrum of the Cr(VI) adsorbed sorbent can be deconvoluted into four individual component peaks, which originate from the Cr(III) atom and overlap on each other. Table 4.3 shows binding energies and relative content of chromium in mixed maghemite-magnetite adsorbents. According to Moulder et al. (1992), the Cr 2p peak for chromium oxides occur at binding energy ranges of 575 eV to 579 eV. Biesinger et al. (2011) observed that $FeCr_20_4$ peaks are found at binding energies of 575.9, 577.0 and 577.9 eV. As shown in Figure 4.10, the peaks at binding energies of 575.80 and 577.22 eV can be assigned to Cr(III) species. The compounds found at the peaks between 575 and 580 eV are Fe-Cr compounds. The results also demonstrate that magnetite was

oxidized to maghemite after the introduction of Cr(VI) into the solution; and at the same time, all Cr(VI) species were reduced to Cr(III) species (Fig. 4.10) on the mixed iron oxides surfaces. Pratt et al. (1996) observed that Cr(VI) has no multiplet structure. In the present study, there is no evidence of Cr(VI) presence in the Cr 2p data. The Cr 2p data has distinct structure and it matches remarkably well that of Cr(III). Thus, the adsorption mechanism of Cr(VI) onto Fe_3O_4-γ-Fe_2O_3 surface is suggested to be a physico-chemical reaction as well as electrostatic attraction at pH of 4. The amount of chromium used in the XPS spectrum analysis was very low (0.1-0.5 atomic percent) compared to the amount of iron detected (25-30 %), any iron-chromium complex contribution to the Fe 2p spectrum would be obscured by the large maghemite-magnetite signal.

To further confirm the interaction between oxide surface and the adsorbed anions and also specify the possible Cr species on the surface, Raman spectroscopy was applied to the same sample and the results are shown in Fig. 4.11. The shift of the main γ-Fe_2O_3-Fe_30_4 peaks at 1403, 1176, 699.1, 484.3, and 377 cm^{-1} is negligible; the presence of a new peak at 826.4 cm^{-1} is observed and the FWHM of this peak is likely on the order of 100 cm^{-1}. Weckhuysen et al. (1997) found Raman peaks for chromium compounds were located between 800 cm^{-1} and 1030 cm^{-1}. In agreement with Weckhuysen et al. (1997), the Raman peak at 826.4 cm^{-1} is interpreted to originate from a chromium species that formed as a result of reaction between chromate ions in solution and iron oxide nanoparticles. From Figure 4.12, it is clearly seen that a chromium compound signal exists on the iron oxide surface after subtraction of Cr adsorbed mixed maghemite-magnetite from fresh mixed maghemite-magnetite particles. Since the amount of

chromium used in the Raman spectrum analysis was very low compared to the amount of iron oxide, any iron-chromium complex contribution to the spectrum would be partially obscured by the large maghemite-magnetite signal. The reliable deconvolution of the peak at 826.4 cm^{-1} was complicated because it is very difficult to draw the small peaks due to the poor signal to noise ratio (Fig. 4.11b). Figure 12 illustrates Raman spectra showing the difference in spectrum between Cr(VI)-adsorbed maghemite-magnetite particles and fresh magnetite-maghemite mixture particles at pH 4.0. Spectra have been subtracted from Cr(VI)-loaded absorbent to fresh adsorbent.

With regard to the basic analysis parameters, both Raman and XPS have a similar minimum detection limit of approximately 1.0 - 0.25 weight percent. From the results of the present study, the Raman data have a very distinct chromium contribution (Fig. 4.11) and the XPS data have a very weak chromium contribution (Fig. 4.7). This difference in Cr peak intensity for the two methods can be explained through consideration of the analysis volume for each method. The XPS data originate from a layer no thicker than 4 nanometres of the surface of the nanoparticle mass, whereas the Raman data originate from both the surface and the bulk of the nanoparticle mass. These results show that the chromium has reacted with a large proportion of the nanoparticle population in the experiment. The weakness of the XPS Cr peak relative to the Raman Cr peak may also be an indication that not all of the Cr is found on the nanoparticle surface but that some is found below the nanoparticle surface. The implication of this interpretation is that, in addition to adsorption reactions, diffusion reactions also occurred during the experiment.

Faria et al. (1997) noted that the Raman spectrum of maghemite can be characterized by three broad structures around 350, 500 and 700 cm^{-1}, which are not present in any other iron oxide spectrum. In Figure 4.11, Cr adsorbed mixed maghemite-magnetite had the peak at 826.4 cm^{-1} indicating the surface interaction species. Faria et al.(1997) reported that the Raman band around 665 cm^{-1} to 670 cm^{-1} was attributed to the high intensity of A_{1g} mode of magnetite (Fe_3O_4) with other weak bands at ca. 298 cm^{-1}, 320 cm^{-1}, 420 cm^{-1} and 550 cm^{-1}. In the present Raman study, there was no sharp peak identified in the given range indicating the reduction of magnetite in the Cr loaded mixed particles. Thus, all Fe(II) in magnetite was transformed to Fe(III) by the redox reaction when Cr(VI) was introduced into the solution.

4.4 Conclusions

Adsorption mechanism studies suggest that the adsorption of Cr(VI) onto maghemite-magnetite nanoparticles involves electrostatic interaction and redox reaction. Application of maghemite-magnetite nanoparticles for chromium removal has great potential in water and wastewater engineering. The results have highlighted three important contributions and applications: i) mechanism of Cr(VI) adsorption; (ii) possible treatment of Cr(VI) contaminated wastewater; and (iii) remediation of Cr(VI) contaminated groundwater. From the study, it is apparent that the removal of Cr(VI) by maghemite-magnetite nanoparticles depends on pH, temperature, contact time, and initial concentration of chromium. The results show that maghemite-magnetite nanoparticles can adsorb Cr(VI) better in an acidic pH range and that equilibrium may be achieved in 2 hours at pH 4.0

and an initial Cr(VI) concentration of 1.5 mg/L. Thermodynamic calculation indicated that Cr(VI) adsorption on the adsorbent is spontaneous and endothermic in nature. The adsorption capacity is enhanced with an increase in reaction temperature. Figures (4.3)-(4.5) clearly show that the adsorption of Cr(VI) on maghemite-magnetite particles increased with an increase in temperature. The effects of temperature on the removal rate of targeted compounds are important design-parameters for field application. The temperature of the groundwater in the field application is generally lower than the room temperature used in the experiment. Thus, temperature-reaction rate relationships are important for the removal of any hazardous compounds. The identification of the chemical states of the adsorbed Cr using XPS and Raman analyses during the removal of Cr(VI) from aqueous solution by mixed maghemite–magnetite nanoparticles is a major contribution of the study. The Raman and XPS data suggest that electrostatic attraction and oxidation–reduction reactions between chromium species and mixed maghemite-magnetite are the main mechanisms for the removal of chromium from aqueous solutions. Theoretical multiplet analysis of the Cr adsorbed γ-Fe_2O_3-Fe_3O_4 mixture presented in the study provides additional contribution to the literature on XPS studies. From the Raman study, it may be inferred that, in addition to adsorption reactions, diffusion reactions are also important during the experiments. These findings may be used to develop mixed maghemite- magnetite adsorbent systems for water treatment and site remediation.

4.5 References

Amin, M.M., Khodabakhshi, A., Mozafari, M., Bina, B., Kheiri, S., 2010. Removal of Cr(VI) from simulated electroplating wastewater by magnetite nanoparticles. Env. Eng. Mngt. J., 9, 921-927.

Altundogan, H.S., Altundogan, S., Tumen, F., Bildik, M., 2000. Arsenic removal from aqueous solutions by adsorption on red mud. Waste Management 20, 761-767.

Astrup, T., Stipp, S.L.S., and Christensen, T.H., 2000. Immobilization of chromate from coal Fly Ash leachate using an attenuating barrier containing zero-valent iron. Environmental Science and Technology, 34, 19, 4163-4168.

Blowes, D., 2002. Tracking Hexavalent Cr in Groundwater. Science J. 295, 2024-2025.

Blowes,, D.W., Ptacek,, C.J., Benner, S.G., McRae, C.W.T., Bennett, T.A.,, Puls, R.W., 2000. Treatment of inorganic contaminants using permeable reactive barriers. Journal of Contaminant Hydrology 45, 123–137.

Biesinger, M.C., Payne, B.P., Grosvenor, A.P., Lau, L.W.M., Gerson, A.R., and Smart, R.S.C., 2011. Resoving surface chemical states in XPS analysis of first row transition metals, oxides and hydroxides. Applied Surface Sciences, 257, 2717-2730.

Candela, M.P., Martínez, M.J., and Maciá, R.T., 1995. Chromium removal with activated carbons. Wat. Res. 29, 2174-2180.

Cornell, R., and Schwetmann, U., 2003. The Iron Oxides: Structure, Properties, Reactions, Occurrence and Uses. Weinheim: Willey-VCH, 2003.

Dupont, L., and Guillon, E., 2003. Removal of hexavalent chromium with a lignocellusic substrate extracted from wheat bran. Environ. Sci. Technol. 37, 4235–4241.

Dash, S.S., and Parida, K.M., 2007. Studies on selenite adsorption using manganese nodule leached residues, J. Colloid Interf. Sci. 307, 333-339.

Faria, D.L.A., Venaüncio, S., and Oliveira, M.T., 1997. Raman Microspectroscopy of some iron oxides and oxyhydroxides. Journal Of Raman Spectroscopy, 28, 873.

Fairley, N., 1999-2003. CasaXPS Version 2.2.19.

Gavaskar, A., Tatar, L., and Condit, W., 2005.Cost and performance report nanoscale zero-valent iron technologies for source remediation. Naval Facilities Engineering Command (NAVFAC). Contract report: (2005) CR-05-007-ENV.

Grosvenor, A.P., Kobe, B.A., and McIntyre, N.S., 2004. Examination of the oxidation of iron by oxygen using X-ray photoelectron spectroscopy and QUASES. Surafce Science 565, 151-162.

Gupta, K.S., Chen, K.Y., 1978. Arsenic removal by adsorption. J WPCF (Wineries, fresh pack food processors, 50, 493.

Gupta. R.P., Sen, S.K., 1975. Calculation of multiplet structure of core *p* -vacancy levels. Phys. Rev. 12, 15-19.

Hu, J., Chen, G., and Lo, I.M.C., 2006. Selective removal of heavy metals from industrial wastewater using maghemite nanoparticle: performance and mechanisms. Journal of Environmental Engineering, 132, 709-715.

Hu, J., Lo, I.M.C., and Chen, G., 2004. Removal of Cr(VI) by magnetite nanoparticle. Water science and Technology 50, 12, 139-146.

Hu, J., Chen, G., Lo, I.M.C., 2005. Removal and recovery of Cr(VI) from wastewater by maghemite nanoparticles. Water Research 39, 4528–4536.

Li, H., Zhou, Q., Wu, Y.F.J., Wang, T., and Jiang, G., 2009. Effects of waterborne nano-iron on medaka (Oryzias latipes): Antioxidant enzymatic activity, lipid peroxidation and histopathology. Ecotoxicol Environ Saf. 72, 3, 684-692.

McKay, G., Bino, M.J., Altamemi, A.R., 1985. The adsorption of various pollutants from aqueous solutions on to activated carbon. Wat Res. 14, 277.

Moulder, J.F., Stickle, W.F., Sobol, E.F., and Bomben, K.D., 1992. Handbook of X-ray Photoelectron Spectroscopy. ISBN: 0-9627026-2-5, 1992.

Nriagu, J.O., and Nieboer, E., 1988. Historical perspectives. iN: Chromium in the natural and human environments. John Wiley & Sons, New York: 20 (1988) 1-20.

Palmer, C.D., and Wittbrodt, P.R., 1991. Processes affecting the remediation of chromium-contaminated sites. Environmental Health Perspectives, 92, 25-40.

Petrova, T.M., Fachikov, L., and J. Hristov, J., 2011. The magnetite as adsorbent for some hazardous species from aqueous solutions: a review. International Review of Chemical Engineering (I.RE.C.H.E.), 3,2, 134.

Phenrat, T., Long, T.C., Lowry, G.V., and Veronesi, B., 2009. Partial oxidation ("aging") and surface modification decrease the toxicity of nanosized zerovalent iron. Environ Sci Technol. 43, 195-200.

Pratt, A.R., Muir, I.J., and Nesbitt, H.W., 1994. X-ray photoelectron and auger electron spectroscopic studies of pyrrhotite and mechanism of air oxidation. Geochimica et Cosmochimica Acta 58, 827-841.

Pratt, A.R., Blowes, D.W., Ptacek, C.J., 1997. Products of chromate reduction on proposed subsurface remediation material. Environ. Sci. Technol. 31 (1997), 2492–2498.

Pratt, A.R., and McIntyre, N.S., 1996. Curve fitting of Cr(2p) photoelectron spectra of Cr_2O_3 and CrF_3". Surface and Interface Analysis 24, (1996), 529-530.

Richard, F.C., and Bourg, A.C.M., 1991. Aqueous Geochemistry of Chromium: A Review. Water Research 25 (1991), 807-816.

Singh, D.B., Gupta, G.S., Prasad, G., and Rupainwar, D.C., 1993. The use of Hematite for Cr(VI) removal. J. Environ. Sci. Health, A28,8 (1993), 1813-1826.

Santiago, V.R., Fedkin, M.V., Lvov, S.N., 2012. Protonation enthalpies of metal oxides from high temperature electrophoresis. Journal of Colloid and Interface Science 371 (2012) 136–143.

Sawyer, C.N., Mccarty, P.L., and Parkin, G.F., 1994. Chemistry for environbmental engineering- Four Edition. McGraw-Hill, Inc. New York, NY 100200, 1994.

Sadiq, M., and Lindsay, W.L., 1988. The solubility product of maghemite. Soil Science, 46,1, 1-5.

Tuutijärvi, T., Sillanpääa, L.J.M., Chenb, G., 2009. As(V) adsorption on maghemite nanoparticles. Journal of Hazardous Materials 166, 1415–1420.

Weng, C.H., Wang, J.H., and Huang, C.P., 1997. Adsorption of Cr(VI) onto TiO_2 from dilute aqueous solutions. Wat. Sci. Tech. 35, 7, 55-62.

Weckhuysen, B.M., and Wachs, I.E., 1997. In Situ Raman Spectroscopy of supported chromium oxide catalysts: $^{18}O_2$-$^{16}O_2$ isotopic labeling studies. J. Phys. Chem. B, 101 (1997), 2793-2796.

Yuan, P., Fan, M., Yang, D., He, H., Liu, D., Zhu, T., Chn, T., 2009. Motmorillonite-supported magnetite nanoparticles for the removal of Cr(VI) from aqueous solutions. J.Haz.Mat., 166, 821-829.

Yean, S., Cong, L., Yavuz, C.T., Mayo, J.T., and Yu, W.W., 2005. Effect of magnetite particle size on adsorption and desorption of arsenite and arsenate. J. Mater. Res. 20 (12).

List of Tables

Tables

Table 4.1: Multiplet peak positions, FWHM and areas used to fit the XPS data. Peak parameters were obtained from Grosvenor et al. (2004).

Sample Name	Metal Oxide	Binding	FWHM	Area (%)

		Energy (eV)		
Maghemite-magnetite Mixture	Maghemite	714.05	1.7	2.4
	Maghemite	712.95	1.4	7.5
	Maghemite	711.75	1.4	16.8
	Maghemite	710.75	1.3	22.70
	Maghemite	709.75	1.2	22.70
	Fe(III) Magnetite	714.45	3.3	2.4
	Fe(III) Magnetite	713.35	1.4	1.5
	Fe(III) Magnetite	712.25	1.4	3.2
	Fe(III) Magnetite	711.15	1.4	4.6
	Fe(III) Magnetite	710.15	1.4	6.2
	Fe(II) Magnetite	709.15	1.2	3.9
	Fe(II) Magnetite	708.35	1.2	4.3
Cr(VI) Loaded Sorbent	Maghemite	714.15	1.7	5.1
	Maghemite	713.05	1.4	9.0
	Maghemite	711.85	1.4	20.2
	Maghemite	710.85	1.3	27.2
	Maghemite	709.85	1.2	27.2
	Fe(III) Magnetite	714.45	3.3	3.5
	Fe(III) Magnetite	713.35	1.4	0.6
	Fe(III) Magnetite	712.25	1.4	1.4
	Fe(III) Magnetite	711.15	1.4	2.0
	Fe(III) Magnetite	710.15	1.4	2.7
	Fe(II) Magnetite	709.44	1.2	1.7
	Fe(II) Magnetite	708.15	1.2	1.9

Table 4.2: Langmuir constant and thermodynamic parameters at different temperature for Cr(VI) removal by maghemite and magnetite mixtures.

Species	Temperature, ^0C	Langmuir Constant		Thermodynamic Parameters	
		b (L/mg)	q_{max} (mg/g)	$-\Delta G^0$ (Kj mol^{-1})	ΔS^0 (Kj mol^{-1} K^{-1})
Cr(VI)	10	3	6	28	0.1
	22	3.1	6.9	29.4	0.1
	50	4.8	7	33.45	0.13

Table 4.3: Binding Energies and relative content of Chromium in mixed maghemite and magnetite adsorbents.

Valence state	**Sample**	**Elemental Oxidation State**	**Binding energy (eV)**	**Peak Area (%)**	**FWHM**
Cr 2p/5	Cr(VI) Loaded sorbent	Cr(III) (Cr_2O_3)	579.72	4.0	1.09
		Cr(III) (Cr_2O_3)	578.90	6.2	1.09
		Cr(III) (Cr_2O_3)	577.90	14.7	1.09
		Cr(III) ($Cr(OH)_3$)	577.20	19.3	2.5
		Cr(III) (Cr_2O_3)	577.10	27.5	1.09
		Cr(III) (Cr_2O_3)	576.11	28.3	1.09

List of Figures

Figure 4.1: Image of maghemite-magnetite nanoparticles (20-60 nm) using Hitachi S4500 scanning electron microscopy (SEM).

Figure 4.2: The equilibrium solute concentration of Cr(VI) in the solution after adsorption at different pH values (Adsorbent: maghemite- magnetite and Ce: equilibrium solute concentration (mg/L)).

Figure 4.3: Effect of contact time on the adsorption of Cr(VI) by maghemite-magnetite nanoparticles at different temperatures and pH 4 . (Initial concentration, C_e: 1.5 mg/L).

Figure 4.4: Langmiur isotherm plots for Cr(VI) adsorption by maghemite-magnetite nanoparticles at different temperatures (initial concentration: 0.4 – 3.1 mg/L; contact time: 24 hrs; pH = 4; maghemite-magnetite nanoparticles dosage: 0.4 g/L).

Figure 4.5: Lagergren plot for adsorption of Cr(VI) on maghemite-magnetite nanoparticles at different temperatures.

Figure 4.6: XRD patterns showing maghemite-magnetite particles: sample 1 before Chromium (VI) adsorption; sample 1-Cr indicates after Chromium (VI) adsorption.

Figure 4.7: XPS wide scan spectra: (a) and (b) fresh maghemite-magnetite mixture; and (c) and (d) Cr(VI) loaded maghemite- magnetite mixture. (Binding energy scale in order of descending values).

Figure 4.8: XPS spectra (a) nanoscale magheamite-magnetite particles and (b) Cr(VI)-adsorbed maghemite-magnetite mixture particles at pH 4.0.

Figure 4.9: XPS spectra: Difference of Fe 2p3/2 spectrum between maghemite-magnetite particles and Cr(VI)-adsorbed maghemite-magnetite mixture particles at pH 4.0. Spectra has been background subtracted, normalized, and then subtracted from fresh adsorbent to Cr(VI)-adsorbed absorbent.

Figure 4.10: Cr 2p XPS spectra of Cr(VI) loaded maghemite-magnetite mixture (state background subtracted in data).

Figure 4.11: Raman spectra of (a) virgin mixed maghemite-magnetite particles (b) Cr adsorbed mixed maghemite-magnetite.

Figure 4.12: Raman spectra: Difference of spectrum between Cr(VI)-adsorbed maghemite-magnetite particles and fresh magnetite-maghemite mixture particles at pH 4.0. Spectra has been subtracted from Cr(VI)-adsorbed absorbent to fresh adsorbent.

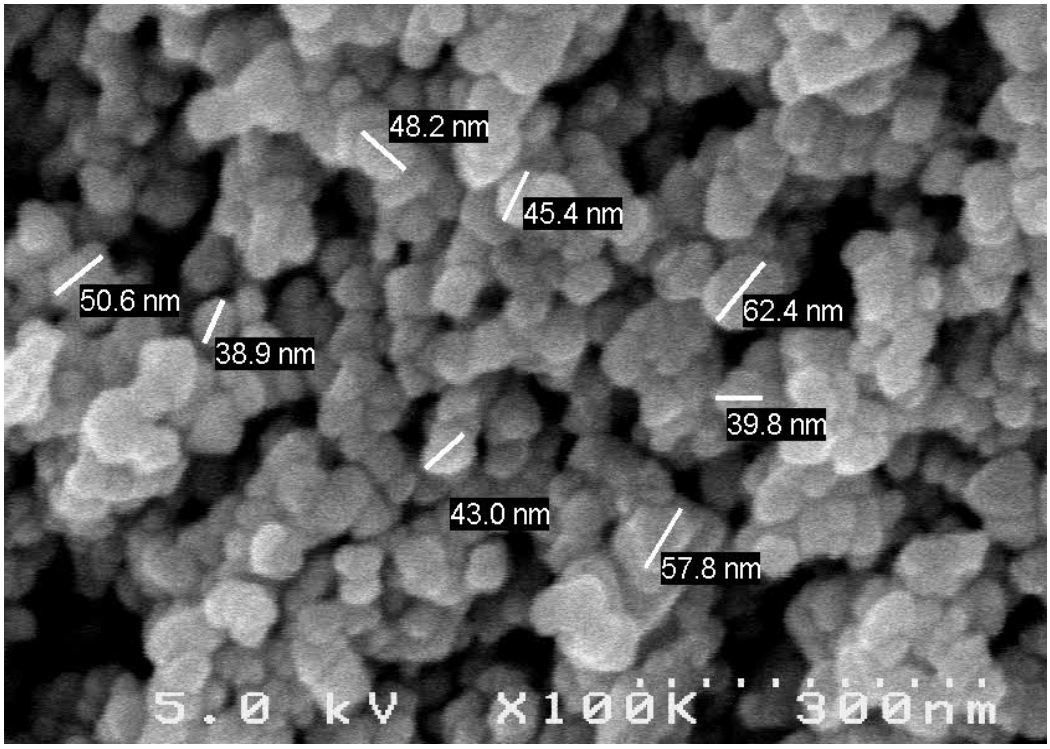

Figure 4.1: Image of maghemite- magnetite nanoparticles (20-60 nm) using Hitachi S4500 scanning electron microscopy (SEM).

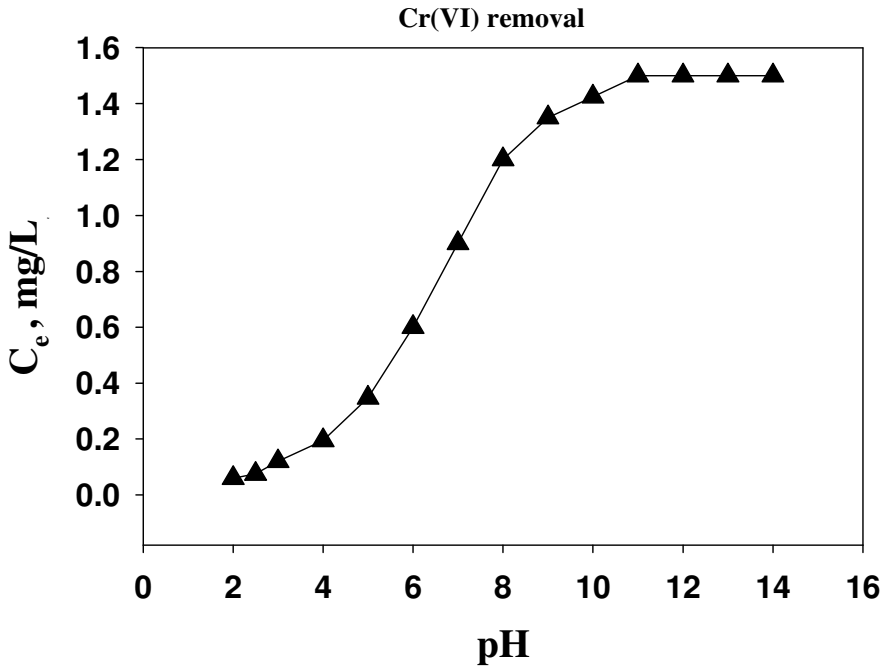

Figure 4.2: The equilibrium solute concentration of Cr(VI) in the solution after adsorption at different pH values (Adsorbent: maghemite- magnetite and Ce: equilibrium solute concentration (mg/L)).

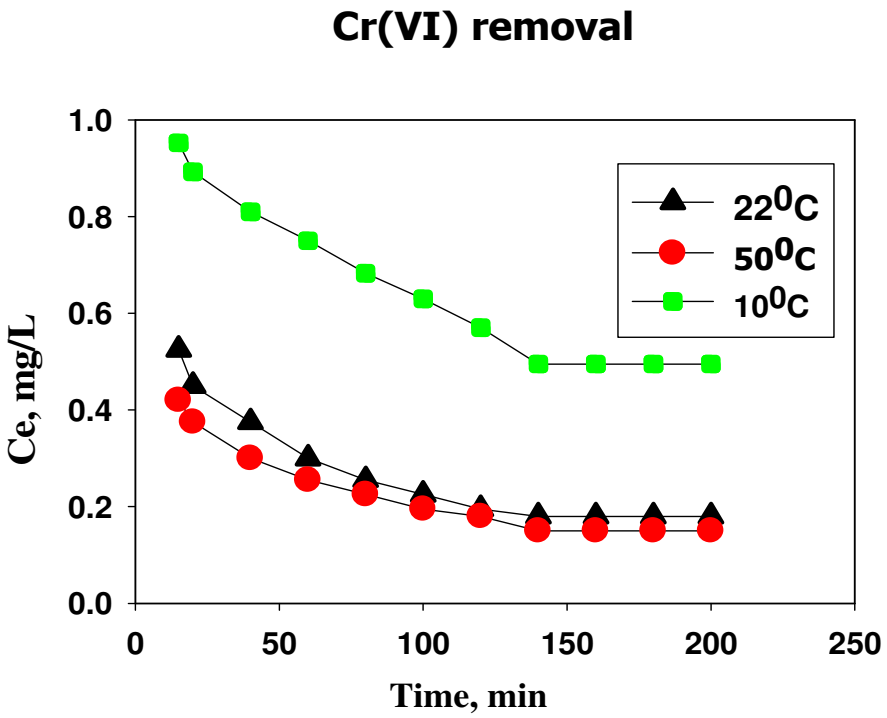

Figure 4.3: Effect of contact time on the adsorption of Cr(VI) by maghemite-magnetite nanoparticles at different temperatures and pH 4 . (Initial concentration, C_e: 1.5 mg/L)

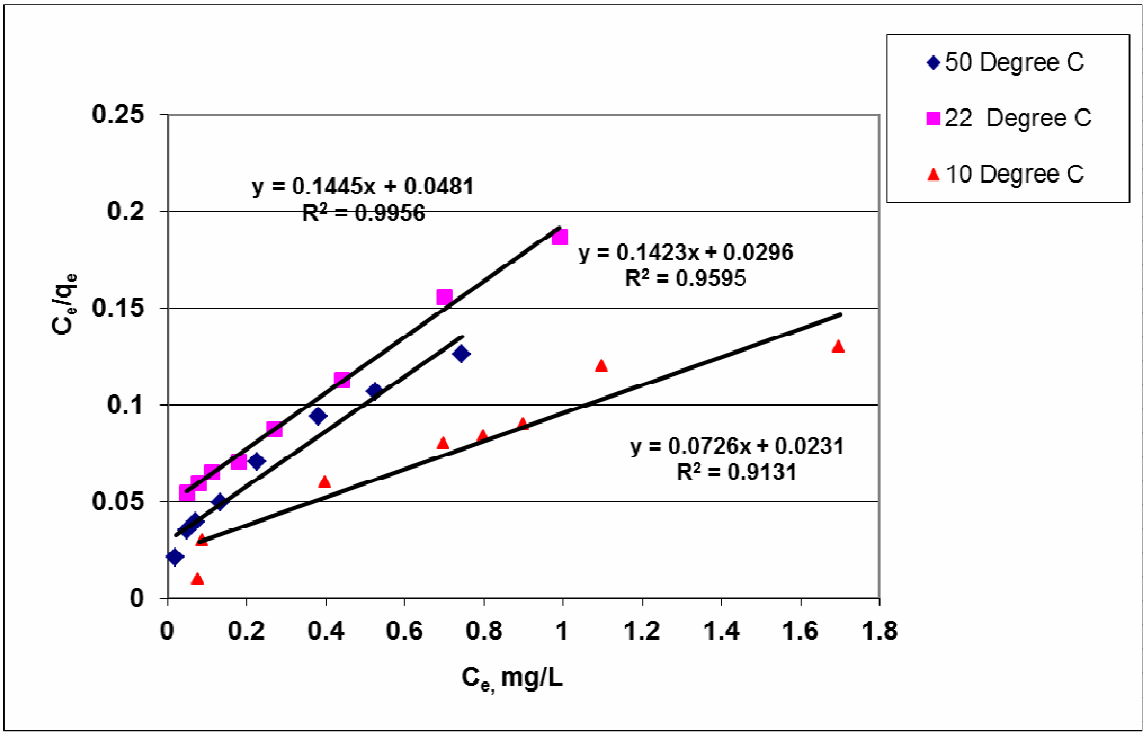

Figure 4.4: Langmuir isotherm plots for Cr(VI) adsorption by maghemite-magnetite nanoparticles at different temperatures (initial concentration: 0.5 – 3.5 mg/L; contact time: 24 hrs; pH = 4; maghemite-magnetite nanoparticles dosage: 0.4 g/L).

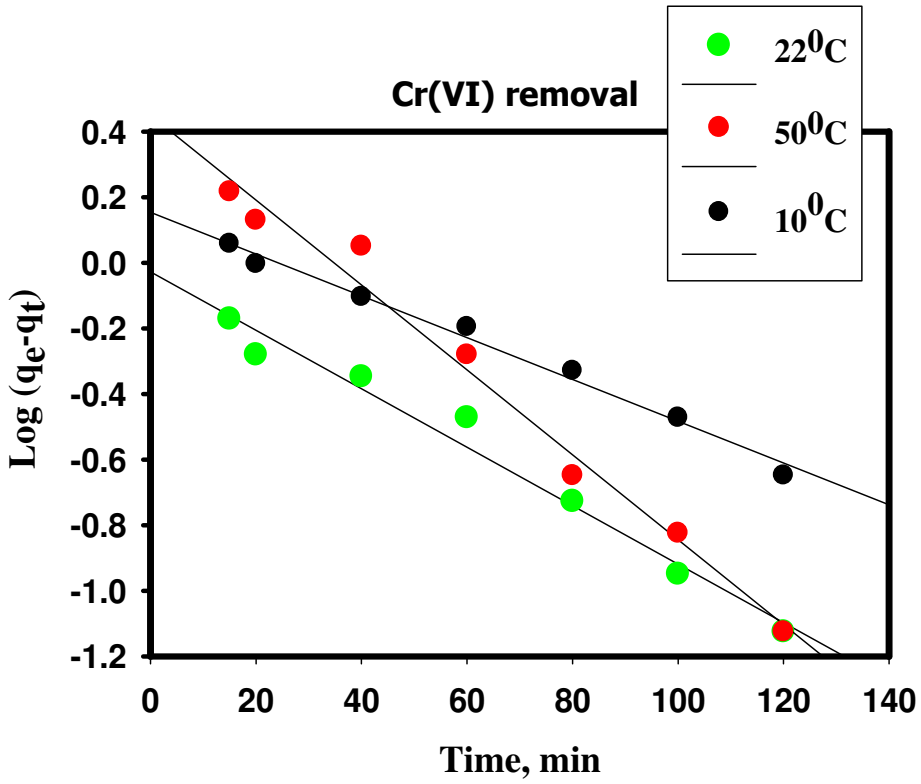

Figure 4.5: Lagergren plot for adsorption of Cr(VI) on maghemite-magnetite nanoparticles at different temperatures.

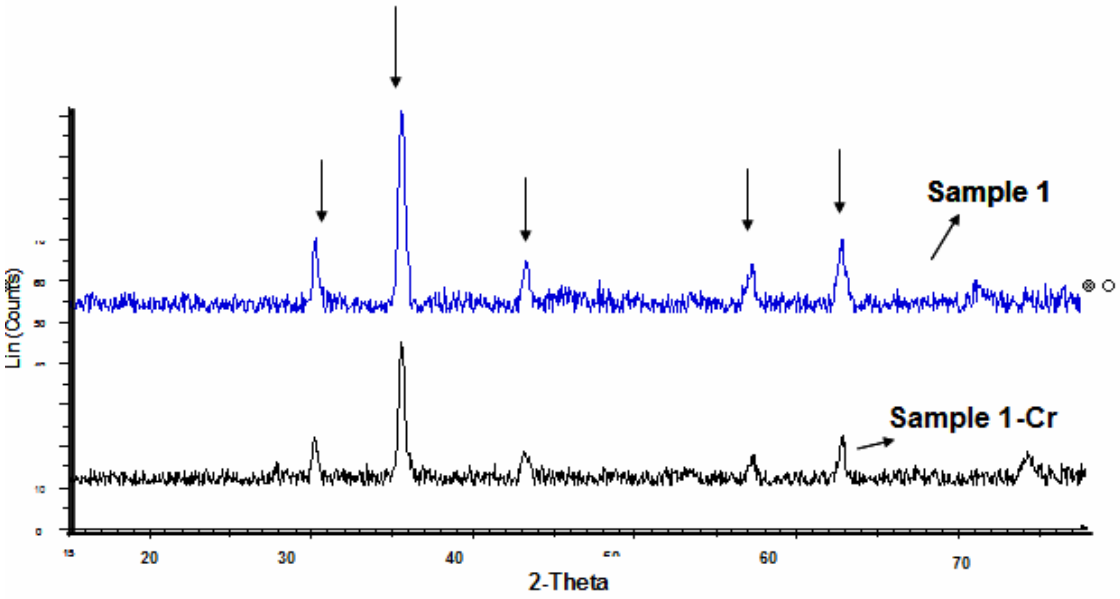

Figure 4.6: XRD patterns showing magheamite-magnetite particles: sample 1 before Chromium (VI) adsorption; sample 1-Cr indicates after Chromium (VI) adsorption.

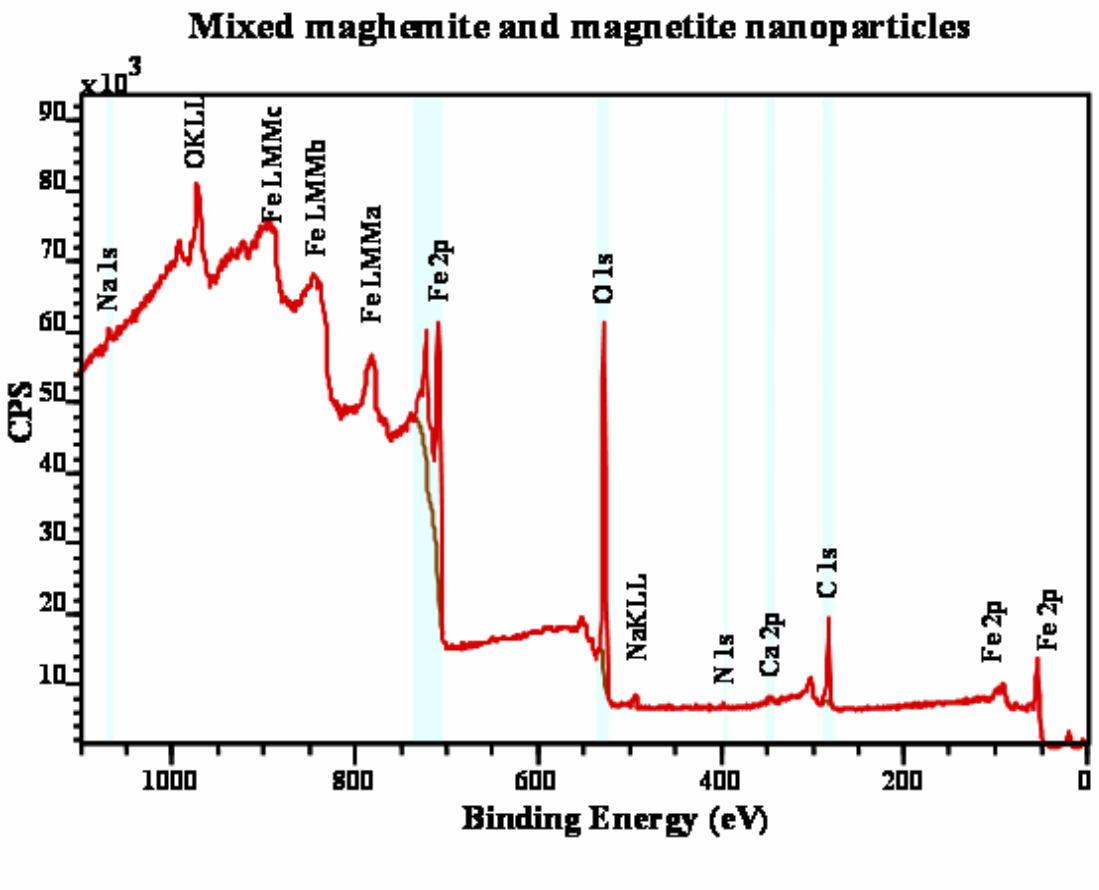
Mixed maghemite and magnetite nanoparticles
x10^3
CPS
Binding Energy (eV)
Na 1s
O KLL
Fe LMMc
Fe LMMb
Fe LMMa
Fe 2p
O 1s
NaKLL
N 1s
Ca 2p
C 1s
Fe 2p
Fe 2p

(a)

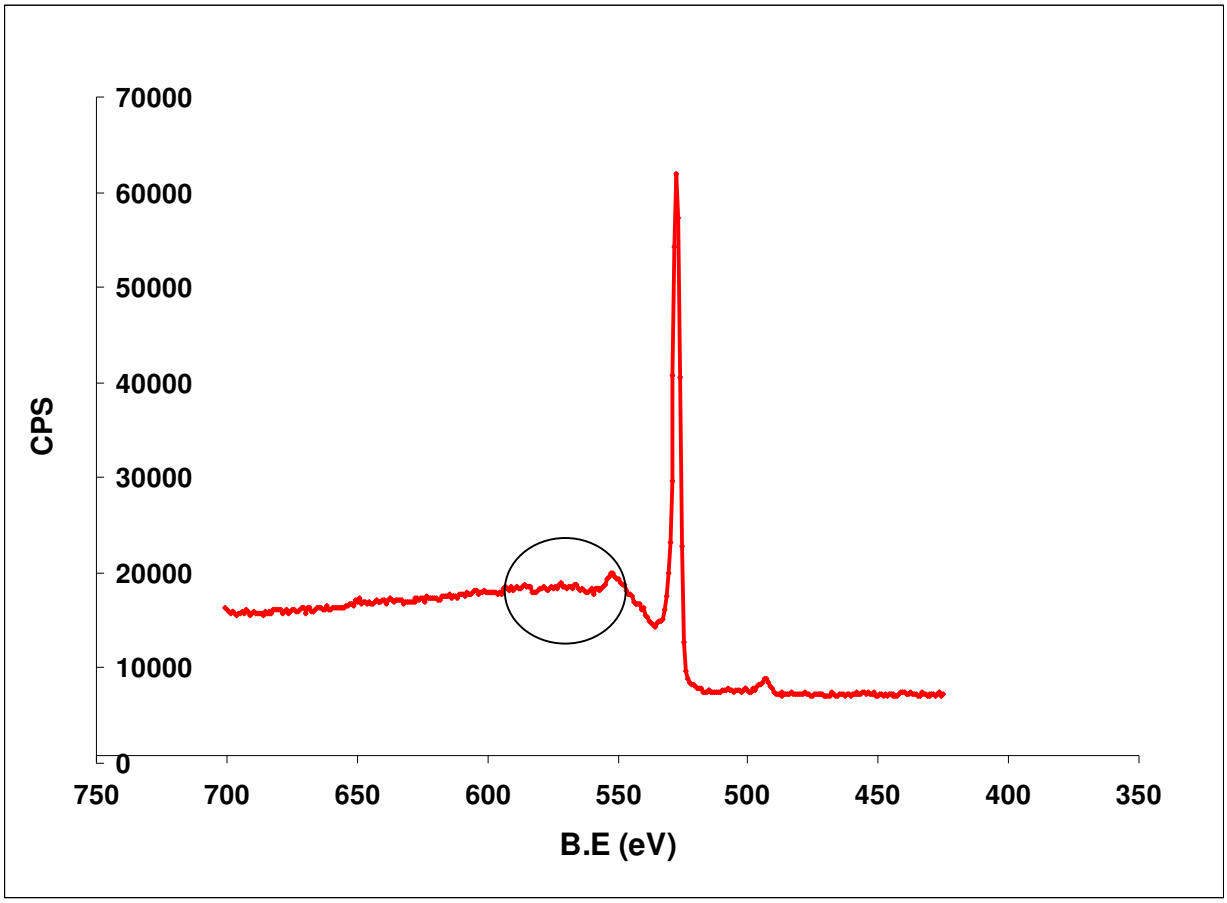
70000
60000
50000
40000
30000
20000
10000
0
CPS
750
700
650
600
550
500
450
400
350
B.E (eV)

(b)

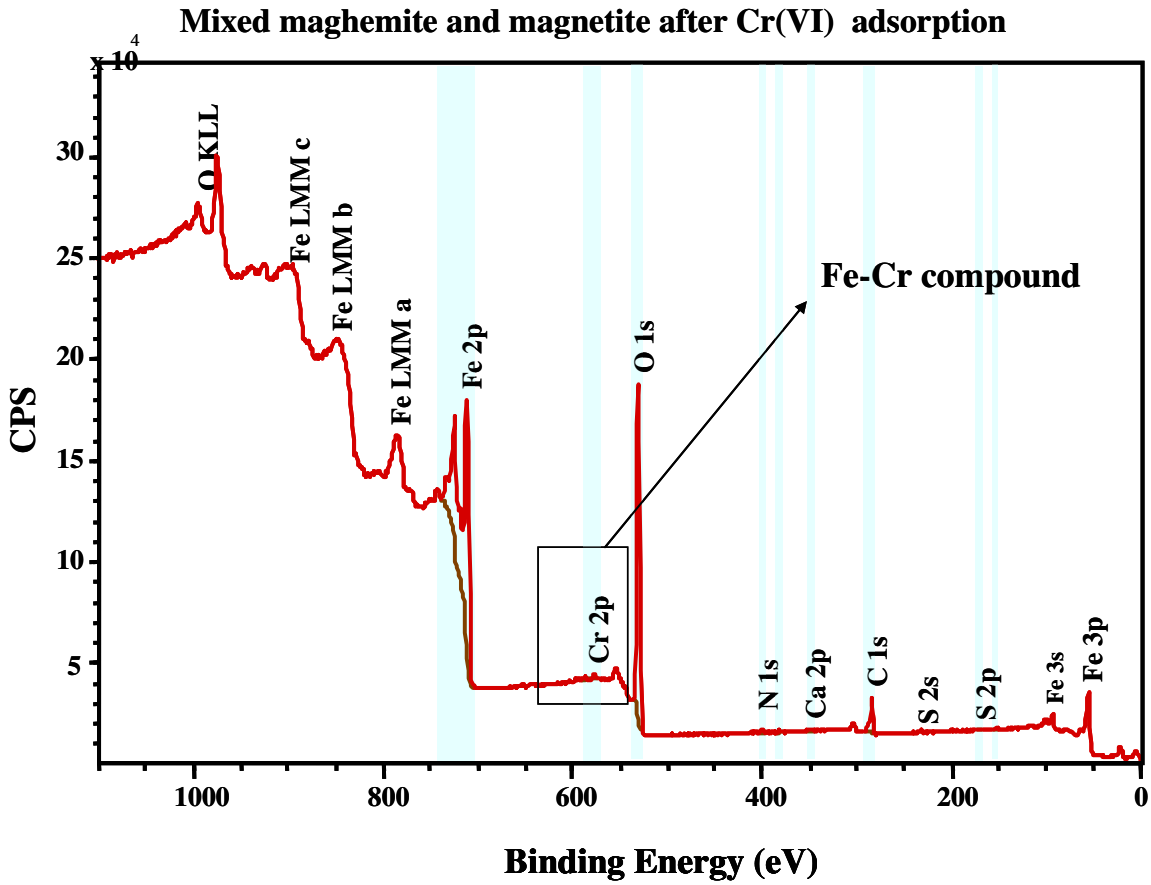
Mixed maghemite and magnetite after Cr(VI) adsorption
x 10^4
CPS
Binding Energy (eV)
O KLL
Fe LMM c
Fe LMM b
Fe LMM a
Fe 2p
Cr 2p
O 1s
N 1s
Ca 2p
C 1s
S 2s
S 2p
Fe 3s
Fe 3p
Fe-Cr compound

(c)

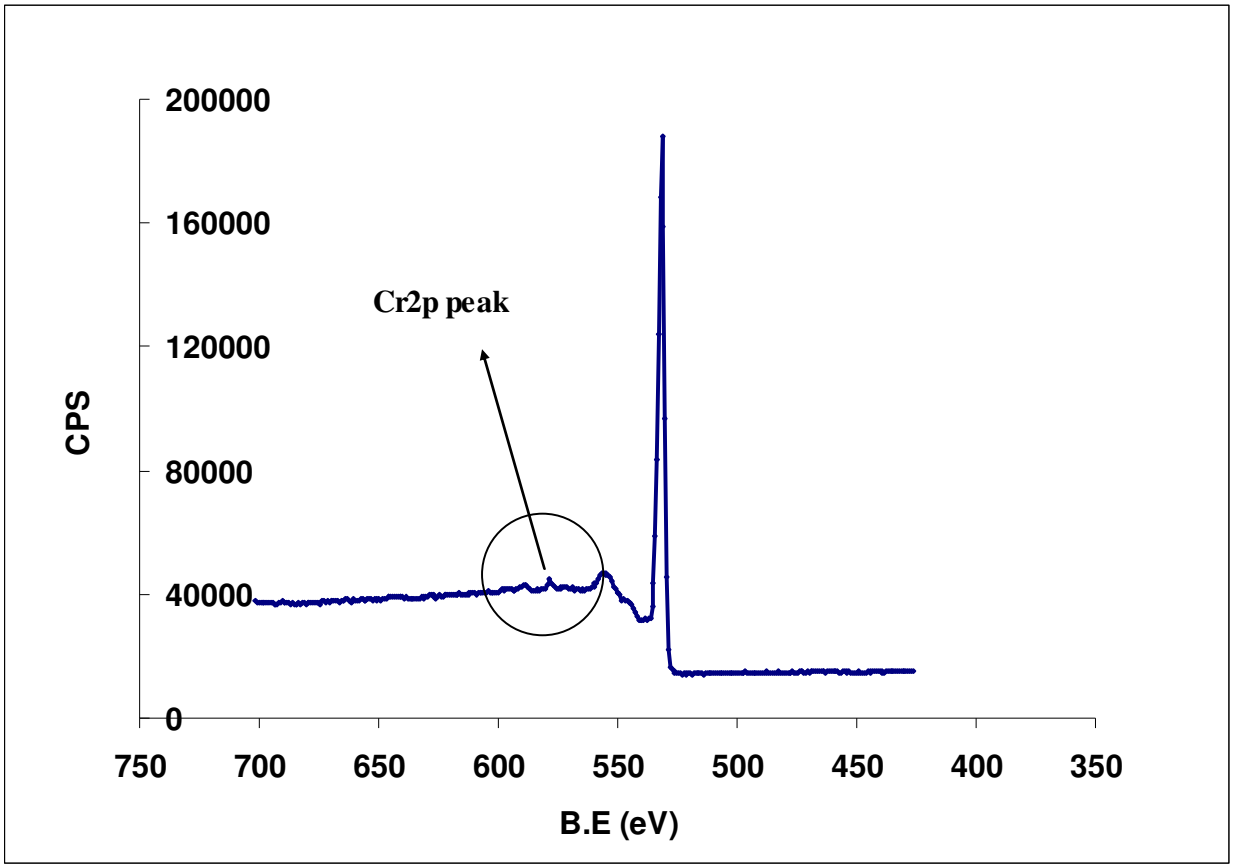

(d)

Figure 4.7: XPS wide scan spectra: (a) and (b) fresh maghemite-magnetite mixture; and (c) and (d) Cr(VI) loaded magnetite–maghemite mixture. (Binding energy scale in order of descending values)

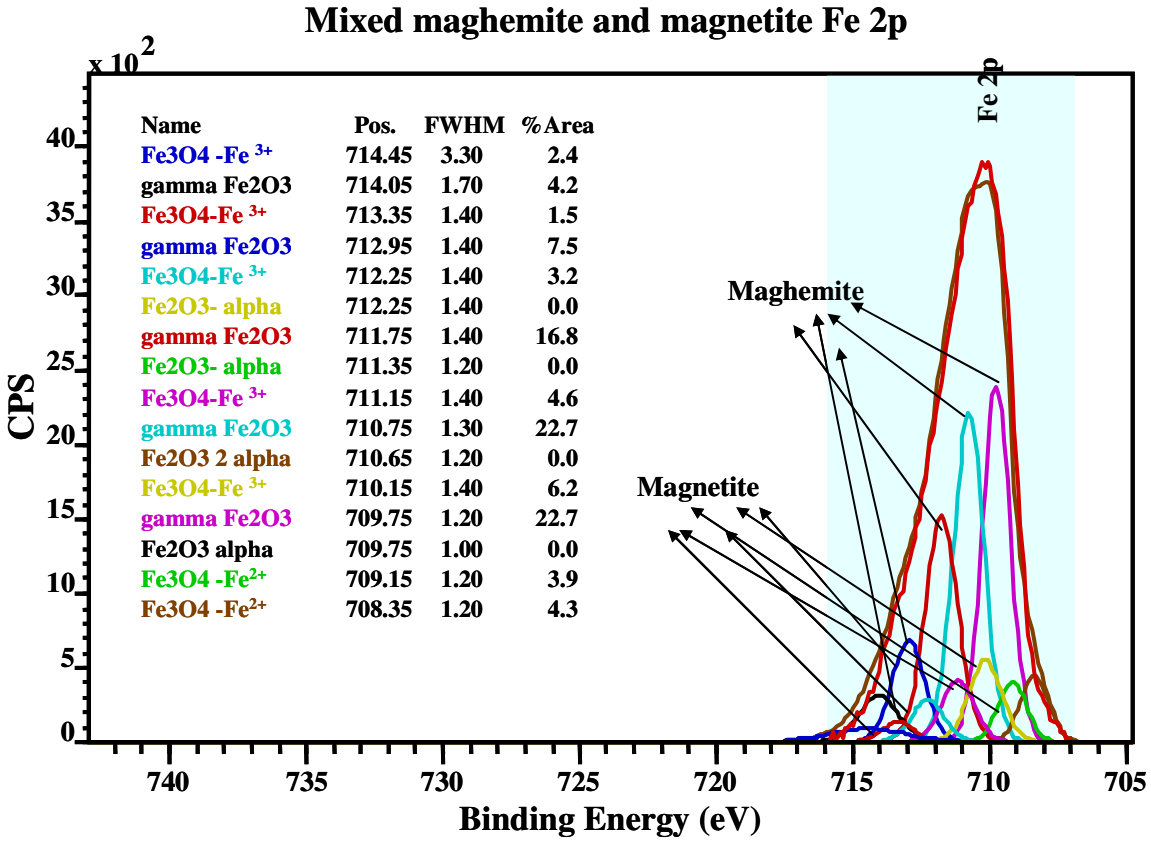
Mixed maghemite and magnetite Fe 2p
x 10^2
CPS
Binding Energy (eV)
Fe 2p
Maghemite
Magnetite
Name Pos. FWHM %Area
Fe3O4 -Fe 3+ 714.45 3.30 2.4
gamma Fe2O3 714.05 1.70 4.2
Fe3O4-Fe 3+ 713.35 1.40 1.5
gamma Fe2O3 712.95 1.40 7.5
Fe3O4-Fe 3+ 712.25 1.40 3.2
Fe2O3- alpha 712.25 1.40 0.0
gamma Fe2O3 711.75 1.40 16.8
Fe2O3- alpha 711.35 1.20 0.0
Fe3O4-Fe 3+ 711.15 1.40 4.6
gamma Fe2O3 710.75 1.30 22.7
Fe2O3 2 alpha 710.65 1.20 0.0
Fe3O4-Fe 3+ 710.15 1.40 6.2
gamma Fe2O3 709.75 1.20 22.7
Fe2O3 alpha 709.75 1.00 0.0
Fe3O4 -Fe2+ 709.15 1.20 3.9
Fe3O4 -Fe2+ 708.35 1.20 4.3

(a)

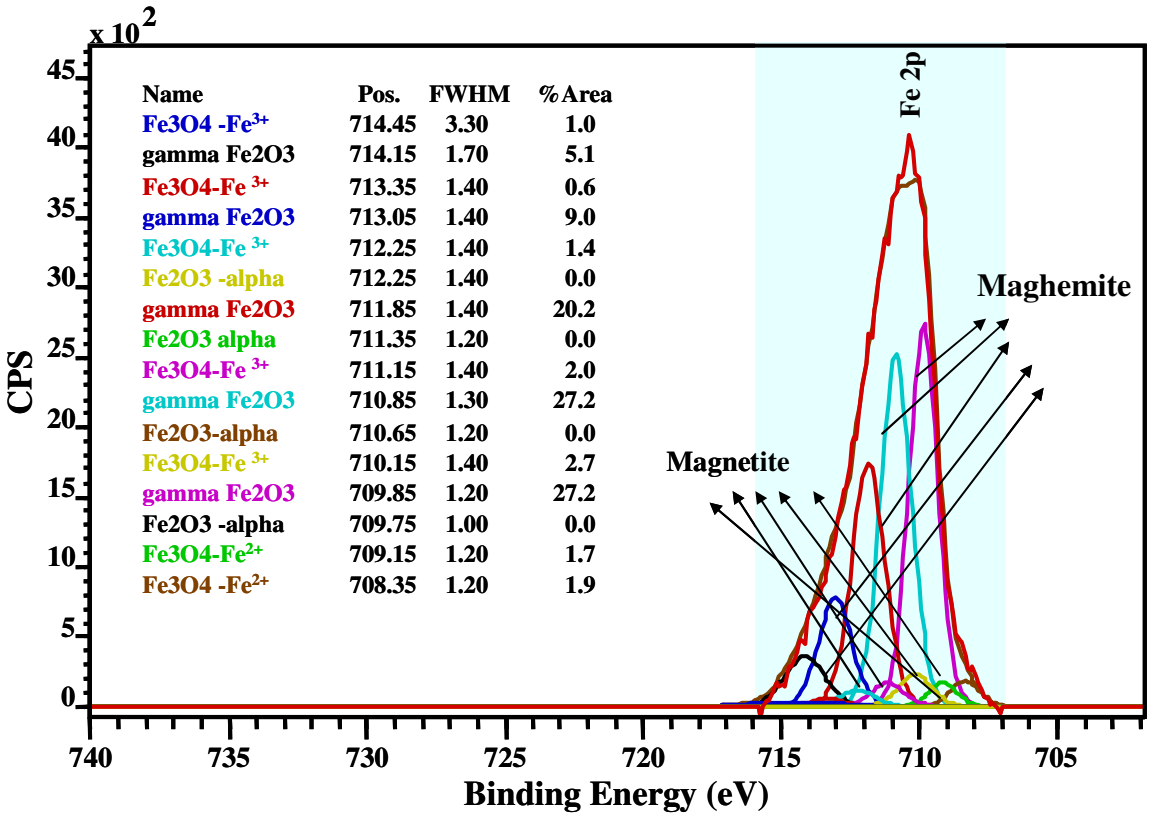

(b)

[a] Component information for each of the theoretically derived GS multiplets came from a digitized reproduction of the graphs found in the original paper (Fairley, 1999-2003).

[b] Fe3O4-Fe (III) means Fe (III) in magnetite; and Fe3O4-Fe (II) means Fe (II) in magnetite.

Figure 4.8: XPS spectra (a) nanoscale maghemite-magnetite particles and (b) Cr(VI)-adsorbed mixed maghemite-magnetite- particles at pH 4.0.

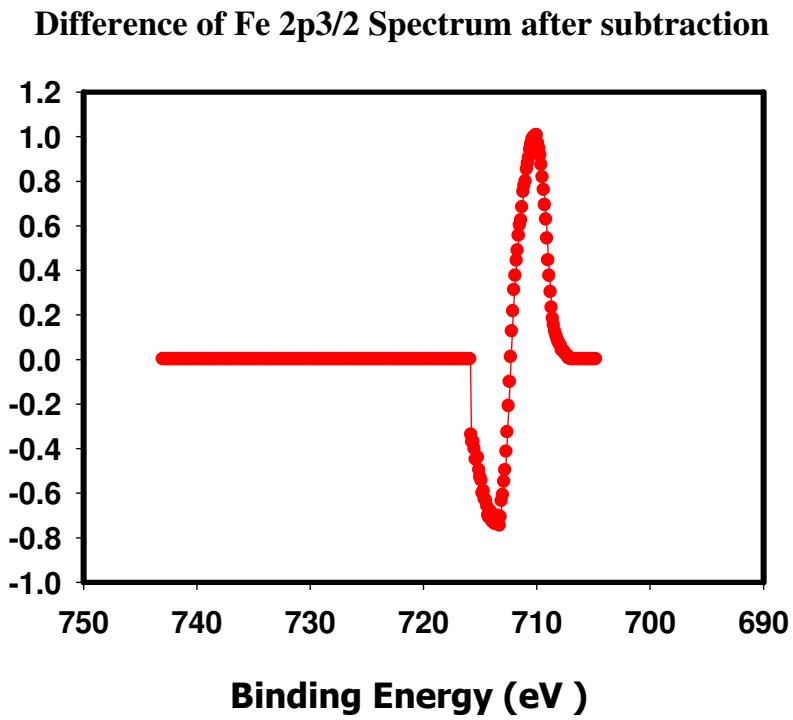

Figure 4.9: XPS spectra: Difference of Fe $2p_{3/2}$ spectrum between maghemite-magnetite particles and Cr(VI)-adsorbed magnetite-maghemite mixture particles at pH 4.0. Spectra have been background subtracted, normalized, and then subtracted from fresh adsorbent to Cr(VI)-adsorbed absorbent.

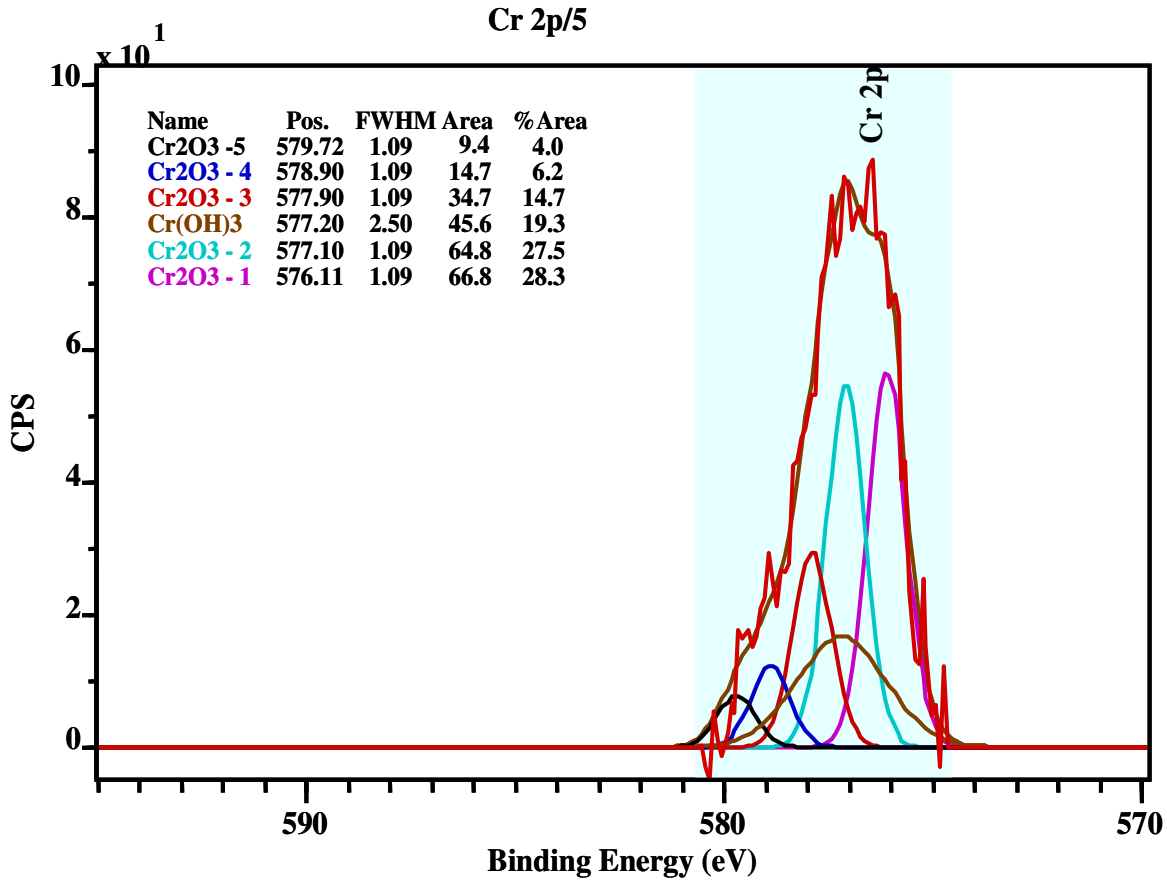

Figure 4.10: Cr 2p XPS spectra of Cr(VI) loaded maghemite-magnetite mixture. (state background subtracted in data).

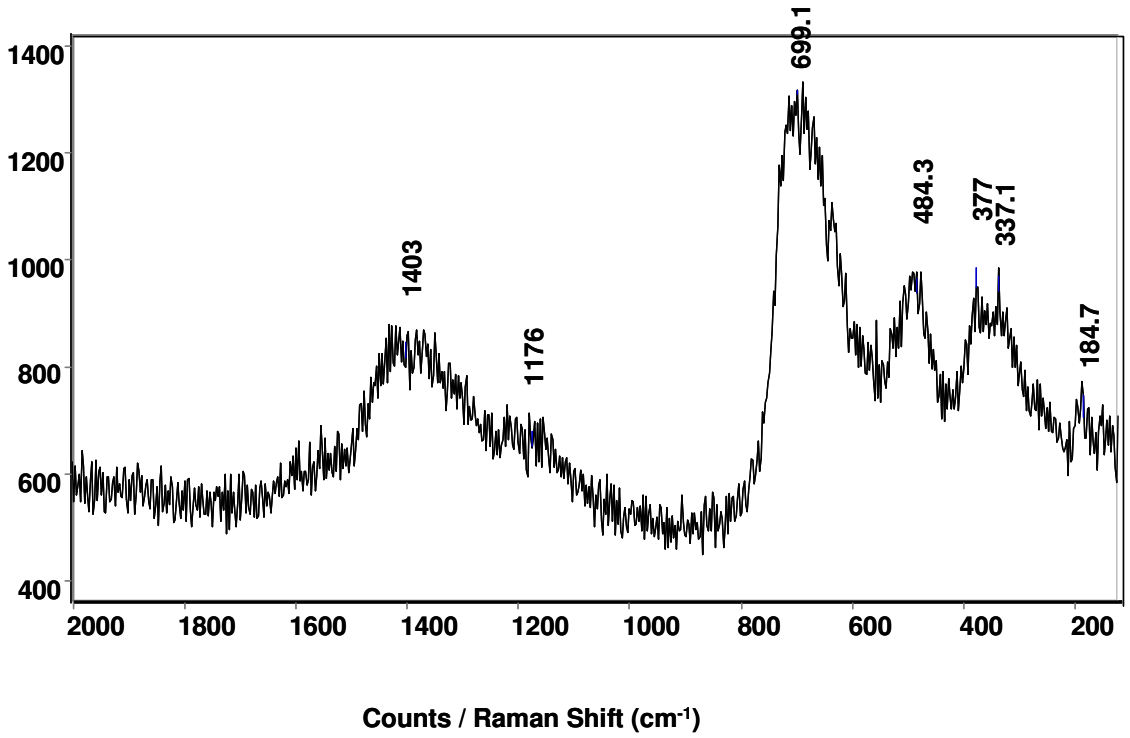
699.1
484.3
377
337.1
1403
1176
184.7
1400
1200
1000
800
600
400
2000
1800
1600
1400
1200
1000
800
600
400
200
Counts / Raman Shift (cm-1)

(a)

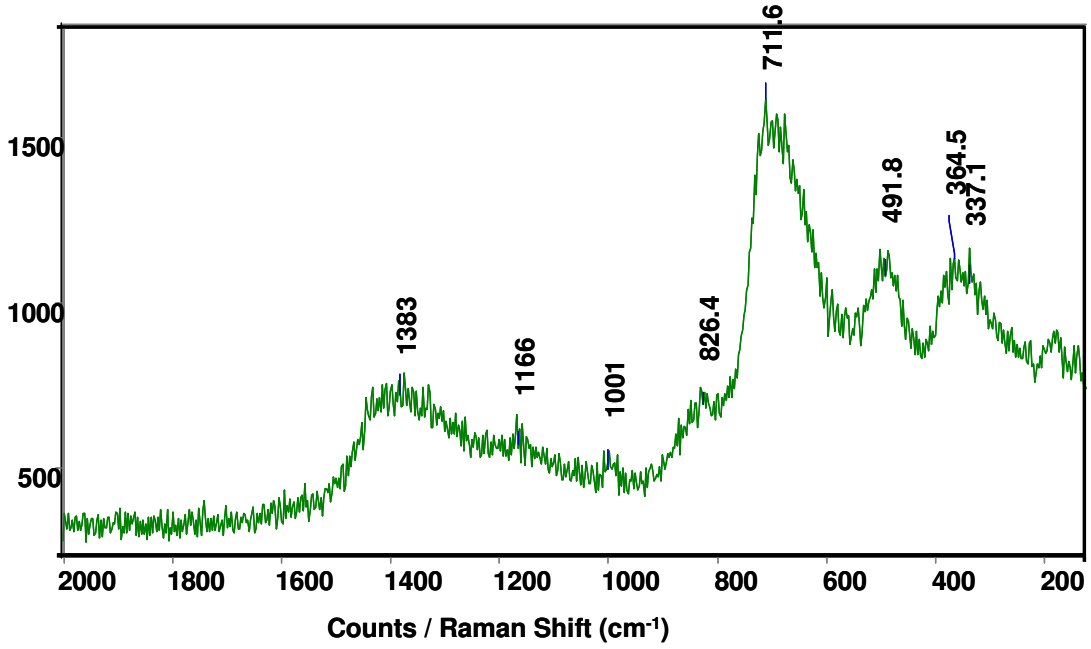

(b)

Figure 4.11: Raman spectra of (a) virgin mixed maghemite-magnetite particles (b) Cr adsorbed mixed maghemite-magnetite.

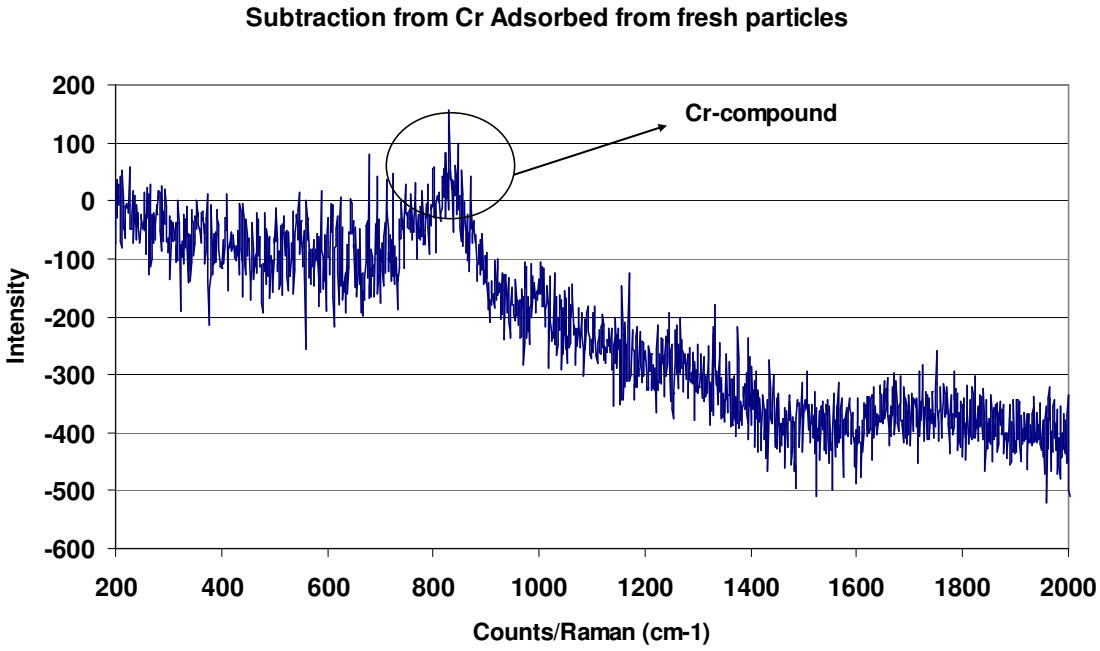

Figure 4.12: Raman spectra: Difference of spectrum between Cr(VI)-adsorbed maghemite-magnetite particles and fresh magnetite-maghemite mixture particles at pH 4.0. Spectra have been subtracted from Cr(VI)-adsorbed absorbent to fresh adsorbent.

CHAPTER 5

KINETICS OF CADMIUM(II) UPTAKE BY MIXED MAGHEMITE-MAGNETITE NANOPARTICLES

5.1 Introduction

Cadmium, a toxic heavy metal, is a relatively less abundant metallic element and one of the toxic substances released to the environment through anthropogenic activities including the combustion of fossil fuels, metal production, application of phosphate fertilizers, electroplating and the manufacturing of batteries, pigments, and screens (Sharma, 2008; and Marin et al. 2007). According to Rao et al. (2010), cadmium exists naturally in the subsurface and water bodies by the gradual process of erosion and abrasion of rocks and soils, and from singular events such as forest fires and volcanic eruptions. The best known cadmium minerals are greenockite, cadmium sulfide (77.6% Cd), otavite, cadmium carbonate (61.5% Cd) and pure cadmium oxide (87.5% Cd).

According to Waalkes (2000) and Sharma (2008), cadmium is reportedly a potent carcinogen and teratogen impacting lungs, kidneys, liver and reproductive organs. According to WHO (2008) guideline, the maximum cadmium concentration in drinking water is 0.003 mg/L. Singh et al. (1998) reported that cadmium has toxic effects when its concentration exceeds the threshold limit value (TLV) of 0.005 mg/L and causes different types of acute and chronic disorders. As cadmium is a well- known toxic metal and has a low drinking water guideline, Cd contaminated waters must be treated prior to their disposal.

The persistence and mobility of Cd in soils are determined largely by the extent of adsorption by soil particles (Naidu et al. 1994) and the adsorption of Cd by hydrous oxides and it is influenced by variables such as pH and the ionic composition (both species and concentration) of the support medium. Naidu et al. (1994) reported that the effect of pH on Cd adsorption has been studied extensively using both pure systems, such as goethite, silicate clay minerals and soils. They further explained that Cd adsorption increases with an increase in pH, attributed mainly to the preferential adsorption of Cd-hydroxy complexes. The study of the effect of ionic strength on Cd adsorption was largely limited to pure systems, such as clay minerals. Boekhold et al. (1993) attributed the decrease in Cd adsorption with increasing ionic strength to competition between Cd and background cations.

The conventional methods for treating wastewaters containing cadmium involve alkaline precipitation and ion exchange. However, due to high maintenance costs, these methods do not suit the needs of many developing and emerging economies such as India (Naidu et al. 1994). These authors further reported that out of the available treatment methods, adsorption was selected because of its sludge-free clean operation and the feasibility of using a variety of adsorbents, such as activated carbon discarded automotive tyres, agricultural products and by-products, and starch Xanthate, for cadmium removal. A variety of adsorbents, including clays, zeolites, dried plant parts, agricultural waste biomass, biopolymers, metal oxides, microorganisms, sewage sludge, fly ash, activated carbon, magnetite and hematite have been used for cadmium removal (Mahalik et al 1995, Singh et al. 1998, Alloway et al. 1999, Cornell et al. 2003, Marin et al. 2007 and

Tan et al. 2009). Singh et al. (1998) reported that the maximum Cd removal by hematite was 98% at a cadmium concentration of 44.88 μmol/L, a temperature of 20^0 C and pH 9.2 with 40 g/L of hematite of particle size <200 μm and equilibrium contact time, 2 h. Hu et al. (2004) and Petrova et al. (2011) reported that different nano iron oxide particles are particularly attractive for remediation purposes due to their significant surface area to mass ratio leading to a relatively high density of reactive sites and heavy metal removal capacity. They further reported that heavy metals are either reduced at the mixed magnetite-maghemite nanoparticles surface (e.g., Cr(III), As(III)) or directly adsorbed to the magnetite- maghemite nanoparticles surface where they are rendered immobile (e.g., Cr(III), As(III)). Petrova et al. (2011) reported that in an oxidizing atmosphere, magnetite is oxidized to maghemite or hematite, namely:

$$4Fe_3O_4 + O_2 \rightarrow 6Fe_2O_3 \quad \text{---------- (1)}$$

According to Cornell et al. (2003) and Petrova et al. (2011), magnetite (Fe_3O_4) is commonly found in the environment and can form via several pathways, including biotic and abiotic reduction of ferric iron Fe^{3+} oxides and the oxidation of ferrous iron Fe^{2+} and iron metal (Fe^0). Magnetite can also adsorb cadmium (Cd), cobalt, chromium and arsenic from aqueous solution. The controlling mechanism of the adsorption process is generally a function of the standard redox potential of the contaminant metal. The standard redox potential of Cd^{2+} (–0.2 to - 0.40 V, 25 ^{0}C) is very close to that of iron oxide (–0.25 to - 0.45V, 25 ^{0}C), and thus, the removal of Cd^{2+} ions by iron oxide is due to sorption (Pang et al. 2007 and Geological Survey of Japan, 2005).

Boparai et al. (2010) found that the maximum Cd uptake capacity of Zero-Valent Iron (nZVI) for Cd^{2+} was 769.2 mgg^{-1} at pH 8.5 and 297 K. These authors showed further that the adsorption process was endothermic, spontaneous and chemisorptive. However, there has been limited use of nZVI in site remediation because of its extremely reactive nature, improper handling during application and its toxicity (Li et al 2009, and Phenrat et al. 2009). These authors further reported that nZVI produces highly reactive and unstable molecule free radicals through the transformation process. These free radicals need additional electrons for stabilization and can effect antioxidant enzymatic activities, peroxidation of membrane lipids, modification of nucleic acids, and eventually cause cell death and tissue injury. In addition, nZVI particles can also affect wildlife through consumption and respiration if they are directly introduced to lakes or streams during surface water remediation. Gavaskar et al. (2005) noted that the toxicity of the potential by-products needs to be considered when assessing the pros and cons of using nZVI for remediation. If the contaminant cannot be completely degraded by nZVI and the by-products formed in the system pose a greater environmental hazard than the original target contaminant, then the application of nZVI in site remediation might not be the best solution. Phenrat et al (2009) reported that nZVI particles can be more toxic than nanoscale iron oxides (e.g. γ-Fe_2O_3, Fe_3O_4 and Fe_2O_3 etc.). They further demonstrated that oxidative stress increased in rodent (BV2) microglia in the following order: fresh nZVI > aged nZVI (11 days)> magnetite = surface-modified nZVI. These researchers showed that fresh nZVI generated morphological evidence of mitochondrial swelling and apoptosis. Thus, it can be concluded that iron oxide is less toxic than nZVI.

According to Sharma (2008), different parameters, such as contact time, adsorbate concentrations, pH, and particle size of adsorbent, play important roles in the removal of metals from aqueous solutions. The objective of the present work is to investigate the adsorption kinetics of cadmium removal by mixed iron oxide nanoparticles (γ-Fe_2O_3-Fe_3O_4). Sorption kinetics was examined to develop an understanding of the rate and the controlling mechanisms (e.g., surface versus intraparticle diffusion) of sorption. Kinetic data can be used to predict the rate at which the target contaminant is removed from solution. The results from the study can be used to assess the utility of mixed maghemite-magnetite nanoparticles for heavy metal removal, in particular cadmium adsorption. This is one of the very few studies that have, to date, investigated the feasibility of Cd(II) removal from aqueous solution by mixed maghemite-magnetite (γ-Fe_2O_3-Fe_3O_4) nanoparticles. It is probably more realistic to evaluate the removal efficiency of the mixture because, in nature, these minerals commonly occur together. The identification of the chemical states of the adsorbed Cd using XPS analysis was a major contribution of the study. Theoretical multiplet analysis of the Cd adsorbed γ-Fe_2O_3-Fe_3O_4 presented in the study is a novel contribution to the literature on XPS studies. In addition, no published study has, to date, examined the effect of contact time, pH, solid/liquid ratio and temperature on the adsorption and distribution coefficient of Cd on mixed γ-Fe_2O_3-Fe_3O_4 surfaces.

5.2 Materials and Methods

5.2.1 Characterization of the adsorbent

Magnetite nanoparticles were purchased from Reade Advanced Materials (Rhode Island, U.S.A.). The size range for this commercial grade 'magnetite' was 20-80 nm. The sample arrived in powder form in an airtight plastic bag. Pre-adsorption laboratory characterization of the sample, however, showed that the sample was actually a mixture of maghemite and magnetite nanoparticles. The surface area of the sample was determined using the N_2 adsorption method and applying the Brunauer, Emmett, Teller (BET) equation and found to have an average value of 49.5 m^2/g. Further examination and characterization of the sample showed that the particles were dispersed and contained 99.9% pure 20-80 nm magnetite-maghemite particles that had a black and spherical morphology and a bulk density of 0.8 g/cm^3. X-ray photoelectron spectroscopy analysis confirmed that the mixed oxide (γ-Fe_2O_3-Fe_3O_4) comprised 74.8% maghemite (γ-Fe_2O_3) and 25.2% magnetite (Fe_3O_4) (Fig 5.10a).

5.2.2. Reagents

Stock solutions of cadmium (Cd) were prepared by dissolving a hydrated cadmium nitrate salt ($Cd(NO_3)_2.4H_2O$) in distilled water. Certified reagent grade chemicals were used to prepare all solutions for the experiments without further purification. Glass volumetric flasks and reaction vessels were treated with 10% HNO_3 and rinsed several times with de-ionized water before they were used.

A known amount (0.8 g/L) of maghemite-magnetite sample was added to a desired concentration of stock (Cd) solution in plastic bottles. Solutions were prepared with de-ionized water. Standard acid (0.1 M HNO_3) and base (0.1 M NaOH) solutions were used for pH adjustment. The pH of each solution was measured using an Orion combination electrode. In the batch test, Cd concentrations were kept in the range of 0.2-1.5 mg/L.

5.2.3 Batch adsorption procedure

Batch adsorption experiments were carried out by agitating 0.2 g of the adsorbent (20-80 nm mixed maghemite-magnetite particles) with 250 mL aqueous solution of cadmium of desired concentration, temperature, pH, and ionic strength in different polyethylene bottles on a shaking thermostat at 100-120 rpm. After predetermined time intervals, the adsorbent was separated from solutions by centrifugation. Adsorption was determined by measuring the concentration of cadmium (Cd) left in the aliquot by ICP-OES (inductively coupled plasma-optical emission spectroscopy). The pH of the solutions was maintained at the desired value by the addition of either 0.1 M HNO_3 or 0.1 M NaOH. In equilibrium and thermodynamic studies, experiments were carried out at different temperatures with solutions of different concentrations of cadmium. The experiments were carried out in triplicate and the mean values were reported. The results were found to vary within ±5%. The standard deviation of each point on the graphs was calculated. The resulting error bars representing standard deviation for the figures were found to be small. Blank experiments (distilled water plus adsorbent alone) did not reveal any detectable Cd adsorption by the adsorbent. The supernatant solutions were separated and solid samples

were dried in a vacuum desiccator. The dried Cd adsorbed maghemite-magnetite nanoparticles were kept in an airtight ceramic dish to prevent any reaction with air.

5.2.4 Instrumentation for XPS

All spectra were collected using a Kratos Axis Ultra X-ray Photoelectron Spectrometer (XPS). The samples were analyzed using a monochromatic Al Kα X-ray source (15 mA, 14 KV) and chamber pressures of 10^{-7}-10^{-6} Pa. The resolution function of the XPS instrument was found to be 0.35 eV using silver Fermi edge (Grosvenor et al. 2004), During the experiments, a charge neutralizer filament was used to control or minimize charging of the samples. The following conditions were used in the survey scans : energy range =0-1100 eV, pass energy =160 eV, step size = 0.7 eV, sweep time = 180 s and x-ray spot size = 700 * 400 μm. An energy range of 20–40 eV was used for the high-resolution spectra, depending on the peak being examined. The sampling volume of the XPS for a 10 nm depth of penetration and a slot of 700 microns by 160 microns was approximately 100 cubic microns. The photons interact with atoms in the surface region, causing electrons to be emitted by the photoelectric effect. XPS spectral lines are identified after the ejection of electron from the shell (1s, 2s, 2p, etc.). The ejected photoelectron has electron Binding Energy (BE):

$$BE = hv - E_k - \Phi \quad \ldots\ldots\ldots\ldots\ldots\ldots\ldots\ldots\ldots\ldots \quad (5.1)$$

Where: BE= Electron Binding Energy; E_k= Electron Kinetic Energy; Φ_{spec}= Spectrometer Work Function. Each electron contains its binding energy. By knowing this binding energy one can identify what element it is coming from. An important advantage of XPS

is its capability to obtain information on chemical states from the variations in binding energies, or chemical shifts, of the photoelectron lines.

All dried samples were transferred into the spectrometer via a glove box filled with N_2 (g) or Ar (g). This was done to minimize the exposure of the samples to air or airborne impurities. In order to provide fresh and clean mineral faces for the analysis, the dried samples were fractured in a vacuum prior to the analysis.

5.2.5 Theory

5.2.5.1 The distribution coefficient K_D

The uptake distribution coefficient, K_D, in Equation. 5.2 is defined as the concentration of the species adsorbed per gram of the sorbent divided by its concentration per L in the liquid phase:

$$K_D = (C_i - C_{eq})V/C_{eq}\ m\ (L/g) \quad \ldots\ldots\ldots\ldots (5.2)$$

Here, V is the volume of the solution in L and m is the mass of sorbent in g.

5.2.5.2 Pseudo first-order equation

The pseudo first-order equation for any chemical system can generally be illustrated as (Lagergren, 1898):

$$dq_t/dt = k_{1ads}\,(q_e - q_t\,) \quad \text{----------(5.3)}$$

where q_e and q_t represent the adsorption capacities (mg/g) at equilibrium and at time t, respectively, and k_{1ads} is the rate constant for pseudo first-order adsorption (min^{-1}). After

integration and considering the boundary and initial conditions, $t = 0$ to $t = t$ and $q_t = 0$ to $q_t = q_t$, Eq. (5.3) can be expressed as :

$$\text{Log}\,(q_e - q_t) = \text{Log}\,q_e - k_{1ads} * t/2.303 \quad \text{----------(5.4)}$$

2.5.3 The pseudo second-order equation

According to Ho et al. (2000), the pseudo second-order adsorption kinetic rate equation may be illustrated by equation (5.5):

$$dq_t/dt = k_{2\,ads}(q_e - q_t)^2 \quad \text{----------(5.5)}$$

where, k_{2ads} indicates the rate constant of pseudo second-order adsorption ($g*mg^{-1}min^{-1}$). Applying the boundary conditions t=0 to $t = t$ and q_t =0 to $q_t = q_t$, the integrated form of Eq. (5.5) can be reduced to equation (5.6):

$$1/(q_e - q_t) = 1/q_e + k_{2ads} * t \quad \text{----------} \quad (5.6)$$

which is the integrated rate law for a pseudo second-order reaction. Eq. (5.6) can be re-arranged to give Eq. (5.7):

$$t/q_t = 1/k_{2\,ads}\,q_e^{\,2} + t/q_e \quad \text{----------(5.7)}$$

If the initial adsorption rate, h (mg/g min) is:

$$h = k_{2\,ads} * q_e^{\,2} \quad \text{----------(5.8)}$$

then Eqs. (5.7) and (5.8) can be expressed as:

$$t/q_t = 1/h + t/q_e \quad \text{----------(5.9)}$$

5.2.5.3 The intraparticle diffusion model

The intraparticle diffusion model was illustrated by Srivastava et al. (1989) and Weber et al (1963):

$$Y_{id} = k_{id}(t)^{a} \quad \text{----------(5.10)}$$

A linearized form of the equation can be expressed by

$$\log Y_{id} = \log k_{id} + a \log t \text{----------(5.11)}$$

where, Y_{id}, t, a and k_{id} represent the percent chemical species adsorbed, the contact time (min), the gradient of linear plots and the intra-particle diffusion rate constant (min^{-1}), respectively. The value of a also depicts the adsorption mechanism and k_{id} is considered a rate factor, i.e., percent adsorbate adsorbed per unit time.

5.3 Results and discussion

5.3.1 Parameters affecting the removal of cadmium

5.3.1.1 Effect of pH and distribution coefficient (K_D)

Batch experiments were conducted at different pH values to determine the optimum condition for Cd(II) removal by mixed maghemite-magnetite nanoparticles. The distribution coefficient, K_D, increased with increasing pH and the maximum K_D was observed at a pH of approximately 9.3 (Fig. 5.1). It is clear from Fig. 5.1 that the adsorption of cadmium is higher in the alkaline pH range of 8.0–10.0 than in the acid range. The standard deviation of each point on the graph was calculated as shown in Figure 5.1. The maximum standard deviation for 90% Cd removal was ±0.8 while the maximum standard deviation for distribution coefficient (K_D) was found to be ±0.3. Removal is very small in the acidic range and reaches a maximum at approximately pH

9.3. In a highly acidic medium, there is a chance of dissolution of the adsorbent (Stumn, 1987) and a consequent decrease in the number of active sites. In addition to this effect, the adsorbent surface is highly protonated in an acidic medium which is not favorable for cadmium uptake because in such a medium, Cd(II) is the dominant ion (Singh et al. 1998). As a result, the adsorption of cadmium is hindered due to electrical repulsion. As pH increases, the degree of protonation of the surface reduces gradually and approaches zero at pH 7.0 resulting in a gradual increase in adsorption. Above pH 8.0, where Cd^{2+} and $CdOH^{+}$ species are present in solution (Singh et al. 1998; Geological Survey of Japan, 2005), the adsorbent surface starts taking up a net negative charge creating an electrostatically favorable environment for higher cadmium uptake. Thermodynamic calculations show that different hydroxyl forms of the Cd ion can be observed depending on the pH of the solution. These forms include $Cd(OH)^{+}$, $Cd(OH)_2$, $Cd(OH)_3^{-}$ and $Cd(OH)_4^{2-}$ for Cd (Geological Survey of Japan, 2005). Within the pH ranges measured in the present adsorption experiments, Cd is expected to be dominantly present in its divalent ionic forms.

The functional groups of iron oxides consist of surface hydroxyl groups that usually arise from water adsorption or from structural OH. The surfaces of metal oxides in aqueous solution are generally attached with hydroxyl groups that can change in form at different pH values. These groups contain a double pair of electrons together with a dissociable hydrogen atom that can generate suitable conditions for them to react with both acids and bases. The charge on the iron oxide surface dominates the adsorption or desorption of protons and it is generated by the dissociation (ionization) of the surface hydroxyl groups

depending on the pH of the solution. Cornell et al. (2003) have noted that magnetite will produce Fe^{2+} and its hydrolysis products ($FeOH^+$, $Fe(OH)_2^0$, and $Fe(OH)_3^-$), depending on solution pH. Reported acidity constant, pKa, values for most iron oxides are usually between 5 and 10. The mixed maghemite-magnetite used in the present study consists of two types of iron oxides, γFe_2O_3 and Fe_3O_4. Thus, the abundance of Fe^{2+} or Fe^{3+} and the hydrolysis products of Fe^{2+} would influence the acidity constants of a specific surface group. Cornell et al. (2003) also reported that the acidity constant, pKa_1, of magnetite (25.2% of the adsorbent used in the present study), is 5.6. At pH greater than 5.6, the dominant functional groups at the iron oxide surface are $Fe(OH)_2^0$, and $Fe(OH)_3^-$. Moreover, most iron oxide surfaces hold the dominant functional groups of Fe^{2+} or $FeOH^+$ when solution pH is acidic, and $Fe(OH)_2^0$ and $Fe(OH)_3^-$ when basic. Thus, it is clear that iron oxide attracts positive Cd(II) species at high pH. The hydroxyl groups on the iron oxide surface at high pH are $Fe(OH)_2^0$, and $Fe(OH)_3^-$ which enhance the attraction of positively charged Cd(II) species at the higher pH value. The oxidation of magnetite produces maghemite (Cornell et al. 2003). Therefore, hydrated ferric oxide (HFO) nanoparticles can be produced by Fe(III) compound in aqueous solution. Adsorption would keep Cd(II) on the maghemite-magnetite surface through a Lewis acid base (LAB) interactions and iron oxide surfaces would coordinate with hydroxyl ions or water molecules that share their lone electron pair with Fe surface (Cornell et al. 2003). Thus, surface Fe atoms behave like Lewis acids in aqueous solution that react with Lewis bases (e.g. water). Cornell et al. (2003) further noted that the surface hydroxyl groups of the iron oxides in an aqueous environment work as a chemically reactive entities at the surface of the solid. These surface properties allow them to react with acid and bases.

Figure 5.1 shows the percent removal and uptake distribution coefficient (K_D) of Cd(II) in the solution after adsorption at different pH values and the results show high pH dependency during Cd(II) removal by mixed maghemite-magnetite particles. A maximum adsorption or removal efficiency of 90% was found at pH 9.3 and the adsorbed amount was 1.69 mg/g for an initial Cd(II) concentration of 1.5 mg/L. The affinities of the maghemite-magnetite for the different species of Cd(II) existing at different pH values, namely Cd^{2+} and $CdOH^{+}$ (Singh et al. 1998 and Geological Survey of Japan, 2005), may be different and attributable to the variation in removal efficiency at pH values above 8. From potentiometric titrations, it was found that the surface of magnetite particles had a positive surface charge up to pH 6.8, the point of zero charge, and a negative surface charge in the pH range 6.8-9.5 (Yean et al. 2005). Tuutijarvi et al. (2009) found that maghemite had a point of zero charge at pH_{pzc} 7.5 and the more alkaline the condition the more negative was the surface charge of the adsorbent and, accordingly, the more attractive to positive Cd(II) species at higher pH. Thus, it was postulated that mixed maghemite-magnetite particles can adsorb either negatively or positively charged metal species by electrostatic attraction as well as by redox reaction depending on pH.

The possibility of Cd^{2+} precipitation was also investigated. Since the system contained mixed iron oxides and cadmium nitrate solution, the only anions that could precipitate with Cd^{2+} at high pH were OH^{-} and NO_3^{-}. Geochemical equilibrium calculations using MINTEQA2 or PHREEQC gave negative saturation indices for Cd solids (for example, $Cd(OH)_2$), indicating that the solution was undersaturated with respect to these solids. From these results, it can be concluded that Cd^{2+} did not precipitate, but was instead

adsorbed. In fact, a number of researchers (Moore et al. 1984; Singh et al. 1998; and Geological Survey of Japan, 2005) have noted that cadmium would not precipitate at pH less than 10 when the solution contains very low Cd concentration.

5.3.1.2 Time of Equilibrium

The kinetics of Cd(II) adsorption was studied by varying the contact time between maghemite-magnetite and the respective solution from 10 to 140 min using 0.8 g/L adsorbent at a Cd concentration of 1.5 mg/L and pH 9.3. Batch adsorption experiments were carried out in order to find the optimum retention time. The results showed that the sorption efficiency increases rapidly and more than 75% of the adsorbed Cd occurred within 60 mins when a solid–liquid ratio of 0.8 was used. The rapid uptake of Cd(II) by mixed maghemite-magnetite nanoparticles is perhaps due to external surface sorption, which is different from microporous adsorption. Although nearly all the adsorption sites of maghemite-magnetite nanoparticles are present on the exterior of the adsorbent compared to the porous adsorbent, it is easy for the adsorbate to contact these active sites, thus resulting in a rapid approach to equilibrium. The current study illustrates that 120 minutes are needed to reach equilibrium. Figure 5.2 presents the adsorption and uptake distribution coefficient (K_D) of Cd on mixed maghemite-magnetite nanoparticles. In Figure 5.2, the range of standard deviations for the adsorbed Cd concentration (mg/g) on the graph was found to be very small, that is, ±0.002 to ±0.025.

Cd uptake increases with elapsed time and reaches equilibrium in 2 hrs for the initial concentration of 1.5 mg/L. Such observations were also noted at various pH values and temperatures of the system with the 20-60 nm adsorbent particles. However, the uptake of cadmium from water by mixed maghemite-magnetite depended on the initial concentration of cadmium. The maximum removal was found to be 1.68 mg/g or 90% at an initial concentration of 1.5 mg/L and maghemite-magnetite nanoparticle concentration of 0.8 g/L. The distribution coefficient, K_D, increases with increasing contact time and the maximum K_D was found to be 11.25 L/g after 2 hours (Fig. 5.2).

The process was not spontaneous and it took 2 h to complete the adsorption under the given conditions. There are three possible reasons for this. First, Cd(II) species may transfer from the bulk fluid phase to the outer particle surface of the adsorbent for contact (film diffusion). Second, the Cd species can migrate within the micro and macro pores of the mixed maghemite-magnetite particles (intra-particle diffusion) (Singh et al. 1998). Finally, there might be electrostatic attraction or reaction occurring between adsorbate (Cd(II) species) and adsorbent.

5.3.1.3 Effect of Solid/liquid ratio (S/L) and distribution Coefficient (K_D)

The operating conditions used were: initial cadmium concentration = 1.5 mg/L, pH 9.3 and T =22 ± 0.5^0 C. The solid/liquid (S/L) ratio was varied from 0.1 to 1. Figure 5.3 shows the effect of S/L ratio on the adsorption of cadmium. It can be seen that the percentage cadmium adsorption increased at the high S/L ratio. This is due to an

increasing surface area at a high S/L ratio. The resulting standard deviations were small, as indicated by the error bars in Figure 3. The standard deviations for the Cd removal (%) at S/L ratios of 0.8, 0.9 and 1.0 were calculated to be ±0.25, ±0.3 and ±0.3 respectively.

The distribution coefficient, $K_{D,}$ showed the reverse trend (Fig. 5.3) for different concentrations of adsorbents during the removal of Cd(II). Similar results were reported by Barkat et al. (2009). In the experimental conditions used in the present study, the surface of mixed maghemite-magnetite contained negative hydroxyl groups (OH^-) that were likely replaced by positive Cd-O ligands. The adsorption capacity (Fig. 5.3) was found to be almost 91% or 1.7 mg/g when the S/L ratio and K_D were 0.8 and 12.63 L/g, respectively. In equation (5.2), the mass of adsorbent, m, increases with S/L ratio, which results in a decrease in K_D value. The Cd removal was found to be constant beyond an adsorbent concentration of 0.8 g/L, although the adsorbent concentration (m, the denominator in equation (5.2)) increased with S/L. This would explain the observed reverse trend in the distribution coefficient, K_D (Figure 5.3).

5.3.1.4 Effect of temperature on Cd removal

Santiago et al. (2012) found that the point of zero charge for magnetite particles depends on the solution temperature. They further reported that pH_{pzc} decreased from 7.1 to 6.5 when the solution temperature was increased from 0 to 50^0C. Since the point of zero charge of iron oxides does not vary significantly in the temperature range of 10-50^0C, the change in protonation/deprotonation (acidity) constants of the surface groups would be

negligible in the case of Cd adsorption on mixed maghemite-magnetite. Cornell et al. (2003) found the pHzpc of mixed iron oxide to be 6.8-7.5 depending on temperature.

In the present study, the effect of temperature on Cd (II) adsorption by mixed maghemite-magnetite was examined from 10^0 to 50^0C at pH 9.3, S/L = 0.8 and C_0 = 1.5 mg/L. The removal of Cd from a solution containing 1.5 mg/L initial concentration of Cd (II) decreased from 1.9 to 1.2 mg/g upon increasing the temperature from 10 to 50^0C. Figure 5.4 shows the effect of temperature on distribution coefficient and percent Cd removal by 20-60 nm mixed maghemite-magnetite nanoparticles. The resulting standard deviation on the graph was found to be very small. As indicated, percent removal decreases with increase in temperature. During Cd(II) removal, the distribution coefficient was 1248.75, 23.75,10.11, 6.5, 4.4,and 2.9 L/g at 10, 15, 22, 30, 40 and 50^0C, respectively. In other words, the distribution coefficient decreased from 1248.75 to 2.9 L/g, as shown in Figure 5.4. The percent Cd(II) removal also showed a decreasing trend, that is, 99.9% removal was found at 10^0C while almost 70% removal was observed at 50^0C. This indicates the exothermic nature of the process. The decrease in percent removal may be attributed to a relative increase in the escaping tendency of the solute from the solid phase to the bulk phase with an increase in solution temperature. The distribution coefficient, K_D varied in the same way (Figure 5.4).

5.3.2 Adsorption kinetics study

The adsorption kinetics study explains the solute sorption rate. It is obvious that this rate controls the residence time of adsorbate adsorption at the solid-solution interface. The adsorption of Cd on mixed maghemite-magnetite is not an instantaneous process because the Cd species have to diffuse from the solution to the surface of the mixed maghemite-magnetite, and then to the internal surface areas. The overall rate of approach of this process to equilibrium delineates the sorption kinetics. The kinetics of Cd(II) sorption on the mixed maghemite-magnetite was investigated using pseudo first-order, pseudo second-order and intraparticle diffusion kinetic models. The closeness of the experimental data and the model predicted values were expressed by the correlation coefficients (R^2, values close or equal to 1). The relatively high R^2 value implies that the model successfully illustrates the kinetics of Cd (II) adsorption.

5.3.2.1 Pseudo first-order equation and the pseudo second-order equation

Experimental data were fitted with the pseudo first-order and second-order equations to determine the reaction rate constant (k_{1ads}) of Cd removal by mixed maghemite-magnetite nanoparticles. Eq. (5.4) represents pseudo first-order equation. This equation means that the values of $\log(q_e - q_t)$ are linearly correlated with t. Thus a plot of $\log(q_e - q_t)$ versus t should give a linear relationship if the reaction follows first-order. The values k_{1ads} and q_e can be determined from the slope and intercept of the plot (Fig. 5.5). Figure 5.5 shows that the maximum standard deviation on the graph is ±0.05. The experimental data produced a trend line with correlation coefficient of $R^2 = 0.91$. From the plot, k_{1ads} was found to be 3.6×10^{-2} min^{-1}.

Similarly, Eq. 5.9 represents pseudo second-order equation. A plot of (t/q_t) against t in Eq. (5.9) should yield a linear relationship from which q_e and k_{2ads} can be calculated from the slope and intercept of the model equation (5.9). In Figure 5.6, the resulting standard deviation is very small. The value of k_{2ads} was found from the plot to be 3.96 x 10^{-2} g/mg*min. The adsorption kinetics data were modeled using the pseudo first order and pseudo-second order kinetic equations. It is seen from the results that the pseudo second-order adsorption kinetic equation is a better sorption kinetics model than the pseudo first-order kinetic equation, since it gave a better fit with the experimental data (correlation coefficient, $R^2 = 0.99$).

5.3.2.2 The intraparticle diffusion model

The intraparticle diffusion model was demonstrated by Srivastava et al. (1989) and Weber et al (1963). The application of the intraparticle diffusion model (shown in equation 5.11) to the experimental data in the present study gave a good fit plot with a correlation coefficient, $R^2 = 0.98$ and a value of "a" that is less than unity (0.27). This supports an enhanced rate of adsorption (Srivastava et al. 1989, Erhan et al. 2004 and Barkat et al. 2009) which, in turn, is linked to improved bonding. The resulting R^2 values (average 0.98) also show that the intra-particle diffusion process may be the rate-limiting step (Barkat et al. 2009). Thus, higher values of k_{id} demonstrate an enhancement of adsorption (Erhan et al. 2004), indicating a better adsorption mechanism that facilitates bonding between Cd(II) ions and adsorbent particles. The value of k_{id} (also considered as

a rate factor, i.e., percent Cd(II) adsorbed per unit time) was estimated to be 24.56 min^{-1} from the slope of such plots (Fig. 5.7). Thus, it may be assumed that the adsorption of cadmium is partly diffusion controlled and partly due to an electrostatic effect along with specific adsorption involving the adsorption of Cd^{++} and $CdOH^{+}$ on mixed maghemite-magnetite nanoparticles in the alkaline pH range (Singh et al. 1998).

5.3.3 Multiple linear regression modelling for the Cd adsorption data

The simultaneous effect of several independent variables, such as pH, contact time, S/L ratio and temperature on the dependent variable, percentage Cd removal was modelled using multiple regression analysis (MRA) and statistical computation software, R. The results are presented in Table 5.1 and 5.2. These results show that the independent variables have a significant effect ($p<0.05$) on the percentage removal of Cd by mixed maghemite-magnetite nanoparticles. Using these data, the following model has been suggested to predict the uptake of Cd under given conditions:

$$Y = 21.2095799X_1 + 0.299232X_2 + 42.2337443X_3 - 0.75027340X_4 - 165.09903 \ldots\ldots \quad (5.12)$$

Where, Y indicates the percentage removal of Cd and X_1, X_2, X_3 and X_4 represent the sample pH, contact time in minute, solid-liquid ratio and temperature (^0C) of the system respectively. Table 5.2 and 5.3 demonstrate the model values estimated using Eq. 5.12 and the experimental values. The results show that the coefficients for pH, contact time and S/L ratio are highly significant at 0.1% level ($p < 0.001$) while the coefficient of temperature is significant at 1% level ($p <0.01$). This indicates that pH, contact time and S/L have a greater effect on cadmium removal than temperature. The model shows that

an increase in temperature (X_4) would decrease the removal efficiency (Y) under the given conditions. The overall F-test and t-test also support the significance level of the different independent variables in the proposed model. The multiple correlation coefficient (R^2) value from the fitted multiple regression model was 0.8841, which means that 88.41% of the total variation in Cd removal could be explained by the independent variables in the fitted model. Figure 5.8 illustrates the experimental and model predicted values of the Cd percentage removal at different conditions.

5.3.4 X-ray Photoelectron Spectroscopy (XPS)

X-ray Photoelectron Spectroscopy (XPS) studies were carried out to assess the elemental composition and chemical oxidation states of surface and near-surface species. The Casa-XPS software was used to draw and analyze all spectra (Fairley, 2003). XPS wide scan spectra of fresh maghemite-magnetite and Cd adsorbed maghemite-magnetite sorbents are shown in Figure 5.9. Four major peaks at binding energies of 281.55, 396.35, 526.55 and 707.15 eV, representing C 1s, N 1s, O 1s, and Fe 2p respectively, are observed for the virgin sorbent (Figure 5.9a). Significant changes can be seen in Figure 5.9b after Cd(II) adsorption; the peak at binding energy of 401.25 eV for Cd 3d appears in the Cd(II) loaded sorbent (Fig 5.9b and 5.9c).

The XPS survey of Fe 2p on the mixed γ-Fe_2O_3- Fe_3O_4 (Figure 5.10a) shows two photoelectron peaks centered at 709 and 711-714 eV, indicating the presence of both Fe(II) and Fe(III) at the adsorbent surface. The Fe 2p high resolution spectra were fitted following the example of Pratt et al. (1994) using theoretical multiplet peak (Gupta et al.

1975). In the present study, the peak full width at half maximum (FWHM) was found to be between 1.0 and 3.3 eV. Mutiplet splitting can occur for more core level photopeaks when the atom contains unpaired valence electrons. Grosvenor et al. (2004) reported that multiplet-splitting of p and higher sublevels is complicated due to orbital-angular momentum coupling. According to Hochella (1988), 2p sublevels of transition metals in high-spin or paramagnetic states exhibit considerable line broadening due to complex multiplet splitting phenomena and despite the complexity of these line shapes, spectra of this sort can still be used to determine the oxidation state of the iron in the near-surface of minerals.

The XPS results, shown in Fig 10, present the theoretical multiplet peaks for iron and Cd adsorbed iron oxide at the surface of the γ-Fe_2O_3 and Fe_3O_4 mixture. Theoretical multiplet analysis of the γ-Fe_2O_3-Fe_3O_4 mixture gave 74.8% of maghemite and 25.2% of magnetite (Fig. 5.10a). No sharp hematite peak was observed in the XPS spectra. After Cd(II) adsorption on the maghemite-magnetite mixture, it was found that the percent of maghemite decreased to 68.5% (Fig 5.10b). At the same time, the percentage of magnetite was increased (Fig. 5.10b). These results suggest that a redox reaction occurred on the mixed maghemite-magnetite surface when Cd(II) was introduced. Changes in the relative abundance of Fe(II) and Fe(III) in magnetite and maghemite spectra (Fig. 5.10a and 5.10b) upon Cd(II) adsorption are quantitatively elucidated. The data show that in magnetite spectra, the relative content of the Fe(III) and Fe(II) increases from 17.3 to 21.6 % for Fe(III) and 7.9 to 9.9 for Fe(II) indicating the reduction of maghemite in the

mixture particles. This indicates reduction at the mixed oxides surface as well as an increase in the amount of magnetite from 25.2% to 31.5%.

The Cd 2d spectrum of the Cd(II) adsorbed sorbent can be found at the peak containing binding energy of 405.06 eV shown in Figure 11. Additional Auger line has also been observed with MNN group for cadmium at 786.2 eV. The $Cd3d_{5/2}$ peak and Auger parameter analysis suggest the presence of a Cd(II) compound, possibly a mixture of CdO and $Cd(OH)_2$. The Cd $3d_{5/2}$ peak for the native oxide (polished Cd metal surface, air exposed) was found at 405.06 eV with a FWHM of 1.25 eV (10 eV Pass Energy). The XPS surveys showed that Cd^{2+} ions may undergo oxidation-reduction mechanism upon exposure to mixed maghemite-magnetite as well as the Cd^{2+} ions are most probably fixed by complexation mechanism with the oxygen atoms in the oxy-hydroxyl groups at the shell surface of the iron oxide nanoparticles. Cd(II) may be attracted to the iron oxide surface by adsorption or surface complex formation, which include electrostatic interactions or specific surface bonding. Cd(II) is thus retained on the iron oxide surface by chemical reduction as well as by electrostatic interactions. The amount of cadmium used in the XPS spectrum analysis was very low (0.1-0.4 atomic percent) compared to the amount of iron detected (10-20 %) and any iron-Cd complex contribution to the Fe 2p spectrum would be obscured by the large maghemite-magnetite signal.

5.4. Conclusions

In the present study, batch adsorption experiments for the adsorption of Cd (II) ions from aqueous solutions have been carried out using mixed maghemite-magnetite as adsorbent. The adsorption characteristics have been examined at different contact times, pH values, initial Cd (II) ion concentrations, and different adsorbent dosage levels. The obtained results can be summarized as follows:

1. The adsorption rate of Cd (II) ions was fast initially, and about 40% of total Cd (II) was removed within 5 min. Thereafter, the adsorption capacity increased slowly with contact time before reaching a plateau after the contact time of 2 h, and then remained constant.

2. Generally, the adsorption capacity of Cd (II) ions by mixed maghemite-magnetite increased with an increase in the pH of the adsorbate solution.

3. With an increase in initial Cd (II) ion concentration, the adsorption capacity of Cd (II) ions on mixed maghemite-magnetite increased but the removal percentage of Cd (II) ions decreased.

4. An increase in adsorbent dosage increased Cd (II) removal but decreased adsorption capacity.

5. Adsorption of Cd (II) ions by mixed maghemite-magnetite was found to follow the pseudo-second-order kinetics model.

6. X-ray photoelectron spectroscopy studies confirmed that Cd^{2+} ions may undergo oxidation-reduction reactions upon exposure to mixed maghemite-magnetite, or may become fixed by complexation with oxygen atoms in the oxy-hydroxy groups at the shell surface of the iron oxide nanoparticles. Theoretical multiplet analysis identified the γ-

Fe_2O_3- Fe_3O_4 mixture to comprise 74.8% of maghemite and 25.2% of magnetite (Fig. 5.10a). Following Cd(II) adsorption by the maghemite-magnetite mixture, the percent maghemite decreased from 74.8 to 68.5% (Fig 5.10b).

7. Batch adsorption studies indicate that mixed maghemite-magnetite has strong adsorption towards Cd (II) ions. The results of the present work show that 0.8 g/L of 20-80 nm maghemite-magnetite particles removed up to 1.5 mg/L Cd, and the approximate cost of this nano-scale adsorbent is $225/kg (Reade Advance Materials, 2009). Thus the cost of using nano maghemite-magnetite particles adsorbent would be $0.18/L. To take advantage of this, maghemite-magnetite particles can be used in water treatment and site remediation to control or minimize exposure to living organisms. Mixed maghemite-magnetite particles can also be used in the design of permeable reactive barriers for subsurface remediation. Permeable reactive barriers containing maghemite-magnetite particles could be employed for in situ remediation of groundwater contaminated with heavy metals. To develop a decision framework for helping utilities determine the most appropriate adsorbent based on cost and performance, more research and investigations are necessary to determine the applicability of mixed iron oxide particles in the construction of permeable reactive barriers.

5.5 References

Alloway, B.J., Steinnes, E., 1999. Anthropogenic additions of cadmium to soils, in: M.J. McLaughlin, B.R. Singh (Eds.), cadmium in soils and plants, Kluwer Academic Publishers, Boston.

Barkat, M., Nibou, D., Chegrouche, S., Mellah, A., 2009. Kinetics and thermodynamic studies of chromium(VI) adsorption onto activated carbon from aqueous solutions. Chemical Engineering and processing 48, 38-47.

Boekhold, A.E., Temminghoff, E.J.M., & Vander Zee, S.E.A.T.M., 1993. Influence of electrolyte composition and pH on cadmium sorption by an acid sandy soil. Journal of Soil Science, 44, 85-96.

Boparai, H.K., Joseph, M., Caroll, D,M., .2009. Kinetics and thermodynamics of cadmium ion removal by adsorption onto nano zerovalent iron particles. Journal of Hazardous Materials, 186, 458-465.

Cornell, R., and Schwertmann, U., 2003. The Iron Oxides: Structure, Properties, Reactions, Occurrence and Uses. Weinheim: Willey-VCH.

Erhan, D., Kobya, M., and Ehf, S., Ozkan, T., Adsorption kinetics for Cr (Vi) removal from aqueous solution on activated carbon prepared from Agro wastes. J. water, 30 (4),533-541.

Fairley, N., 2003. CasaXPS Version 2.2.19 (2003).

Gavaskar, A., Tatar, L., and Condit, W., 2005. Cost and performance report nanoscale zero-valent iron technologies for source remediation. Naval Facilities Engineering Command (NAVFAC). Contract report: CR-05-007-ENV.

Geological Survey of Japan. 2005. Atlas of Eh-pH diagrams- Intercomparison of thermodynamic databases. National Institute of Advanced Industrial Science and Technology. Open File Report No.419.

Grosvenor, P.A., Kobe, B.A., Biesinger, M.S., and McIntyre, N.S., 2004. Investigation of multiplet splitting of Fe 2p XPS spectra and bonding in iron compounds. Surf. Interface Anal. 36: 1564–1574.

Gupta., R.P., and Sen, S.K., 1975. Calculation of multiplet structure of core *p* -vacancy levels. Phys. Rev. 12 (1975), 15-19.

Ho, Y.S., McKay, G., Wase, D.A.J., and Foster, C.F., 2000. Study of the sorption of divalent metal ions on to peat, Adsorp. Sci. Technol. 18, 639–650.

Hochella, M.F., 1988. Auger electron and X-ray photoelectron spectroscopies. Rivews in mineralogy and geo-chemistry. 18, 573-637.

Li, H., Zhou, Q., Wu, YF.J., Wang, T., and Jiang, G., 2009. Effects of waterborne nano-iron on medaka (Oryzias latipes): Antioxidant enzymatic activity, lipid peroxidation and histopathology. Ecotoxicol Environ Saf. 72, 3, 684-692.

Lo, I.M.C., Lam, C.S.C., and Lai, K.C.K., 2006. Hardness and carbonate effects on the reactivity of zero-valent iron for Cr(VI) removal .Water Research 40, 595 – 605.

Mahalik, M.P., Hitner, H.W., and Prozialeck, W.C., 1995. Teratogenic effects and distribution of cadmium (Cd^{2+}) administered via osmotic minipumps to gravid Cf-1 mice, Toxicol. Lett. 76, 195–202.

Martin, A.B.P., Zapata, V.M., Aguilar, O.M., Saez, J., and Lorens, M.L., 2007. Removal of cadmium from aqueous solutions by adsorption onto orange waste, J. Hazard. Mater. 139, 122–131.

Moore, J.W., and Ramamoorthy, S., 1984. Heavy metals in natural waters. Springer-Verlag New York Inc. ISBN 3-540-90885-4.

Naidu, R., Bolan, N.S., Kookana, R.S., and Tiller, K.G., 1994. Ionic-strength and pH effects on the sorption of cadmium and the surface charge of soils. European Journal of Soil Science, 45, 419-429.

Pang, S.C., Chin, S.F., and Anderson, M.A., 2007. Redox equilibria of iron oxides in aqueous-based magnetite dispersions: Effect of pH and redox potential. Journal of Colloid and Interface Science 311, 94–101.

Perez-Marin, A.B., Zapata, V.M., Ortuno, J.F., Aguilar, M., Saez, J., and Llorens, M., 2007. Removal of cadmium from aqueous solutions by adsorption onto orangewaste, J. Hazard. Mater. 139, 122–131.

Petrova, T.M., Fachikov, L., and J. Hristov, J., 2011. The magnetite as adsorbent for some hazardous species from aqueous solutions: a review. International Review of Chemical Engineering (I.RE.C.H.E.), 3,2,134.

Phenrat, T., Long, T.C., Lowry, G.V., and Veronesi, B., 2009. Partial oxidation ("aging") and surface modification decrease the toxicity of nanosized zerovalent iron. Environ Sci Technol. 43, 195-200.

Pratt, A.R., Muir, I.J., and Nesbitt, H.W., 1994. X-ray photoelectron and Auger electron spectroscopic studies of pyrrhotite and mechanism of air oxidation. Geochimica et Cosmochimica Acta 58, 827-841.

Rao, K.S., Mohapatra, M., Anand, A., and Venkateswarlu, P., 2010. Review on cadmium removal from aqueous solutions. International Journal of Engineering, Science and Technology 2, (7), 81-103.

Santiago, V.R., Fedkin, M.V., and Lvov, S.N., 2012. Protonation enthalpies of metal oxides from high temperature electrophoresis. Journal of Colloid and Interface Science 371, 136–143.

Sharma, Y.C., 2008. Thermodynamics of removal of cadmium by adsorption on an indigenous clay, Chem. Eng. J. 145, 64–68.

Singh, D.B., Rupainwar, D.C., Prasad, G., and Jayaprakas, K.C., 1998. Studies on the Cd (II) removal from water by adsorption. Journal of Hazardous Materials 60, 29–40.

Srivastava, S.K., Tyagi, R., and Pant, N., 1989. Adsorption of heavy metal ions on carbonaceous material developed from the waste slurry generated in local fertilizer plants, Water Res. 23, 1161–1165.

Stumn, W., 1987. Aquatic surface chemistry—chemical process at the particle-water Interface, Wiley, NewYork.

Tan, G.Q., and Xiao, D., 2009. Adsorption of cadmium ion from aqueous solution by ground wheat stems, J. Hazard. Mater. 164, 1359–1363.

Tuutijärvi, T., Sillanpääa, J.L.M., and Chenb, G., 2009. As(V) adsorption on maghemite nanoparticles. Journal of Hazardous Materials 166, 1415–1420.

Waalkes, M.P., 2000. Cadmium carcinogenesis in review, J. Inorg. Biochem. 79, 241–244.

Weber, W.J., Asce, J.M., and Morris, J.C., 1963. Kinetics of adsorption on carbon from solution, in: Proceedings of the American Society of Civil Engineers, J. Sanit. Eng. Div. 89, 31–59.

WHO., 2008. Guidelines for drinking water quality: recommendations, vol. 1, 3rd ed.,World Health Organisation, Geneva.

Yean, S., Cong, L., Yavuz, C.T., Mayo, J.T., and Yu, W.W., 2005. Effect of magnetite particle size on adsorption and desorption of arsenite and arsenate. Materials Research Society. J. Mater. Res. 20, 12, 3255-3264.

List of Tables

Tables

Table 5.1: Multiple regression analysis of Cd percentage removal (dependent variable) against pH, contact time, solid-liquid (S/L) ratio and temperature of the system (independent variables) for Cd- mixed maghemite-magnetite system.

Square of multiple correlation coefficient (R^2)	Regression Coefficients				
	pH , X_1	Contact time in min, X_2	S/L ratio, X_3	Temperature (^{0}C), X_4	Intercept, C
0.8841	21.2095799	0.2992320	42.2337443	-0.7502734	-165.09903

Table 5.2: Other parameters for model equation 5.12

Coefficients:	Std. Error	t value	Pr(>|t|)	Significance level [a]
C (Intercept)	27.46951	-6.010	2.40e-06	***
X_1	2.81835	7.526	5.46e-08	***
X_2	0.02505	11.947	4.62e-12	***
X_3	4.69080	9.004	1.80e-09	***
X_4	0.15945	-4.705	7.32e-04	**
[a]Significant level codes: 0 '***' 0.001 '**' 0.01 '*' 0.05 '.' 0.1 ' ' 1 [b]Adjusted R-squared: 0.8663 [c]F-statistic : 49.59 on 4 and 26 DF, [d]p-value: 8.499e-12				

Table 5.3: Percentage removal of Cd at different conditions – (experimental and model predicted values when initial concentration was 1.5 mg/L).

Different pH		Different Contact time in min		Different S/L ratio		Different Temperature (^{0}C)	
Experi-mental Cd removal (%)	Predicted values (%)	Experim-ental Cd removal (%)	Predicted values (%)	Experimen-tal Cd removal (%)	Predicted values (%)	Experimen-tal Cd removal (%)	Predict-ed values (%)
60	57.38819	40	50.9272	50	59.6482	99.9	100.33
60	63.75107	48	53.9195	60	61.7599	95	96.575
75	74.35586	55	56.9118	68	65.9833	89	91.324
80	80.71873	60	59.9042	75	70.2067	84	85.321
86.5	84.9607	70	64.3926	80	74.430	78	77.818
90	89.2026	80	67.385	85	82.8768	70	70.316
90	91.3235	87	73.3696	91	91.3235		
		90	85.3389	91	95.5469		
		90	91.3235	91	99.7703		

List of Figures

Figure 5.9: XPS wide scan spectra of the (a) fresh maghemite-magnetite mixture (b) Cd(II) loaded maghemite-magnetite mixture (c) Cd(II) peak on Cd loaded maghemite-magnetite mixture (binding energy scale in order of descending values).

Figure 5.10: XPS spectra (a) nano-scale maghemite-magnetite particles and (b) Cd(II)-adsorbed mixed maghemite-magnetite- particles.

Figure 5.11: Cd 3d XPS spectra of Cd(II) loaded maghemite-magnetite mixture. (state background subtracted in data).

Figures

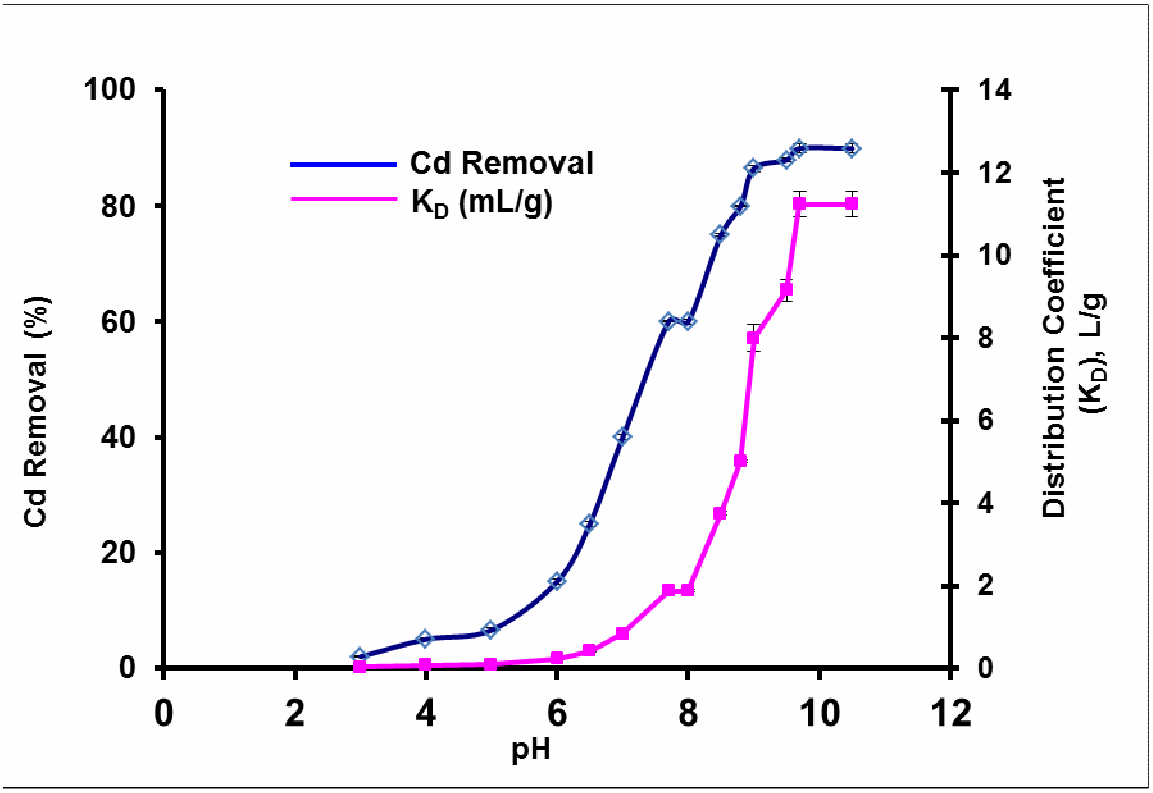

Figure 5.1: The effect of pH on Cd removal (%) and uptake distribution coefficient (K_D). Operating conditions: contact time = 120 min, T=22 ± 0.5^0 C, S/L = 0.8, Co = 1.5 mg/L.

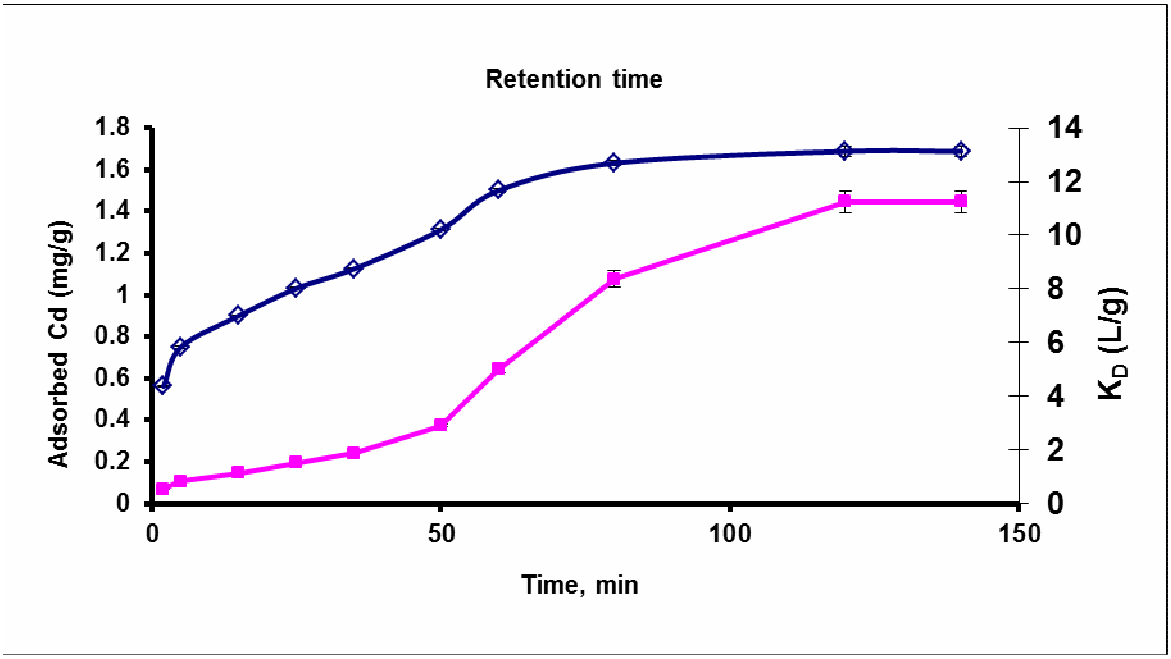

Figure 5.2: The effect of contact time on Cd(II) removal by mixed maghemite-magnetite. Conditions: Particle size: 20-60 nm, Temperature: 22 ± 0.5^0 C, pH: 9.3 and initial concentration: 1.5 mg/L.

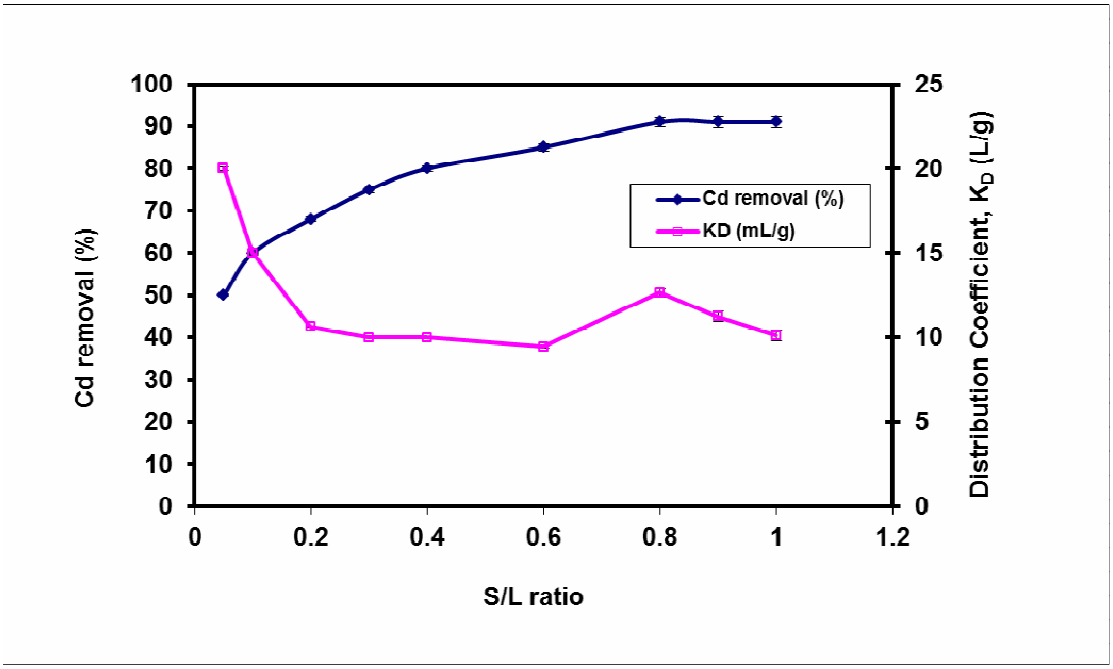

Figure 5.3: Uptake distribution co-efficient K_D and the Cd removal percentage (%) at different solid–liquid ratio.

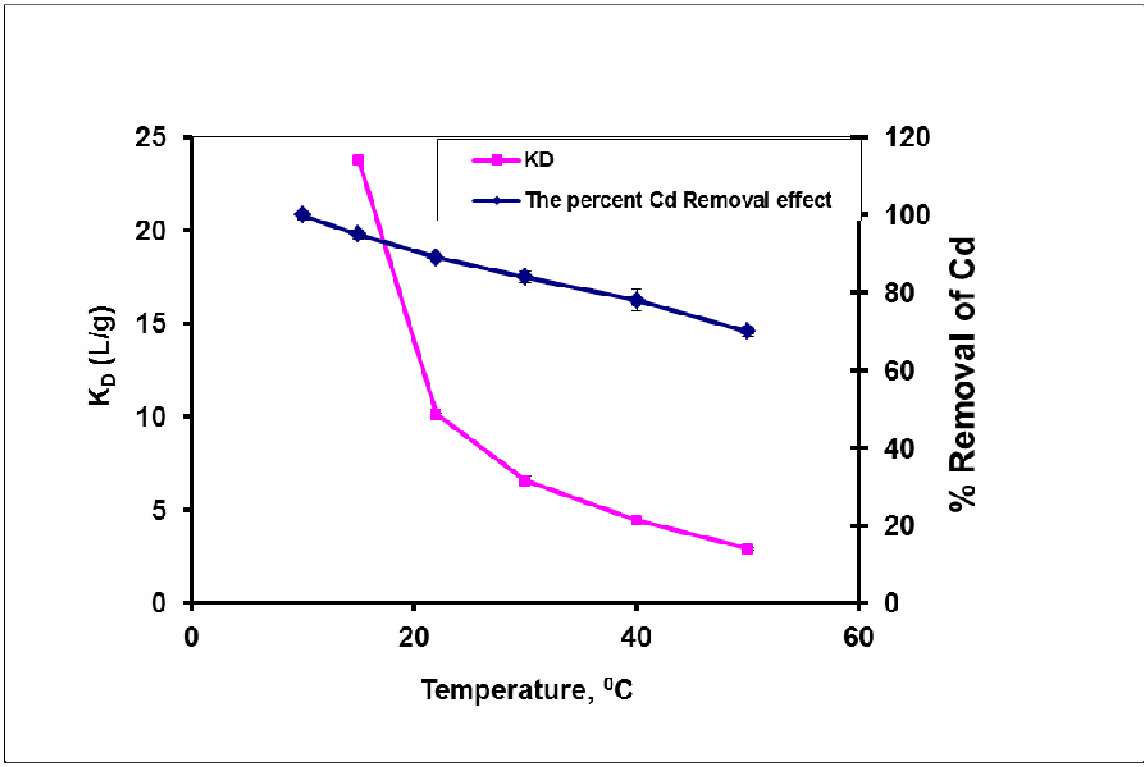

Figure 5.4: Uptake distribution coefficient K_D and Cd removal percentage (%) at different temperature. (Temperature ranges: 10^0 to 50^0C at pH 9.3, S/L = 0.8 and C_0 = 1.5 mg/L

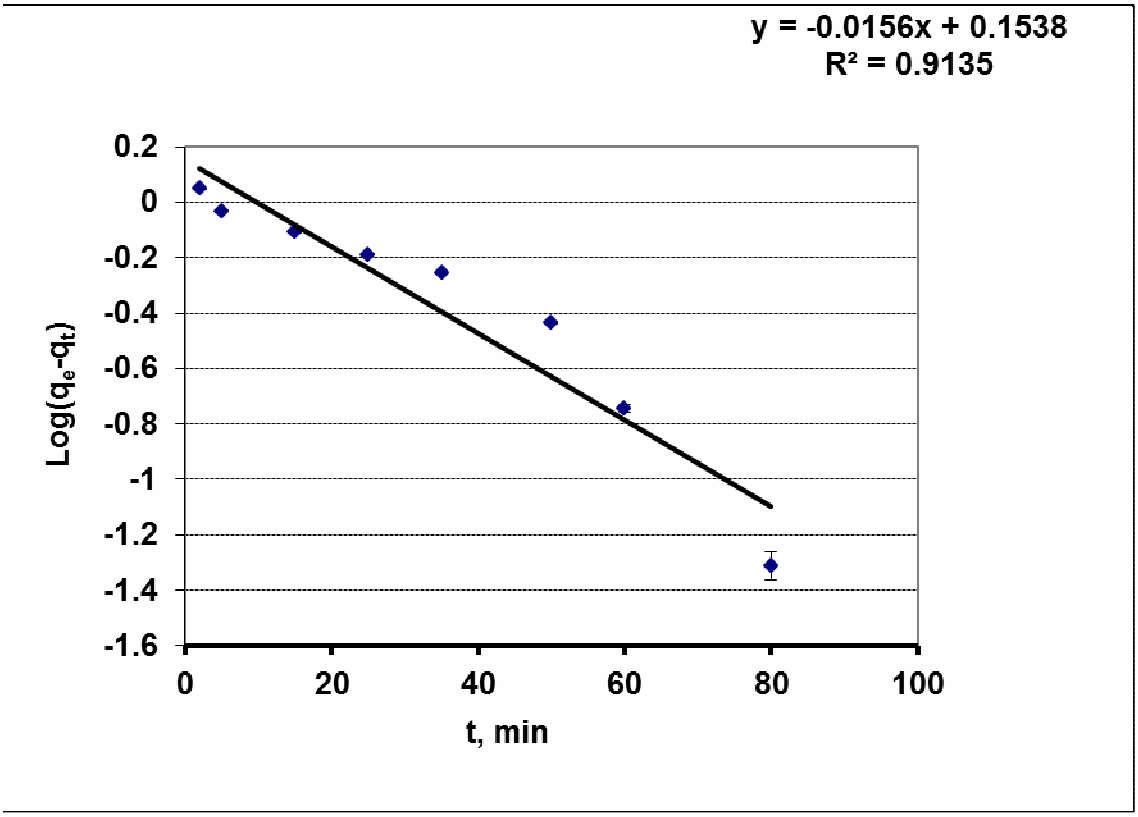

Figure 5.5: The rate constant of pseudo-first order adsorption k_{1ads} and the amount of Cd(II) ion adsorbed at equilibrium, q_e.

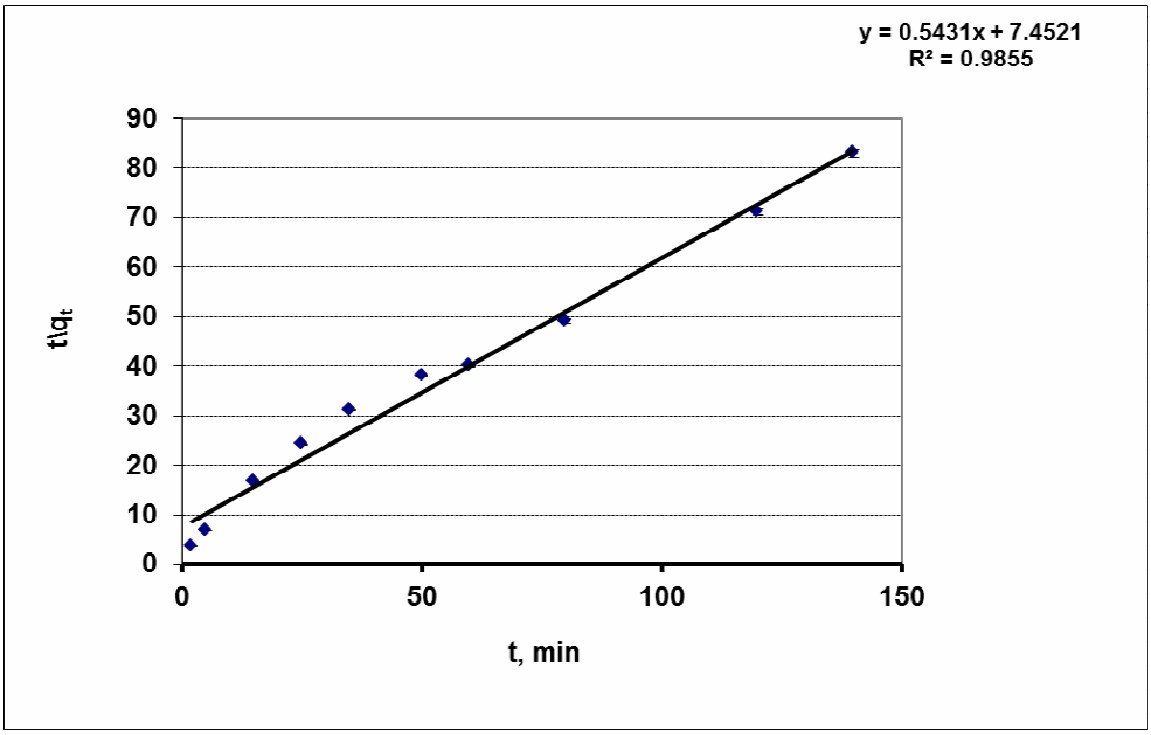

Figure 5.6: The rate constant of pseudo-second order adsorption $k_{2\,ads}$ and the amount of Cd(II) ion adsorbed at equilibrium, q_e.

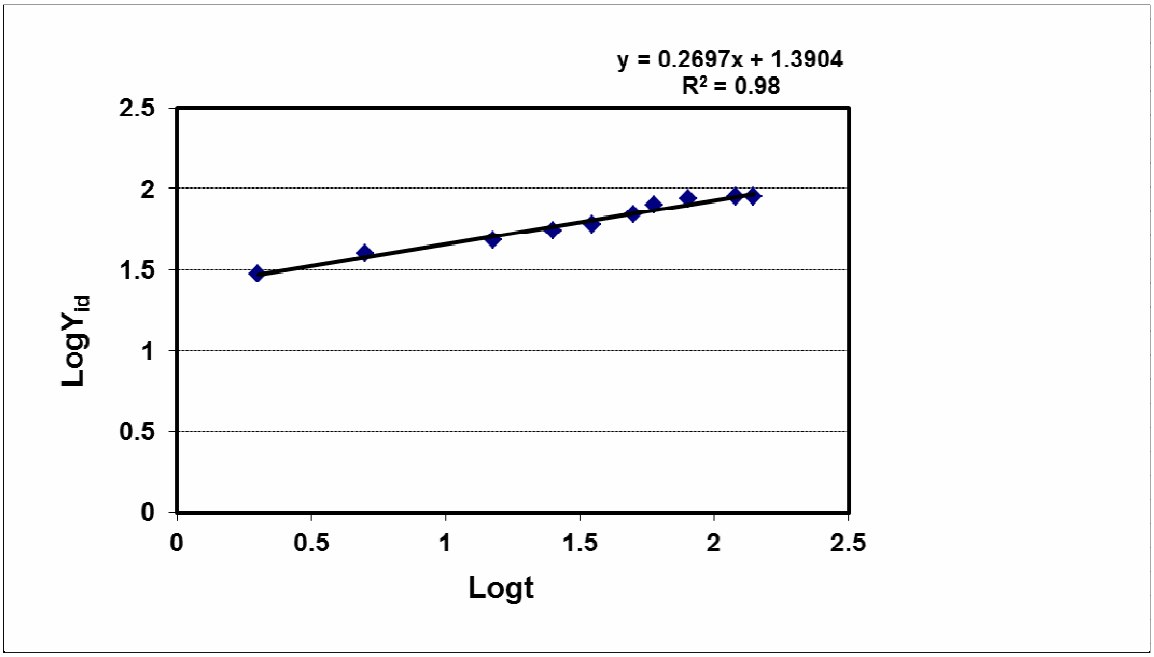

Figure 5.7: Determination of the intra-particle diffusion rate constant, k_{id} (min^{-1}) during Cd(II) removal by mixed mahemite-magnetite.

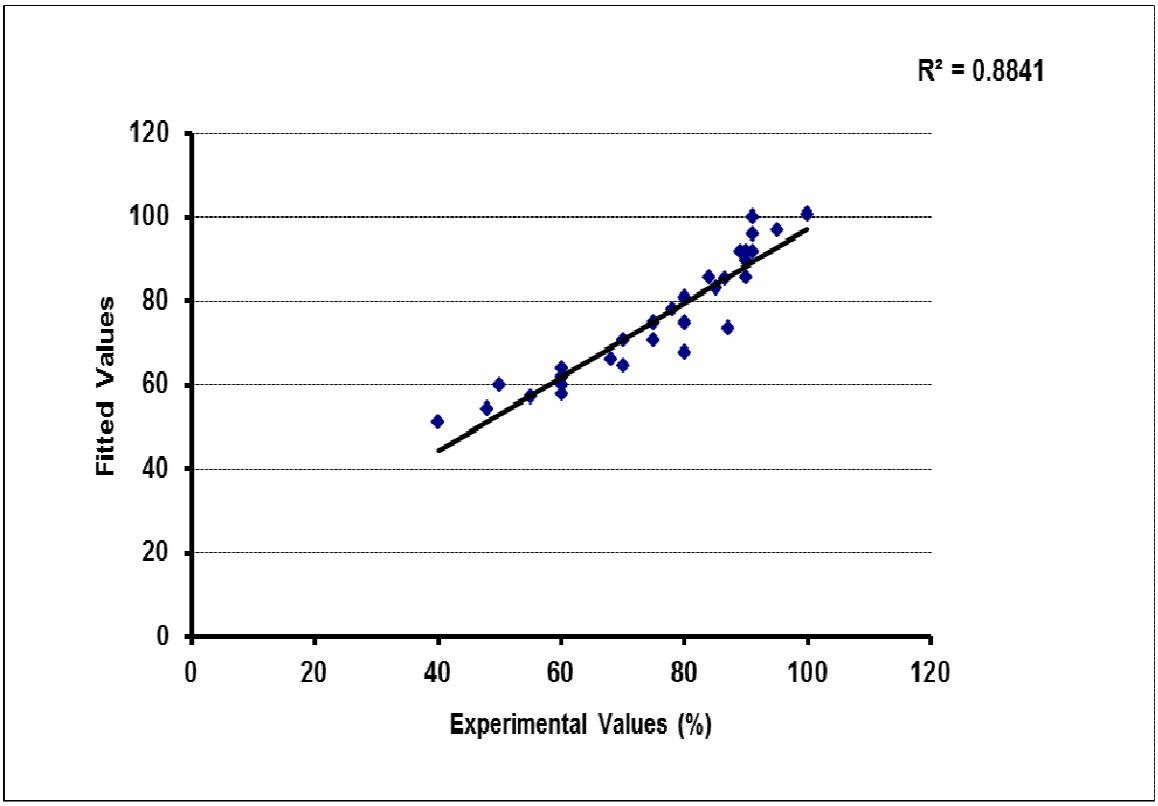

Figure 5.8: Percentage removal of Cd at different conditions– (experimental and model predicted values

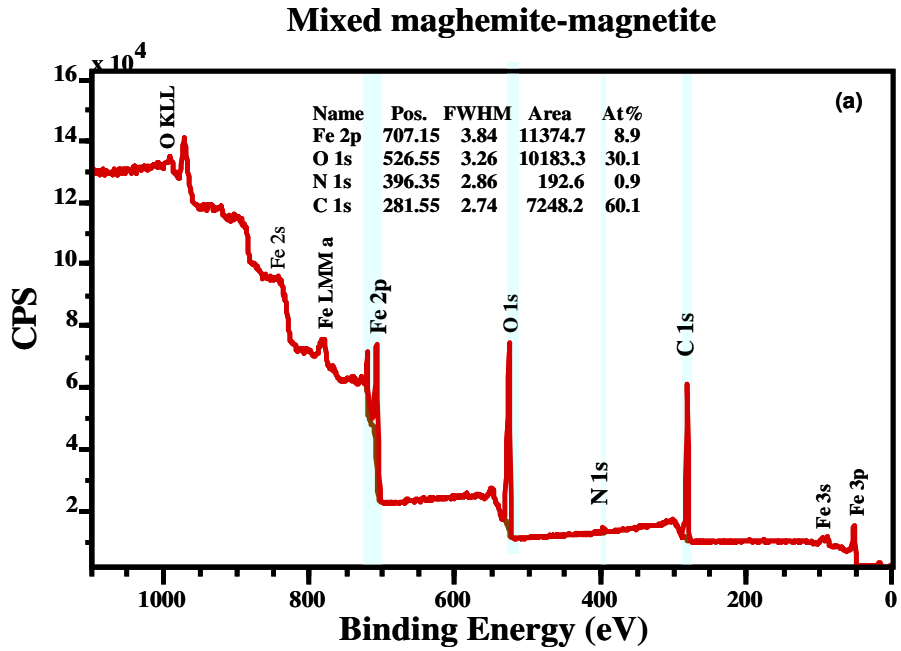
Mixed maghemite-magnetite
x 10^4
CPS
Binding Energy (eV)
(a)
Name Pos. FWHM Area At%
Fe 2p 707.15 3.84 11374.7 8.9
O 1s 526.55 3.26 10183.3 30.1
N 1s 396.35 2.86 192.6 0.9
C 1s 281.55 2.74 7248.2 60.1
O KLL
Fe 2s
Fe LMM a
Fe 2p
O 1s
N 1s
C 1s
Fe 3s
Fe 3p

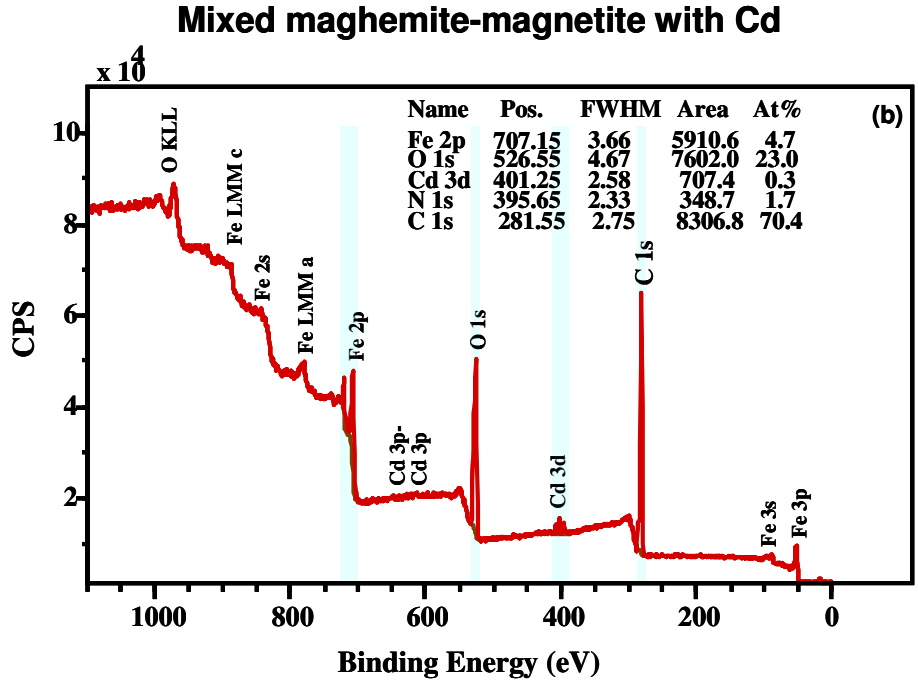
Mixed maghemite-magnetite with Cd
x 10^4
CPS
Binding Energy (eV)
(b)
Name Pos. FWHM Area At%
Fe 2p 707.15 3.66 5910.6 4.7
O 1s 526.55 4.67 7602.0 23.0
Cd 3d 401.25 2.58 707.4 0.3
N 1s 395.65 2.33 348.7 1.7
C 1s 281.55 2.75 8306.8 70.4
O KLL
Fe LMM c
Fe 2s
Fe LMM a
Fe 2p
Cd 3p-
Cd 3p
O 1s
Cd 3d
C 1s
Fe 3s
Fe 3p

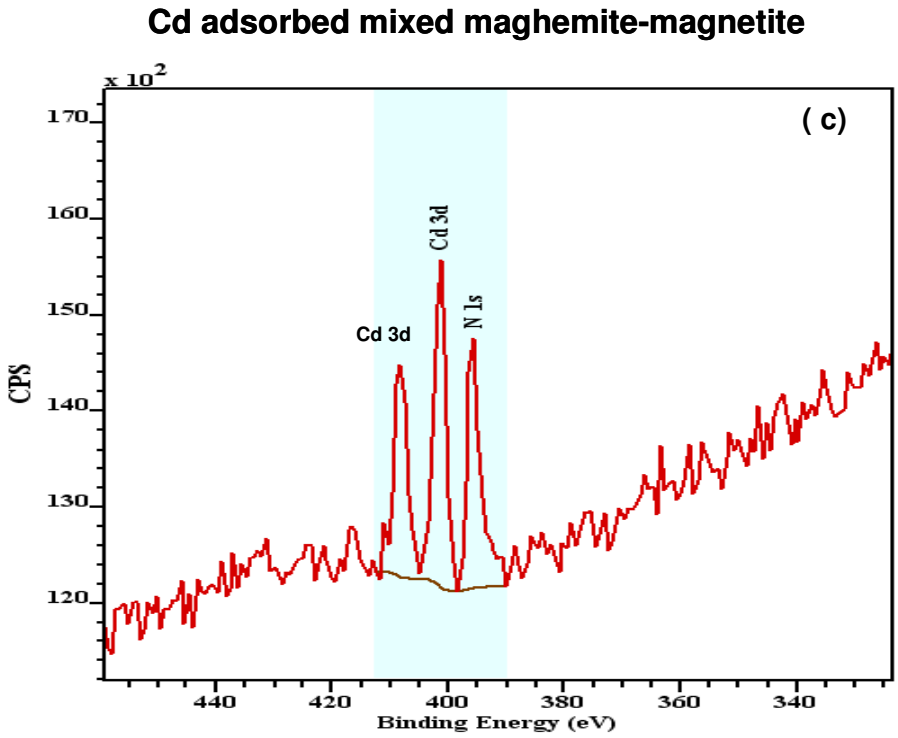

Figure 5.9: XPS wide scan spectra of the (a) fresh maghemite-magnetite mixture (b) Cd(II) loaded maghemite-magnetite mixture (c) Cd(II) peak on Cd loaded maghemite-magnetite mixture (Binding energy scale in order of descending values).

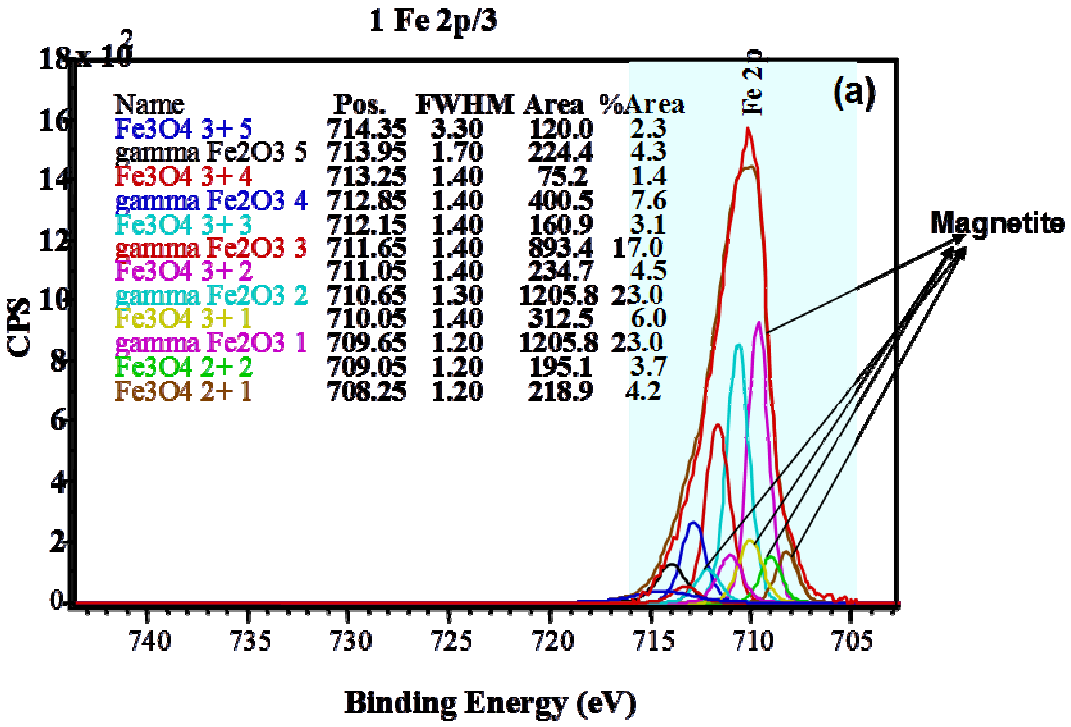
1 Fe 2p/3
x 10^2
CPS
Binding Energy (eV)
Fe 2p
(a)
Magnetite
Name Pos. FWHM Area %Area
Fe3O4 3+ 5 714.35 3.30 120.0 2.3
gamma Fe2O3 5 713.95 1.70 224.4 4.3
Fe3O4 3+ 4 713.25 1.40 75.2 1.4
gamma Fe2O3 4 712.85 1.40 400.5 7.6
Fe3O4 3+ 3 712.15 1.40 160.9 3.1
gamma Fe2O3 3 711.65 1.40 893.4 17.0
Fe3O4 3+ 2 711.05 1.40 234.7 4.5
gamma Fe2O3 2 710.65 1.30 1205.8 23.0
Fe3O4 3+ 1 710.05 1.40 312.5 6.0
gamma Fe2O3 1 709.65 1.20 1205.8 23.0
Fe3O4 2+ 2 709.05 1.20 195.1 3.7
Fe3O4 2+ 1 708.25 1.20 218.9 4.2

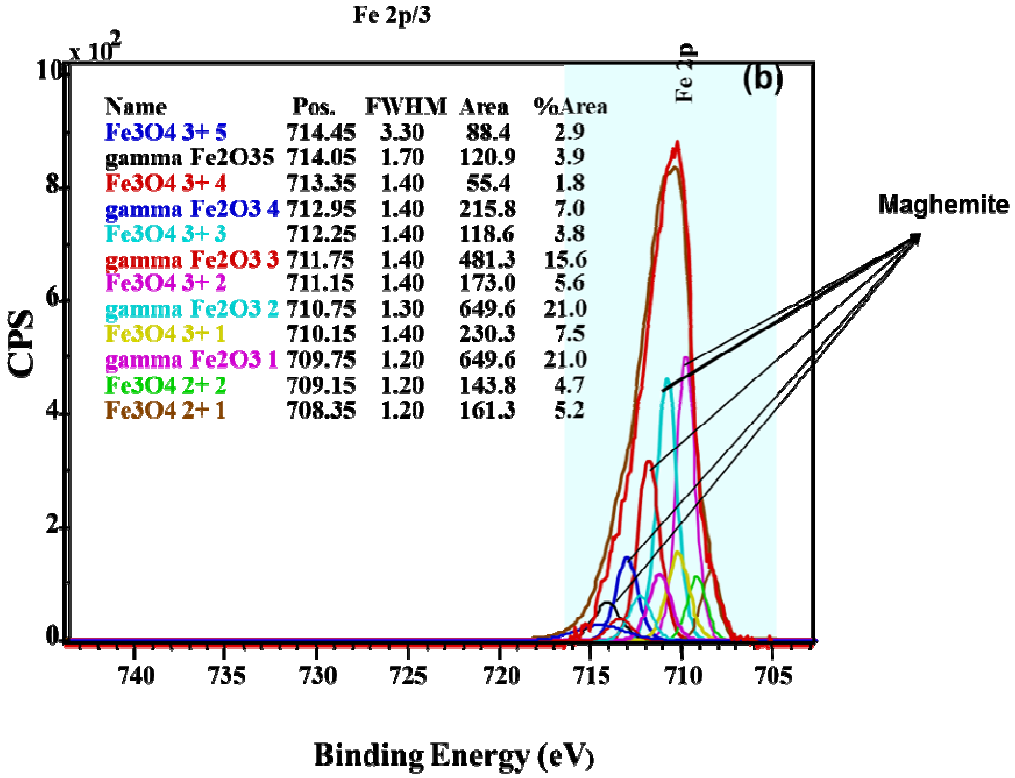

[a] Component information for each of the theoretically derived GS multiplets came from a digitized reproduction of the graphs found in the original paper (Fairley, 1999-2003).

[b] Fe3O4 3+ means Fe (III) in magnetite; and Fe3O4 2+ means Fe (II) in magnetite.

Figure 5.10: XPS spectra (a) nano-scale maghemite-magnetite particles and (b) Cd(II)-adsorbed mixed maghemite-magnetite- particles.

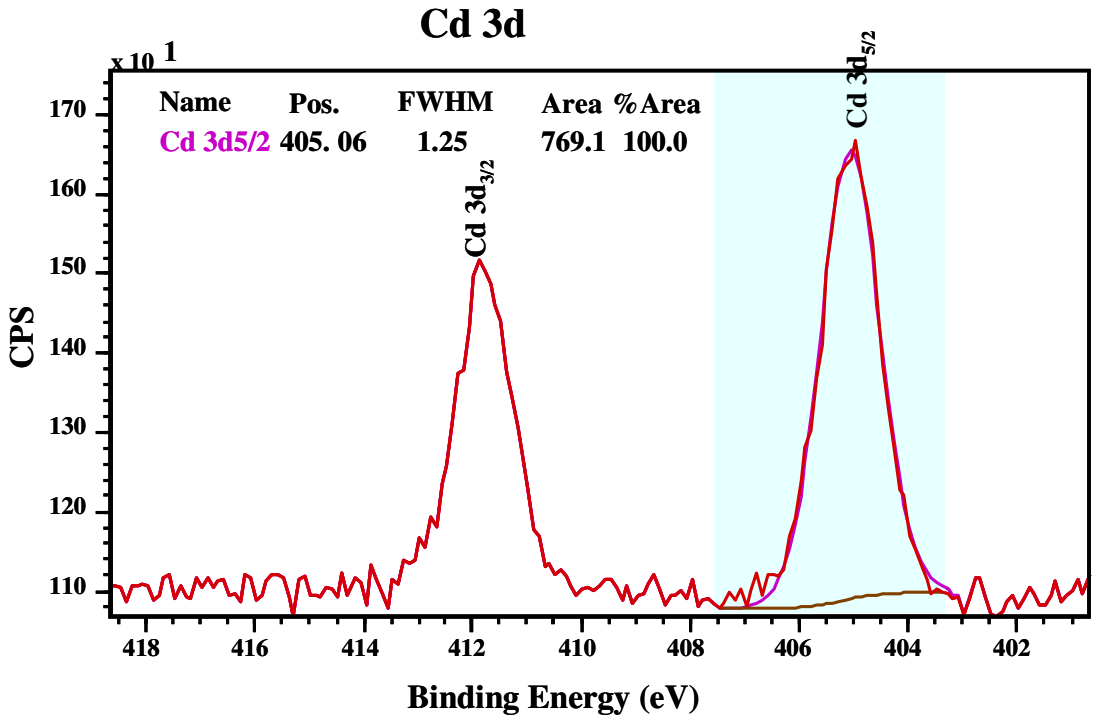

Figure 5.11: Cd 3d XPS spectra of Cd(II) loaded maghemite-magnetite mixture. (state background subtracted in data).

CHAPTER 6

TRANSPORT AND CHEMICAL STATES ANALYSIS DURING ARSENIC REMOVAL BY MONOLITH SLAG FROM NICKEL SMELTER

6.1 Introduction

Groundwater contamination by arsenic (As) has resulted in considerable outbreaks of As toxicity and associated vulnerabilities around the globe (Williams et al. 2003). Arsenic is a known carcinogen in humans and it exists in subsurface as well as in contaminated groundwater as a result of weathering of rocks, industrial waste discharge, and agricultural use of arsenical herbicides and pesticides (Chunming et al. 2001). The United States Environmental Protection Agency (US EPA) has identified arsenic as a group A carcinogen (ATSDR, 2009). Chronic exposure to As-contaminated drinking water is a crucial health problem in many regions of the world, notably Bangladesh, India, the Red River Delta (Vietnam), Taiwan and the western United States (ATSDR, 2009; Lee et al. 2011). Historically, a significant source of As release into the environment has been from the mining and smelting of metals (Williams et al. 2003). Arsenic from both anthropogenic and geologic sources is commonly observed in the subsurface. The use of organic and inorganic arsenic compounds as fertilizer, pesticide and wood preservative has recently been increasing in different countries (Welch et al. 2000). Although the production and use of arsenic and its compounds have been limited by environmental restrictions and regulations, they are still extensively used in metallurgy, agriculture,

forestry, electronics, pharmaceuticals, glass, and the ceramic industry (Welch et al. 2000; Williams et al. 2003). Arsenic is the second most common contaminant of concern at Superfund sites (USEPA, 2002). According to Gotkowitz et al. (2004), the oxidation of bedrock in response to pumping of groundwater is a very common source of As in groundwater. The results are the occurrence of wide spread groundwater As contamination (Welch et al. 2000 and Gotkowitz et al. 2004). The original source of the arsenic was most likely the oxidation of sulfide minerals, principally pyrite (Harvey et al. 2006). These authors further reported that, in the Ganges delta, pyrite oxidation occurred during weathering at the source in the Himalayas and that the released arsenic was transported and deposited in association with the resulting iron oxides. Arsenic is found predominantly in the inorganic form in oxidation states of +5 or +3 (Welch et al. 2000 and Gotkowitz et al. 2004). In oxidizing environments, the oxyanion arsenate [As(V)] is the predominant species (Kundu et al. 2005 and Yean et al. 2005). The interaction of As(V) with subsurface media significantly affects the movement of As in soil and groundwater (Harvey et al. 2006). The equilibrium adsorption of As(V) on pure solid phases and soils has been studied extensively as documented in recent reviews. These studies have shown that Fe oxyhydroxides strongly interact with dissolved As(V) and that the degree of As(V) adsorption is extremely pH-dependent.

Recent studies have also shown that Fe^0 and granular iron or iron coated sand effectively removes inorganic contaminants (CrO_4^{2-}, UO_2^{2+}, MoO_4^{2-}, TcO_4^-, AsO_4^{2-}, and AsO_3^{2-}) from aqueous solution (Chunming et al. 2001; Blowes et al. 2000). These authors further reported that surface precipitation or adsorption appears to be the predominant removal

mechanism for both As(V) and As(III) by Fe^0. It has been presented to be an effective method for removing As from groundwater by using zero-valent iron (ZVI) particles (e.g., using a permeable reactive barrier, or PRB, containing ZVI particles) (Blowes et al. 2000, Chunming et al. 2001, Nikolaidis et al. 2003, and Leupin et al. 2005).

There is interest in finding less costly, but effective, reactive materials that can be used to remove heavy metals from contaminated soil and groundwater. Lee and Benson (2004) reported that low-cost materials that provide or enhance treatment sustainability, such as industrial by-products or waste materials, are particularly attractive. A recent case history reported by Wilkens et al. (2003) demonstrated that a PRB containing crushed steel slag (a by-product of steel production) was effective in removing As from groundwater at a site in Gary, Indiana, USA. The authors suggested that mechanisms responsible for As removal included sorption to metal oxides at the slag surface and precipitation of insoluble compounds (e.g. Ca-As compounds). Metz and Benson (2007) explained that slags from iron foundries can be effective low-cost reactive media for PRBs used in the treatment of arsenic-contaminated aquifers. They noted that although iron foundry slags may not be as reactive as conventional ZVI, they do, however, have sufficient reactivity to be used in the construction of PRBs with a reactive zone typically < 1 m thick.

There has been great interest in the in situ remediation of certain organic and inorganic contaminants in groundwater using iron compounds as a permeable reactive barrier medium. The application of fayalite-iron oxides loaded Ni-smelter slag in subsurface remediation technologies has great potential in geo-environmental engineering. In the

present study, the fayalite and iron oxides loaded slag used was obtained as a by-product of ore smelting (e.g. at the Vale Inco Ni smelter in Sudbury, ON, Canada). Electrostatic attraction as well as redox reactions between mixed iron oxides and heavy metals accelerate the removal of heavy metals from the subsurface (Hu et al. 2004). To capitalize on this benefit of using mixed iron oxides, the present study focused on the investigation of the effectiveness of slag particles in contaminated groundwater remediation. The broad objective of the present research was to select the best reactive medium containing Ni smelter slags for the construction of permeable reactive barriers (PRB) at contaminated sites. The ready availability of the mixed iron oxides rich Ni-smelter slag renders the recycling and use of the material in the treatment of metal bearing wastewaters a potentially innovative and cost-effective venture. The principal aims of the work are to experimentally investigate the adsorption capacity and rate of adsorption of arsenic species onto the Ni-smelter slag sorbent in laboratory columns, and assess the potential utilization of Ni smelter slags as PRB media in the remediation of As contaminated groundwater. Permeable reactive barriers (PRBs) are an emerging technology used for the remediation of acidic leachates and contaminated groundwater (Blowes et al. 2000). The study can also help develop a new reactive medium for barriers used to prevent severe contamination of soil and groundwater. The research provided an opportunity to evaluate the feasibility of using slags (e.g. an iron oxide and iron silicate bearing waste from Ni-ore smelting) in remediation, as well as to highlight the benefits of using renewable waste products for contaminated subsurface restoration.

6.2 Experimental Section

6.2.1 Materials Characterization

The slag was collected from Vale Canada Copper Cliff Smelter, near Sudbury, Ontario, Canada. It was generated from the smelting of Ni ore. This product is a complex mixture of different iron oxides, iron silicate, aluminum, magnesium, calcium and nickel sulphide or oxides. The slag was characterized using various analytical techniques including X-ray fluorescence (XRF), X-ray diffraction (XRD), and X-ray photoelectron spectroscopy (XPS). The slag samples arrived unprocessed in large granular pieces. The granules were crushed to different-scale particles by grinding. The amounts of bulk, trace and crystalline compounds as well as the percentage of different oxides were determined from various tests. After crushing, the fresh slag specific surface area and particle size distribution were measured using a Malvern Laser 2000; and the average size and specific surface area of slag materials were found to be 53.54 μm and 0.51 m^2/g, respectively. The range of slag grain size distribution was found to be 0.325 to 152.5 μm (as shown in Appendix A5).

6.2.2 Sample Preparation

Certified reagent grade chemicals and de-ionized distilled water were used to prepare all solutions for experiments. A 10% HNO_3 solution in deionized water was used to treat and rinse glass volumetric flasks and reaction vessels before they were used. As (V) stock

solutions were prepared by dissolving As_2O_5 in de-ionized water using 4 g/L NaOH solution since oxides have enhanced solubility in NaOH solution. For each stock solution, redox potential and pH were assessed using a WTW Multi 340i ORP electrode (Wellheim, Germany) and an Orion combination pH electrode respectively. To confirm the presence of the targeted species, ICP-OES (inductively coupled plasma- optical emission spectroscopy) was used to measure arsenic and other metal concentrations in the influent and effluent. The solution was acidified with 3% nitric acid before using ICP-OES. The experiments were carried out in duplicate and the mean values were considered. In ICP-OES analysis, a group of experiments was repeated a few times and the data were found to vary within ±5%. Analytical quality was controlled throughout by using control and blank samples.

6.2.3 Instrumentation and Surface techniques

Detailed studies using the different surface analytical techniques, such as field emission scanning electron microscopy, X-ray diffraction (XRD), X-ray fluorescence (XRF) and X-ray photoelectron spectroscopy (XPS) were conducted to detect the differences between heavy metal adsorbed fayalite slags and mixed iron oxide loaded slags.

The fresh slag was analyzed by a PAN-analytical PW-2400 Wavelength Dispersive XRF Spectrometer at the Western University. Exactly 1.0 g of powdered sample was weighed and roasted at 1000^0C for "Loss on Ignition (LOI)" determination. The oxide composition of the Ni smelter slag was determined by X-ray fluorescence (XRF) analysis and Table

6.1 shows the major oxide contents of the slag. The iron (Fe) oxide of the slag was found to be more than 50% by weight.

Hitachi SU6600 Field Emission Scanning Electron Microscope (FESEM) was used to scan the surface of the samples. The backscattered and secondary electrons for the surface analyses were used to identify the differences in surface patterns between original natural slag and As-reacted slag. Sample imaging was conducted at 150 Pa with variable pressures and 1x to 25Kx magnification. For SEM imaging, the variable pressure condition was run at 20 kV electron beam accelerating voltage. Figure 6.1a shows the 1Kx magnification image of the pure slag particles. A 1 to 25000Kx magnification was also used to check uniformity. Figure 6.1a presents SEM photomicrographs of the pure or original slag showing a non-uniform surface with porosity as well as botryoidal clusters at the slag surface.

X-ray diffraction (XRD) powder patterns were obtained using a Rigaku D/MAX 2500 rotating anode powder diffractometer and a monochromatic Cu Kα radiation generated at 50 kV and 260 mA. Diffraction patterns for selected samples were recorded using continuous scans from 10 to 70° 2θ at a speed of 1°/min.

X-ray photoelectron spectroscopy (XPS) was employed to probe the interactions of the sorbent with arsenic. XPS was considered potentially useful for speciation determination of arsenic on the As reacted slag surface. Moreover, multiplet analysis of As-FeO products, such as As-magnetite, As-maghemite and As-goethite, shows that these

products form a passivated layer on the slag surface thus affecting the behavior of the Fe0-As interaction. In the XPS studies, all spectra were generated using A Kratos Axis Ultra XPS instrument. All samples were tested using a monochromatic Al Kα X-ray source (15 mA, 14 KV) using analysis chamber pressures of 10^{-7}-10^{-6} Pa. The conditions used for the survey scans were as follows: energy range =1100–0 eV, pass energy =160 eV, step size = 0.7 eV, sweep time = 180 s and x-ray spot size = 700 * 400 μm. All dried samples were kept in the spectrometer via a glove box. The glove box was filled with N_2 (g) so as to reduce the chance of the samples reacting with air. The XPS Fe mutiplet analysis showed that the slag surface was actually a mixture of mixed iron oxides such as Fe_3O_4-γ-Fe_2O_3-Fe00H, consisting of 50% magnetite, 28% maghemite and 22% goethite. Moreover, 21% SiO_4 was detected in Figure 6.11a that supports the presence of fayalite ($FeSiO_4$) content in the slag. A detailed discussion was included in the mineralogical investigation of monolith slag.

A Renishaw Model 2000 Raman Spectrometer system equipped with a 633 nm He-Ne laser was used to measure Raman spectrum. Laser Raman spectroscopy depends on a change in the polarization of a molecule to create Raman scattering. Approximately, 40,000 cubic microns of the sampling volume are used for the Raman analysis. In the present study, the spent or As-sorbed iron oxides were transferred to a Teflon®-faced vial with a butyl rubber septum cap, immediately following vacuum drying. The sample was analyzed with the spectrometer system in macro mode with a laser spot size on the order of tens of microns and an approximate laser power of 1 mW. In general, the photons are scattered elastically (Rayleigh scattering) and inelastically (Raman scattering) generating

Stokes and anti-Stokes lines when a beam of photons strikes a molecule. In the Raman analysis, samples are much larger in volume than those used in XPS, on the order of 40 times. Units for Raman spectra are expressed in wave numbers which have units of inverse length.

6.2.4 Column study

To assess arsenic removal efficiencies in contaminated aqueous solutions, three columns were assembled to simulate arsenic contaminated water flow through fayalite-iron oxide loaded slag samples packed in columns. For the column experiments, two 2-inch (5.05 cm) diameter by 4-inch (10.16 cm) long and one 2-inch (5.05 cm) diameter by 4.5 inch (11.43 cm) long acrylic tube columns were packed with fayalite-iron oxide loaded slag particles as shown in Figure 6.2. In this study, the purpose of using three columns is to compare the results under the same condition. The As contaminated water was fed in from the base of the columns at Darcy velocities of 0.258 to 0.264 m/day by using a multi-channel precision peristaltic pump. The seepage velocities ranged from 0.63 to 0.66 m/day in the three columns. Usually, in the subsurface, the seepage velocity ranges from 10 to 2000 m/year or 0.03-5.5 m/day (Lai and Lo, 2002). There were four sampling ports located at 2.5, 4.5, 7.5 and 10.16 cm from the influent end in two columns and 2.5, 4, 6.25, 8.5 and 11.43 cm in one column. The porosities and bulk density of the three columns were found to be 0.39 to 0.41 and 2.19 to 2.37 g/cm^3 respectively. In the three columns, one pore volume was found to range from 80.3 to 94.96 mL. The residence time and the number of pore volume (PV) per day were calculated to be 9.24 to 10.6 h and 5.5

to 6.5 for the three columns respectively. The time required to achieve one pore volume (PV) of flow for the columns were 3.7 to 4.35 h. The hydraulic conductivity of the slag in the column was measured using constant pressure head. Two pressure gauges were installed to monitor inlet and outlet pressure. Hydraulic head difference was determined from pressure differences. Hydraulic conductivities of three columns were found to be approximately 3.24×10^{-5} cm/s to 4.43×10^{-5} cm/s throughout the operation periods. Sampling ports equipped with Teflon-faced septa were positioned along the column at approximately 1.5 to 2 cm intervals. Teflon tubing was used except for the tubes, which were made of acrylic tube, passing through the pump. Water samples were collected every 10 to 50 PV from the sampling ports as well as from the polyethylene ‘‘T’’ valves connected to both ends of the columns. Before collecting the samples, about 0.5 mL of the solution was added in order to push out stagnant water sitting in the tubing of the sampling ports. Two additional ports containing WTW Multi 340i ORP electrodes (Wellheim, Germany) were located on the wall of one column at a 90^{o} angle to the flowing water (Fig. 6.2) for in-place measurements of redox potential of the medium. To confirm the targeted As(V) or As(III) species or slag compound in the column, the pH and Eh of the column influent, pore fluid and effluent were monitored. Lab-scale experiments with appropriate reactive mixtures were conducted to determine the applicability of mixed iron oxide loaded slags for the construction of PRBs. The experimental set up of the columns is illustrated in Figure 6.2.

6.2.5 Batch Study and distribution coefficient, (K_D)

Batch adsorption experiments were carried out by shaking 4.5 g of slag in 300 mL aqueous solution of As(V) of desired initial concentration (0.1-10 mg /L) in plastic bottles at pH 5 and a constant speed of 100 rpm in a mechanical shaker. After predetermined time intervals, the adsorbent was separated from the solutions by centrifugation and filtration. Adsorption was determined by measuring the concentration of As left in the aliquot by ICP-OES (inductively coupled plasma-optical emission spectroscopy). The uptake distribution coefficient, $K_{D,}$ was determined from the isotherm equation.

6.3 Results and Discussion

6.3.1 Arsenic removal and migration through columns

According to Metz et al (2006), Zhang et al (2007) and Vu et al (2003), arsenic removal by Fe^0 or FeO compound generally follows Pseudo first-order reaction kinetics. A pseudo first-order rate constant for the removal of As(V) across each column ($k_{overall}$) was calculated according to eq 6.1 (Shen et al. 2007).

$$K_{overall} = - Ln(C_{out}/C_{in})/\Gamma \qquad (6.3.1)$$

Where, (C_{out}) is the concentration in the column effluent, (C_{in}) is the concentration in the column influent, and (Γ) is the mean residence time of water in the three columns (9.24 to 10.6 h). Data were analyzed by checking the changes in the calculated rate constants ($K_{overall}$) for removal over time of contaminant in the columns. Figure 6.3 shows the

comparison of the pseudo first-order rate constants in the columns after 20 d, 50 d and 100 d of operation; 50 d represents the center of the period of operation as well as the rate constants for all the sampling intervals. The rate constants varied from 0.05 to 0.9 h^{-1} for three columns. Figure 6.3 illustrates the changes in the calculated rate constants for As(V) removal over time in the mixed iron oxide loaded slag columns. The removal rate constant was initially very high because of the availabilities of reactive medium and subsequently decreased with operation time. The column reactive medium lost arsenic adsorption capacities when $K_{overall}$, the removal rate constant, reached almost zero. This figure also indicates the life span of the column under the given conditions.

Column testing was used to verify the reactivity of the slag under continuous flow conditions. Three laboratory columns were set up to investigate the As removal capacity and migration rate. The normalized migration front of the As, N (cm/cm^3), provides a good parameter for evaluating the reactivity of slag compounds in engineering applications. In this study, N is defined as the distance traveled by the As front at a desired relative concentration (C/C_0) per the number of pore volumes passed through the column divided by the volume of one pore volume. As shown in Fig. 6.4(b), the straight line confirms that the As(V) front moves at a constant rate. For instance, the migration of column 1 at C/C_0 equal to 0.5 was 0.02 cm/PV while its normalized migration was $0.23*10^{-3}$ cm/cm^3. The As(V) removal or adsorption capacity of Ni smelter slag, RC (mg As/g slag), can be estimated using the following equation:

$$RC\ (mg/g) = [As(V)]/N*A*p_b \quad \ldots\ldots\ldots\ldots\ldots\ldots\ldots\ldots\ldots\ldots \quad (6.3.2)$$

Where, [As(V)] is the initial concentration of As(V) (mg/L), N is the normalized migration of As(V) front (cm/cm^3) at a desired C/C_0. A is the cross-sectional area of the column (cm^2) and ρ_b is the bulk density of slag packed in the column (g/cm^3). By applying Eq. (6.3.2), the As(V) capacity of column 1 was calculated to be approximately 1 mg As/g slag. This value is used as a reference value for comparing the reactivity of mixed iron oxide loaded slag on the removal of As(V) under geochemical conditions and the results for three columns are summarized in Table 6.2.

The first two columns contained the same amount of reactive medium (e.g. slag) and same dimensions while the third column was almost 12.7 mm (1/2 inch) longer than the other two columns and, therefore, had more reactive medium. In addition, these laboratory-determined removal capacities can be used in engineering applications to estimate the lifespan of slag-loaded permeable reactive barrier from the given As(V) loading rates and the physical properties of the barrier.

Results from previous work (Petrova et al. 2011 and Hu et al. 2004) suggest that the removal of As(V) by iron oxides may involve a process in which both continuous adsorption and redox reactions can occur between As(V) contaminated water and iron oxide compounds. The exhaustion of reactive compounds results in the migration of As fronts through the columns, and the columns do get eventually exhausted if a continuous loading of As(V) is applied. Initially, all the arsenic ions were adsorbed resulting in zero adsorbate concentration in the effluent. As the arsenic species uptake continued, the solute concentration in the effluent gradually rose (Fig.6.5). In the up-flow direction,

when As(V)-bearing water is introduced at the bottom of the mixed-iron oxide slag medium, most of the As(V) removal initially occurred in a narrow band at the bottom of the column, referred to as the adsorption zone. As column permeation continued and due to the continuous injection at fixed rate, the lower layers of the reactive adsorbent became saturated with arsenic species and the adsorption zone progressed upward through the column bed. When the adsorption zone reached the top of the column, the arsenic concentration in the effluent began to increase and eventually became equal to the influent concentration (i.e. 10 mg/L As concentration). When effluent concentration of target contaminant is equal to the influent concentration in the column, the adsorption capacities of column became zero indicating full saturation of columns with the targeted species. The XPS results presented in Section 6.3.5 also confirm the presence of elevated concentration of As species on the reacted slag surface and near surface at the end of the entire operational periods of the three columns. A breakthrough curve is obtained by plotting the effluent to influent arsenic concentration ratio (C/C_0) against pore volume, as shown in Figure 6.4-6.5. The breakthrough curves for As(V) (using arsenics drinking water standard of 0.05 mg/L set by WHO or USEPA as the effluent concentration) are illustrated for different bed depths, 10-11.43 cm, at Darcy velocities of approximately 0.258 to 0.264 m/day and a residence time of 9.24 to 10.6 hours. In the present study, the point on the breakthrough curve at which the arsenic concentration reaches its maximum permissible value (in this study, 0.05 mg/L) is referred to as the breakthrough. The breakthrough times (corresponding to $C/C_0 = 0.005$) for columns 1, 2 and 3 were found to be 13.5, 14, and 18 days, respectively (Fig. 6.4 and 6.5). As well, we define the point of column exhaustion as the point where the effluent arsenic concentration reaches 90% of

the influent value (10 mg/L). The exhaustion times (corresponding to C/C_0 = 0.9) for three different columns were 88.5, 91, and 113 days, respectively.

Different column parameters have been calculated from the above data. Initially, Fe and Ni leaching from the three slag-packed columns during the adsorption process was found to be very minimal, ranging from 0.01 to 0.025 and 0.01 to 0.5 mg/L respectively. The contaminant migration curve, illustrated in Fig. 6.4(a), confirmed the As migration pattern in column 1 in which the propagation of the As migration front was almost constant throughout the experiment. The same phenomenon was also observed in the remaining columns but with different migration rates shown in Figures 6.5(a)–(b). In this study, the dissolved oxygen (DO) of the effluents from the three columns was low (< 2 mg/L), while the DO of the influents ranged from 4 to 7 mg/L. Tanboonchuy et al. (2011) found arsenic removal rates in their system to be higher with lower initial pH and higher DO. In the present column study, the measured DO at the first sampling port (i.e. 2.5 cm away from the influent point) was always lower than 2.0 mg/L. To evaluate the DO effect on As removal capacity by the slag, higher and lower concentrations of influent DO were used. The results showed no significant effect of influent DO on As(V) removal. Thus, DO may not be an important factor in our study.

6.3.2 Pore-water redox potential (Eh) and pH

Redox potential, Eh, is the potential naturally adopted by an isolated metal when the total rate of oxidation exactly equals the total rate of reduction. It represents a property of a

metal rather than an aqueous phase (Odizemskowski et al. 1998). The redox potentials were measured at Port A and Port B in column 3 (as shown in Figure 6.2) along with the pH values measured close to these two ports. After injecting 30 PV of electrolyte solution, the adsorbent pores were saturated with electrolyte thereby creating anaerobic condition in the column. After passing 40 PV of electrolyte solutions through the column, the contaminant solution was injected resulting in 130 mV initial drop in redox potential at Port A (from -380 mV to -510 mV) during the first 50 pore volumes of As(V) addition; thereafter, the potential remained relatively stable up to 380 PV of injection. In Port B, it appears that there was a similar drop in redox potential, from -550 mV to -620 mV; however, unlike Port A, this was followed by a slight decrease with the continuing addition of As(V), reaching -704 mV at ca. 300 PV, followed by an increase in potential with the continuing addition of As(V), reaching -432 mV at ca. 450 PV. At Port A, the potential reached -232 mV at ca 450 PV.

According to Geological Survey of Japan (2005), Kundu et al. (2005) and Yean et al. (2005), As(III) species are present in anoxic and reducing condition (i.e. -800 mV to -1 mV) while As(V) species are dominant in oxidizing conditions (i.e. more than 1 mV Eh values). Thus, from redox values, it can be concluded that reducing condition exists when As(V) contaminated solution is introduced in to the column. Redox result also indicates that the As(III) species may be dominant in the mixed iron oxide loaded slag medium used in the laboratory columns. The figure 6.6 shows the changes of Redox potential (Eh) values throughout operation periods.

Although the input solution pH was kept at 4-5, the range of pH for the samples collected close to Ports A and B was 6 to 8. Yean et al. (2005) and Hu et al. (2006) reported that arsenic species can be removed by iron oxides in the range of pH 2 to 9. Thus it can be concluded that the continuous change in redox potential (Eh) and pH indicates the redox reaction occurring between As(V) and reactive slag medium under the given conditions.

6.3.3 Modeling

a) Column dispersion coefficient (D) and distribution coefficient (K_d)

In this study, the movement of As(V) through the column was modelled using the one-dimensional advection dispersion equation incorporating sorption based retardation. For steady-state flow and transport, the adsorption or solute reaction with adsorbent in the column was assumed to be under saturated, uniform, homogeneous and isotropic conditions. The column experiments were modelled using a semi-analytic solution to the advection-dispersion-adsorption equation incorporated in the commercial software, POLLUTE (Rowe and Booker, 1985 and Rowe et al. 1994). The 1-D contaminant migration equation for an intact material is as follows:

$$n\frac{dc}{dt} = nD\frac{d^2c}{dx^2} - nv\frac{dc}{dx} - \rho_b K_d \frac{dc}{dx} \quad \text{---------- (6.3.3)}$$

Where, ρ_b = dry density of adsorbent; n= porosity of the medium; K_d = distribution coefficient (L/g); D = hydodynamic dispersion coefficient at depth x; and v = Darcy velocity (m/day). In this case, χ = decay constant= zero.

The commercial software POLLUTEv7 (Rowe and Booker, 1995) was used to best-fit a theoretical curve to the experimental data points. In this study, the columns' length was small (10.16 to 11.43 cm). In general, short-column data include an entrance effect, independent of the mode of injection and amplitude discrepancy (Fahien and Smith, 1955; and Carberry and Bretton, 1958). Dispersion over a small distance is usually less than the dispersion along the entire flow path (Fetter et al. 1993). Moreover, most researchers used sufficient flow-path (long columns) to measure dispersion coefficient and other parameters (Carberry and Bretton, 1958; Fetter et al. 1993; Sperlich et al. 2005; Westerhoff et al. 2005 and Delgado, 2006). To avoid any discrepancies, we considered the entire flow-path (10.16 to 11.43 cm) to achieve dispersion coefficients along the columns and ran model for the best fit curve. Modelling was performed by changing both the hydrodynamic dispersion coefficient and distribution coefficient while keeping other parameters constant. In this study, contaminated water is flowed from the column bottom to the top. Consequently, the bottom of the column was considered a constant concentration boundary ($C = C_0$, $t > 0$) while the top of the column was modelled as a fixed outflow with a calculated velocity of Q/A, where Q is the discharge (m^3/s) and A is the column area (m^2). In POLLUTEv7, the model was run assuming linear adsorption. The results show that there is a good agreement between modelling and experimental results (Fig. 6.7).

Based on the fitting of both experimental and modelled results, the hydrodynamic dispersion coefficient (D) was found to be 0.02823 and 0.021756 m^2/day for column 1 and column 2, respectively, and 0.024985 m^2/day for column 3. The hydrodynamic dispersion coefficient (D) is equal to the sum of the effective diffusion coefficient and

mechanical dispersion coefficient ($D= D_e + D_H$). Mechanical dispersion coefficient (D_H) can be determined from the dispersivity (m) and pore water or seepage velocity [i.e. $D_H= \alpha_L*v$]. Dispersivity describes the maximum longitudinal dispersion or spread of contaminant in a porous medium. Previous researchers found that the hydrodynamic dispersion coefficient (D) can be regarded as an effective diffusion coefficient under the very low seepage velocity conditions (Rowe et al 1988; Camur and Yazicigil, 2001). Westerhoff et al. 2005 and Hildebrandt (2000) reported an effective surface diffusion ($53*10^{-11}cm^2/s$) and film diffusion ($1.53*10^{-3}$ cm^2/s) coefficients from arsenate breakthrough curves in experimental columns packed with activated alumina. Lange et al. (2009) reported the effective diffusion coefficient of arsenic in geo-synthetic clay liner to be in the range of 0.88 x 10^{-10} to 1.3 x 10^{-10} m^2/s when the arsenic initial concentration was kept at 1 to 5.4 mg/L. In the present study, we found the values of the hydrodynamic dispersion coefficient (D) to range from 2.51 x 10^{-7} to 3.26 x 10^{-7} m^2/s when 0.258 to 0.264 m/day of Darcy velocities were applied in the three columns.

The Stokes-Einstein equation [$De = KT/(6*\pi*r*\eta)$] can also be used to calculate contaminant effective diffusion coefficient (De) in intact porous materials. In this relation, K represents the Boltzman constant (1.38 x 10^{-23} J/K); η indicates water viscosity (0.000955 kg/ms) at 22^0C; r is the radius of spherical arsenic molecule (114-139 pm or $114*10^{-12}$-$139*10^{-12}$ m) (Macdonald,et al. 2009); and T is 295^0K. Using these values, the effective diffusion (De) for arsenic molecule at 22^0C is calculated to be 1.4 x 10^{-4} m^2/d to 1.64 x 10^{-4} m^2/d. Thus, the dispersivities (α_L) for the slag at a given pore water velocity are 32.7 mm to 42.4 mm.

From model results, the values of distribution coefficient (K_d) were 0.22, 0.21 and 0.21 m^3/kg or L/g for the three columns. The detailed model results were presented in Appendix A5. Figure 6.7 shows the As(V) breakthrough curves of experimental and model results. The retardation factor, R, ($R= 1+ \rho_b/n* K_d$) was calculated to be more than 1 for the three columns confirming the adsorption of As species on the slag.

The distribution coefficient (K_d) was also obtained from batch tests for the range of concentrations (0.1-10 mg/L) of As(V) and 15 g/L of adsorbent used in the study. From the batch experiments, the adsorption of As(V) on slag particles was found to follow a linear isotherm in the same concentration range used in the column tests. K_d was found to be 0.24 L/g. Batch experiments show that adsorption was linear. The experimental K_d values were close to the K_d obtained from the model (0.21-0.22 L/g). Calculated correlation coefficient (R^2) of the isotherm using linear regression analysis for As(V) adsorption at pH 5 was found to be 0.9414 (as shown in Appendix A5). Distribution coefficients (K_d) of As(V) with different adsorbents (e.g. laterite soil, red mud, activated alumina, ferruginous manganese ore and granular ferric hydroxide (GFH)) have been reported to be 0.055, 0.123, 22.77, 0.95, and 10.3 L/g respectively (Maji et al. 2007, Altundogan et al. 2000; Lin et al. 2001, Chakravarty et al. 2002, and Thirunavukkarasu et al. 2003). According to Kanel (2006) and Kuriakose et al. (2004), K_d values of As(III) with blast furnace slag and iron oxide impregnated activated alumina were 0.502 and 0.554 L/g respectively at 25^0C. In the present study, arsenic dispersion coefficient (K_d) on Ni smelter slag was also found to be almost 0.21 to 0.24 L/g.

Despite the small scattered experimental data points on the breakthrough curves (Fig. 6.7), a steady increasing tendency was observed during the operation of the columns

indicating linear adsorption of As(V) on the slag particles. Moreover, sampling or experimental errors may be attributed to the scattering of data points on breakthrough curves. The best fit curves are illustrated in Figure 6.7 and similar increasing trends are observed on model and experimental curves. Thus, it can be concluded from the model and batch tests that the adsorption in the column may follow a linear adsorption. The design parameters calculated from best fit model as well as the batch and column tests could be used to aid the design of a real reactive barrier at site when Ni smelter slag particles are used as reactive medium for As removal.

b) Column modeling based on bed depth/service time approach

A number of mathematical models have been developed for use in adsorption bed design. Kundu and Gupta (2005) and Chu et al. (2011) noted that column experimental data can be used to determine different characteristic parameters by using different model. Among various models, Kundu and Gupta (2005) and Sotelo et al. (2012) used a modified Bohart and Adams equation to determine the characteristic parameters, such as maximum adsorption capacity, adsorption rate constant as well as critical bed depth of column. Kundu and Gupta (2005) used this equation to determine As(V) adsorption capacity on to iron oxide-coated cement (IOCC) sorbent in laboratory fixed bed columns. They further reported that the bed service time (BDST) model proposed a simple approach to the Bohart-Adams equation. The Bohart Adams theory is based on the assumption that the rate of reaction in fixed filter bed is proportional to the fraction of sorbent capacity remaining and to the concentration of the sorbate in the vapour or liquid phase (Bohart and Adams, 1920; and Karpowicz et al. 1995). This equation is used to describe adsorption profiles for a number of adsorbate-adsorbent system. In the Bohart-Adams

fixed bed model, the sorbate-sorbent interaction is expressed by a surface reaction rate. In this equation, axial dispersion is assumed to be zero. According to the Bohart Adams theory, the changes in adsorptive capacities as well as solute removal by adsorption can be expressed as follows:

$$\frac{\partial N}{\partial t} = -KNC \quad \text{.....(6.3.4)}$$

$$\partial C/\partial D = -KNC/V \quad \text{.....(6.3.4a)}$$

where, N is the residual adsorbing capacity [at t= 0, N=N_0= adsorptive capacity (mg/g)] and D is the depth of adsorbent (total depth, D =D_0 (cm)]. Using equations 6.3.4 and 6.3.4a, a simplified version of the Bohart-Adams equation is written as follows (Kundu and Gupta, 2005 and Chu et al. 2011):

$$C_t/C_0 = 1/ [1+ \exp [(kN_{0*}x/V) - k*C_0*t] \quad \text{..... (6.3.5)}$$

Rearranging Equation 6.3.5 and considering $C_t = C_B$, the service time can be determined from the Equation 6.3.6 (Kundu and Gupta, 2005 and Sotelo et al. 2012):

$$t= N_o*x/(C_o*V) - 1/C_o\, k* \text{Ln}(C_0/C_B -1) \quad \text{..... (6.3.6)}$$

where, C_0 represents initial solute concentration (mg/L); C_B is desired solute concentration at breakthrough (mg/L), and k, N_0, x, V, and t indicate adsorption rate constant (L/mg.h); adsorption capacity (mg/g); bed depth of column (cm); flow velocity of solution past the adsorbent (1.075 and 1.1 cm/h for column 1 and 2, respectively); and service time of column under above conditions (h,) respectively. This equation can be used to determine the values of N_0, C_0, and k, which must be measured for laboratory columns operated over a certain period at a given velocity.

The breakthrough concentration of a particular contaminant is determined by the process specifications. This would be the allowable concentration set by government regulation.

If a contaminant is being removed, the breakthrough concentration might be the regulated discharge limit for the installed subsurface system. Setting t = 0 in Equation 6.3.6 leads to the following (Kundu and Gupta, 2005):

$$x_o = V/kN_o*Ln(C_0/C_B -1) \quad \ldots\ldots\ldots\ldots\ldots\ldots\ldots\ldots \quad (6.3.7)$$

Where, x_o indicates the minimum column height necessary to yield an effluent concentration C_B (equal to 0.05 mg/L set by WHO or USEPA).

Equation 6.3.6 may also be written as follows:

$$t= ax+ b \quad \ldots\ldots\ldots\ldots\ldots\ldots.. \quad \ldots\ldots\ldots\ldots\ldots\ldots\ldots\ldots..(6.3.8)$$

Where, a = slope= $N_o/(C_0*V)$ ……. ……..(6.3.9)

and b= intercept = $-1/C_ok* Ln(C_0/C_B -1)$….. ……..(6.3.10)

The model requires three different depth data to calculate the necessary parameters. According to Kundu and Gupta (2005) and Sotelo et al. (2012), the data calculated from this model can be used as design tools for practical applications. From the breakthrough times (corresponding to $C/C_0 = 0.005$) and the exhaust times (corresponding to $C/C_0 = 0.9$) for bed depth 4.5, 7.5, and 10.16 cm in column 1 and 2, graphs were plotted, as illustrated in Fig. 6.8, which show depth versus service time for 0.5 and 90% saturation of the columns. Breakthrough times (column saturation 0.5%) for column 1 was found to be 4, 7, and 13.5 days at 4.5, 7.5 and 10.16 depths, respectively. For column 2, it was found to be 5, 9 and 14 days at 4.5, 7.5 and 10.16 depths, respectively.

Using equation (6.3.8), the plot of experimental data generated linear relationships indicating the applicability of the model (Kundu and Gupta, 2005 and Sotelo et al. 2012). From the slope and intercept of the 0.5 and 90% saturation line shown in Fig 6.8, design

parameters K and N_0 were calculated using Eqs. (6.3.9) and (6.3.10). The minimum column height (x_0) necessary to generate an effluent concentration of C_B was determined using Eq. (6.3.7). For column 1, the values of K, N_0 (for 90% saturation) and x_0 were found to be 5.35 mL/mg*h, 0.9 mg of As(V) /g, and 2.47 cm, respectively. For column 2, the values of K, N_0 (for 90% saturation) and x_0 were found to be 9.29 mL/mg*h, 0.82 mg of As(V) /g, and 2.1 cm, respectively. The adsorption capacities for two columns calculated from this model were close to the adsorption capacities shown in Table 6.2.

6.3.4 Reactive slag effectiveness

The above results can be very helpful in the design of PRBs at field scale. Figure 6.9 illustrates the effectiveness of the mixed iron oxide loaded slag medium used in the laboratory columns. From the figure, it is clear that 10-11 cm columns containing almost 451-550 g of slag can be operated in more than 65 days to remove almost 99-100 percent As species from continuously flowing contaminated water that has an initial As concentration of 10 mg/L and a pH of 4-5. Under this condition, the maximum adsorption capacity was found to be 0.8 to 1.1 mg/g of slag. Thus, those parameters can be used as a design tool for simulating field scale PRB. The thickness and residence time of PRB depends on initial concentration as well as on the removal capacity of the medium (that is, the overall removal rate constant, $K_{overall}$), groundwater velocity as well as site conditions.

Moreover, the Ni smelter slag also contained Al_2O_3, MnO_2, MgO and quartz (SiO_2) with FeO. Those compounds generally have strong heavy metal adsorption affinity. Lin et al. (2001) showed almost almost 90% arsenic removal by activated alumina and the Freundlich and Langmuir isotherm equations were used to describe the partitioning behavior for the system at different pH values. These authors also showed from experimental data that the adsorption and diffusion of arsenate and arsenite by activated alumina could be simulated by the proposed model. Approximately 76% MnO_2 containing ferruginous manganese ore (FMO) adsorbed As(III) and As(V) in the pH range of 2–8 and the presence of bivalent cations, namely, Ni^{2+}, Co^{2+}, Mg^{2+} enhanced the adsorption capability of the FMO (Chakravarty, et al. 2002). In all three cases, the presence of 30 ppm of the bivalent cation had a remarkable effect on As(III) adsorption, and increased it by 14%. Chakravarty, et al. (2002) further reported that the FMO used in their study comprised goethite (FeO(OH)), which could directly adsorb arsenite and arsenate anions. The presence of fayalite containing quartz (SiO_2) and perovskite ($MgSiO_3$) was also found to enhance arsenic removal (Zou, 2009). These authors found that the layer having a mixture of fayalite (Fe_2SiO_4) and magnetite/hematite in pre-corroded steel adsorbent enhanced the arsenic removal from aqueous solution. In our study, we found that the fayalite-iron oxides loaded Ni smelter slag also contained those compounds. Thus, it can be concluded from our results that the slag used in our study can be very effective in removing heavy metals form subsurface as well as from groundwater.

6.3.5 Mineralogy of Monolith slag from a Nickel Smelter

The analysis of XRD powder patterns (Figure 6.10a) shows the slag is made up of fayalite ($FeSiO_4$) and magnetite (Fe_3O_4). A close examination of the XRD data shows a small broad hump in the background between 20 and 30 degrees 2-theta. This is most likely due to the presence of amorphous material in the slag. The XRD powder patterns for ground slag reacted with arsenic laden solutions are shown in Figure 6.10b. The XRD powder pattern shown in Figure 6.10b is identical to that of the fresh slag. No arsenic phases are identified. The absence of any arsenic phases in the XRD powder patterns could be an indication that any secondary arsenic-bearing mineral that formed in this experiment were either poorly crystalline or present in quantities that were below the detection limit for the method.

XPS can detect the elemental composition and chemical oxidation states of surface and near-surface species. The Casa-XPS software was used to draw and analyze all spectra (Fairley, 1999-2003). XPS wide scan spectra of fresh slag as well as arsenic-bearing slag are illustrated in Figure 6.11. Six clear peaks at binding energies of 99.55, 281.55, 345.25, 527.95, 852.05 and 929.05 eV designated for the Si 2p, C 1s, Ca 2p, O1s, Ni 2p and Cu 2p respectively, are observed for the fresh and reacted slag sorbents (Figure 6.11a). Significant changes can be seen in Figure 6.11b after the reaction of the slag with As(V) aqueous species; the peak at binding energy of 345.25 eV for Ca 2p and 929.05 eV for Cu 2p disappears from the spectra for the As(V) loaded adsorbent while a new peak at a binding energy of approximately 45-47.09 eV for As 3d (Fig. 6.11c) appears in the arsenic-reacted slag.

The As 3d spectrum of the arsenic adsorbed slag can be deconvoluted into different individual component peaks, which originate from the arsenic atom of different valence states and which overlap with each other. Nesbitt et al., (1995) and Lim et al., (2009) assigned the As $3d_{5/2}$ peaks for As(III) and As(V) to binding energy ranges of 44.0 eV to 45.5 eV and 45.2 eV to 47.8 eV, respectively. As shown in Figure 6.12, the peaks at binding energies of 45.9 and 45.21 eV can be assigned to arsenite (As(III)) and those at 46.4 and 47.09 eV to the arsenate (As(V)) atom. These two assignments reflect the presence of inorganic arsenic atom of different chemical valences on the sorbent. Quantitative analysis of As(V) adsorbed sorbent obtained from Fig 6.12 shows that 67% of As(V) and 33% of As(III) are present. The redox potentials of the pore water in the three columns were found to be in the range of -250 to - 650mV, indicating reducing conditions within the pores of the laboratory column media. These results suggest the reduction of As(V) to As(III) at the adsorbent surface. Moreover, this result also indicates solid state oxidation-reduction between arsenate and mixed iron compounds at the surface of the sorbent.

The Fe 2p high resolution spectra were fitted following the example of Pratt and Nesbitt (1994), and Grosvenor and Bessinger (2004) using theoretical multiplet peak patterns calculated by Gupta et al. (1974 and 1975). By strictly adhering to the multiplet patterns for the various iron oxide model compounds, the XRF and XPS results show 56.23% of the iron in the slag are from iron oxide. Of the 56.23% iron oxides, 28% is maghemite, 50% is magnetite and 22% is goethite (Fig. 6.13a). After reaction with arsenic, the

amount of goethite in the slag increased to 60% (Fig 6.13b). At the same time, the percentage of magnetite was reduced to 40%. It appears that all the maghemite was converted to goethite. These results suggest that a redox reaction occurred on the mixed iron oxide surface when arsenic was introduced. Changes in the relative abundance of Fe(II) and Fe(III) in magnetite (Fig. 6.13a and 6.13b) upon reaction with arsenate show that the relative content of the Fe(II) decreases from 15.9 to 12.0 %. This result indicates that an oxidation reaction has taken place. This interpretation is further supported by the increase in goethite content from 22% to 60%. The absence of the maghemite in the reacted slag further suggests that all maghemite oxidized to Fe(III) containing goethite in the reactive slag after the introduction of As(V) solution (Fig 6.13b).

Figure 6.14 illustrates O 1s spectra of the slag at pH 5-8. The peaks at binding energy of 530.3 and 532.0 eV can be assigned to Fe-O (lattice oxygen in slag), As-O (Wagner et al., 1980) as well as to SiO_3 or SiO_4 (Fig. 6.14). This result may indicate the presence of fayalite-arsenic (Fe-As-SiO_4) or mixed iron oxide-arsenate ($FeAsO_4.2H_2O$) (Welch et al. 2000) or a complex formation on the slag surface after As(V) adsorption. The FWHM spectra at 532.0 to 533.19 eV were changed after the adsorption (Figure 6.14), indicating the occurrence of oxidation-reduction reaction between As-O and Fe-O on the reactive slag surface. The result further shows that the metal oxide (Fe-O) content decreases from 34.2 to 4.0 % and O 1s hydroxide increases from 44.1% to 54.8% indicating the formation of Fe-As-O and goethite (α-FeOOH), which is due to the binding of arsenic to oxygen atoms in the slag. Thus, it can be inferred that the mechanism of adsorption of

As(V) to smelter slag involves physico-chemical reaction as well as electrostatic attraction in the pH range of 5-8.

From XPS, the Si and Fe contents of fresh slag were found to be 11.2% and 9% (atomic wt), respectively, as shown in Figure 6.11a. From the XRF test, the SiO_3 and Fe_3O_4 contents of fresh slag were found to be 36.71% (Si 17%) and 56.53% (Fe 40.93%), as shown in Table 6.1. The SEM photomicrograph presented in Fig 6.1 also shows the presence of magnetite and fayalite. The texture of As reacted slag (Fig 6.1b) also shows the presence of euhedral tabular and botryoidal clusters indicating the presence of magnetite and goethite compounds in the SEM micrographs.

Various mineral compounds, such as fayalite (Fe_2SiO_4), magnetite, goethite and other iron oxides, are capable of adsorbing trace metals from aqueous solutions; thus they can play an important role in the fate and transport of trace element speciation in soils and groundwater (Zou, 2009 and Fendorf et al. 1997). To further confirm the interaction between the slag surface and adsorbed anions, and to detect possible As-Fe compounds on the slag surface, Raman spectroscopy was conducted on the same sample and the results are shown in Fig. 6.15. Fayalite was generally identified by a group of bands with peaks located at 171, 259 and 562 cm^{-1} (Choplelas, 1991). In this Raman study, peaks were found at 172.25, 239.08 and 523.87 cm^{-1} in Ni smelter slag indicating the presence of fayalite mineral. Faria et al. (1997) noted that the Raman band for magnetite (Fe_3O_4) was attributed to bands at ca. 665, 295, 320 and 521 cm^{-1} which were also identified in the unreacted slag spectrum. These authors also noted that the Raman spectrum of maghemite can be characterized by three broad structures around 350, 500 and 700 cm^{-1}.

In the present study, the weak Raman band around 699 cm^{-1} was attributed to magnetite-maghemite present in the fresh slag. Das et al. (2011) assigned the Raman band around 162, 297, 384, and 545 cm^{-1} to goethite. The Raman band at ca 239.08, 285 and 523.87 cm^{-1} indicated the presence of goethite in fresh slag (Das et al. 2011).

After arsenic adsorption on slag, the peaks at 507 and 523 cm^{-1} shifted to new positions at ca. 559 cm^{-1}, indicating the presence of more goethite on the As-adsorbed slag (Das et al. 2011). The new peak at ca.363.4 cm^{-1} was also assigned to the generation of goethite in As reacted slag. The shift of the fayalite peaks at ca. 172.25, 239.08 and 664.32 cm^{-1} is negligible; however, new peaks at ca 828.54 and 838.5 and 870 cm^{-1} were observed. Das et al. (2011) found Raman peaks for As-Fe compounds located between 800 cm^{-1} and 900 cm^{-1}. In agreement with Das et al. (2011), the Raman peak at 828.54 and 838.5 and 870 cm^{-1} was interpreted to originate from arsenic species that formed as a result of reaction between arsenate ions in solution and the fresh slag. From Figure 6.15, it is clearly seen that an As-Fe compound signal exists on the slag surface after the reaction of As with the slag (Fig.6.15a). Since the amount of arsenic used in the Raman spectrum analysis was very low compared to the amount of slag, any direct iron-arsenic complex contribution to the spectrum would be partially obscured by the large fayalite-mixed iron oxide slag signal.

With regard to the basic analysis parameters, both Raman and XPS have a similar minimum detection limit of approximately 0.25 - 1 weight percent. From the results of the present study, the Raman data have a very clear arsenic contribution (Fig. 6.12) as the XPS data. The As peak intensity for the two methods can be demonstrated through a

consideration of the analysis volume for each method. The XPS data are generated from a layer no thicker than 4 nanometres of the surface of the slag mass, whereas the Raman data are instigated from both the surface and the bulk of the slag mass. These results demonstrate that the As has reacted with a large proportion of the slag population in the experiment. The As Raman peak identifies that not all of the As exists on the slag surface but that some interact below the slag surface. The effect of this analysis is that, in addition to surface adsorption reactions, there might be chance for As(V) species to react with slag particles during the experiment.

Moreover, peak heights of a Raman shift at ca 828.54 and 838.5 cm^{-1} increase linearly with the As/Fe molar ratio. The results of the present study of natural and synthetic iron oxide, oxy(hydroxide), and ferric arsenate minerals as well as arsenate adsorbed onto ferrihydrite show the potential value of applying Raman spectroscopy to other mine tailings and waste rock sites (Das et al. 2011). Some arsenate species have strong peaks in the spectrum between 750 and 900 cm^{-1}. Arsenate commonly attaches to iron oxy(hydroxides) by the formation of bidentate surface complexes with high surface coverage under alkaline conditions (Fendorf et al. 1997; Sun and Doner, 1998). Jia et al. (2006) and Das et al. (2011) reported that the Raman band position at ca. 836 cm^{-1} represents As–O stretching and vibration of the bidentate-complexed arsenate onto the iron oxyhydroxide (FeO-OH) surface. The results of the current study found that the Raman band around 828.54 and 838.5 and 870 cm^{-1} in As reacted smelter slag may be assigned to similar As–O stretching and vibration of bidentate-complexed arsenate onto the iron oxyhydroxide (FeO-OH) surface. Moreover, the XPS and Raman data showed

the formation of a large amount of goethite (e.g. αFeO-OH) in the reacted slag. Thus, there may be a similar chance to form As–O stretching and vibration of the bidentate-complexed arsenate onto iron oxyhydroxide (FeO-OH) in slag generated from the reaction between As(V) species and slag particles.

Moreover, in Figure 6.15, arsenic reacted slag showed peaks at 828.84, 838.5 and 870 cm^{-1}. In this study, it is interpreted that these peaks are to be a surface interaction species. In the present Raman study, there were no sharp peaks identified in the given range (ca. 298 cm^{-1}, 320 cm^{-1}, 420 cm^{-1} and 550 cm^{-1}) indicating the reduction of magnetite in the arsenic reacted slag.. Thus, it can be concluded that Fe(II) in magnetite as well as maghemite was transformed to Fe(III) bearing goethite via a redox reaction when As(V) was introduced into the solution. This is in agreement with the results obtained in the XPS experiments.

6.4 Conclusions

The results from the present study suggest that the use of Ni smelter slag as a reactive medium for site remediation is promising. It may not be as reactive as conventional magnetite or zero valent iron, but it does have sufficient reactivity to be used in the construction of PRBs that have a reactive zone of typical thickness (< 1 m) to effectively remove arsenic. The study shows that mine waste, such as Ni smelter slag, does exhibit substantial affinity towards inorganic arsenic species. Kinetic studies revealed that the slag materials were efficient in arsenic removal, attaining equilibrium sorption capacities

in the range of 1000-1054 µg/g for an initial arsenic concentration of C_o = 10 mg/L. The results further suggest the nature of the sorption by smelter slag (a waste material) likely involves both chemisorption and physical sorption, as revealed by equilibrium studies. Sorption capacities for As(V) were significantly higher for Ni smelter slag. Arsenic sorption process on the waste materials continued at the reaction rate ranged from 0.05 to 0.9 h^{-1}.

The identification of the chemical states of the adsorbed As using XPS and Raman analyses during the removal of As from aqueous solution by Ni smelter slag is a major contribution of the study. The Raman and XPS data also suggest that electrostatic attraction and oxidation–reduction reactions between As species and mixed iron oxide bearing slag are the main mechanisms for the removal of arsenic from aqueous solutions. Theoretical multiplet analysis of the As adsorbed slag mixture presented in the study provides additional contribution to the literature on XPS studies. From the Raman study, it may be inferred that, in addition to adsorption reactions, internal interactions are also important during the experiments. These findings may be used to develop Ni smelter slag adsorbent systems for water treatment and site remediation.

Compared to other reported equilibrium sorption studies, the results of the present work indicate that the application of mixed iron oxide bearing Ni smelter slag in water treatment systems is feasible. Better sorption efficiencies are obtained in continuous flow systems. Moreover, the joint effect of sorption, coagulation, flocculation, sedimentation and filtration that are developed during continuous flow in a fixed bed reactor are

assumed to benefit the efficiency of arsenic sorption in the continuous flow process in drinking water treatment. The results have highlighted three important contributions and applications: i) mechanism of As adsorption; (ii) possible treatment of As contaminated wastewater; and (iii) remediation of As contaminated groundwater. However, the reactivity of the monolith slag from nickel smelter operation was evaluated under a limited set of idealized conditions, and more study is needed to demonstrate the generality of the findings. Additional factors that may be important in the field also need to be studied, such as the effects of other dissolved ions, pH, and dissolved oxygen content on the removal efficiency. The importance of slag heterogeneity, longevity of the reactivity, and the mechanisms controlling removal also needs to be evaluated.

Arsenic loaded slag can be disposed of either by converting the entrapped arsenic in the slag into insoluble inorganic compounds or by bio-transformation of arsenic in the slag. When slag is saturated with arsenic compound, that is, when slag loses its adsorption capability, biotransformation of arsenic may be essentially carried out by microorganisms which form mostly volatile methylated arsenic compounds (Welch et al. 2000 and Chakravarty, et al. 2002). They demonstrated that a novel arsenic loaded waste management scheme is being worked out in which native earthworm species are being used for converting arsenic from plant available to plant unavailable form. Moreover, developing countries, such as Vietnam, India and Bangladesh have limited financial resources and can not afford expensive, large-scale treatments for the removal of arsenic from drinking waters as well as subsurface to acceptable limits (from 10 ppb to 50 ppb). Low-cost, effective technologies and inexpensive treatment materials that are readily

available and easily reusable offer attractive options for such countries. The only cost related to the use of Ni smelter slag in a reactive permeable barrier in Canada is crushing. According to John Aarts Crushing Company, London, Ontario, Canada, the cost of crushing the slag into different-scale particles is $8 per ton slag. Thus, the findings of this study suggest that slags from Ni smelter operation may be effective low-cost reactive media for PRBs used to remove arsenic from groundwater in Canada or elsewhere.

6.5 References

Agency for Toxic Substances and Disease Registry (ATSDR)., 2009. Case studies in environmental medicine. Arsenic toxicity. U.S. Public Health Service, U.S. Department of Health and Human Services, Altanta, GA. http://www.atsdr.cdc.gov/csem/arsenic/docs /arsenic.pdf.

Altundogan, H.S., Altundogan, S., Tumen, F., Bildik, M., 2000. Arsenic removal from aqueous solutions by adsorption on red mud. Waste Management 20, 761-767.

Barkat, M., Nibou, D., Chegrouche, S., and Mellah, A., 2009. Kinetics and thermodynamic studies of chromium(VI) adsorption onto activated carbon from aqueous solutions. Chemical Engineering and processing 48, 38-47.

Bohart, G.S.; and Adams, E.Q., 1920. Some aspects of the behavior of charcoal with respect to chlorine. J. Am. Chem. Soc., 42, 523-529.

Blowes, D.W., Ptacek, C.J., Benner, S.G., McRae, C.W.T., Bennett, T.A., and Puls, R.W., 2000. Treatment of inorganic contaminants using permeable reactive barriers. Journal of Contaminant Hydrology 45, 123–137.

Chunming, S., and Robert. P.W., 2001. Arsenate and Arsenite Removal by Zerovalent Iron: Kinetics, Redox Transformation, and Implications for in Situ Groundwater Remediation. Environ. Sci. Technol. 35, 1487-1492.

Chakravarty, S., Dureja, V., G. Bhattacharyya, G., Maity, S., and Bhattacharjee. S., 2002. Removal of arsenic from groundwater using low cost ferruginous manganese ore. Water Research 36, 625–632.

Choplelas, A., 1991. Single crystal Raman spectra of forsterite, fayalite, and monticellite. American Mineralogist, 76, 1101-1109.

Chu, K.H., Feng, X., Kim, E.Y., and Hung, Y.T., 2011. Biosorption Parameter Estimation with Genetic Algorithm. Water 2011, 3, 177-195; doi:10.3390/w3010177.

Carberry, J.J., and Bretton, R.H., 1958 .Axial Dispersion of Mass in Flow Through Fixed Beds. A.1.Ch.E. Journal. 4(3), 367.

Camur, M.Z., and Yazicigil, H., 2001. Experimental determination of hydrodynamic dispersion coefficients for heavy metals using Compacted clay. Impact of Human Activityon Ground water Dynamics (Proceedings of asymposium held during the Six IAHS Scientific Assembly at Maastricht,The Netherlands, July 2001). IAH S Publ.no.269,2001.

Das, S., and Hendry, M.J., 2011. Application of Raman spectroscopy to identify iron minerals commonly found in mine wastes. Chemical Geology 290, 101–108.

Delgado, J.M.P.Q., 2006. A critical review of dispersion in packed beds. Heat Mass Transfer.42, 279–310. DOI 10.1007/s00231-005-0019-0.

Fahien, R.W., and Smith, J.M., 1955. Mass Transfer in Packed Beds. A.1.Ch.E. Journal. 1(1), 28.

Faria, D.L.A., Venaüncio, S., and Oliveira, M.T., 1997. Raman Microspectroscopy of Some Iron Oxides and Oxyhydroxides. Journal Of Raman Spectroscopy, 28, 873.

Fairley, N., 1999-2003. CasaXPS Version 2.2.19.

Fendorf, S., Eick, M.J., Grossl, P., and Sparks, P.D.L., 1997. Arsenate and chromate retention mechanisms on goethite. 1. Surface structure. Environmental Science and Technology 31, 315–326.

Fetter, C.W., 1993. Contaminant Hydrogeology (Second Edition).Waveland Press, Inc.Illinois.

Gotkowitz, M., Schreiber, M., and Simo, J., 2004. Effects of Water Use on Arsenic Release to Well Water in a Confined Aquifer, Ground Water, 42(4), 568-575.

Grosvenor, A.P., Kobe, B.A., Biesinger, M.C., and McIntyre, N.S., 2004. Investigation of multiplet splitting of Fe 2p XPS spectra and bonding in iron compounds. Surf. Interface Anal. 36: 1564–1574.

Gupta. R.P., S.K. Sen, S.K., 1974. Phys. Rev. 10, 71.

Gupta. R.P., S.K. Sen, S.K., 1975. Phys. Rev. 12, 15.

Harvey, C.F., Ashfaque, K.N., Yu, W., Badruzzaman, A.B.M., Ali, M.A., Oates, P.M., Michael, H.A., Rebecca, B., Neumann, R.B., Beckie, R., Islam, S., Ahmed, S.M., 2006. Groundwater dynamics and arsenic contamination in Bangladesh. Chemical Geology 228, 112–136.

Hildebrandt, U., 2000. Untersuchungen zur adsorption von arsenat(V) an aktiviertem aluminiumoxid. Dokto der Ingenieurwissenschaften dissertation, Werkstoffwissenschaften der Technischen Univ. Berlin, Berlin, Germany.

Hu et al., 2004. Removal of Cr(VI) by magnetite nanoparticle. Water science and Technology 50 (12), 139-146.

Hu, J., Chen, G., and Lo, I.M.C., 2006. Selective removal of heavy metals from industrial wastewater using maghemite nanoparticle: performance and mechanisms. Journal of Environmental Engineering, 132, 709-715.

Geological Survey of Japan., 2005. Atlas of Eh-pH diagrams Intercomparison of thermodynamic databases. National Institute of Advanced Industrial Science and Technology Research Center for Deep Geological Environments Naoto TAKENO.

Jia, Y., Xu, L., Fang, Z., Demopoulos, G.P., 2006. Observation of surface precipitation of arsenate on ferrihydrite. Environmental Science and Technology 40, 3248–3253.

Karpowicz, F., Hearn, J., and Wilkinson, M. C., 1995. The quantitative use of the bohart-adams equation to describe effluent vapour profiles from filter beds. Carbon, 33, (11) 1573-1583.

Kundu, S., and Gupta, A.K., 2005. Analysis and modeling of fixed bed column operations on As(V) removal by adsorption onto iron oxide-coated cement (IOCC). Journal of Colloid and Interface Science, 290, 52–60.

Kanel, S.R., Choi, H., Kim, J.Y., Vigneswaran, S., and Shim, W.G., 2006. Removal of Arsenic(III) from Groundwater using Low-Cost Industrial By-products—Blast Furnace Slag. Water Qual. Res. J.41, (2), 130–139.

Kuriakose, S., Singh, T.S., and Pant, K.K., 2004. Adsorption of As(III) from Aqueous Solution onto Iron Oxide Impregnated Activated Alumina. Water Qual. Res. J. Canada, 39, (3) 258–266.

Lange, R., Rowe, R.K., and Jamieson, H., .2009. Diffusion of metals in geosynthetic clay liners. Geosynthetics International, 16, (1), 11-27.

Lai, K.C.K., and Lo, I.M.C., 2002. Bench-scale study of the effects of seepage velocity on the dechlorination of TCE and PCE by zerovalent iron. In: Proceedings of the Sixth International Symposium on Environmental Geotechnology, Seoul, Korea.

Lee, T., and Benson, C., 2004. Using Waste GreenSands for Treating Alachlor and Metolachlor in Groundwater, J. Environmental Quality, 33(5), 1682-1693.

Lee, S.H., Jung, W., Jeon, B.H., Choi, J.Y., and Kim, S., 2011. Abiotic subsurface behaviors of As(V) with Fe(II). Environ Geochem Health, 33:13–22.

Leupin, O., Hug, S., and Badruzzaman, A., 2005. Arsenic Removal from Bangladesh Tube-Well Water with Filter Columns Containing Zero Valent Iron and Sand, Env. Sci. & Tech, 39, 8032-8037.

Lim, S.F., Zheng, Y.M., and Chen, J.P., 2009. Organic Arsenic Adsorption onto a Magnetic Sorbent. Langmuir**,** 25(9), 4973–4978.

Lin, T.F., and Wu, J.K., 2001. Adsorption of arsenite and arsenate within activated alumina grains: equilibrium and Kinetics. Wat. Res. 35, (8) 2049–2057.

Metz, S., and Benson, C., 2007. Iron Foundry Slags as Permeable Reactive Barriers Materials for Removing Arsenic from Groundwater, Proceedings, GeoDenver, American Society of Civil Engineers.

Metz, S.E., and Benson, H.C., 2006. Iron foundry slags for removing arsenic from water. WRI Project: 05-REM-02, WR04R008. Geo Engineering Report No. 06-23.

Maji, S.K., Pal, M., Pal, T.,and Adak, A., 2007. Adsorption thermodynamic of As on Laterite soil. J. surface Sci. Technol. 22 (3-4), 161-176.

Macdonald, F., Taylor and Francis., 2009. CRC Handbook of Chemistry and Physics: 90 Editions. Cleveland Ohio. http://chemistry.about.com/od/elementfacts/a/arsenic.htm or http://www.webelements.com/arsenic/atom_sizes.html.

Nesbitt, I.J and Pratt, A.R., 1995. Oxidation of arsenopyrite by air and air-saturated, distilled water and implications for mechanism of oxidation. Geochimica et Cosmochimica Acta, 59 (9), 1773-1786.

Nikolaidis, N., Dobbs, G., and Lackovic, J., 2003, Arsenic Removal by Zero-Valent Iron: Field, Laboratory, and Modeling Studies, Water Research, 37, 1417-1425.

Petrova, T.M., Fachikov, L., and Hristov, J., 2011. The magnetite as adsorbent for some hazardous species from aqueous solutions: a review. International Review of Chemical Engineering (I.RE.C.H.E.), 3,2, 134.

Pratt, A.R., Blowes, D.W., and Ptacek, C.J., 1997. Products of chromate reduction on proposed remediation material. Environ. Sci. Technol. 31: 2492-2498.

Pratt, A.R., Muir, I.J., and Nesbitt, H.W., 1994. X-ray photoelectron and Auger electron spectroscopic studies of pyrrhotite and mechanism of air oxidation. Geochimica et Cosmochimica Acta 58, 827-841.

Odziemkowski, M.S., Schuhmacher, T.T., Gillham, R.W., and Reardon, E.J., 1998. Mechanism of oxide film formation on iron in simulating groundwater solutions: Raman spectroscopic studies. Corrosion Science. 40 (2/3), 371-389.

Rowe, R.K., Quigley, R.M., and Booker, J.R., 1995. Clay-leachate compatibility by measurement of hydraulic conductivity. Clay barrier systems for waste disposal facilities, Chap. 4, E & FN Spon,London.

Rowe, R.K., and Booker, J.R.; 1985. 1 D pollutant migration in soils of finite depth, Journal of Geotechnical Engineering, ASCE, Vol. 111, GT4, pp. 479-499.

Rowe, R.K. and Fraser, M.J., 1994. Consideration of Uncertainty Regarding Service Lives of Engineered Systems in Assessing Potential Contaminant Impact, CSCE Special Publication- Engineering Materials for Waste Isolation, pp. 119-146.

Rowe, R.K., Caers, C.J.and Barone, F., 1988. Laboratory determination of diffusion and distribution coefficients of contaminants using undisturbed clayey soil. Can.Geotech. J. 25 ,108-118 .

Shen, H., and Wilson, J.T., 2007. TCE removal from groundwater in flow-through columns simulating a PRB constructed with plant mulch. Environ. Sci. Technol. 41, 4077-4083.

Sotelo, J.L.; Rodríguez, A., Álvarez, S.; and García, J., 2012. Modeling and Elimination of Atenolol on Granular Activated Carbon in Fixed Bed Column. Int. J. Environ. Res., 6(4):961-968.

Sperlich, A., Wener, A., Genz, A., Amy, G., Worch, E., Jekel, G., 2005. Breakthrough behavior of granular ferric hydroxide (GFH) fixed-bed adsorption filters: modeling and experimental approaches. Water Research 39, 1190–1198.

Sun, X., and Doner, H., 1998. Adsorption and oxidation of arsenite on goethite. Soil Science, 163, 278–287.

Tanboonchuy, V., Liao, C.H., and Grisdanurak, N., 2011. Arsenic Removal by Nanoiron in the Gas-bubbled Aqueous Solution. 2011 International Conference on Environment Science and Engineering IPCBEE vol.8 © (2011) IACSIT Press, Singapore.

Thirunavukkarasu1, O.S., Viraraghavan, T., and Subramanian, K.S., 2003. Arsenic removal from drinking water using granular ferric hydroxide. Water SA. 29 (2).

Vu, K.B., Kaminski, M.D., and Nuñez, L., 2003. Review of Arsenic Removal Technologies for Contaminated Groundwaters. ANL-CMT-03/2. Argonne National Laboratory 9700 South Cass Avenue Argonne, IL 60439.

Wagner, C.D., Zatko, D.A., and Raymond, R.H., 1980. Use of the oxygen KLL Auger lines in identification of surface chemical states by electron spectroscopy for chemical analysis. Anal. Chem. 52: 1445–1451.

Westerhoff, P., Highfield, D., Badruzzaman, M., and Yoon, Y., 2005. Rapid Small-Scale Column Tests for Arsenate Removal in Iron Oxide Packed Bed Columns. J. Environ. Eng.131, 262-271.

Wilkens, J., Shoemaker, S., Bazela, W., Egler, A., and Bain, J., 2003. Arsenic Removal from Groundwater Using a PRB of BOF Slag at the Dupont East Chicago Site, Proc. RTDF PRBs Action Team Meeting, Niagara Falls.

Williams, L.E., Barnett, M.B., Kramer, T.A., and Melville, J.G., 2003. Adsorption and Transport of Arsenic(V) in Experimental Subsurface Systems. J. Environ. Qual. 32:841–850.

Welch, A.H., Westjohn, D.B., Helsel, D.R., and Wanty, R.B., 2000. Arsenic in ground water of the United States: Occurrence and geochemistry. Ground Water. 38:589–604.

Yean, S., Cong, L., Yavuz, C.T., Mayo, J.T., and Yu, W.W., 2005. Effect of magnetite particle size on adsorption and desorption of arsenite and arsenate. Materials Research Society. J. Mater. Res. 20 (12).

Zhang, Q. L., Yun, G.N., Lin, Y.C; Bin, X., and Sheng, L., 2007. Removal of Arsenic(V) From Aqueous Solutions Using Iron-Oxide- Coated Modified Activated Carbon. www.redorbit.com › News › Science.

Zou, J., 2009. Tailored granular activated carbon preceded by Pre-corroded steel. Ph.D thesis. Department of Civil and Environmental Engineering, The Pennsylvania State University.

List of Tables

Table 6.1: Chemical analysis of Ni smelter slag by XRF analysis.

Major-Oxide Contents	XRF data (%weight)	Contents	XRF data (%weight)
SiO_2	36.90	K_2O	0.63
Al_2O_3	2.44	Na_2O	0.26
FeO	56.72	P_2O_5	0.11
MnO	0.04	Cr_2O_3	0.20
MgO	1.23	TiO_2	0.2
CaO	1.26	Total	100

Table 6.2: As removal capacity and migration rate in the columns

Columns	Normalized migration rate of As(V) front at $C/C_o = 0.5$ (cm/cm^3)	r^2	Removal capacity of slag at $C/C_o = 0.5$ (mg As/g slag)	Effluent pH range
1	$0.24 * 10^{-3}$	0.97	1	7-8
2	$0.21* 10^{-3}$	0.94	1.054	6.5-8
3	$0.2 * 10^{-3}$	0.99	1.039	6-8

List of Figures

Figures

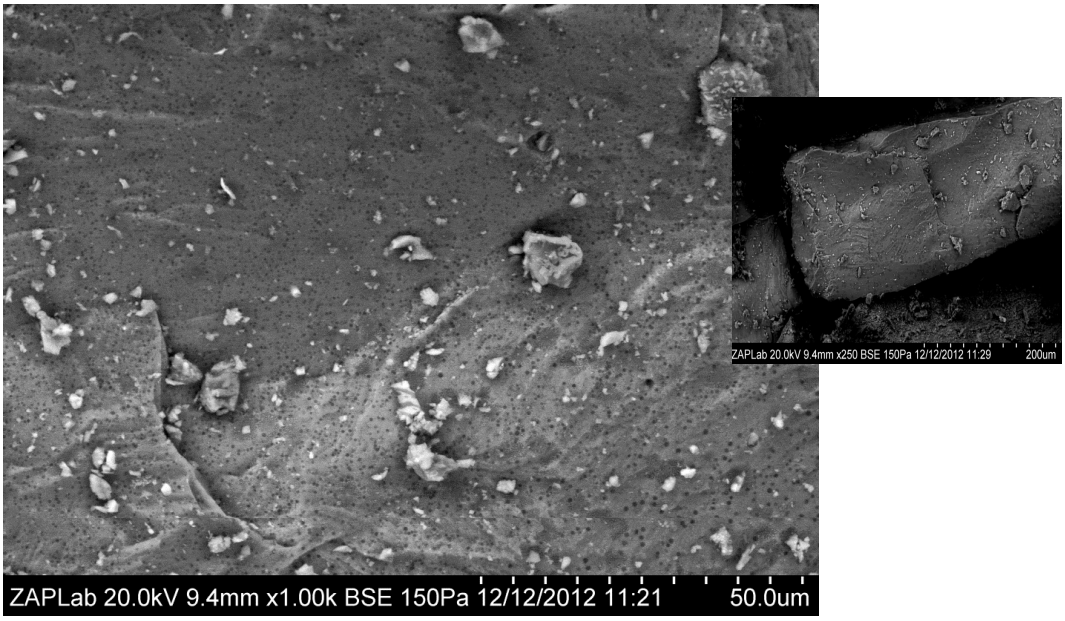

(a)

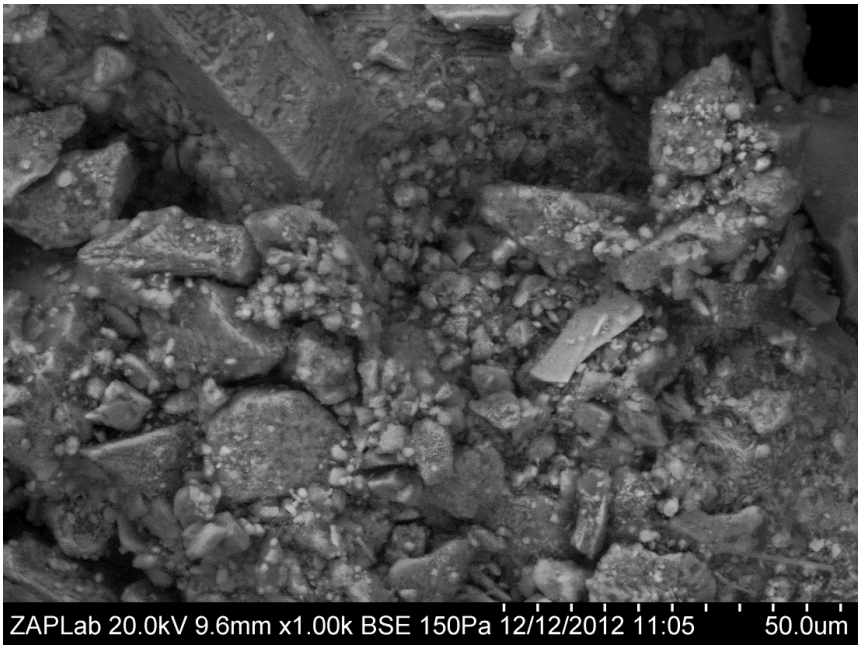

(b)

Figure 6.1: Representative SEM micrographs of (a) fresh slag and (b) As reacted slag.

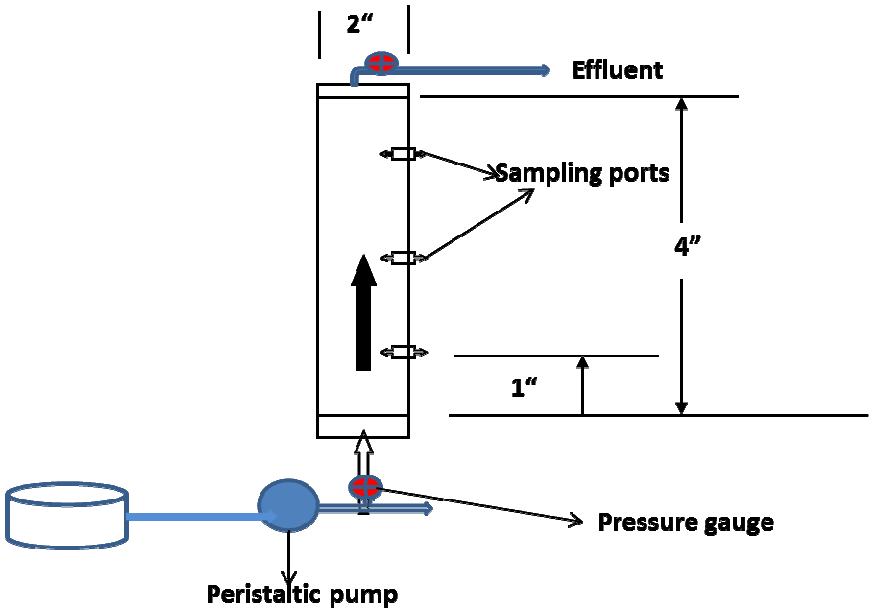

(a)

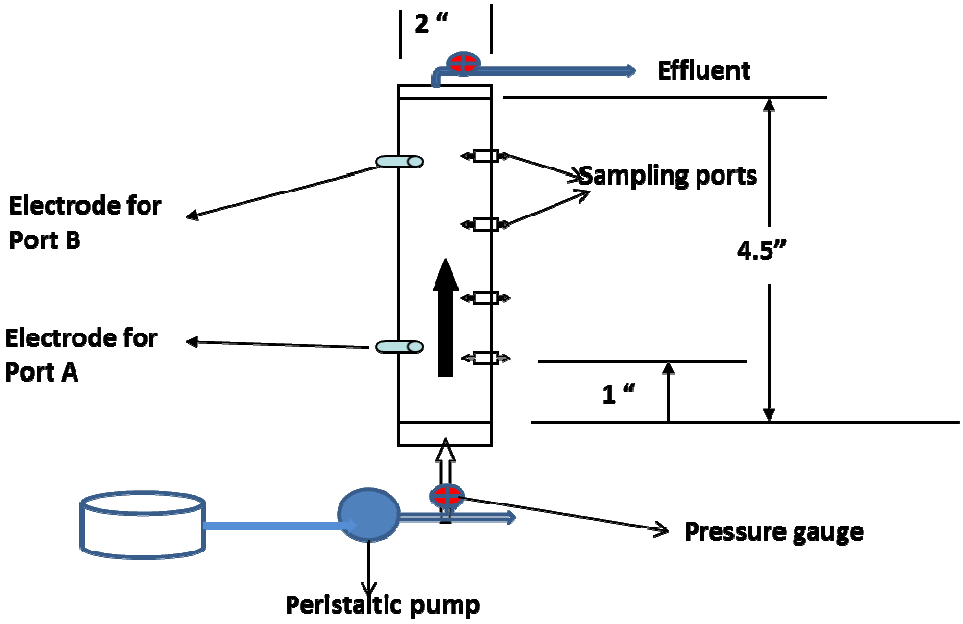

(b)

Figure 6.2: Experimental Column Set-up a) 1 and 2 columns and b) 3 column

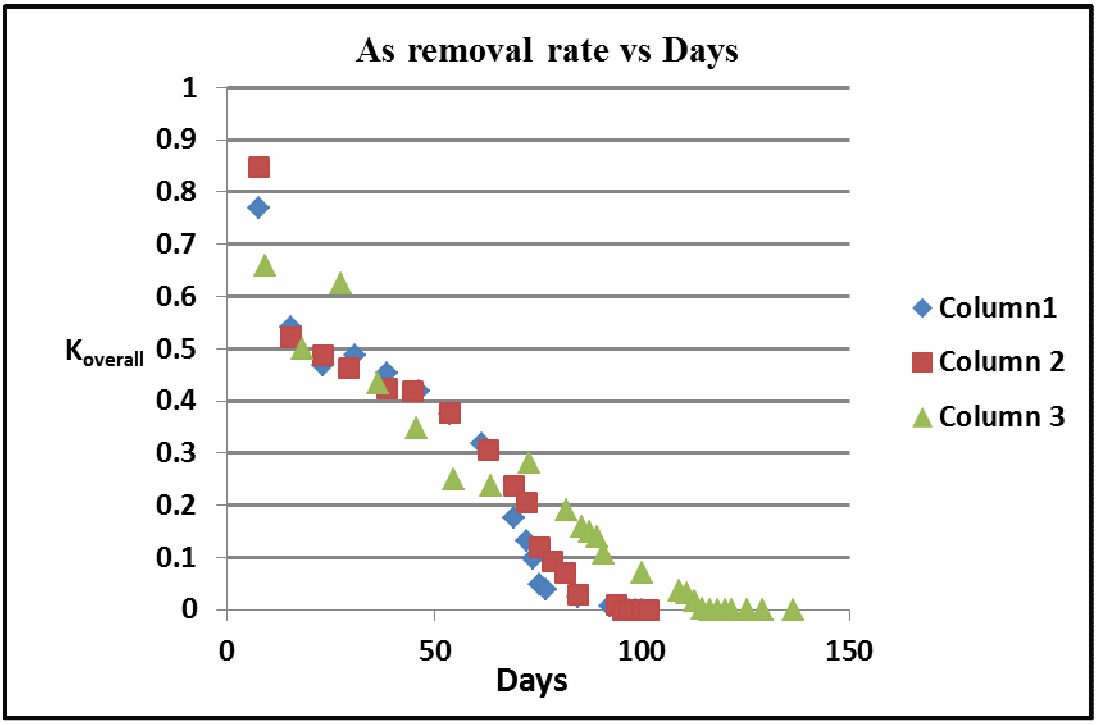

Figure 6.3: The changes in the calculated rate constants for As(V) removal over time in the Ni smelter slag columns simulating PRB.

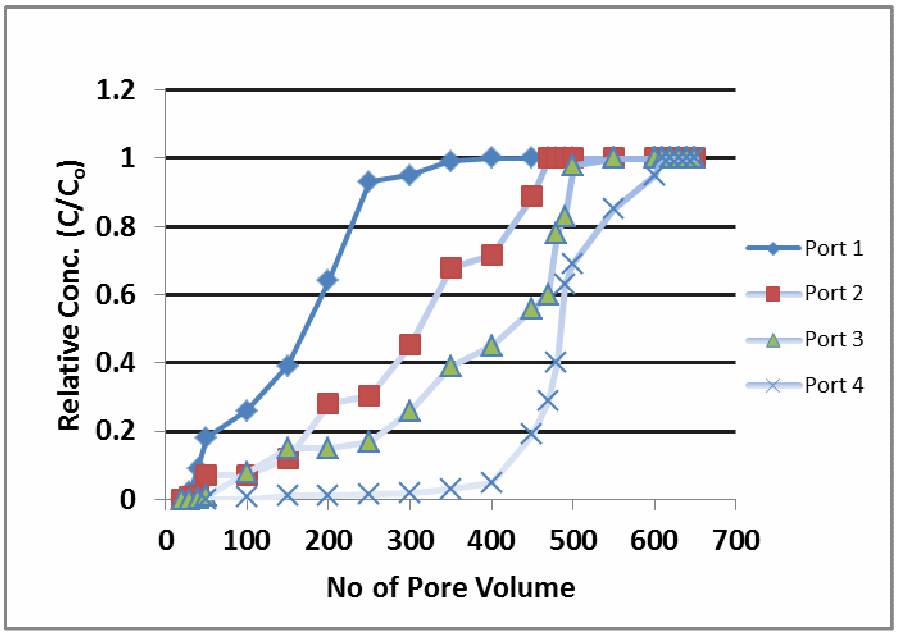

(a)

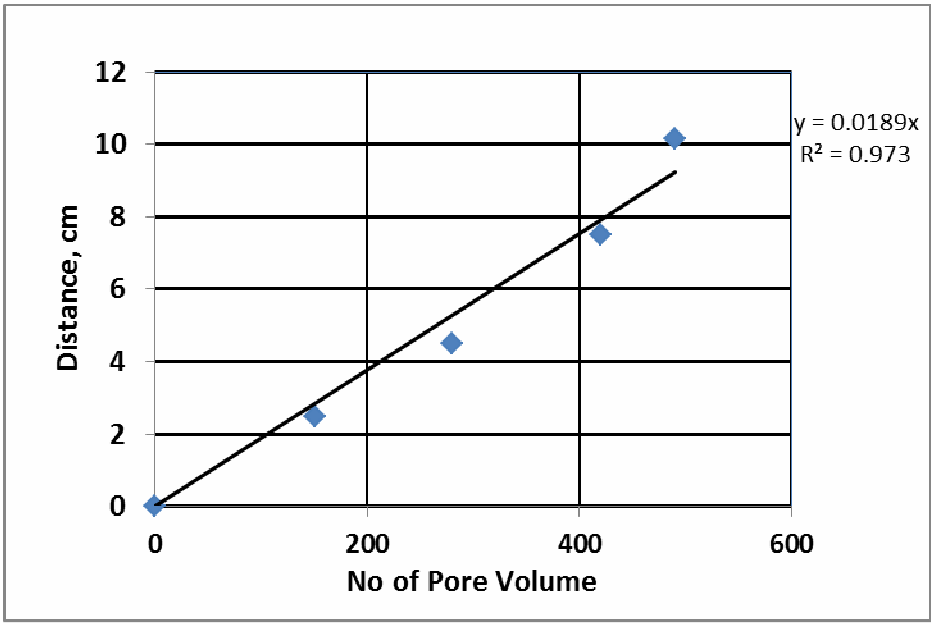

(b)

Figure 6.4: (a) As(V) migration curve through column 1 and (b) distance of the As(V) front migration at C/C_0 =0.5 in column 1. The slope of the line designates the migration rate of As(V) along the column.

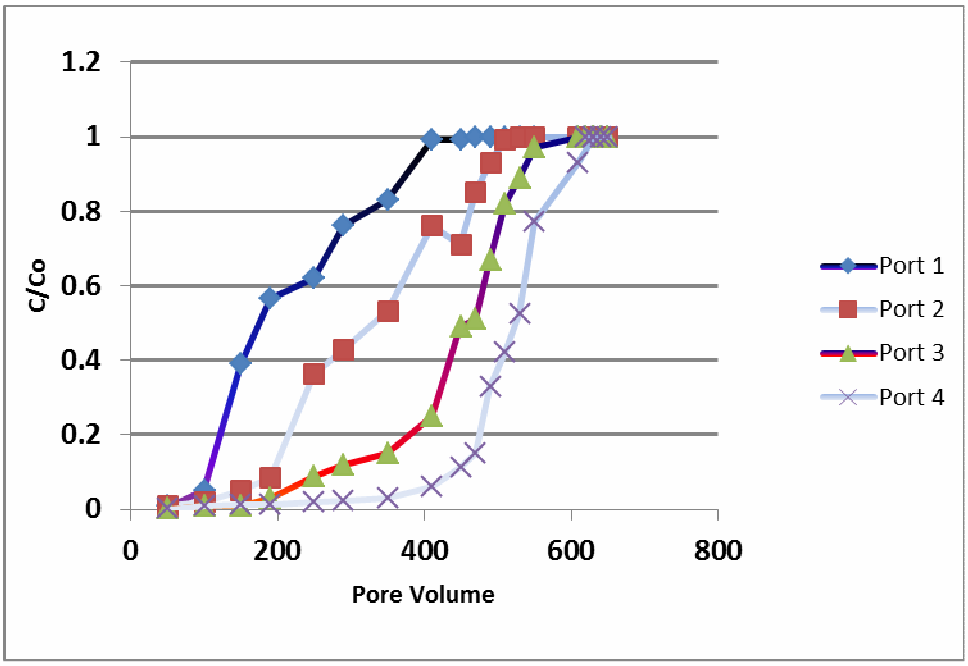

(a)

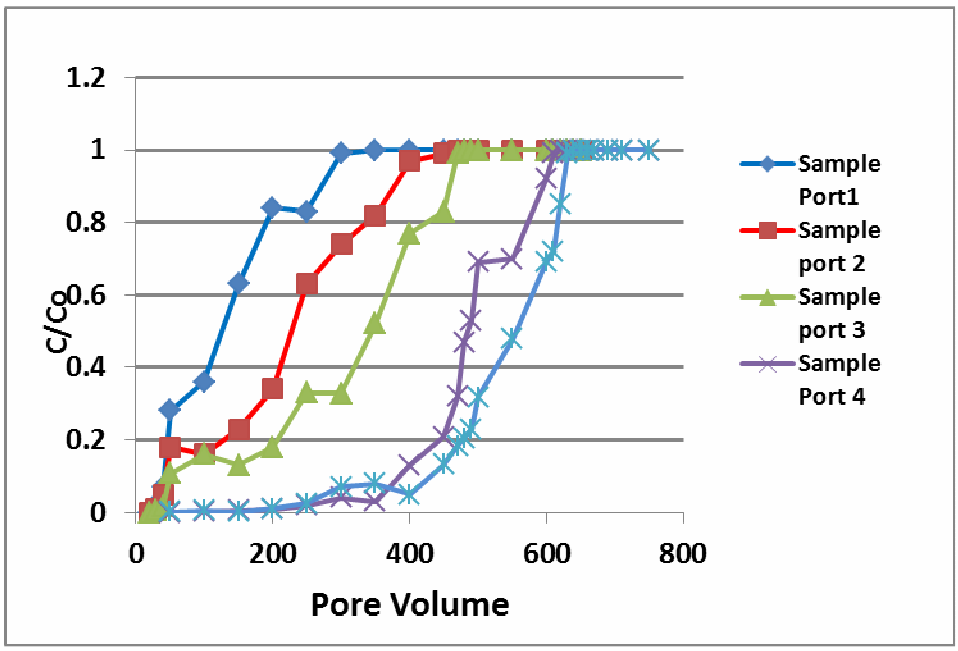

(b)

Figure 6.5: As(V) migration as well as breakthrough curve of (a) column 2, and (b) column 3.

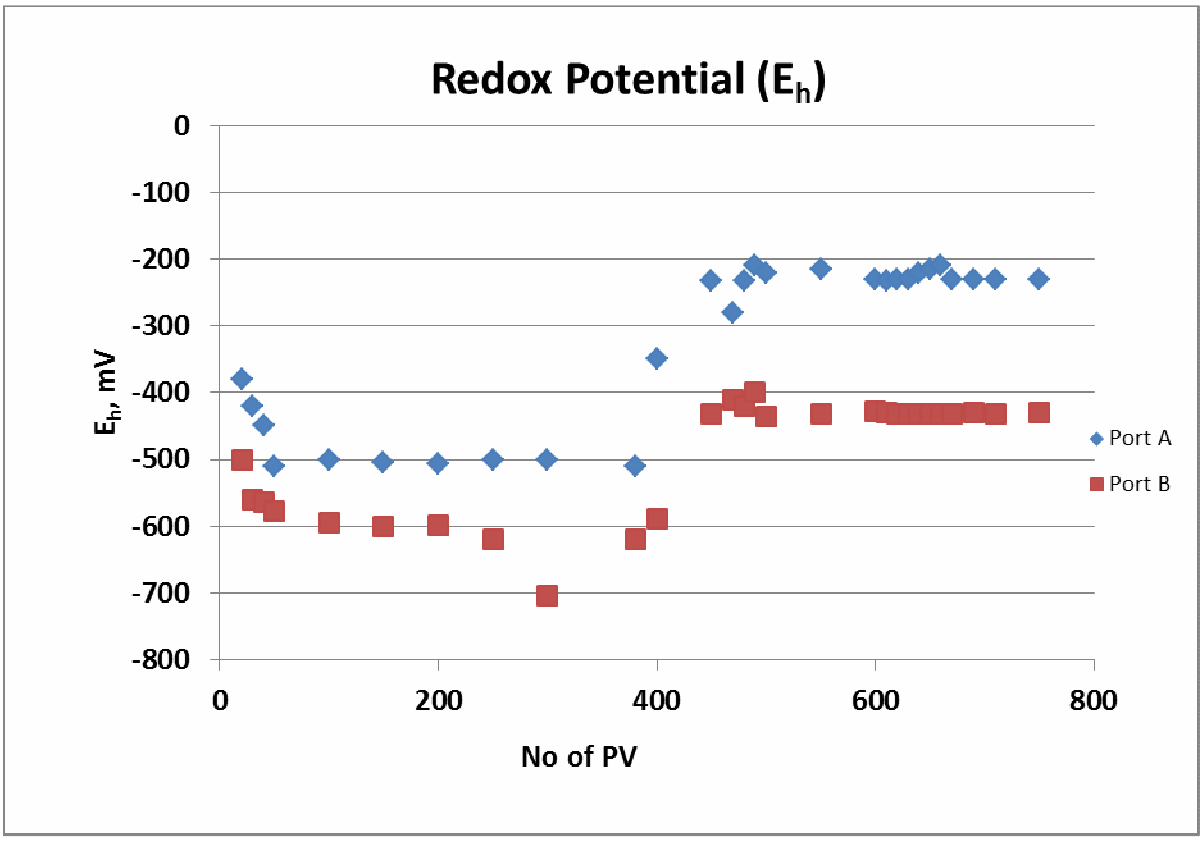

Figure 6.6: The changes of redox potential values (E_h) with times in column 3.

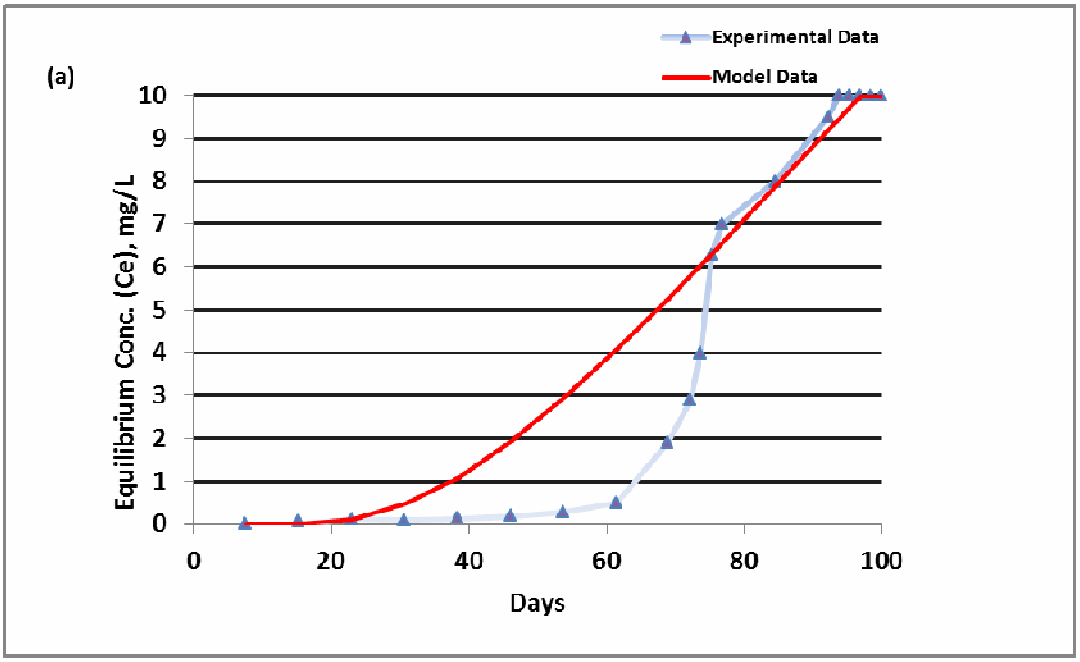
(a)
Experimental Data
Model Data
Equilibrium Conc. (Ce), mg/L
0
1
2
3
4
5
6
7
8
9
10
0
20
40
60
80
100
Days

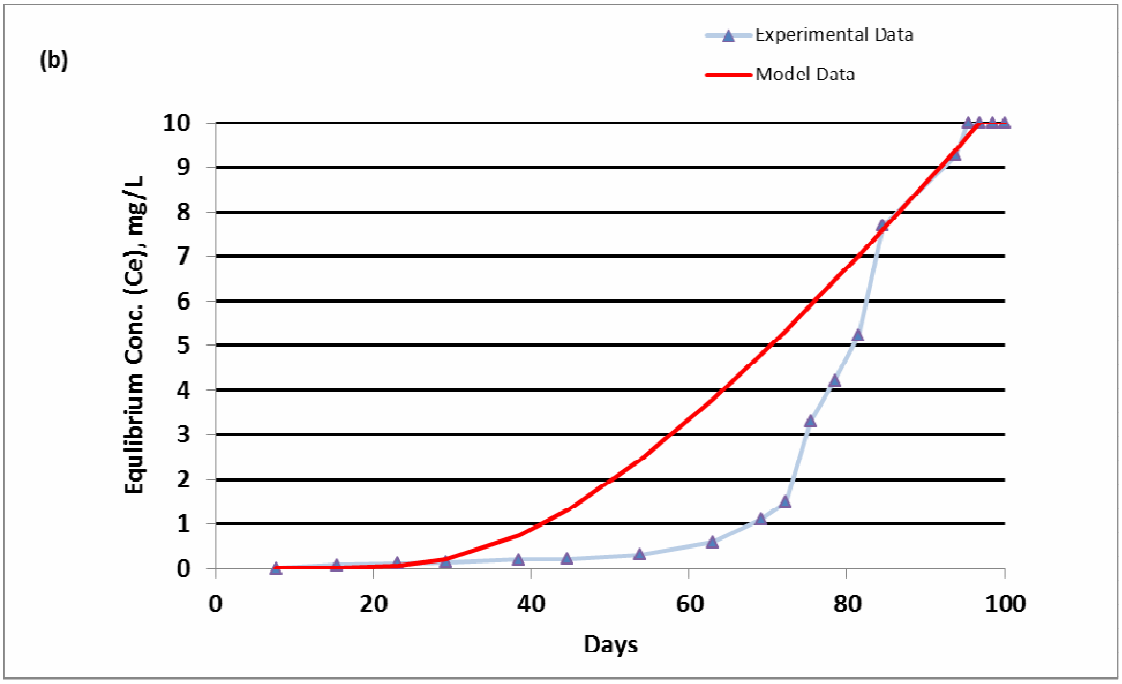
(b)
Experimental Data
Model Data
Equilibrium Conc. (Ce), mg/L
0
1
2
3
4
5
6
7
8
9
10
0
20
40
60
80
100
Days

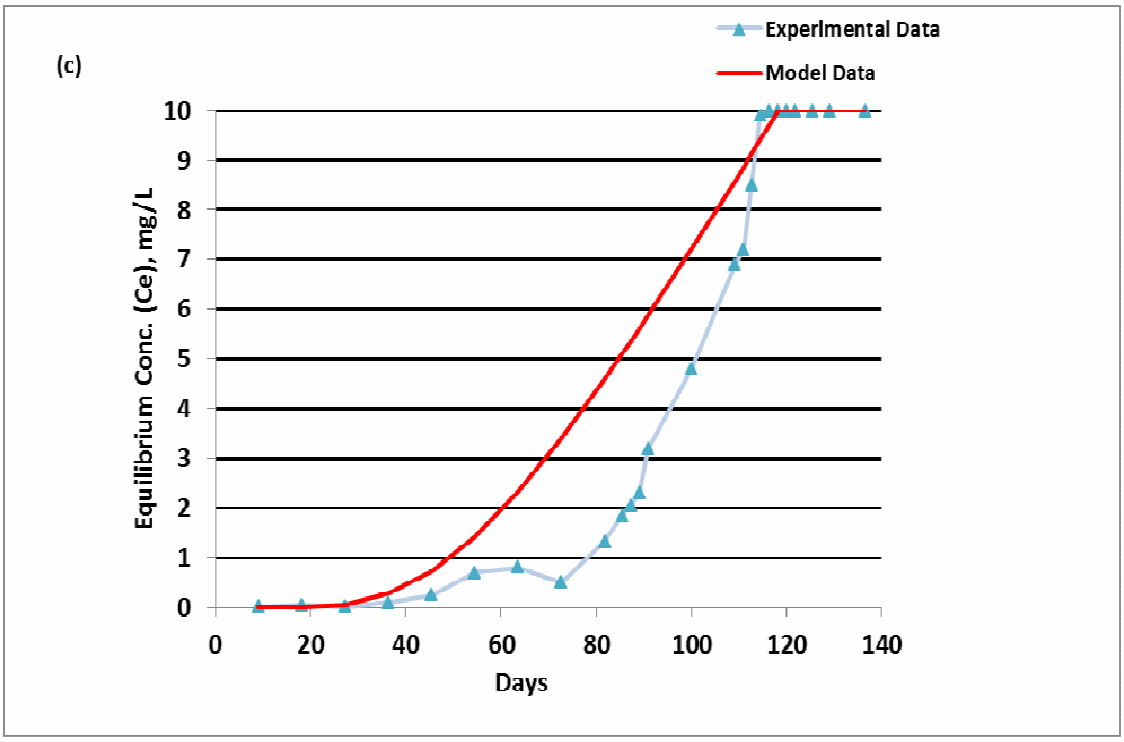

Figure 6.7: As(V) breakthrough curves of experimental and model values for (a) column1 (b) column 2 and (c) column 3.

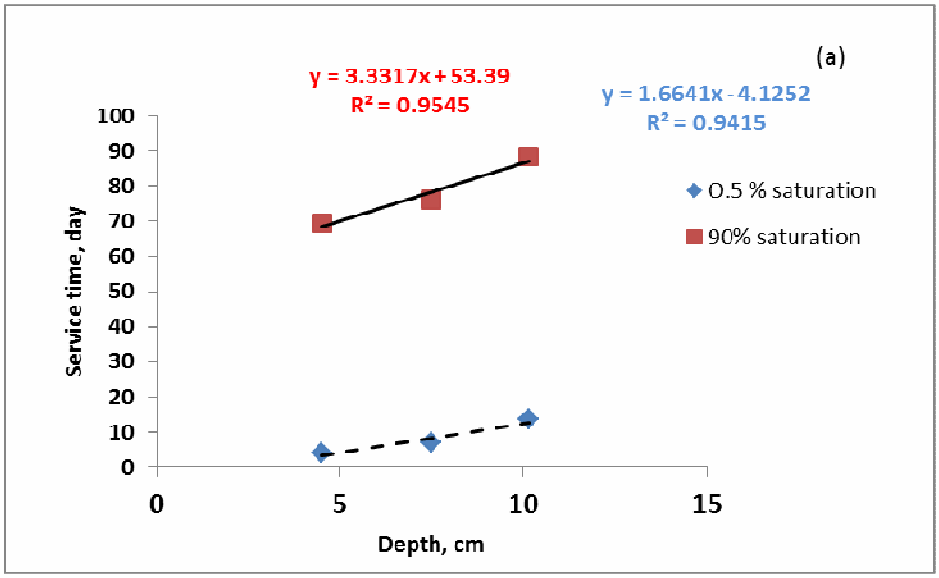

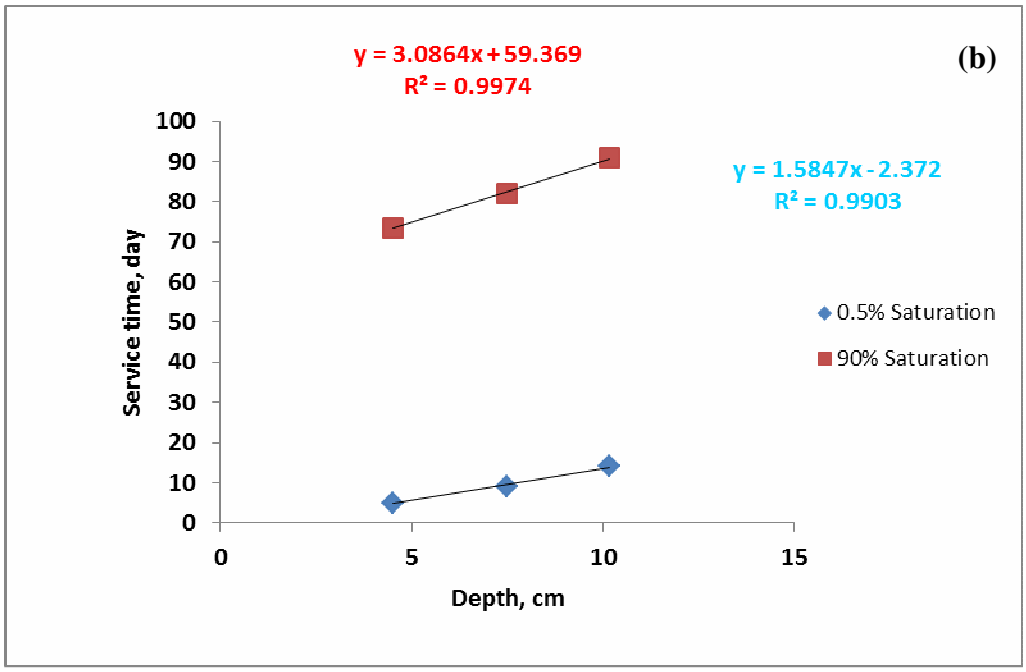

Figure 6.8: The depth vs service time for 0.5 and 90% saturation of (a) the column 1 and (b) Column 2.

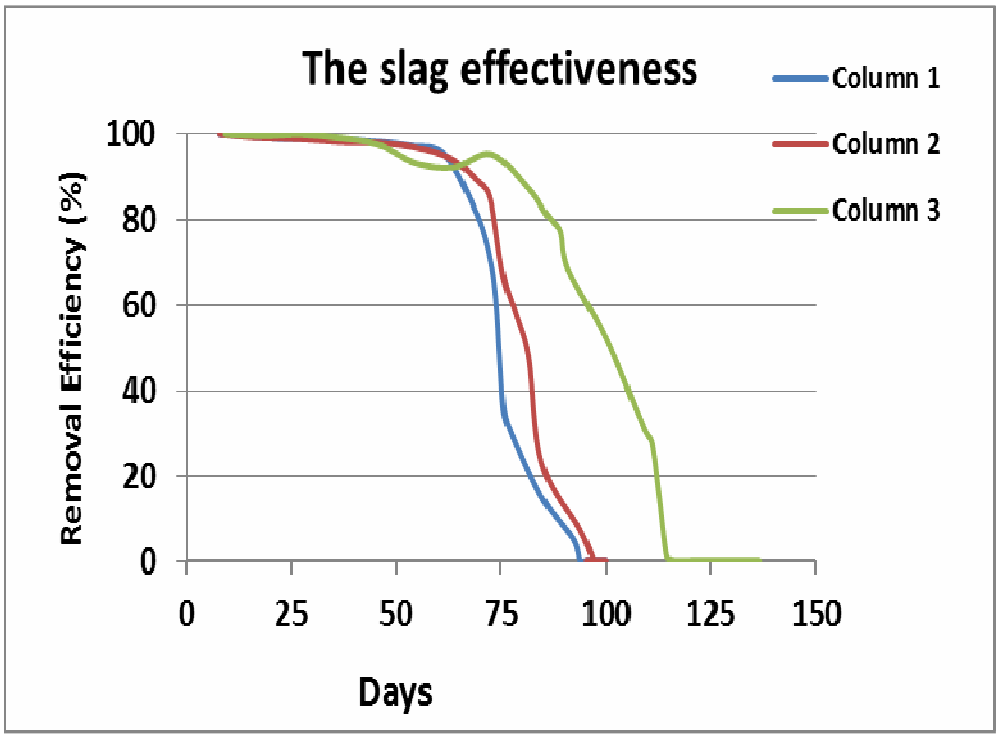

Figure 6.9: The effectiveness of Ni smelter slag medium used in the lab scale.

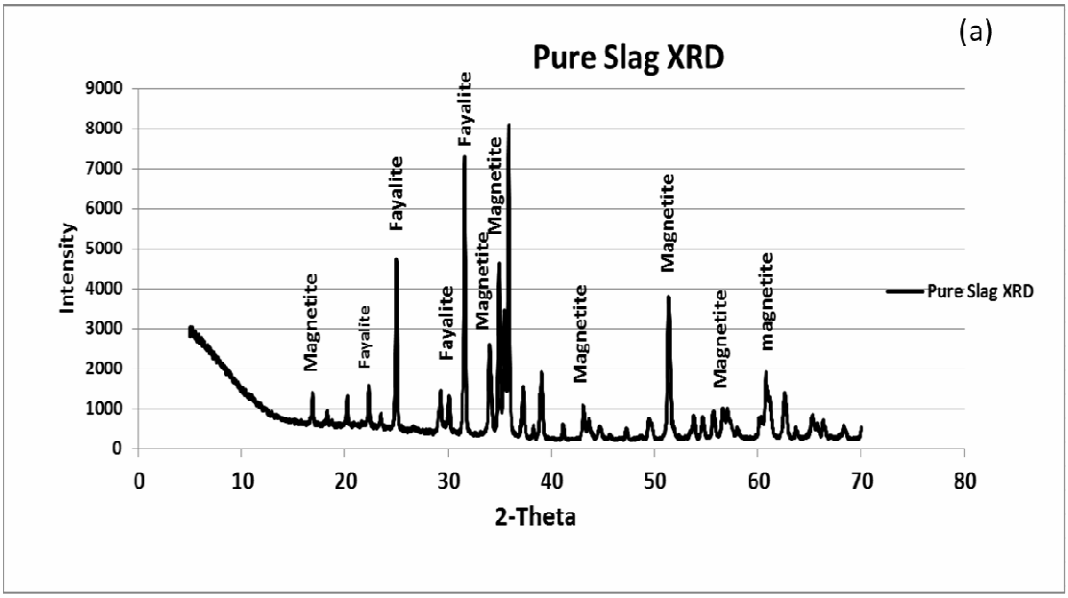

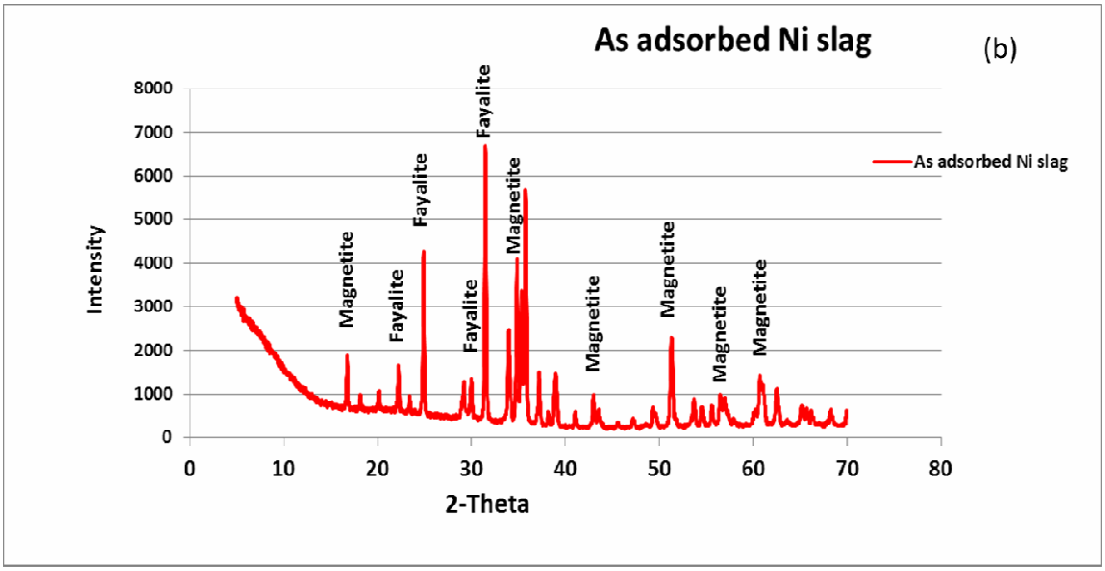

Figure 6.10: XRD patterns showing (a) fresh Ni smelter slag and (b) As-loaded Ni smelter slag.

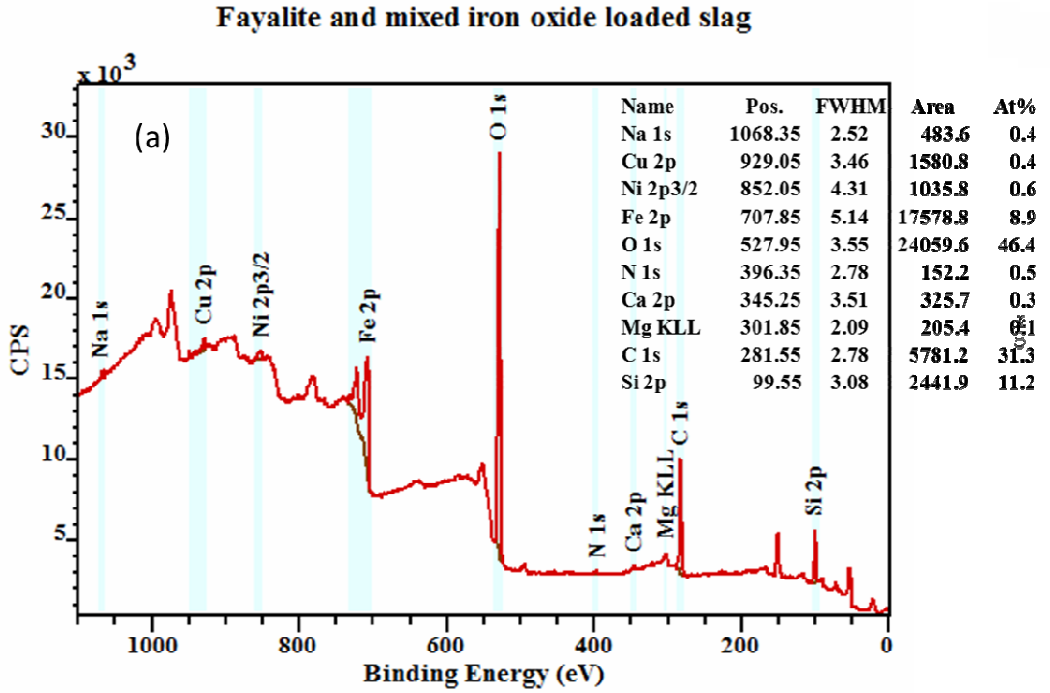
Fayalite and mixed iron oxide loaded slag
x 10^3
(a)
CPS
Binding Energy (eV)
Na 1s
Cu 2p
Ni 2p3/2
Fe 2p
O 1s
N 1s
Ca 2p
Mg KLL
C 1s
Si 2p
Name Pos. FWHM Area At%
Na 1s 1068.35 2.52 483.6 0.4
Cu 2p 929.05 3.46 1580.8 0.4
Ni 2p3/2 852.05 4.31 1035.8 0.6
Fe 2p 707.85 5.14 17578.8 8.9
O 1s 527.95 3.55 24059.6 46.4
N 1s 396.35 2.78 152.2 0.5
Ca 2p 345.25 3.51 325.7 0.3
Mg KLL 301.85 2.09 205.4 0.1
C 1s 281.55 2.78 5781.2 31.3
Si 2p 99.55 3.08 2441.9 11.2

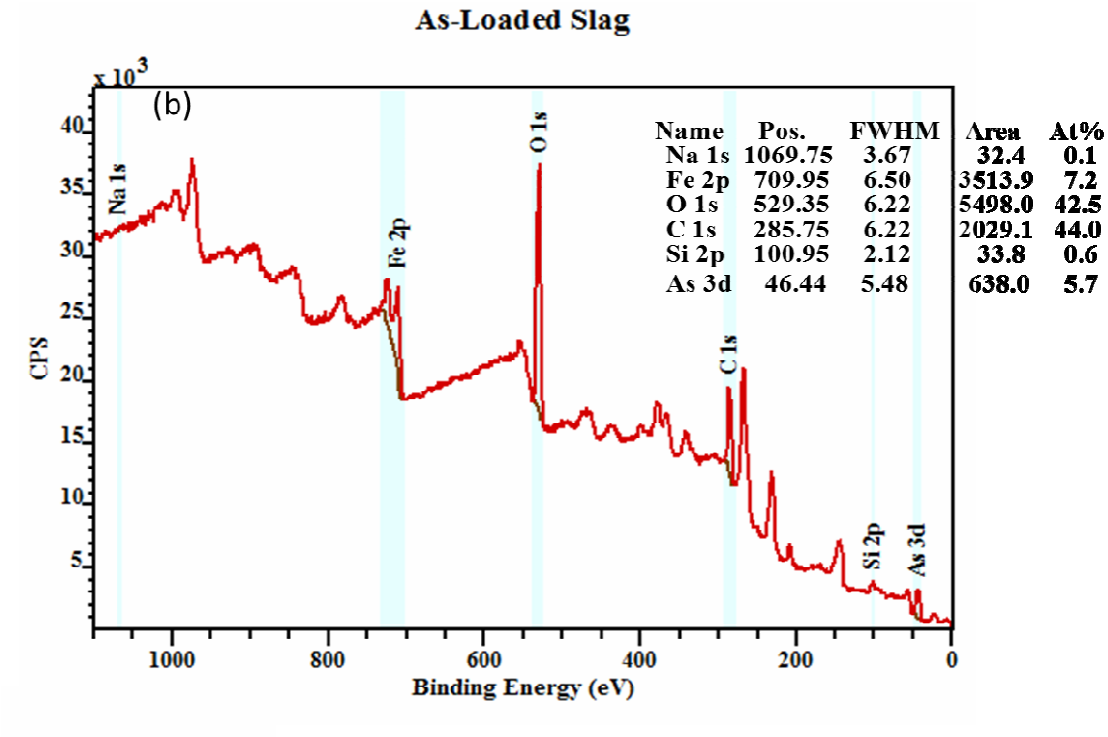
As-Loaded Slag
x 10^3
(b)
CPS
Binding Energy (eV)
Na 1s
Fe 2p
O 1s
C 1s
Si 2p
As 3d
Name Pos. FWHM Area At%
Na 1s 1069.75 3.67 32.4 0.1
Fe 2p 709.95 6.50 3513.9 7.2
O 1s 529.35 6.22 5498.0 42.5
C 1s 285.75 6.22 2029.1 44.0
Si 2p 100.95 2.12 33.8 0.6
As 3d 46.44 5.48 638.0 5.7

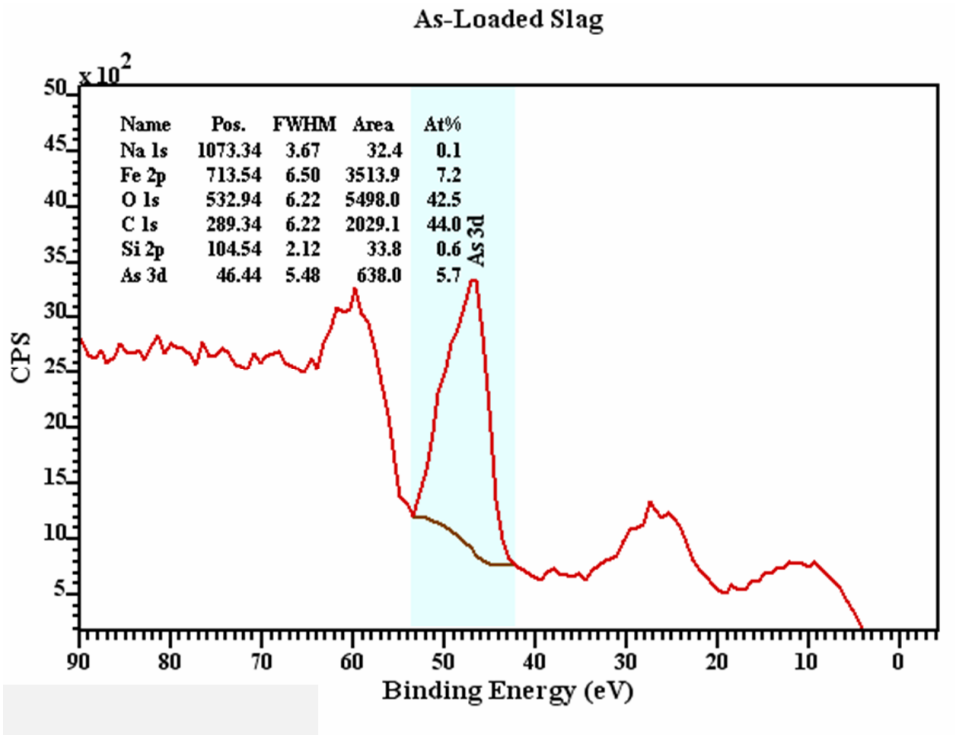

Figure 6.11: XPS wide scan spectra of (a) fresh slag (b) arsenic reacted slag and (c) As peak position on slag surface.

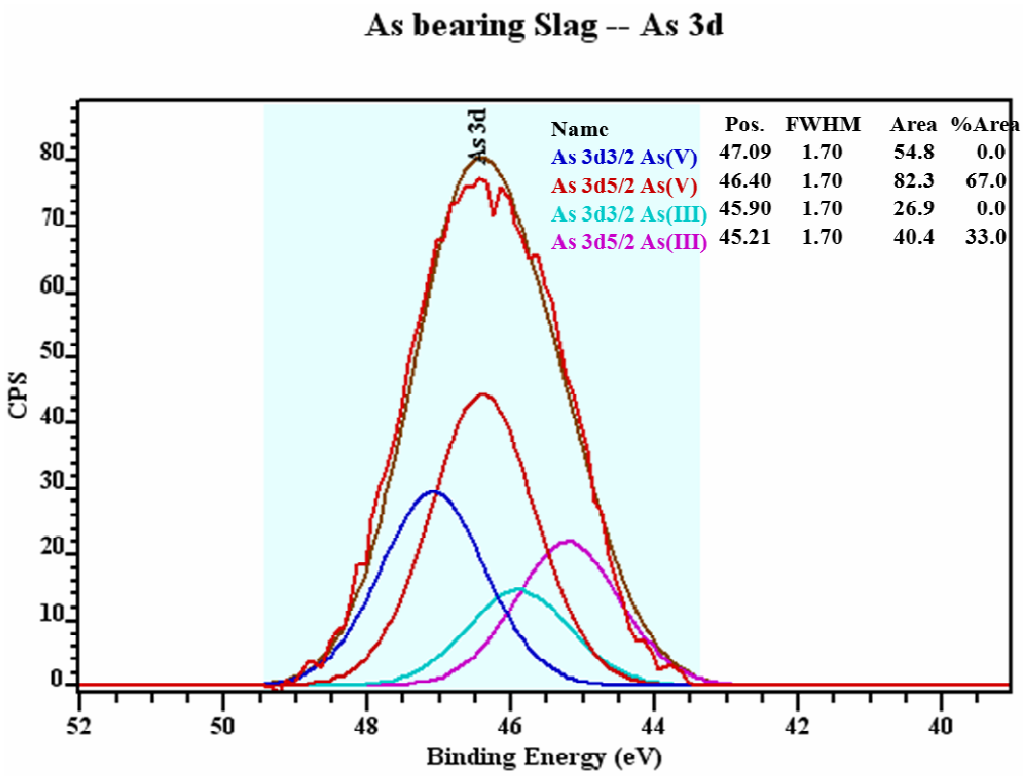

Figure 6.12: As 3d XPS spectra of the Arsenic reacted smelter slag

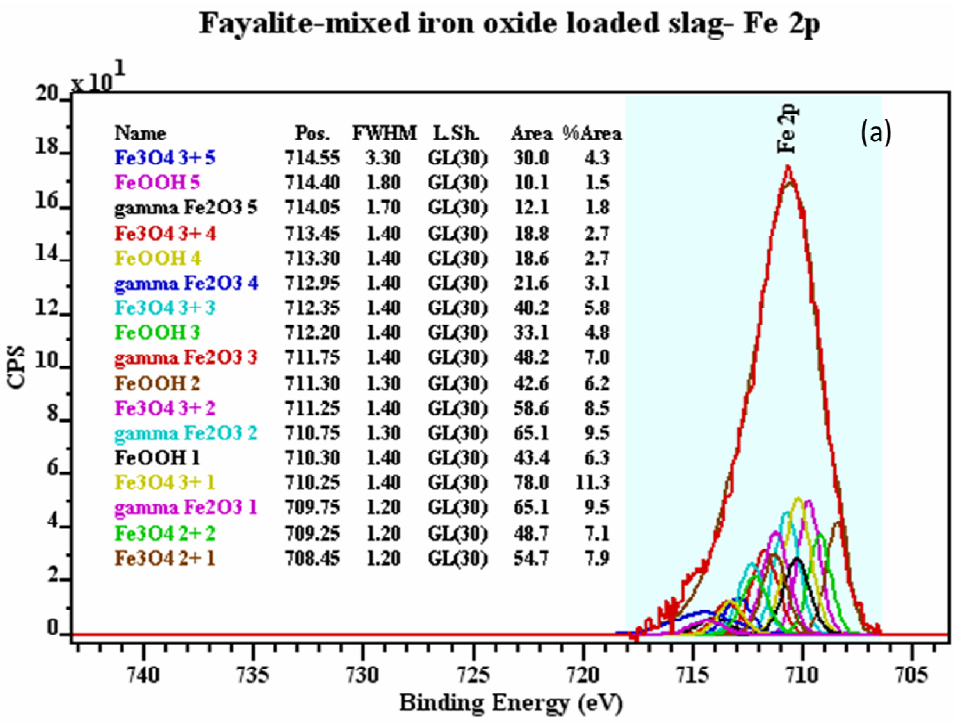
Fayalite-mixed iron oxide loaded slag- Fe 2p
x 10^1
CPS
Binding Energy (eV)
Fe 2p
(a)
Name Pos. FWHM L.Sh. Area %Area
Fe3O4 3+ 5 714.55 3.30 GL(30) 30.0 4.3
FeOOH 5 714.40 1.80 GL(30) 10.1 1.5
gamma Fe2O3 5 714.05 1.70 GL(30) 12.1 1.8
Fe3O4 3+ 4 713.45 1.40 GL(30) 18.8 2.7
FeOOH 4 713.30 1.40 GL(30) 18.6 2.7
gamma Fe2O3 4 712.95 1.40 GL(30) 21.6 3.1
Fe3O4 3+ 3 712.35 1.40 GL(30) 40.2 5.8
FeOOH 3 712.20 1.40 GL(30) 33.1 4.8
gamma Fe2O3 3 711.75 1.40 GL(30) 48.2 7.0
FeOOH 2 711.30 1.30 GL(30) 42.6 6.2
Fe3O4 3+ 2 711.25 1.40 GL(30) 58.6 8.5
gamma Fe2O3 2 710.75 1.30 GL(30) 65.1 9.5
FeOOH 1 710.30 1.40 GL(30) 43.4 6.3
Fe3O4 3+ 1 710.25 1.40 GL(30) 78.0 11.3
gamma Fe2O3 1 709.75 1.20 GL(30) 65.1 9.5
Fe3O4 2+ 2 709.25 1.20 GL(30) 48.7 7.1
Fe3O4 2+ 1 708.45 1.20 GL(30) 54.7 7.9

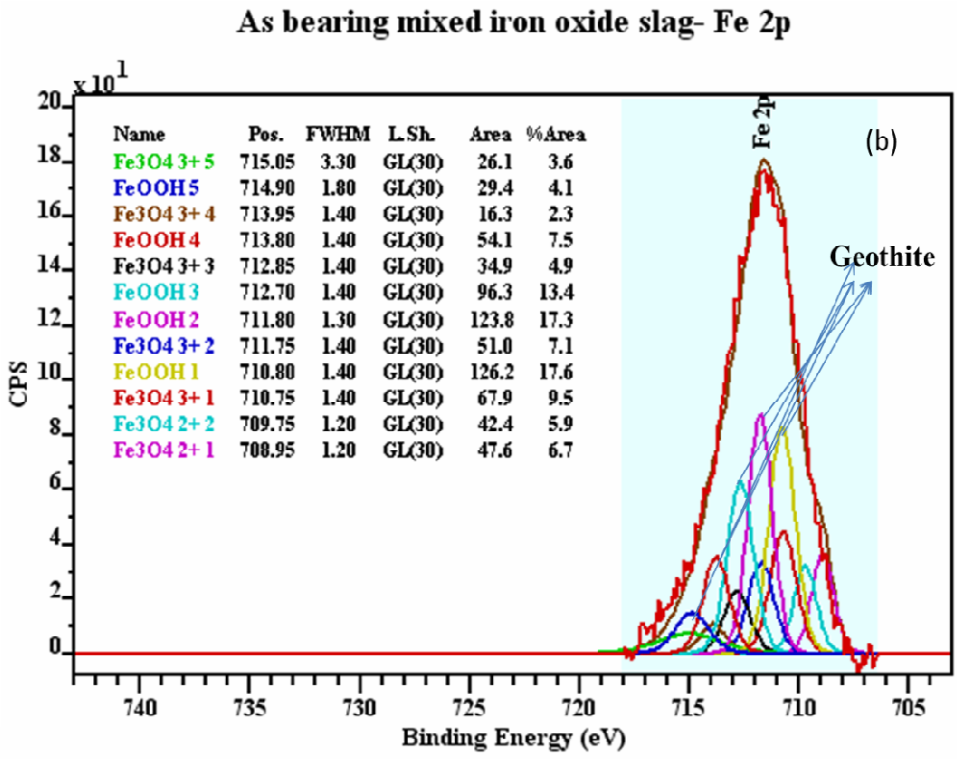

Fe3O4 3+ means Fe (III) in magnetite; Fe3O4 2+ means Fe (II) in magnetite; Gamma Fe2O3 means maghemite peak and FeOOH means goethite peak.

Figure 6.13: XPS spectra (a) fresh slag and (b) arsenic reacted slag.

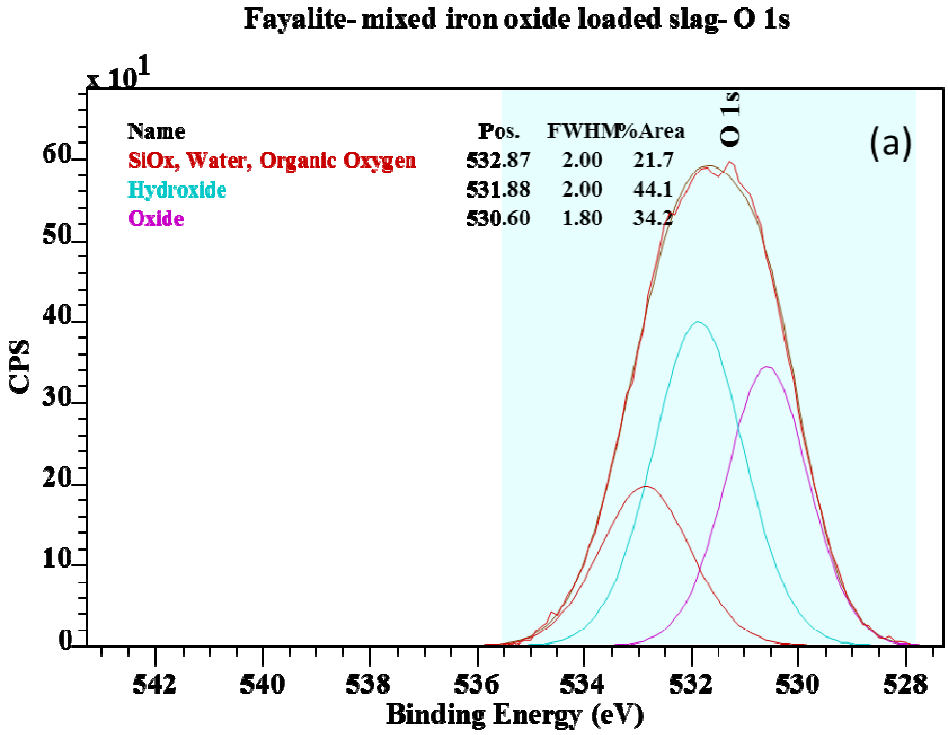
Fayalite- mixed iron oxide loaded slag- O 1s
x 10^1
Name
Pos.
FWHM
%Area
SiOx, Water, Organic Oxygen
532.87
2.00
21.7
Hydroxide
531.88
2.00
44.1
Oxide
530.60
1.80
34.2
O 1s
(a)
CPS
60
50
40
30
20
10
0
542
540
538
536
534
532
530
528
Binding Energy (eV)

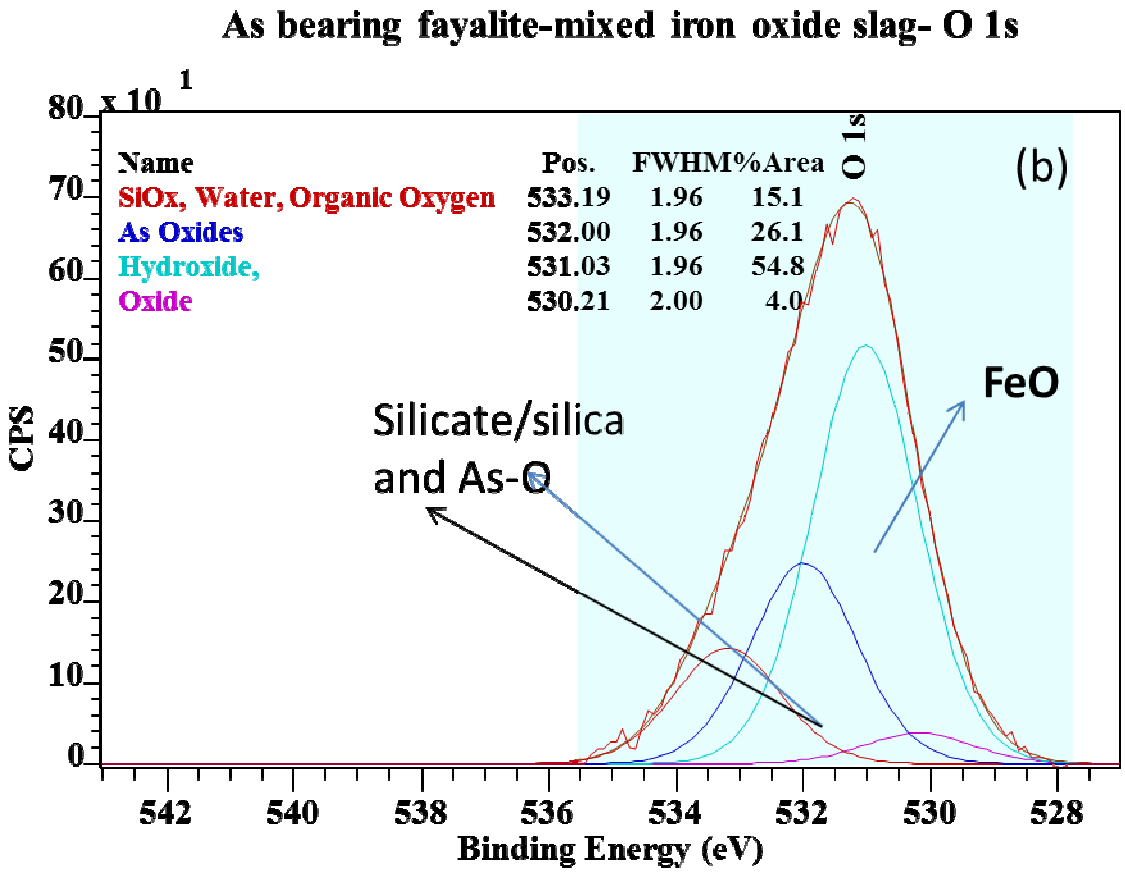

Figure 6.14: O 1s spectra of the (a) fresh slag and b) arsenic reacted slag

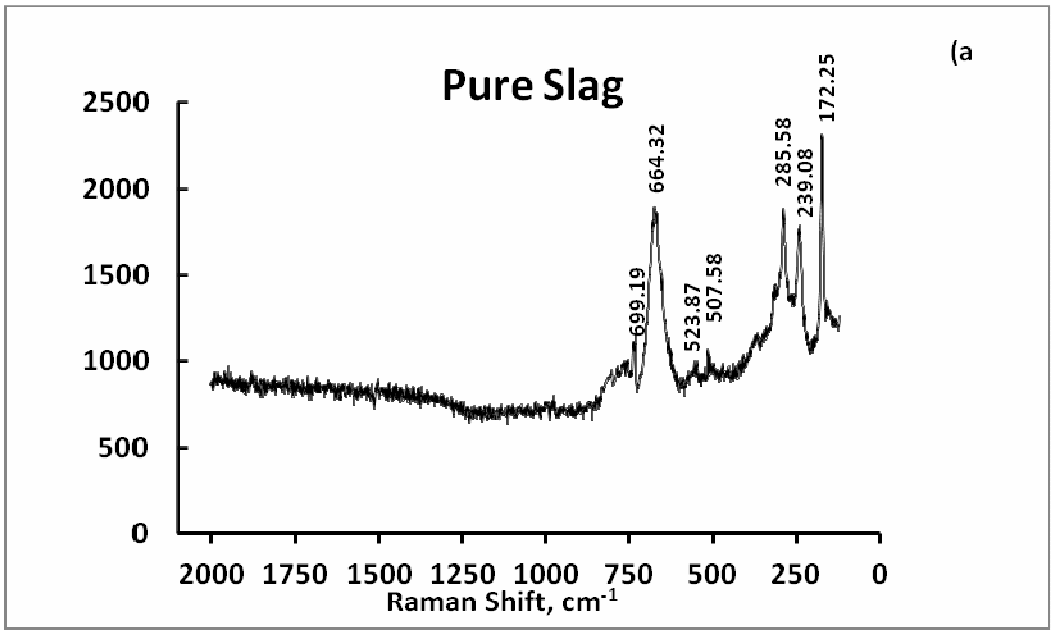
(a
Pure Slag
2500
2000
1500
1000
500
0
664.32
699.19
523.87
507.58
285.58
239.08
172.25
2000 1750 1500 1250 1000 750 500 250 0
Raman Shift, cm-1

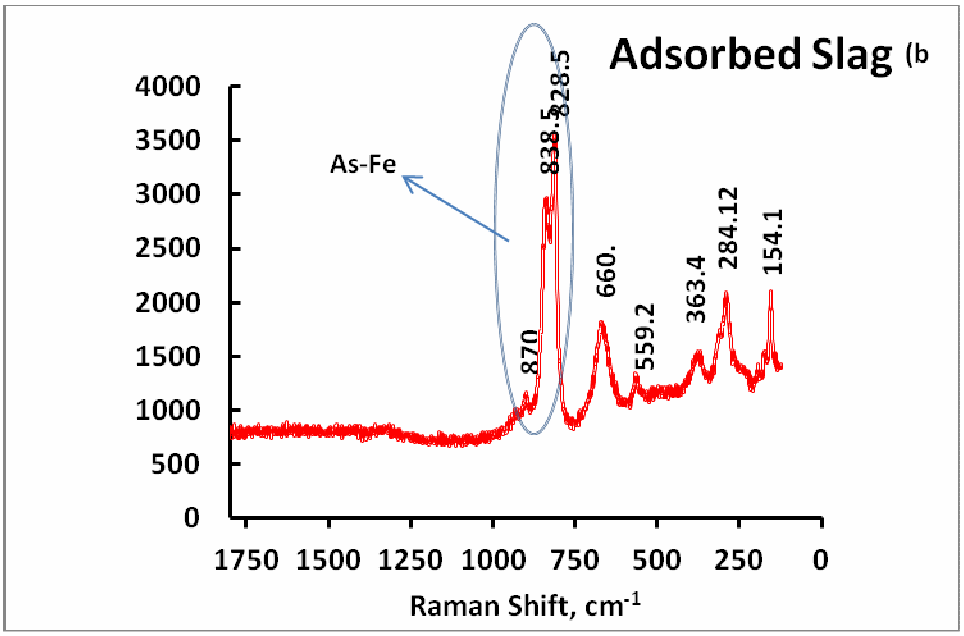

Figure 6.15: Raman spectra of (a) fresh slag and (b) arsenic reacted slag.

CHAPTER 7

CONCLUSIONS AND RECOMMENDATION

7.1 Conclusions

In this study, mixed iron oxide nanoparticles were used to treat arsenic, chromium and cadmium contaminated aqueous solutions. X-ray photoelectron spectroscopy (XPS) studies showed the presence of arsenic, chromium and cadmium on the surface of mixed magnetite-maghemite or maghemite-magnetite nanoparticles. The results show that redox reaction occurred on magnetite-maghemite mixture surface when heavy metals were introduced. The study showed that, apart from pH, the removal of arsenic, chromium and cadmium from contaminated water also depends on contact time and initial concentration of arsenic, chromium(VI) and cadmium(II) and temperature.

Equilibrium was achieved in 3 hrs in the case of 2 mg/L of As(V) and As(III) concentrations at pH 6.5. The results further suggest that arsenic adsorption involved the formation of weak arsenic-iron oxide complexes at the magnetite-maghemite surface. Arsenic adsorption capacity of magnetite-maghemite nanoparticles at room temperature, calculated from the Langmuir isotherm, was 50 μmol/g and Gibbs free energy (ΔG^0, kJ/mol) for arsenic removal was –32 to 32.5 kJ/mol, indicating the spontaneous nature of adsorption on magnetite-maghemite nanoparticles.

Application of maghemite-magnetite nanoparticles for chromium removal has great potential in water and wastewater engineering. Mixed maghemite-magnetite has been used as adsorbent for Cr(VI) removal in this study. Results show that the adsorption capacity is enhanced with an increase in reaction temperature and a decrease in free energy change. Thermodynamic study shows that Cr(VI) adsorption on the mixed maghemite and magnetite is endothermic in nature and is dependent on solution pH between 3 and 6. X-ray Photoelectron Spectroscopy (XPS) results demonstrate the theoretical multiplet peaks for iron and chromium adsorbed iron at the surface of the γ-Fe_2O_3 and Fe_3O_4 mixture. Theoretical multiplet analysis shows that during Cr adsorption, the amount of maghemite increases (from 70 to 89%). In magnetite spectra, the relative content of Fe(II) decreases from 8.2 to 3.6% indicating the reduction of magnetite in the mixture particles. In Raman spectroscopy studies, clear peaks of chromium on iron oxide were generated at 826 cm^{-1}, which was attributed to chemical interactions between chromium compound and iron oxide. From the results of Raman and XPS studies, electrostatic attraction and oxidation–reduction between chromium and mixed maghemite-magnetite are postulated as mechanisms for the removal of Cr(VI) from aqueous solutions. Among electrostatic attraction and oxidation–reduction, phsio-sorption has more engineering significance. Because, the portion that undergoes phsio-sorption (i.e. electrostatic binding) can be easily recovered. The results have highlighted three important contributions and applications such as the mechanism of Cr(VI) adsorption; possible treatment of Cr(VI) contaminated wastewater; and remediation of Cr(VI) contaminated groundwater. The results illustrate that maghemite-magnetite nanoparticles can adsorb Cr(VI) better in an acidic pH range and that equilibrium can be

achieved in 3 h at pH 4.0 and an initial Cr(VI) concentration of 1.5 mg/L. The adsorption capacity is enhanced with an increase in reaction temperature. The Raman and XPS data suggest that electrostatic attraction and oxidation–reduction reactions between chromium species and mixed maghemite-magnetite are the main mechanisms for the removal of chromium from aqueous solutions. Theoretical multiplet analysis of the Cr adsorbed γ-Fe_2O_3-Fe_3O_4 mixture presented in this study provides an additional contribution to the literature on XPS studies. From the Raman study, it can be concluded that diffusion reactions are also important during the experiments.

The uptake capacity of Cd(II) ions by mixed maghemite-magnetite increased with an increase in the pH of the adsorbate solution. An increase in adsorbent dosage increased Cd (II) removal but decreased adsorption capacity and it was found to follow the pseudo-second-order model. The adsorption of cadmium may be partially diffusion controlled and partially due to an electrostatic effect along with specific adsorption involving the adsorption of Cd^{++} and $CdOH^{+}$ on mixed maghemite-magnetite nanoparticles in the alkaline pH range. The XPS surveys also confirmed that Cd^{2+} ions may undergo oxidation-reduction reactions upon exposure to mixed maghemite-magnetite. After Cd(II) adsorption by the maghemite-magnetite mixture, the percent maghemite decreased from 74.8 to 68.5%.

The results of the present work found that 0.8 g/L of 20-60 nm maghemite-magnetite particles removed up to 1.5 mg/L Cd, and 0.4 g/L of 20-60 nm maghemite-magnetite or magnetite-maghemite particles removed up to 3 mg/L As and Cr(VI). The approximate cost of this nano-scale adsorbent is $225/kg (Reade Advance Materials, 2009). Thus, it

can be concluded that the cost of using this nano mixed particles adsorbent would be $0.09/L to $0.18/L for heavy metal removal. To take advantage of this, mixed iron oxide particles can be used in water treatment and site remediation. Moreover, mixed iron oxide particles were cheaper than other nano-scale iron particles. According to Phenrat et al (2009), magnetite and maghemite are not harmful to human body. Thus, the study of mixed iron oxides as adsorbent is very promising, more realistic and practical than other iron oxide particles.

Mixed iron oxide particles can be applied in the design of permeable reactive barriers for groundwater remediation. Permeable reactive barriers containing magnetite-maghemite-goethite particles could be employed for in situ remediation of groundwater contaminated with redox active metals. Developing countries like Vietnam, India, Nepal and Bangladesh have enough money to operate expensive, large-scale treatments for the removal of heavy metal from drinking water as well as subsurface to acceptable limits (from 10 ppb to 50 ppb). The findings of this study suggest that slags from Ni smelter may be effective low-cost reactive media for the PRBs. Fayalite-iron oxide loaded Ni smelter slag may not be as reactive as conventional magnetite or zero valent iron, but do have sufficient reactivity so that PRBs containing a reactive zone of typical small thickness could be constructed to effectively remove arsenic from the subsurface. The better sorption efficiencies were obtained in continuous flow system. The complex nature of the sorption process in smelting waste including both chemisorption and physical sorption was revealed by XPS and Raman studies. The Raman and XPS data indicate that electrostatic attraction and oxidation–reduction reactions between As species and slag are the main mechanisms for the removal of arsenic from aqueous solutions. These findings

can be utilized to build the mixed iron oxide loaded Ni smelter slag PRB as well as surface water treatment technology.

7.2 Recommendation for future study

1) Field study

Proper design and field investigation are necessary to find out the applicability of magnetite-maghemite or maghemite-magnetite particles for the construction of permeable reactive barriers or any treatment units. Permeable reactive barriers containing mixed iron oxide will be more widely used to remediate contaminated groundwater. More field study would be necessary to find out much uncertainty in predicting their long-term performance. Mineral precipitation and mineralogical investigation during field operation should be investigated. Moreover, the importance of slag heterogeneity, longevity of the reactivity and the mechanisms controlling removal at field scale also needs to be evaluated. Due to the availability of a large number of adsorbents on the adsorption of As and Cr (VI), development of eco-friendly and economically viable adsorbents are more demanding. Thus, more research is recommended.

2) Natural magnetite-maghemite-goethite loaded soil

Natural deposits of iron oxide minerals (hematite, magnetite, maghemite-goethite) should be collected and investigated to compare the removal efficiencies with those of commercial iron oxide and natural iron oxide deposits.

3) Competitive anions and alkalinity studies

At field scale, more studies should be required to find out the removal efficiencies of the targeted metal ion in the presence of elevated concentrations of other contaminating species at field scale. The macromolecules studies for contaminated site sample will also be required. Potential industrial importance of the study needs to be verified by practical application of these particles. Moreover, the performance should be checked at lab scale in the presence of elevated concentration of carbonate and hardness ions in groundwater.

4) Reuse of spent mixed iron oxides

Many researchers showed 20-30% recovery of magnetite or maghemite from the portion that underwent electrostatic binding. According to Cornell et al. (2003), the desorption rate from magnetite and hematite in base solution was 20%. To reach 80-90% recovery of iron oxides from any treatment unit, extensive research is required.

Appendix

A.1 Operational condition for ICP-OES (inductively coupled plasma-optical emission spectroscopy)

Table A 1.1: Operational condition for ICP-OES analysis

Power (kW)	1.1
Plasma flow (L/min)	15
Nebulizer flow (L/min)	0.8
Auxiliary flow (L/min)	1.5
Replicate read time (s)	5
Instrument stabilization delay (s)	15
Frequency (MHz)	40
Sample uptake delay (s)	30
Pump rate (rpm)	15
Rinse time (s)	25
Wavelength for As	188-197.2
Wavelength for Cr	205-267
Wavelength for Cd	214-288

ICP-OES results:

Every experiment was run in triplicate and average values were used in the graph. Every data showed lower than 5% RSD (relative standard deviation) in ICP-OES analysis. The smaller the value, the higher is the precision of the measurements.

Here, RSD (%) = (Standard deviation / mean) * 100

A.2 Gibbs free energy calculation for arsenic uptake by mixed magnetite-maghemite (supplementary information of Chapter 3)

Langmuir equation

$$C_e/q_e = 1/bq_m + C_e/q_m \qquad (3.1a)$$

Standard Gibbs free energy (ΔG^0, kJ/mol) for the adsorption process was measured using the following equation:

$$Ln(1/b) = \Delta G^0/ RT \qquad (3.3)$$

Where, b represents the Langmuir constant related to the energy of adsorption, R is the ideal gas constant (8.314 J/K mol) and T is temperature (K).

From equation (3.3) ΔG^0 can be calculated

a) For As(V) at room temperature

ΔG^0= RT Ln(1/b), where b= 6.7 L/mg = $515*10^3$ L/moL. b is calculated from equation (3.1a))

ΔG^0= 8.314*298*Ln ($1/515*10^3$) = -32.6 KJ/moL.

b) For As(III) at room temperature

ΔG^0= RT Ln (1/b) where, b= 6.63 L/mg= $510*10^3$ L/moL

ΔG^0= 8.314*298*Ln ($1/515*10^3$) = -32.5 KJ/moL.

Figure A.2.1: Dispersed mixed magnetite-maghemite in electrolyte solution

A. 3 Thermodynamic parameter calculation for chromium uptake by mixed maghemite-magnetite (supplementary information of Chapter 4)

According to Altundogan et al. (2000), standard Gibbs free energy (ΔG^0), standard enthalpy (ΔH^0) and standard entropy changes (ΔS^0) for the adsorption process may be calculated from Eqs. (4.3)-(4.5):

$$\text{Ln}(1/b) = \Delta G^0 / RT \qquad (4.3)$$

$$\text{Ln } b = \text{Ln } b_0 - \Delta H^0 / RT \qquad (4.4)$$

$$\Delta G^0 = \Delta H^0 - T\,\Delta S^0 \qquad (4.5)$$

1) For Temperature = 10 ^{0}C;

ΔG^0= RT Ln(1/b), where b= 3 L/mg = 1.58*10^5 L/moL.

ΔG^0= 8.314*295*Ln (1/1.58*10^5) = -28 KJ/moL.

Using equation 4.4 and from Figure A.2.1,

ΔH^0= 1156.1* 8.314 = 9.6 kJ/moL.K

Using equation 4.5,

$\Delta S^0 = (\Delta G^0+\Delta H^0)/T$ = (9.6+28)/283 = 0.1 kJ/moL.K

1) For Temperature = 22 ^{0}C;

ΔG^0= RT Ln(1/b), where b= 3.1 L/mg = 1.63*10^5 L/moL.

ΔG^0= 8.314*295*Ln (1/1.63*10^5) = -29.4 KJ/moL.

Using equation 4.4 and from Figure A.2.1,

ΔH^0= 1156.1* 8.314 = 9.6 kJ/moL.K

Using equation 4.5,

$\Delta S^0 = (\Delta G^0+\Delta H^0)/T$ = (9.6+29.4)/295 = 0.1 kJ/moL.K

1) For Temperature = 50 ^{0}C;

ΔG^0= RT Ln(1/b), where b= 4.8 L/mg = 2.52*10^5 L/moL.

ΔG^0= 8.314*295*Ln (1/2.52*10^5) = -33.45 KJ/moL.

Using equation 4.4 and from Figure A.2.1,

ΔH^0= 1156.1* 8.314 = 9.6 kJ/moL.K

Using equation 4.5,

$\Delta S^0 = (\Delta G^0 + \Delta H^0)/T = (9.6+28)/323 = 0.13$ kJ/moL.K

Table A.2.1: Adsorption energies (b) at different temperature (K).

Temperature	Temperature (1/T)	b, L/mg	Lnb
283	0.003533569	3	1.09
295	0.003389831	3.1	1.13
323	0.003095975	4.8	1.57

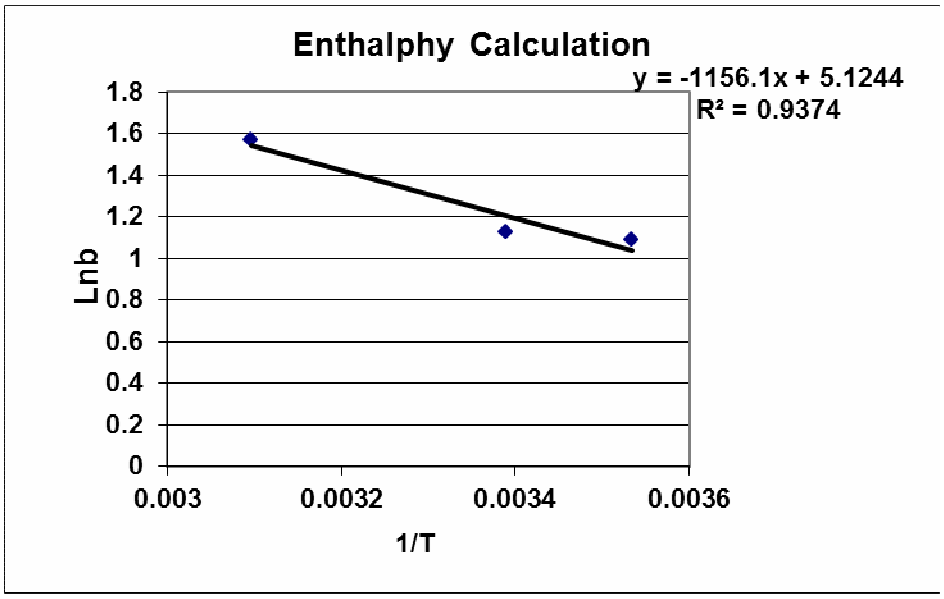

Figure A.2.1: Lnb vs 1/T for Standard enthalpy (ΔH^0) calculation using equation (4.4)

A. 4 Experimental data used for multiple regression analysis of cadmium uptake by maghemite-magnetite particles (Supplementary information of Chapter 5)

1) Table A.3.1: Data for XPS wide scan spectra of the fresh maghemite-magnetite mixture and Cd(II) loaded maghemite-magnetite mixture

Compound	Name	Pos.	FWHM	Area	At%
Mixed maghemite-magnetite	Fe 2p	707.15	3.84	11374.7	8.9
	O 1s	526.55	3.26	10183.3	30.1
	N 1s	396.35	2.86	192.6	0.9
	C 1s	281.55	2.74	7248.2	60.1
Cd adsorbed Mixed maghemite-magnetite	Fe 2p	707.15	3.66	5910.6	4.7
	O 1s	526.55	4.67	7602.0	23.0
	N 1s	395.65	2.33	348.7	1.7
	C 1s	281.55	2.75	8306.8	70.4
	Cd 3d	401.25	2.58	707.4	0.4

2) **Adsorption kinetics study**

a) Pseudo first-order equation

$\text{Log}\,(q_e - q_t) = \text{Log}\,q_e - k_{1ads} * t/2.303$ ----------(5.3.4)

Using Figure 5.5 for the determination of the rate constant of pseudo-first order adsorption k_{1ads} and the amount of Cd(II) ion sorbed at equilibrium, q_e

Equation 5.3.4 can be written: y = -0.0156x + 0.1538

From the above equation, $k_{1ads}/2.303 = 0.0156$

Thus, $k_{1ads} = 3.6 \times 10^{-2}\ min^{-1}$

b) The pseudo second order equation

$h = k_{2ads} * q_e^2$ ……(5.3.8)

$t/q_t = 1/h + t/q_e$----------(5.3.9)

From Figure 5.6 for the determination of the rate constant of pseudo-second order adsorption $k_{2\ ads}$ and the amount of Cd(II) ion adsorbed at equilibrium, q_e.

Equation 5.3.9 can be written: y = 0.5431x + 7.4521;

Thus, using the above equation, $1/q_e = 0.5431$; $q_e = 1.8413$ (mg/g) and $h = 0.1342$

$$k_{2ads} = h/ q_e^2 = 0.1342/1.8413^2$$

Thus, $k_{2ads} = 3.96 \times 10^{-2}$ g/mg*min

c) The intraparticle diffusion model

From figure 5.7 for the determination of the intra-particle diffusion rate constant, k_{id} (min^{-1})

$\log Y_{id} = \log k_{id} + a \log t$ ---------- (5.3.11)

Equation 5.3.11 can be written: Y = 0.2697x + 1.3904

Thus, $k_{id} = 24.56\ min^{-1}$

A.5 Important column parameters used for contaminant transport determination (supplementary information of Chapter 6)

1)

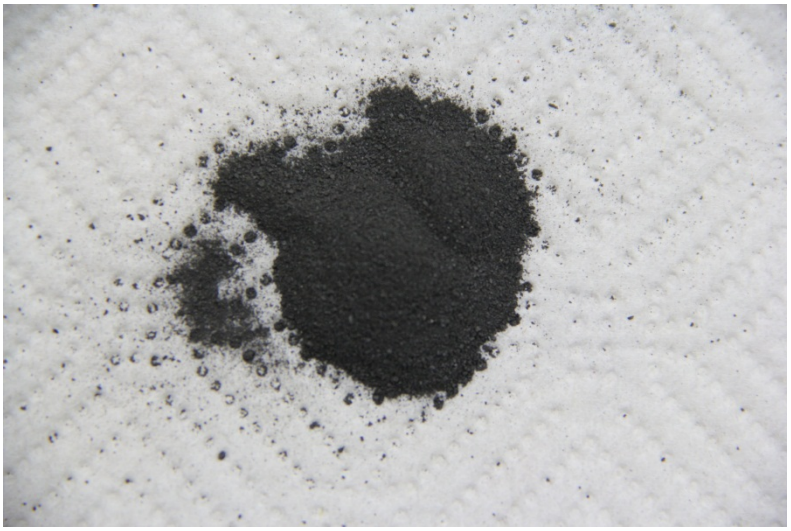

Figure A.5.1: Slag particles: crushed.

2) Pump type: Master Flex multi-channel high precision peristaltic pump

Pump speed= 2.5 rpm and 1 rpm= 0.17 mL/min;

Thus, pump velocity = 0.425 mL/min.

Table A. 5.1: Parameters for Columns

Parameters	Values	Units
influent, pH	3.5-5.5	
Effluent, pH	6-8	

Column inside, Eh	-232-704	mV
Effluent, DO	0.5-3	ppm

a) For Column 1: Weight of Slag in the column = 451 g;

Weight of water in the column = 80.1 g

Table A. 5.2: Important parameters for Column 1

Parameters	**Values**	**Unit**
Length = L	10.16	cm
Diameter, D	5.08	cm
V= volume= $\pi r^2 * L$	205.9	cm^3
Porosity= n= Vv/V	0.39	
A= Area= πr^2	20.26	cm^2
Bulk Density, ρ_b	2.19	g/cm^3
1 PV = n*V	80.3	mL
Flow rate	522.5	mL/day
No of P.V	6.5	
Darcy velocity= v= (Q/A)	v=(522.5/20.26) = 0.258	m/d
T=Resident Time(L/v)	9.45	hrs
Slag particles size	0.3-152.5	micro-meter
Specific Surface area	0.5	m^2/g
Total Volume of water passed by resident time	205.73	mL
No of P.V by resident time	2.5	
Approximate pressure differences	1.0 for 200 PV 1.0 for 450 PV	psi
Hydraulic conductivities (k) K= V*L/(A*h*t)	$4.4 * 10^{-5}$	cm/s

Notes: V= collected Vol^n of water (mL); L= length (cm); t= required time

b) For Column 2

Weight of Slag in the column = 453 g; Weight of water in the column = 83g.

Table A 5.3: Important Parameters for Column 2

Parameters	**Values**	**Unit**
Length = L	10.16	cm
Diameter =D=	5.08	cm
V= volume	205.9	cm^3
Porosity= n	0.40	
A= Area	20.26	cm^2
Bulk Density, ρ_b	2.2	g/cm^3
1 PV	82.36	mL
Flow rate	535	mL/day
No of P.V	6.5	6.5
Darcy velocity= v= (Q/A)	v=(535/20.26) = 0.264	m/d
T=Resident Time(L/v)	9.24	hrs
Slag particles size	0.3-152.5	micro-meter
Specific Surface area	0.5	m^2/g
Total Volume passed by resident time	205.98 mL	mL
No of P.V passed by resident time	2.5	by resident time
Approximate pressure	1.0 for 200 PV	psi

differences	1.0 for 450 PV	
Hydraulic conductivities (k) K= V*L/(A*h*t)	4.43* 10^{-5}	cm/s

Notes: V= collected Vol^{n} of water (mL); L= length (cm); t= Required time; A= Area

C) For Column 3

Weight of Slag in the column = 550 g; Weight of water in the column = 95 g.

Table A.5.4: Important Parameters for Column 3

Parameters	**Values**	**Unit**
Length = L	11.43	cm
Diameter, D	5.08	cm
V= volume	231.62	cm^3
Porosity= n	0.41	
A= Area	20.26	cm^2
Bulk Density, ρ_b	2.37	g/cm^3
1 PV	94.96	mL
Flow rate	523	mL/day
No of P.V	5.5	5.5
Darcy velocity= v= (Q/A)	v= (523/20.26) =0.258	m/d
T=Resident Time(L/v)	10.6	hrs
Slag particles size	0.3-152.5	micro-meter
Specific Surface area	0.5	m^2/g
Total volume passed by resident time	231 mL	mL
No of P.V by resident time	2.5	
Approximate pressure	1.5 for 200 PV	psi

differences	1.5 for 500 PV	
Hydraulic conductivities (k) K= V*L/(A*h*t)	3.24* 10^{-5}	cm/s

Notes: V= collected Vol^{n} of water (mL); L= length (cm); t= Required time; A= Area

3) Redox potential Data for operation periods

Table A.5.6: Important Redox (mV) data

		Redox (Eh); - mV	
Days	**No of P.V**	**Port A**	**Port B**
3.6	20	380	500
5.5	30	420	560
7.3	40	450	565
9.1	50	510	578
18.2	100	500	595
27.3	150	505	600
36.4	200	507	599
45.5	250	501	620
54.5	300	500	704
63.6	380	510	620
72.7	400	350	590
81.8	450	232	432
85.5	470	280	410
87.3	480	232	420
89.1	490	210	400
90.9	500	220	435
100	550	215	432
109.1	600	230	428
110.9	610	232	430
112.7	620	231	432
114.5	630	230	432
116.4	640	220	432
118.2	650	215	431
120	660	210	432
121.8	670	231	431
125.5	690	230	430

129.1	710	231	432
136.4	750	230	430

4) Grain Size distribution

MALVERN INSTRUMENTS

MASTERSIZER 2000

Result Analysis Report

Sample Name: Sept 2012 C3 - Average **SOP Name:** **Measured:** 09/27/12 14:36:16

Sample Source & type: Works **Measured by:** malvern **Analysed:** 09/27/12 14:36:17

Sample bulk lot ref: **Result Source:** Averaged

Particle Name: Iron III Oxide 2.98 **Accessory Name:** Hydro 2000S (A) **Obscuration:** 13.13 %

Particle RI: 2.980 **Absorption:** 1 **Analysis model:** General purpose (spherical)

Dispersant Name: Water **Size range:** 0.358 to 152.500 um **Weighted Residual:** 1.600 %

Dispersant RI: 1.330 **Result Emulation:** Off

Concentration: 0.0392 %Vol **Vol. Weighted Mean D[4,3]:** 53.540 um **Specific Surface Area:** 0.509 m²/g

Span : 2.617 **Uniformity:** 0.806 **Surface Weighted Mean D[3,2]:** 11.794 um

Result units: Volume

d(0.1): 5.284 um d(0.5): 43.967 um d(0.9): 120.326 um

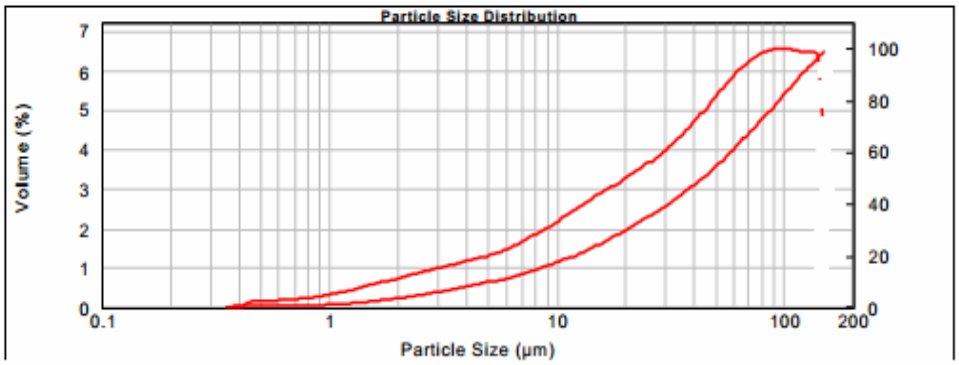

Size (µm)	Vol Under %	Size (µm)	Vol Under %	Size (µm)	Vol Under %	Size (µm)	Vol Under %	Size (µm)	Vol Under %	Size (µm)	Vol Under %
0.010	0.00	0.105	0.00	1.096	0.36	11.482	15.00	120.226	90.53	1258.925	100.00
0.011	0.00	0.120	0.00	1.259	0.62	13.183	17.33	138.038	95.78	1445.440	100.00
0.013	0.00	0.138	0.00	1.445	0.93	15.136	19.88	158.489	100.00	1659.587	100.00
0.015	0.00	0.158	0.00	1.660	1.28	17.378	22.63	181.970	100.00	1905.461	100.00
0.017	0.00	0.182	0.00	1.905	1.68	19.953	25.57	208.930	100.00	2187.762	100.00
0.020	0.00	0.209	0.00	2.188	2.11	22.909	28.71	239.883	100.00	2511.886	100.00
0.023	0.00	0.240	0.00	2.512	2.60	26.303	32.11	275.423	100.00	2884.032	100.00
0.026	0.00	0.275	0.00	2.884	3.13	30.200	35.84	316.228	100.00	3311.311	100.00
0.030	0.00	0.316	0.00	3.311	3.72	34.674	40.00	363.078	100.00	3801.894	100.00
0.035	0.00	0.363	0.00	3.802	4.38	39.811	44.67	416.869	100.00	4365.158	100.00
0.040	0.00	0.417	0.00	4.365	5.12	45.709	49.90	478.630	100.00	5011.872	100.00
0.046	0.00	0.479	0.00	5.012	5.97	52.481	55.66	549.541	100.00	5754.399	100.00
0.052	0.00	0.550	0.00	5.754	6.95	60.256	61.81	630.957	100.00	6606.934	100.00
0.060	0.00	0.631	0.00	6.607	8.11	69.183	68.13	724.436	100.00	7585.776	100.00
0.069	0.00	0.724	0.00	7.586	9.47	79.433	74.34	831.764	100.00	8709.636	100.00
0.079	0.00	0.832	0.00	8.710	11.07	91.201	80.18	954.993	100.00	10000.000	100.00
0.091	0.00	0.955	0.08	10.000	12.91	104.713	85.55	1096.478	100.00		

Operator notes:

Malvern Instruments Ltd.
Malvern, UK
Tel := +[44] (0) 1684-892456 Fax +[44] (0) 1684-892789

Mastersizer 2000 Ver. 3.01 C:\Program Files\Malvern Instruments\Mastersizer 2000\Measureme...\sAIDUR
Serial Number : 34315-55

5) Data for Figure 6.4, 6.5 and 6.7

1) Tables for Column 1:

Column 1					
Sample port-1					
Distance = 2.5 cm					
Days	**P.V**	**C_e, mg/L**	**Initial, C_o, mg/L**	**C_e/C_o**	**Removal (%)**
3.1	20	0	10	0	100
4.6	30	0.21	10	0.021	97.9
6.2	40	0.9	10	0.09	91
7.7	50	1.8	10	0.18	82
15.4	100	2.6	10	0.26	74
23.1	150	3.9	10	0.39	61
30.8	200	6.4	10	0.64	36
38.5	250	9.3	10	0.93	7
46.2	300	9.5	10	0.95	5
53.8	350	9.9	10	0.99	1
61.5	400	10	10	1	0
69	450	10	10	1	0
72.3	470	10	10	1	0
73.8	480	10	10	1	0
75.4	490	10	10	1	0
76.9	500	10	10	1	0
84.6	550	10	10	1	0
92.3	600	10	10	1	0
93.8	610	10	10	1	0
95.4	620	10	10	1	0
96.9	630	10	10	1	0

98.5	640	10	10	1	0
100	650	10	10	1	0

Sample port 2
Distance= 4.5 cm

Days	**P.V**	**C_e, mg/L**	**Initial, C_o, mg/L**	**C_e/C_o**	**Removal (%)**
3.1	20	0.003	10	0.0003	99.97
4.6	30	0.07	10	0.007	99.3
6.2	40	0.1	10	0.01	99
7.7	50	0.72	10	0.072	92.8
15.4	100	0.7	10	0.07	93
23.1	150	1.2	10	0.12	88
30.8	200	2.81	10	0.281	71.9
38.5	250	3.05	10	0.305	69.5
46.2	300	4.52	10	0.452	54.8
53.8	350	6.79	10	0.679	32.1
61.5	400	7.15	10	0.715	28.5
69	450	8.9	10	0.89	11
72.3	470	10	10	1	0
73.8	480	10	10	1	0
75.4	490	10	10	1	0
76.9	500	10	10	1	0
84.6	550	10	10	1	0
92.3	600	10	10	1	0
93.8	610	10	10	1	0
95.4	620	10	10	1	0
96.9	630	10	10	1	0
98.5	640	10	10	1	0
100	650	10	10	1	0

Sample port 3
Distance= 7.5 cm

Days	**P.V**	**C_e, mg/L**	**Initial, C_o, mg/L**	**C_e/C_o**	**Removal (%)**
3.1	20	0	10	0	100
4.6	30	0.01	10	0.001	99.9
6.2	40	0.02	10	0.002	99.8
7.7	50	0.1	10	0.01	99
15.4	100	0.8	10	0.08	92
23.1	150	1.5	10	0.15	85
30.8	200	1.49	10	0.149	85.1
38.5	250	1.7	10	0.17	83

46.2	300	2.59	10	0.259	74.1
53.8	350	3.9	10	0.39	61
61.5	400	4.5	10	0.45	55
69	450	5.6	10	0.56	44
72.3	470	6	10	0.6	40
73.8	480	7.8	10	0.78	22
75.4	490	8.3	10	0.83	17
76.9	500	9.8	10	0.98	2
84.6	550	10	10	1	0
92.3	600	10	10	1	0
93.8	610	10	10	1	0
95.4	620	10	10	1	0
96.9	630	10	10	1	0
98.5	640	10	10	1	0
100	650	10	10	1	0

Sample port 4 **Distance= 10.16 cm**					
Days	**P.V**	**C_e, mg/L**	**Initial, C_o, mg/L**	**C_e/C_o**	**Removal (%)**
7.7	50	0.007	10	0.0007	99.93
15.4	100	0.06	10	0.006	99.4
23.1	150	0.12	10	0.012	98.8
30.8	200	0.1	10	0.01	99
38.5	250	0.14	10	0.014	98.6
46.2	300	0.19	10	0.019	98.1
53.8	350	0.29	10	0.029	97.1
61.5	400	0.5	10	0.05	95
69	450	1.9	10	0.19	81
72.3	470	2.9	10	0.29	71
73.8	480	4	10	0.4	60
75.4	490	6.3	10	0.63	37
76.9	500	7	10	0.7	30
84.6	550	8	10	0.8	20
92.3	600	9.5	10	0.95	5
93.8	610	10	10	1	0
95.4	620	10	10	1	0
96.9	630	10	10	1	0
98.5	640	10	10	1	0
100	650	10	10	1	0

2) Tables for Column 2:

Column 2					
Sample port-1					
Distance = 2.5 cm					
Days	**P.V**	**C_e**	**Initial, C_o, mg/L**	**C_e/C_o**	**Removal (%)**
7.7	50	0.08	10	0.008	99.2
15.4	100	0.5	10	0.05	95
23.1	150	3.9	10	0.39	61
29.2	190	5.64	10	0.564	43.6
38.5	250	6.2	10	0.62	38
44.6	290	7.61	10	0.761	23.9
53.8	350	8.31	10	0.831	16.9
63.1	410	9.9	10	0.99	1
69.2	450	9.9	10	0.99	1
72.3	470	10	10	1	0
75.4	490	10	10	1	0
78.5	510	10	10	1	0
81.5	530	10	10	1	0
84.6	550	10	10	1	0
93.8	610	10	10	1	0
95.4	620	10	10	1	0
96.9	630	10	10	1	0
98.5	640	10	10	1	0
100	650	10	10	1	0
101.5	660	10	10	1	0

Sample port 2					
Distance= 4.5 cm					
Days	**P.V**	**C_e, mg/L**	**Initial, C_o, mg/L**	**C_e/C_o**	**Removal (%)**
7.7	50	0.1	10	0.01	99
15.4	100	0.2	10	0.02	98
23.1	150	0.51	10	0.051	94.9
29.2	190	0.84	10	0.084	91.6
38.5	250	3.62	10	0.362	63.8
44.6	290	4.28	10	0.428	57.2
53.8	350	5.31	10	0.531	46.9
63.1	410	7.6	10	0.76	24
69.2	450	7.11	10	0.711	28.9
72.3	470	8.5	10	0.85	15
75.4	490	9.3	10	0.93	7
78.5	510	9.92	10	0.992	0.8
81.5	530	9.99	10	0.999	0.1
84.6	550	10	10	1	0
93.8	610	10	10	1	0
95.4	620	10	10	1	0

96.9	630	10	10	1	0
98.5	640	10	10	1	0
100	650	10	10	1	0
101.5	660	10	10	1	0

Sample port 3					
Distance= 7.5 cm					
Days	**P.V**	**C_e, mg/L**	**Initial, C_o**	**C_e/C_o**	**Removal (%)**
7.7	50	0.006	10	0.0006	99.94
15.4	100	0.078	10	0.0078	99.22
23.1	150	0.091	10	0.0091	99.09
29.2	190	0.31	10	0.031	96.9
38.5	250	0.87	10	0.087	91.3
44.6	290	1.2	10	0.12	88
53.8	350	1.49	10	0.149	85.1
63.1	410	2.5	10	0.25	75
69.2	450	4.9	10	0.49	51
72.3	470	5.1	10	0.51	49
75.4	490	6.69	10	0.669	33.1
78.5	510	8.2	10	0.82	18
81.5	530	8.9	10	0.89	11
84.6	550	9.7	10	0.97	3
93.8	610	10	10	1	0
95.4	620	10	10	1	0
96.9	630	10	10	1	0
98.5	640	10	10	1	0
100	650	10	10	1	0
101.5	660	10	10	1	0

Sample port 4					
Distance= 10.16 cm					
Days	**P.V**	**C_e, mg/L**	**Initial, C_o, mg/L**	**C_e/C_o**	**Removal (%)**
7.7	50	0.004	10	0.0004	99.96
15.4	100	0.08	10	0.008	99.2
23.1	150	0.11	10	0.011	98.9
29.2	190	0.14	10	0.014	98.6
38.5	250	0.2	10	0.02	98
44.6	290	0.21	10	0.021	97.9
53.8	350	0.31	10	0.031	96.9

63.1	410	0.6	10	0.06	94
69.2	450	1.11	10	0.111	88.9
72.3	470	1.5	10	0.15	85
75.4	490	3.3	10	0.33	67
78.5	510	4.22	10	0.422	57.8
81.5	530	5.24	10	0.524	47.6
84.6	550	7.7	10	0.77	23
93.8	610	9.28	10	0.928	7.2
95.4	620	10	10	1	0
96.9	630	10	10	1	0
98.5	640	10	10	1	0
100	650	10	10	1	0
101.5	660	10	10	1	0

3) Tables for Column 3:

Column 3					
Sample port-1					
distance = 2.5 cm					
Days	**P.V**	**C_e, mg/L**	**Initial, C_o, mg/L**	**C_e/C_o**	**Removal (%)**
3.6	20	0	10	0	100
5.5	30	0.21	10	0.021	97.9
7.3	40	0.69	10	0.069	93.1
9.1	50	2.8	10	0.28	72
18.2	100	3.6	10	0.36	64
27.3	150	6.3	10	0.63	37
36.4	200	8.4	10	0.84	16
45.5	250	8.3	10	0.83	17
54.5	300	9.9	10	0.99	1
63.6	350	10	10	1	0
72.7	400	10	10	1	0
81.8	450	10	10	1	0
85.5	470	10	10	1	0
87.3	480	10	10	1	0
89.1	490	10	10	1	0
90.9	500	10	10	1	0
100	550	10	10	1	0
109.1	600	10	10	1	0
110.9	610	10	10	1	0
112.7	620	10	10	1	0
114.5	630	10	10	1	0

116.4	640	10	10	1	0
118.2	650	10	10	1	0

Sample port-2 distance = 4.5 cm					
Days	**P.V**	**C_e, mg/L**	**Initial, C_o, mg/L**	**C_e/C_o**	**Removal (%)**
3.6	20	0	10	0	100
5.5	30	0.11	10	0.011	98.9
7.3	40	0.49	10	0.049	95.1
9.1	50	1.8	10	0.18	82
18.2	100	1.6	10	0.16	84
27.3	150	2.3	10	0.23	77
36.4	200	3.4	10	0.34	66
45.5	250	6.3	10	0.63	37
54.5	300	7.39	10	0.739	26.1
63.6	350	8.2	10	0.82	18
72.7	400	9.7	10	0.97	3
81.8	450	9.9	10	0.99	1
85.5	470	10	10	1	0
87.3	480	10	10	1	0
89.1	490	10	10	1	0
90.9	500	10	10	1	0
100	550	10	10	1	0
109.1	600	10	10	1	0
110.9	610	10	10	1	0
112.7	620	10	10	1	0
114.5	630	10	10	1	0
116.4	640	10	10	1	0
118.2	650	10	10	1	0

Sample port-3 distance = 6.25 cm					
Days	**P.V**	**C_e, mg/L**	**Initial, C_o, mg/L**	**C_e/C_o**	**Removal (%)**
3.6	20	0	10	0	100
5.5	30	0.071	10	0.0071	99.29
7.3	40	0.149	10	0.0149	98.51
9.1	50	1.08	10	0.108	89.2
18.2	100	1.6	10	0.16	84
27.3	150	1.3	10	0.13	87
36.4	200	1.8	10	0.18	82
45.5	250	3.3	10	0.33	67
54.5	300	3.29	10	0.329	67.1
63.6	350	5.2	10	0.52	48

72.7	400	7.7	10	0.77	23
81.8	450	8.3	10	0.83	17
85.5	470	9.9	10	0.99	1
87.3	480	10	10	1	0
89.1	490	10	10	1	0
90.9	500	10	10	1	0
100	550	10	10	1	0
109.1	600	10	10	1	0
110.9	610	10	10	1	0
112.7	620	10	10	1	0
114.5	630	10	10	1	0
116.4	640	10	10	1	0
118.2	650	10	10	1	0

Sample port-4					
distance = 8.5 cm					
Days	**P.V**	**C_e, mg/L**	**Initial, C_o, mg/L**	**C_e/C_o**	**Removal (%)**
9.1	50	0.03	10	0.003	99.7
18.2	100	0.0071	10	0.00071	99.929
27.3	150	0.049	10	0.0049	99.51
36.4	200	0.08	10	0.008	99.2
45.5	250	0.2	10	0.02	98
54.5	300	0.4	10	0.04	96
63.6	350	0.3	10	0.03	97
72.7	400	1.3	10	0.13	87
81.8	450	2.09	10	0.209	79.1
85.5	470	3.2	10	0.32	68
87.3	480	4.7	10	0.47	53
89.1	490	5.3	10	0.53	47
90.9	500	6.9	10	0.69	31
100	550	7	10	0.7	30
109.1	600	9.2	10	0.92	8
110.9	610	9.9	10	0.99	1
112.7	620	10	10	1	0
114.5	630	10	10	1	0
116.4	640	10	10	1	0
118.2	650	10	10	1	0
120	660	10	10	1	0
121.8	670	10	10	1	0

125.5	690	10	10	1	0
129.1	710	10	10	1	0
136.4	750	10	10	1	0

Sample port-5 distance = 11.43 cm					
Days	**P.V**	**C_e, mg/L**	**Initial, C_o, mg/L**	**C_e/C_o**	**Removal (%)**
9.1	50	0.009	10	0.0009	99.91
18.2	100	0.05	10	0.005	99.5
27.3	150	0.0132	10	0.00132	99.868
36.4	200	0.1	10	0.01	99
45.5	250	0.25	10	0.025	97.5
54.5	300	0.7	10	0.07	93
63.6	350	0.8	10	0.08	92
72.7	400	0.5	10	0.05	95
81.8	450	1.33	10	0.133	86.7
85.5	470	1.84	10	0.184	81.6
87.3	480	2.05	10	0.205	79.5
89.1	490	2.3	10	0.23	77
90.9	500	3.177	10	0.3177	68.23
100	550	4.79	10	0.479	52.1
109.1	600	6.9	10	0.69	31
110.9	610	7.2	10	0.72	28
112.7	620	8.5	10	0.85	15
114.5	630	9.9	10	0.99	1
116.4	640	10	10	1	0
118.2	650	10	10	1	0
120	660	10	10	1	0
121.8	670	10	10	1	0
125.5	690	10	10	1	0
129.1	710	10	10	1	0
136.4	750	10	10	1	0

6) Tables for Figure 6.8

a) Data for 0.5% saturation in column 1

Depth	Service time, day	P.V	Ce, mg/L	C/C_0
4.5	4	26	0.05	0.005
7.5	7	45.5	0.05	0.005
10.16	13.5	87.5	0.05	0.005

b) Data for 90% saturation in column 1.

Depth	Service time, day	P.V	Ce, mg/L	C/C_0
4.5	69.5	451.5	0.05	0.9
7.5	76	494	9	0.9
10.16	88.5	575.3	9	0.9

c) Data for 0.5% saturation in column 2

Depth	Service time, day	P.V	Ce, mg/L	C/C_0
4.5	5	32.5	0.05	0.005
7.5	9	585	0.05	0.005
10.16	14	91	0.05	0.005

d) Data for 90% saturation in column 2

Depth	Service time, day	P.V	Ce, mg/L	C/C_0
4.5	73.5	477.5	0.05	0.9
7.5	82	533	9	0.9
10.16	91	591.5	9	0.9

7) Distribution coefficient calculation

Table A.5.5: Batch test results

Initial Conc. mg/L	Final Conc (Ce)	% removal	q (mg/g)
0.1	0	100	0.00666667
1	0.12	88	0.05866667
2	0.32	84	0.112
3	0.495	83.5	0.167
4	0.7	82.5	0.22
5	0.95	81	0.27
8	1.688	78.9	0.4208
10	2.36	76.4	0.50933333

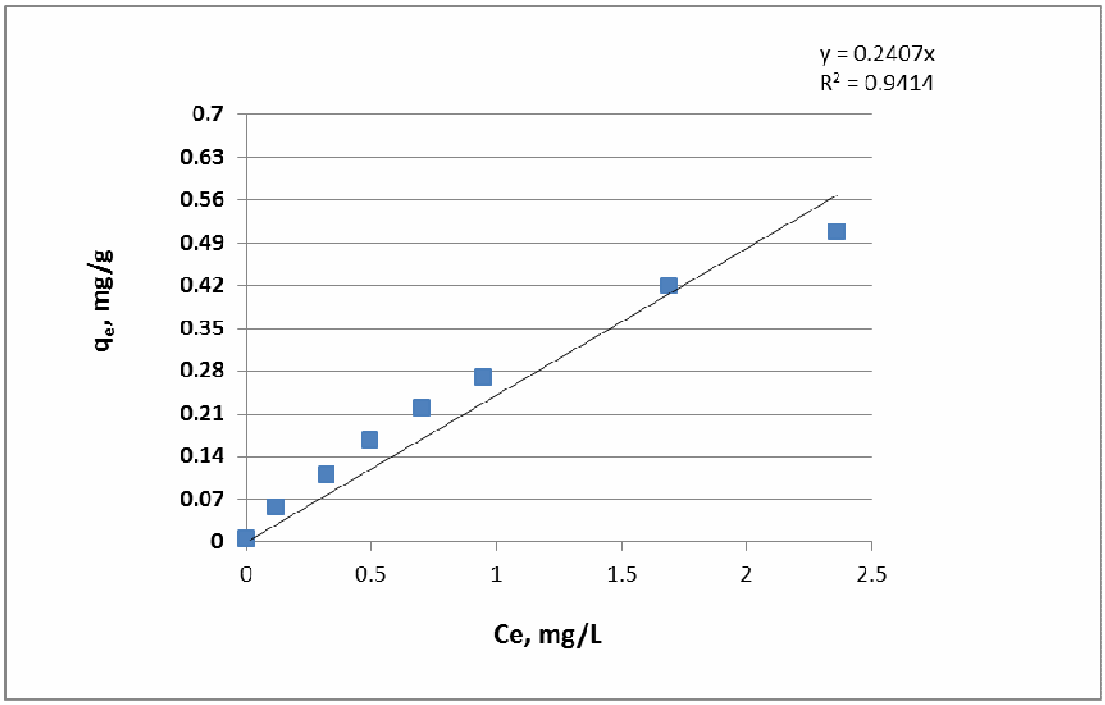

Figure A.5.2: Linear Isotherm plot

Distribution Coefficient (K_D) = q_e/C_e= 0.2407 L/g.

8) Model results (for Figure 6.7)

POLLUTEv7

Version 7.00

Column-1

THE DARCY VELOCITY (Flux) THROUGH THE LAYERS Va = 94.17 m/year

Layer Properties

Layer	Thickness	Number of Sublayers	Coefficient of Hydrodynamic Dispersion	Matrix Porosity	Distributon Coefficient	Dry Density
1	0.1016 m	1	0.02823 m^2/day	0.39	0.22 m^3/kg	2.19 g/cm^3

Boundary Conditions

Contant Concentration
Source Concentration = 10 mg/L

Fixed Outflow Bottom Boundary
Landfill Length = 0.1016 m
Landfill Width = 1 m
Base Thickness = 0.1 mm
Base Porosity = 0.39
Base Outflow Velocity = 0.258 m/day

Laplace Transform Parameters

TAU = 7 **N =** 20 **SIG =** 0 **RNU =** 2

Calculated Concentrations at Selected Times and Depths

Time day	Depth m	Concentration mg/L
7.7	0.000E+00 1.016E-01	1.000E+01 4.024E-06
15.4	0.000E+00 1.016E-01	1.000E+01 8.656E-03
23.1	0.000E+00 1.016E-01	1.000E+01 1.213E-01
30.8	0.000E+00 1.016E-01	1.000E+01 4.722E-01

38.5	0.000E+00 1.016E-01	1.000E+01 1.093E+00
46.2	0.000E+00 1.016E-01	1.000E+01 1.944E+00
53.8	0.000E+00 1.016E-01	1.000E+01 2.952E+00
61.5	0.000E+00 1.016E-01	1.000E+01 4.094E+00
69	0.000E+00 1.016E-01	1.000E+01 5.283E+00
72.3	0.000E+00 1.016E-01	1.000E+01 5.823E+00
73.8	0.000E+00 1.016E-01	1.000E+01 6.072E+00
75.4	0.000E+00 1.016E-01	1.000E+01 6.338E+00
76.9	0.000E+00 1.016E-01	1.000E+01 6.589E+00
84.6	0.000E+00 1.016E-01	1.000E+01 7.892E+00
92.3	0.000E+00 1.016E-01	1.000E+01 9.209E+00
93.8	0.000E+00 1.016E-01	1.000E+01 9.467E+00
95.4	0.000E+00 1.016E-01	1.000E+01 9.742E+00
96.9	0.000E+00 1.016E-01	1.000E+01 1.000E+01

POLLUTEv7

Version 7.00

Column-2

THE DARCY VELOCITY (Flux) THROUGH THE LAYERS Va = 96.36 m/year

Layer Properties

Layer	Thickness	Number of Sublayers	Coefficient of Hydrodynamic Dispersion	Matrix Porosity	Distributon Coefficient	Dry Density
1	0.1016 m	1	0.021756 m^2/day	0.4	0.21 m^3/kg	2.2 g/cm^3

Boundary Conditions

Contant Concentration
Source Concentration = 10 mg/L

Fixed Outflow Bottom Boundary
Landfill Length = 0.1016 m
Landfill Width = 1 m
Base Thickness = 0.1 mm
Base Porosity = 0.4
Base Outflow Velocity = 0.264 m/day

Laplace Transform Parameters

TAU = 7 **N =** 20 **SIG =** 0 **RNU =** 2

Calculated Concentrations at Selected Times and Depths

Time day	Depth m	Concentration mg/L
7.7	0.000E+00 1.016E-01	1.000E+01 2.268E-07
15.4	0.000E+00	1.000E+01

	1.016E-01	2.330E-03
23.1	0.000E+00 1.016E-01	1.000E+01 5.495E-02
29.2	0.000E+00 1.016E-01	1.000E+01 2.121E-01
38.5	0.000E+00 1.016E-01	1.000E+01 7.508E-01
44.6	0.000E+00 1.016E-01	1.000E+01 1.310E+00
53.8	0.000E+00 1.016E-01	1.000E+01 2.421E+00
63.1	0.000E+00 1.016E-01	1.000E+01 3.802E+00
69.2	0.000E+00 1.016E-01	1.000E+01 4.813E+00
72.3	0.000E+00 1.016E-01	1.000E+01 5.352E+00
75.4	0.000E+00 1.016E-01	1.000E+01 5.904E+00
78.5	0.000E+00 1.016E-01	1.000E+01 6.470E+00
81.5	0.000E+00 1.016E-01	1.000E+01 7.027E+00
84.6	0.000E+00 1.016E-01	1.000E+01 7.611E+00
93.8	0.000E+00 1.016E-01	1.000E+01 9.390E+00
95.4	0.000E+00 1.016E-01	1.000E+01 9.704E+00
96.9	0.000E+00 1.016E-01	1.000E+01 1.000E+01

misrepresentations that may occur from the use of this computer program. The user accepts full responsibility for assessing the validity and applicability of the results obtained with this program for any specific case.

POLLUTEv7

Version 7.00

Column-3

THE DARCY VELOCITY (Flux) THROUGH THE LAYERS Va = 94.17 m/year

Layer Properties

Layer	Thickness	Number of Sublayers	Coefficient of Hydrodynamic Dispersion	Matrix Porosity	Distributon Coefficient	Dry Density
1	0.1143 m	1	0.024985 m^2/day	0.41	0.21 m^3/kg	2.37 g/cm^3

Boundary Conditions

Contant Concentration
Source Concentration = 10 mg/L

Fixed Outflow Bottom Boundary
Landfill Length = 0.1143 m
Landfill Width = 1 m
Base Thickness = 0.1 mm
Base Porosity = 0.41
Base Outflow Velocity = 0.258 m/day

Laplace Transform Parameters

TAU = 7 **N =** 20 **SIG =** 0 **RNU =** 2

Calculated Concentrations at Selected Times and Depths

Time day	Depth m	Concentration mg/L
9.1	0.000E+00	1.000E+01

	1.143E-01	2.956E-07
18.2	0.000E+00 1.143E-01	1.000E+01 2.545E-03
27.3	0.000E+00 1.143E-01	1.000E+01 5.658E-02
36.4	0.000E+00 1.143E-01	1.000E+01 2.776E-01
45.5	0.000E+00 1.143E-01	1.000E+01 7.381E-01
54.5	0.000E+00 1.143E-01	1.000E+01 1.430E+00
63.6	0.000E+00 1.143E-01	1.000E+01 2.335E+00
72.7	0.000E+00 1.143E-01	1.000E+01 3.402E+00
81.8	0.000E+00 1.143E-01	1.000E+01 4.591E+00
85.5	0.000E+00 1.143E-01	1.000E+01 5.101E+00
87.3	0.000E+00 1.143E-01	1.000E+01 5.354E+00
89.1	0.000E+00 1.143E-01	1.000E+01 5.610E+00
90.9	0.000E+00 1.143E-01	1.000E+01 5.868E+00
100	0.000E+00 1.143E-01	1.000E+01 7.207E+00
109.1	0.000E+00 1.143E-01	1.000E+01 8.590E+00
110.9	0.000E+00 1.143E-01	1.000E+01 8.867E+00
112.7	0.000E+00 1.143E-01	1.000E+01 9.145E+00
114.5	0.000E+00 1.143E-01	1.000E+01 9.424E+00
116.4	0.000E+00 1.143E-01	1.000E+01 9.719E+00

118.2	0.000E+00 1.143E-01	1.000E+01 1.000E+01

NOTICE

Although this program has been tested and experience would indicate that it is accurate within the limits given by the assumptions of the theory used, we make no warranty as to workability of this software or any other licensed material. No warranties either expressed or implied (including warranties of fitness) shall apply. No responsibility is assumed for any errors, mistakes or misrepresentations that may occur from the use of this computer program. The user accepts full responsibility for assessing the validity and applicability of the results obtained with this program for any specific case.

VITA

Name Saidur Rahman Chowdhury

Post-secondary Education

The University of Western Ontario (UWO)
London, ON, Canada
Ph.D Candidate in Civil and Environmental Engineering (CEE), 2009-2013.

The University of Western Ontario
London, ON, Canada
M.E.Sc in Civil and Environmental Engineering, 2006-2008.

	Shahjalal University of Science and Technology, Sylhet, Bangladesh. B.Sc. in Civil and Environmental Engineering, 1997-2002.
Academic Honors	Ontario Graduate scholarship, Canada, 2012-13
	R.M. Quigley Award (2011), Geotechnical Research Center, CEE, UW, Canada.
	Ontario Graduate scholarship, Canada, 2011-12
	Western Graduate Scholarship, Canada (2009-12)
	Western Graduate Research Scholarship, Canada (2007-08)
	International Graduate Student Scholarship Western University London, ON, Canada, 2006-2008
	Excellence Award in Undergraduate studies Shahjalal University of Science and Technology, Sylhet, Bangladesh, 1999-2002.
Related Work Experiences	Graduate Teaching and Research Assistant The University of Western Ontario London, ON, Canada, 2006-2012.
	Lecturer, Dept of Civil and Environmental Engineering, Shahjalal University of Science and Technology, Sylhet, Bangladesh, 2004-2006.

Publications

a) Articles published in refereed journals

1) Chowdhury, S.R., Yanful, E.K., and Pratt, A.R., (2012). Chemical states in XPS and Raman analysis during removal of Cr(VI) from contaminated water by mixed maghemite–magnetite nanoparticles. Journal of Hazardous Materials. 235–236, 246–256.
2) Chowdhury, S.R., Yanful, E.K., and Pratt, A.R., (2011). Arsenic removal from aqueous solutions by mixed magnetite-maghemite nanoparticles. Environmental Earth Sciences, 64(2), 411-423. ISSN 1866-6280.
3) Chowdhury, S.R., and Yanful, E.K., (2011). Arsenic removal from aqueous solutions by adsorption on magnetite nanoparticles. Water and Environment Journal. 25(3), 429-437.

4) Chowdhury, S.R., and Yanful, E.K., (2010). Arsenic and chromium removal by mixed magnetite-maghemite nanoparticles and the effect of phosphate on removal. Journal of Environmental Management. 91(11), 2238-2247.

b) Articles submitted to refereed journals

1) Chowdhury, S.R., and Yanful, E.K., (2012). Kinetics of Cadmium(II) uptake by mixed maghemite- magnetite nanoparticles. Journal of Environmental Management. JEMA-D-12-02234 (Under Review).
2) Chowdhury, S.R., Yanful, E.K., and Pratt, A.R., (2013). Transport and chemical states analysis during arsenic removal by monolith slag from nickel smelter. Water Research. WR-S-13-01424 (Under Review).

c) Non-refereed Contributions

1) Chowdhury, S.R. and Yanful, E.K**.,** (2008). Application Of Nano Scale Magnetite Particles For Arsenic Contaminated Ground Water Remediation. Canadian Water and Wastewater Association (CWWA), 13th Canadian National Conference & 4th Policy Forum on Drinking Water Conference Proceedings. Page no 448-468.
2) Chowdhury, S.R., Chowdhuary, R.K., Mahzuz, H.M.A., Chowdhury, M.A.I., Sharmin, R., Faruque, S.B., and Saleem, S.M., (2008). Feasibility study of a Composting Plant in Sylhet City. Proceedings of the National Seminar on Solid Waste Management-Waste Safe 2008. Khulna, Bangladesh.
3) Hoque, M.A., **Chowdhury, S. R.,** and Islam, M. F., (2004). Effect of Unplanned Urbanization on Air Quality -A Case Study on Sylhet City. Published on International Symposium on Environmental Management (ISEM), BUET, 7-16.
4) Alam, M. J.B., **Chowdhury, S.R.,** Reza, I., and Rahman, A.M., (2007). Management of Effluent from Textile Industries; Proceedings of International Conference and Exhibition on Water and Waste water Treatment (Asia Pro Eco Project INNOWA Results), 135-139.